PUBLICATION P1

Trousil J., Syrová Z., Dal N. K., Rak D., Konefał R., Pavlova E., Matějková J., Cmarko D., Kubíčková P., Pavliš O., Urbánek T., Sedlák M., Fenaroli F., Raška I., Štěpánek P., Hrubý M. *Biomacromolecules*. 2019, 20 (4), 1798–1815. IF = 5.67

J.T. synthesized the polymers, carried out the physicochemical characterizations, conceptualized all the biological experiments, and wrote the paper. Z.S. carried out the cytotoxicity and confocal microscopy investigations and contributed to the final version of the manuscript. N.K.D. and F.F. were responsible for the experiments with zebrafish and contributed to the final version of the manuscript. D.R. and M.S. were responsible for the AFFFF investigations. R.K. carried out the NMR experiments. E.P. and D.C. carried out the TEM investigations. O.P. and P.K. supervised the in vitro infection experiment and contributed to the final version of the manuscript. U.T. carried out some of the physicochemical characterizations. I.R. contributed to the final version of the paper. P.Š. contributed to the final version of the paper. M.H. supervised the project and contributed to the final version of the paper.

BIOMACROMOLECULES
Article
Cite This: Biomacromolecules 2019, 20, 1798−1815
pubs.acs.org/Biomac

Rifampicin Nanoformulation Enhances Treatment of Tuberculosis in Zebrafish

Jiří Trousil,[*,†,‡] Zdeňka Syrová,[§] Nils-Jørgen K. Dal,[∥] Dmytro Rak,[⊥] Rafał Konefał,[†] Ewa Pavlova,[†] Jana Matějková,[#] Dušan Cmarko,[§] Pavla Kubíčková,[¶] Oto Pavliš,[¶] Tomáš Urbánek,[†] Marián Sedlák,[⊥] Federico Fenaroli,[∥] Ivan Raška,[§] Petr Štěpánek,[†] and Martin Hrubý[*,†]

[†]Institute of Macromolecular Chemistry, Czech Academy of Sciences, Heyrovského náměstí 2, 162 00 Prague 6, Czech Republic

[‡]Department of Analytical Chemistry, Faculty of Science, Charles University, Hlavova 8, 128 43 Prague 2, Czech Republic

[§]Institute of Biology and Medical Genetics, First Faculty of Medicine, Charles University and General University Hospital in Prague, Albertov 4, 128 00 Prague 2, Czech Republic

[∥]Department of Biosciences, University of Oslo, Blindernveien 31, 0371 Oslo, Norway

[⊥]Institute of Experimental Physics, Slovak Academy of Sciences, Watsonova 47, 040 01 Košice, Slovakia

[#]Department of Medical Microbiology, Second Faculty of Medicine, Charles University and Motol University Hospital, V Úvalu 84, 150 06 Prague 5, Czech Republic

[¶]Center of Biological Defense, Military Health Institute, Military Medical Agency, 561 66 Těchonín, Czech Republic

Supporting Information

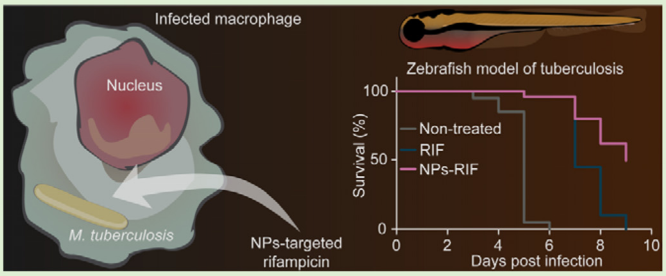

ABSTRACT: *Mycobacterium tuberculosis*, the etiologic agent of tuberculosis, is an intracellular pathogen of alveolar macrophages. These cells avidly take up nanoparticles, even without the use of specific targeting ligands, making the use of nanotherapeutics ideal for the treatment of such infections. Methoxy poly(ethylene oxide)-*block*-poly(ε-caprolactone) nanoparticles of several different polymer blocks' molecular weights and sizes (20−110 nm) were developed and critically compared as carriers for rifampicin, a cornerstone in tuberculosis therapy. The polymeric nanoparticles' uptake, consequent organelle targeting and intracellular degradation were shown to be highly dependent on the nanoparticles' physicochemical properties (the cell uptake half-lives 2.4−21 min, the degradation half-lives 51.6 min−ca. 20 h after the internalization). We show that the nanoparticles are efficiently taken up by macrophages and are able to effectively neutralize the persisting bacilli. Finally, we demonstrate, using a zebrafish model of tuberculosis, that the nanoparticles are well tolerated, have a curative effect, and are significantly more efficient compared to a free form of rifampicin. Hence, these findings demonstrate that this system shows great promise, both *in vitro* and *in vivo*, for the treatment of tuberculosis.

■ INTRODUCTION

Tuberculosis (TB) represents a global health problem, despite the fact that a potentially curative therapy has been available for approximately 50 years. Infectious diseases, including tuberculosis, remain the leading cause of preventable death in the world.[1,2] Tuberculosis is caused by *Mycobacterium tuberculosis*, a slender, nonmotile and acid-fast bacillus, that is approximately 0.5−3 μm in size.

In general, the ability of mycobacteria to survive and persist in alveolar and other types of macrophages (Mϕ), which are reservoirs of this intracellular pathogen, is the main cause of failure of the treatment and eradication of TB. This strategy allows mycobacterial cells to not only become invisible to the immune defense but to also be insusceptible to the effects of conventional drugs. The standard treatment regimen consists of an intensive phase of 2 months of treatment with first-line anti-TB drugs, including isoniazid, rifampicin, pyrazinamide, and ethambutol, followed by a 4-month continuation phase of treatment with isoniazid and rifampicin (RIF).[3,4] Finally, the development of multidrug-resistant (MDR-TB) and extensively drug-resistant (XDR-TB) strains of *M. tuberculosis* as well as the increase in the number of patients with TB who are coinfected with HIV represent important complications for TB treatment.[5,6]

Recently, nanomedicine has emerged as one of the most promising approaches for overcoming the above-listed challenges associated with TB therapy. The utilization of nanocarriers for drug delivery into the lungs, the primary target organ for TB treatment due to the presence of *M. tuberculosis*-infected alveolar Mϕ, offers an elegant way to circumvent numerous difficulties associated with conventional

Received: February 12, 2019
Published: February 20, 2019

ACS Publications © 2019 American Chemical Society

DOI: 10.1021/acs.biomac.9b00214
Biomacromolecules 2019, 20, 1798−1815

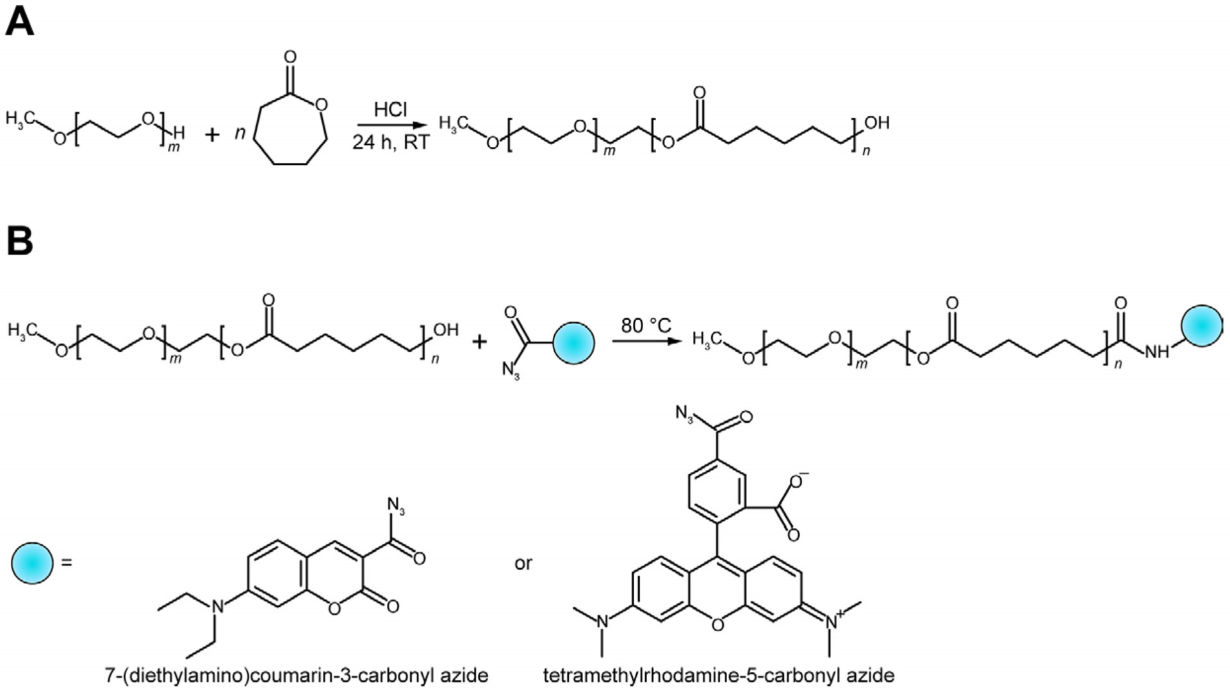

Figure 1. Reaction schemes. (A) Synthesis of the amphiphilic block copolymer poly(ethylene oxide)-*block*-poly(ε-caprolactone) using hydrogen chloride as a catalyst. (B) Conjugation with fluorescent dyes.

therapy.[7−9] For example, these systems enhance the therapeutic effectiveness and minimize the undesirable side effects of numerous antibacterial drugs.[5,10]

In this context, several types of anti-TB nanoformulations including for example solid lipid nanoparticles,[7,11] inorganic nanoparticles,[8,12,13] micelles,[14] and polymeric nanoparticles[15−18] have been utilized. In other words, a wide variety of nanocarriers and biomaterials have been explored for mono- and multidrug delivery in TB. Most of these interesting systems elucidated for TB regimens, however, need further preclinical study and robust biorelevant analysis both *in vitro* and *in vivo* to move on to the next step and reach to the patients.

The objective of the present study was to study the biorelevant properties of biodegradable and biocompatible rifampicin nanoformulations based on MPEO-*b*-PCL, which were prepared using a ring-opening polymerization. We critically quantitatively compared behavior of the formulations in relation to different molecular weights of the polymer blocks and different physicochemical properties allowing fine-tuning and generalization for Mϕ-targeted nanomedicines. We tested these systems with a virulent strain *M. tuberculosis* H37Rv as well as using a zebrafish-based *in vivo* model of tuberculosis. On the basis of our previous work, we studied the effect of this passively targeted drug delivery system on *M. tuberculosis*-infected Mϕ, with subsequent testing of its antimycobacterial properties *in vivo*.

■ MATERIALS AND METHODS

Materials. ε-Caprolactone (CL, 97%), calcium hydride (CaH_2, 95%), 1,4-diaminobutane (99%), 7-(diethylamino)coumarin-3-carbonyl azide (DACCA, BioReagent, ≥92%), hydrogen chloride (2.0 M in diethyl ether solution), lipase from *Pseudomonas* sp. (type XIII), α-methoxy-ω-hydroxy poly(ethylene oxide) (MPEO, M_n of 2 000 and 5 000 Da), Nile red (BioReagent, ≥98%), 4-nitrophenyl chloroformate (96%), penicillin−streptomycin solution (BioReagent), phosphate-buffered saline (tablets), *N*-phenylthiourea (PTU), rifampicin (RIF, ≥97%), thiazolyl blue tetrazolium bromide (MTT), triethylamine (≥99%) and Triton X-100 (BioUltra, 10%, for molecular biology) were purchased from Sigma-Aldrich Ltd. (Prague, Czech Republic).

Amphotericin B (250 μg/mL), CellMask Deep Red plasma membrane stain, CO_2 Independent Medium, Dulbecco's Modified Eagle Medium (DMEM, high glucose, GlutaMAX), fetal bovine serum (FBS, heat-inactivated), L-glutamine (200 mM), LysoTracker Deep Red, and tetramethylrhodamine-5-carbonyl azide (TMR) were purchased from Life Technologies Czech Republic Ltd. (Prague, Czech Republic).

Lead citrate, LRWhite resin and uranyl acetate were purchased from Electron Microscopy Sciences (Hatfield, USA).

The CL was dried over CaH_2 with continuous stirring at room temperature for 48 h and distilled under reduced pressure before use. MPEO was dehydrated by the azeotropic distillation of water in toluene, precipitated with cool diethyl ether (Et_2O), filtered, washed with Et_2O, and dried *in vacuo* at room temperature.

All of the other chemicals that were used were of the highest quality that is commercially available and were used in the form in which they were received.

Synthesis and Characterization of the Copolymers. The copolymers were prepared using the metal-free method (Figure 1A) described by the Lee group.[19,20] Briefly, calculated amounts of azeotropically dried MPEO (1 equiv) and dried CL were added to a flame-dried glass tube containing 10 mL of dry CH_2Cl_2 and a magnetic stirring bar that was connected to a vacuum system. Subsequently, an exhausting-refilling process using argon was repeated multiple times, with continuous cooling provided by the solid CO_2/ethanol mixture. Polymerization was then initiated by the addition of a 2.0 M HCl solution (2 equiv) at 25 °C and the reaction mixture was incubated with stirring overnight. The resulting copolymers were precipitated using cool Et_2O and filtered. The filtrate was washed with cool Et_2O and dried *in vacuo* at room temperature.

The resulting yields ranged from 85% to 90%. The ^1H NMR (300 MHz, $CDCl_3$, δ) results were as follows: peak a (δ = 3.37 ppm, $\mathbf{CH_3}$−O−); peaks b+c (δ = 3.63 ppm, PEO repeating unit −$\mathbf{CH_2}$−$\mathbf{CH_2}$−O−); peak d (δ = 4.21 ppm, −O−CH_2−$\mathbf{CH_2}$−); peak e (δ = 2.29 ppm, CL repeating unit −CO−$\mathbf{CH_2}$−CH_2−CH_2−CH_2−CH_2−O−); peaks f+h (δ = 1.64 ppm, CL repeating unit −CO−CH_2−

$\mathbf{CH_2}-CH_2-\mathbf{CH_2}-CH_2-O-$); peak g ($\delta$ = 1.37 ppm, CL repeating unit $-CO-CH_2-CH_2-\mathbf{CH_2}-CH_2-CH_2-O-$); peak i ($\delta$ = 4.05 ppm, CL repeating unit $-CO-CH_2-CH_2-CH_2-CH_2-\mathbf{CH_2}-O-$); peak j ($\delta$ = 2.54 ppm, $-\mathbf{OH}$).

Fluorescent Labeling of the Block Copolymer Matrix. The prepared MPEO-*b*-PCL copolymers were labeled (Figure 1B) with both 7-(diethylamino)-coumarin-3-carbonyl azide (DACCA) and tetramethylrhodamine-5-carbonyl azide (TMR).

The labeling with both DACCA and TMR were performed as previously described.[21] Briefly, 10 mg (1 equiv) of azeotropically dried MPEO-*b*-PCL and either tetramethylrhodamine-5-carbonyl azide or 7-(diethylamino)coumarin-3-carbonyl azide (3 equiv) were dissolved in 10 mL of freshly distilled toluene in an argon atmosphere. The resulting solution incubated at 80 °C overnight, with stirring. Subsequently, the reaction mixture was placed in a dialysis bag (MWCO 3500 Da) and dialyzed against demineralized water for 5 days. The aqueous solutions were then freeze-dried.

In both cases, UV/vis and fluorescence spectroscopy were used to confirm covalent bonding of the DACCA to the polymer backbone (Figure S1C and S1D). The efficiency of the labeling, expressed as the ratio of the determined amount of the dye to the theoretical amount of dye, ranged from 83% to 92%. To ensure the use of material containing the same amount of DACCA (i.e., 12 μg/mg, cf. Table SII, Supporting Information), mixtures of the fluorescent conjugates and the nonlabeled copolymers were used for subsequent experiments. For this purpose, a product with the lowest dye content (i.e., **P5**) was used as the default for making the calculations.

Proton Nuclear Magnetic Resonance. To confirm the structure of the prepared and labeled MPEO-*b*-PCL copolymers, proton nuclear magnetic resonance (^{1}H NMR) was used. ^{1}H NMR spectra were recorded using a Bruker Avance DPX 300 (and/or Avance III 600 MHz) spectrometer (Bruker Daltonik GmbH, Bremen, Germany) operating at 300.1 MHz (or 600.2 MHz). All NMR spectra were measured using samples in 5 mm NMR tubes with $CDCl_3$ as the solvent at 25 °C. The chemical shifts are relative to TMS, using hexamethyldisiloxane (HMDSO, δ = 0.05 ppm from TMS) as the internal standard. The typical conditions that were used for the spectra collection were as follows: $\pi/2$ pulse width, 15.6 μs (10 μs); relaxation delay, 10 s; spectral width, 6.6 kHz; acquisition time, 4.95 s (2.18 s).

Gel Permeation Chromatography. Gel permeation chromatography (GPC) was used to determine the M_w, M_n and M_w/M_n (dispersity, $Đ$) values, and for molar mass distribution control. GPC separations were performed using a Deltachrom pump (Watrex Ltd., Prague, Czech Republic), Midas Spark autosampler (DataApex Ltd., Prague, Czech Republic) and two PLgel MIXED-B-LS columns (30 × 1 cm, particle size 10 μm) for separation in the molecular weight range of approximately 400−10,000 000 Da. Tetrahydrofuran (THF) was used as the mobile phase. The detector was a PL ELS-1000 evaporative light scattering detector (Polymer Laboratories, Varian Inc., Amherst, USA). The data were accumulated and processed using Clarity Software version 6.0.0.295 (DataApex Ltd.). The injection volume of the GPC system was 0.1 mL. Separations were performed with a mobile phase (THF) flow rate of 1 mL/min. Evaluation of the chromatograms utilized calibration that was based on a set of polystyrene (PS) standards.

Preparation of Nanoparticles. Nanoformulations were prepared using a nanoprecipitation method that was previously described.[18] Briefly, the copolymer (10 mg) was dissolved in 2.5 mL of acetone at room temperature. The resulting polymer solution was subjected to the quick addition of 10 mL of Milli-Q water or PBS with continuous stirring (200 rpm). RIF-loaded formulations were prepared in the presence of RIF using the same method, i.e. the acetone solution of the polymer and rifampicin was subjected to the quick addition of water or PBS. Acetone was removed via evaporation at a reduced pressure (40 °C) in both cases. All of the prepared formulations were subjected to filtration through a 0.22 μm PVDF filter before all subsequent experiments.

Critical Aggregation Concentration (CAC). The NPs solutions of the copolymers were prepared by the above-described protocol and subjected to serial dilution to obtain a concentration as low as 10^{-6} mg/mL, with subsequent stabilization overnight. Each sample was then prepared with the addition of 5 μL of Nile red solution (in ethanol) to 100 μL of the diluted solution, with subsequent stabilization overnight. The final concentration of Nile red in the samples was 1×10^{-6} mol/L.

The fluorescence of the samples were recorded using a Synergy H1 Hybrid Reader instrument (Biotek, Winooski, USA) at an excitation wavelength of 550 nm. The fluorescence emission intensities at 650 nm were then evaluated and a graph of fluorescence intensity vs negative logarithm of the concentration was plotted. From this graph, the CAC was determined as the intersection of two straight lines drawn through points at low and high concentrations.

Drug Loading and Entrapment Efficiency. The drug incorporation efficiency was expressed in the form of both the drug content (drug loading, DL, %) and the entrapment efficiency (EE, %), which are represented by eqs 1 and 2, respectively.

$$\mathrm{DL} = \frac{\text{mass of the drug contained in nanoparticles}}{\text{mass of the nanoparticles containing drug}} \times 100 \tag{1}$$

$$\mathrm{EE} = \frac{\text{mass of drug in nanoparticles}}{\text{mass of drug used for the formulation}} \times 100 \tag{2}$$

The mass of the drug contained in nanoparticles was calculated as the difference between the total mass of RIF used and the mass of free (i.e., nonencapsulated) RIF in the nanoformulation. For the separation of NPs, ultrafiltration of the nanoformulations using an Amicon Ultra-15 Centrifugal Filter Unit with an Ultracel 100 kDa membrane (Millipore, Ireland), with centrifugation at 1 000 rpm, was used.

The RIF was then quantified using UV/vis spectroscopy. Briefly, an aliquot (200 μL) of the filtrate or the initial formulation was diluted with 3.8 mL of acetonitrile. Absorbance measurements (477 nm) were performed on a Synergy H1 Hybrid Reader instrument (Biotek, Winooski, USA). Quantification of RIF was performed using a set of RIF standards. The mass of the nanoparticles containing the drug was determined gravimetrically.

Dynamic Light Scattering. Nanoformulations were investigated using dynamic light scattering (DLS). The measurements were carried out on a Model ZEN3600 Nano-ZS instrument (Malvern Instruments Ltd., UK) using an angle of 173°. A He−Ne 4.0 mW laser, operating at 633 nm, was used. The data were analyzed using the DTS (Nano) program (Malvern Instruments Ltd., UK). The mean positions of the peaks within the intensity-hydrodynamic diameter (D_h) distributions were used to represent the data. The hydrodynamic diameter of the particles was calculated from the diffusion coefficient using the Stokes−Einstein equation:

$$D = \frac{k_B T}{3\pi\eta D_h} \tag{3}$$

where T is the absolute temperature, η is the viscosity of the solvent and k_B is the Boltzmann constant.

Asymmetric Flow Field-Flow Fractionation (AFFFF). The instrument setup for the asymmetric flow field-flow fractionation consisted of an Eclipse 3+ Separation System (Wyatt Technology Europe, Dernbach, Germany) coupled to a 1260 Infinity isocratic pump and degasser (Agilent Technologies, Santa Clara, CA, USA), a DAWN HELEOS-II MALS detector with a 120 mW gallium-arsenide laser at a wavelength of 661 nm (Wyatt Technology, Santa Barbara, CA, USA), and a RI-101 RI detector (Shodex, Munich, Germany). Experiments were performed using a 275 mm long trapezoidal channel assembled with a 490 μm spacer and a regenerated cellulose membrane with a 5 kDa cutoff. Filtered deionized water was employed as the mobile phase. The data were collected and processed using the ASTRA 6 software.

All of the separations were conducted according to the following description. A 100 μL sample was injected into the channel at a flow rate of 0.2 mL/min. The focusation proceeded for 5 min with a cross-flow of 3.0 mL/min. After the focusation step, the system was

P1

switched into elution mode and the sample was separated with either constant or linearly decreasing cross-flow, or with a combination of the two. The procedures were specifically optimized for each sample to achieve the best separation and analysis conditions. The detector flow rate was kept constant at 0.5 mL/min throughout the entire separation procedure. The sample concentration was 0.1 mg/mL for all samples. The molar masses (M_w) and the diameters of gyration (D_g) were calculated from the acquired data using the Zimm formalism. The refractive index increments, d*n*/d*c*, were 0.145 and 0.15 mL/g for the samples that contained and did not contain RIF, respectively.

Morphology of the Nanoparticles. A 4 μL sample of the nanoformulation was applied to an electron microscopy grid covered with lacey carbon supporting film (400 mesh, Cu, Agar Scientific, UK) after hydrophilization by glow discharge (Expanded Plasma Cleaner, Harrick Plasma, USA). The excess solution was absorbed using Whatman filter paper No. 1 for approximately 1 s. Subsequently, the grid was immediately plunged into liquid ethane held at −182 °C. The vitrified sample was immediately transferred, without being allowed to thaw, into the microscope and observed at −173 °C.

All of the samples, except for those containing $MPEO_{44}$-*b*-PCL_{18} (**P1**), were examined using a Tecnai G2 Spirit Twin 120 kV microscope (FEI, Czech Republic) equipped with a cryo-holder (cryo-specimen holder, Gatan) using a bright field imaging mode at an accelerating voltage of 120 kV; whereas the $MPEO_{44}$-*b*-PCL_{18}-based nanoformulations were observed using a Talos 200C microscope (FEI, Czech Republic) equipped with phase-plates, which are used to enhance the image contrast.

Enzymatic Degradation of the MPEO-*b*-PCL NPs. Nanoparticle degradation was measured in the presence of lipase from *Pseudomonas* sp. using DLS and ^{1}H NMR.

During the degradation experiment, an appropriate amount of lipase (4 U/mL in PBS) was added to the MPEO-*b*-PCL formulation (1 mg/mL in PBS) to initiate biodegradation. The final concentrations of the enzyme and the nanoparticles were 0.36 U/mL and 0.91 mg/mL, respectively. The biodegradation was conducted at 37 °C. During the DLS experiments, degradation was allowed to proceed inside a DLS cuvette to the light scattering intensity (derived count rate) *in situ* over time.

During the ^{1}H NMR degradation study, the same concentrations were used but with deuterated PBS. The ^{1}H NMR spectra were recorded using a Bruker Avance III 600 MHz spectrometer operating at 600.2 MHz at 37 °C with 4 scans, using 5 mm NMR tubes.

Rifampicin Release. The *in vitro* release of RIF was studied by way of a dialysis method using Spectra/Por 6 dialysis tubes (MWCO 3.5 kDa) without and in the presence of lipase (lipase from *Pseudomonas* sp.). For this purpose, 2 mL of **P4-RIF** formulation and an appropriate amount of lipase or PBS were transferred to the dialysis tube. The final concentration of the copolymer and the enzyme were 0.91 mg/mL and 0.36 U/mL, respectively. The dialysis was performed in 200 mL of PBS (pH 7.4) with continuous shaking (150 rpm) at 37 °C. The RIF release was evaluated based on a decrease in the measured absorbance at a wavelength of 477 nm (Synergy H1 Hybrid Reader instrument, Biotek, Winooski, USA) after aliquots were withdrawn from the inside space of the dialysis tubing.

Hemolysis Assay. For the analysis of the blood compatibility of the prepared NPs, fresh human blood was collected into heparin-coated vacutainers (Becton Dickinson Czechia Ltd., Prague, Czech Republic). The plasma was removed from the blood by centrifugation at 3 000 rpm for 10 min, and the red blood cells (RBCs) were washed three times with PBS solution. For the hemolysis experiment, the RBCs suspension was diluted with PBS and the final concentration corresponded to full blood dilution of 1/49.

To 0.3 mL of diluted RBCs was added 1.2 mL of appropriately diluted MPEO-*b*-PCL nanoformulation. Using this procedure, several dilutions of NPs (100, 200, 400 and 800 μg/mL) were prepared. Triton X-100 (1% in PBS) and PBS served as the positive and negative controls, respectively.

After incubation at 37 °C for 4 or 8 h, the samples were centrifuged at 3,000 rpm for 10 min. Subsequently, the supernatants were collected and their absorbance values were measured at 541 nm using a Synergy H1 Hybrid Reader instrument (Biotek, Winooski, USA) with Nunc Cell Culture Microplates (Thermo Scientific Nunc, USA). The percent hemolysis of the RBCs in each sample was calculated using the following eq 4:

$$\text{hemolysis} = \frac{\text{sample absorbance} - \text{negative control}}{\text{positive control} - \text{negative control}} \times 100 \tag{4}$$

The results of the hemolysis assay were expressed as a percentage of the value of the positive control (1% Triton X-100 in PBS), which was considered to be 100%. Hemoglobin release of up to 2% was classified as nonhemolytic, according to the ASTM F756-08 standard.[22] The results of this assay are expressed as the mean value obtained from three parallel samples.

An informed signed consent was obtained from the blood donor.

Cell Culture and Bacteria. Murine monocyte-macrophage Raw 264.7 cells[23] were purchased from Sigma-Aldrich Ltd. (Prague, Czech Republic) and grown in full Dulbecco's Modified Eagle Medium (DMEM) containing 10% FBS, 100 U/mL penicillin and 100 μg/mL streptomycin in a humidified atmosphere containing 5% CO_2 at 37 °C.

Zebrafish embryonic fibroblast ZF4 cells[24] were kindly provided by Dr. Malgorzata Cebrat (Ludwik Hirszfeld Institute of Immunology and Experimental Therapy, Warsaw, Poland) and maintained in a CO_2-independent medium (10% FBS, 100 U/mL penicillin, 100 μg/mL streptomycin, 2.5 μg/mL amphotericin B and 2 mM L-glutamine) in a humidified atmosphere at 28 °C.

The bacterial strains *Mycobacterium* sp. (CCM 2853), *Mycobacterium smegmatis* (CCM 4622), *Mycobacterium phlei* (CCM 5639), *Staphylococcus aureus* subsp. *aureus* (CCM 4223) and *Escherichia coli* (CCM 3954) were purchased from the Czech Collection of Microorganisms (Masaryk University, Faculty of Science, Brno, Czech Republic). *Mycobacterium tuberculosis* H37Rv strain (ATCC 27294) was purchased from the Public Health England Culture Collection (Salisbury, UK). *Mycobacterium marinum* was obtained from the collection of the Department of Biosciences, University of Oslo. DsRed-expressing *Mycobacterium bovis* BCG were kindly provided by Prof. Gareth Griffiths (Department of Biosciences, University of Oslo, Norway). This study also included *Mycobacterium fortuitum* clinical isolate from blood culture. Strain identification was done by MALDI-TOF MS (data not shown).

E. coli and *S. aureus* subsp. *aureus* were grown on Columbia blood agar plates for 18−24 h at 37 °C and in 5% CO_2. Nontuberculous mycobacteria and slower-growing microorganisms (*M. tuberculosis*, *M. bovis* BCG) were grown on Löwenstein−Jensen egg-based medium at 35 °C and in 5% CO_2 for 72−96 h and 2−3 weeks, respectively. To culture the recombinant *M. bovis* strain, Löwenstein−Jensen medium was supplemented with hygromycin B at a concentration of 100 μg/mL.

All of the microbiological media that were used in this study were purchased from LabMediaServis Ltd. (Jaroměř, Czech Republic).

Cytotoxicity Assay. MTT assays were performed using Raw 264.7 M*ϕ* and ZF4 cells. The cells were seeded in 96-well plates at a concentration of 15 000 cells/well for the Raw 264.7 cells and 15 000 cells/well for the ZF4 cells.

After 24 h of incubation at 37 °C in 5% CO_2, the cell culture medium was replaced with 100 μL of fresh culture medium containing the formulations to be tested. After 24 or 48 h of incubation, the medium was aspirated and the cells were incubated with 50 μL of MTT solution (1 mg/mL in PBS) for 2 h. Subsequently, the MTT solution was aspirated and 100 μL of isopropyl alcohol was added. A Sunrise microplate reader (Tecan Group Ltd., Switzerland) and a Synergy H1 Hybrid Reader instrument (Biotek, Winooski, USA) were used to assess the cell viability via spectrophotometry at 570 nm (reference wavelength 690

DOI: 10.1021/acs.biomac.9b00214
Biomacromolecules 2019, 20, 1798−1815

nm). The results of the MTT assay were expressed as a percentage of the control value (obtained from cells in the control medium), which was considered to be 100%. Reduction of cell viability by more than 30% is considered a cytotoxic effect, according to the ISO 10993-5.[25] The testing was performed using at least three separate experiments.

Microscopic Investigation of Cellular Uptake. Live cell microscopy was used for the study of cellular uptake in Raw 264.7 M*ϕ*, the measurement of the cellular distribution of DACCA-labeled nanoparticles and the determination of the colocalization of lysosomes and nanocarriers. The cells were cultured in 4-chamber glass bottom dishes (Cellvis, USA), to which the nanoparticles to be tested were added at a concentration of 40 μg/mL and then incubated with 0.0125 μM of LysoTracker Deep Red for 40 min. Imaging was performed after 20 min using a spinning disc confocal system based on the Olympus IX81 microscope that was equipped with an Olympus UPlanSApo 100×/1.4NA oil immersion objective, a CSU-X spinning disc module (Yokogawa, Japan) and an Ixon Ultra EMCCD camera (Andor, UK). The cells were maintained at 37 °C and in 5% CO_2 using a microscope incubator (Okolab, USA). The image analysis was performed using ImageJ software.

Flow Cytometry. The cells were incubated for 24 h at 37 °C in 5% CO_2 at a density of 50 000 cells/cm^2. Subsequently, the nanoformulations were added at a defined concentration. The samples were measured after the addition of the nanoparticles at the indicated time intervals. The cells were analyzed using the CytoFlex flow cytometer (Beckman Coulter Inc., USA). CytExpert software (Beckman Coulter Inc. USA) was used to measure and analyze approximately 100 000 cells per sample.

Antibacterial Activity Study. The minimal inhibitory concentrations (MIC) of free RIF, RIF-loaded NPs and empty NPs were determined using broth microdilution for the nontuberculous mycobacteria, *E. coli* and *S. aureus* subsp. *aureus*. Briefly, a standard dilution series for each formulation that was tested (0.016–256 μg/mL) was prepared in a volume of 100 μL per dilution using Müeller–Hinton broth in a 96-well microtiter plate. Freshly grown colonies were used to prepare the inoculum suspensions in physiological saline solution (0.5 McFarland units). Then, the inoculation of the prepared dilutions was performed with a flame-sterilized inoculation applicator. The inoculated plates were grown at 37 °C with 5% CO_2 for 18–24 or 72–96 h, depending on the strain used. The results were recorded after observable turbidity appeared in the control wells (containing broth inoculated with any of the studied formulations). Each formulation was assayed ten times.

Time Kill Curve Assay. Time-kill curve analyses were performed by culturing *M. fortuitum* in Middlebrook 7H9 broth with oleic acid/bovine albumin/dextrose/catalase (OADC) growth supplement, in the presence of 3 antimicrobial concentrations in dilutions ranging from 1 × MIC to 16 × MIC estimated for the free RIF. Individual bottles of 30 mL of the broth containing increasing concentrations of both free RIF and RIF-loaded NPs were cultured with the inoculum (ca. 10^6 CFU/mL) at 37 °C, under shaking conditions (120 rpm). A control bottle, with inoculum but without antibiotic, as well as a sterility control (broth only) were included, as well.

At defined time intervals (0, 24, 48 and 120 h), the size of the bacterial population was quantified to characterize the effect of the formulations. Samples of 0.5 mL were taken from each bottle and serial 10-fold dilutions in PBS were prepared. Volumes of 100 μL from undiluted samples and from each dilution were plated in duplicate on Löwenstein-Jensen plates for further CFU counting after 3–5 days of incubation at 37 °C. The assay was performed in duplicate.

Macrophage Infection and Treatment. Raw 264.7 cells were seeded in 24-well plates at a density of 25 000 cells per well and incubated in full-strength DMEM for 24 h at 37 °C with 5% CO_2. A *M. tuberculosis* stock suspension was prepared using a method that utilized glass beads in DMEM (containing 5% FBS with no antibiotics) with continuous control of the optical density. The suspension used for infection of *M. tuberculosis* was prepared in DMEM (containing 5% FBS and no antibiotics) at a final density of 625 000 CFU/mL. During infection, the medium was replaced with 1 mL of the infection suspension, corresponding to a multiplicity of infection (MOI) of 2.5. After the 4 h infection procedure (at 37 °C in 5% CO_2), the cells were washed twice with 2 mL of preheated PBS to remove the extracellular bacteria and incubated overnight with 1 mL of DMEM (containing 5% FBS with no antibiotics) per well.

The formulations containing NPs or free RIF used for treatment were prepared in DMEM (containing 5% FBS with no antibiotics) using PBS-based stock solutions containing NPs or RIF. During the treatment, the medium was replaced with 1 mL of a formulation (20 μg of NPs or RIF were added to each well). M*ϕ* that were treated with a corresponding volume of PBS in DMEM (containing 5% FBS with no antibiotics) were used as a control.

Lysis of the M*ϕ* was performed using 1 mL of Triton X-100 solution (0.25% in buffered salt solution) for 5 min during the first, second and fifth days of the treatment. For the cells that were treated for 5 days, the treatment and control solutions were replaced with 1 mL of fresh medium on the third day.

Serial dilutions of the lysates were prepared in a buffered salt solution and plated on Löwenstein-Jensen plates supplemented with ampicillin (25 μg/mL). After 2–3 weeks of incubation at 35 °C in 5% CO_2, the CFU values were determined.

The infection assay was performed in duplicate. The seeding and CFU determination were performed in two parallel duplicates. The results of the assay were expressed as a percentage of the value of the control.

Microscopic Investigation of Mycobacteria-Infected M*ϕ*. Raw 264.7 cells were seeded on the bottom of ibidi μ-Dishes (ibidi GmbH, Planegg/Martinsried, Germany) and allowed to adhere overnight. The infection and treatment of the cells were performed using the previously described protocol with slight modifications. Briefly, the *M. tuberculosis* H37Rv strain was replaced with the DsRed-expressing *M. bovis* BCG carrying hygromycin B resistance, and the RIF-loaded NPs were replaced with DACCA-labeled NPs. The cells were treated for 1 day with a concentration of 20 μg/mL.

For the confocal laser scanning microscopy study, the cells were washed with PBS, stained with CellMask Deep Red according to the manufacturer's protocol, and fixed using a paraformaldehyde solution (4% in PBS). The cells were rapidly examined using an Olympus FV 10 confocal laser scanning microscope (Olympus Czech Group Ltd., Prague, Czech Republic) with a 60× oil objective. The signals were detected using channels Ch1 (DACCA, exc. 405 nm, em. 425–475 nm), Ch2 (DsRed-expressing *M. bovis* BCG, exc. 543 nm, em. 555–605 nm) and Ch3 (CellMask Deep Red, exc. 635, em. 655–755).

For the transmission electron microscopy study, the cells were washed with PBS and fixed with 2% paraformaldehyde and 2.5% glutaraldehyde (in 0.1 M PBS) and kept on ice before the subsequent preparation. Within a few hours, the aldehyde-fixed monolayers were washed, dehydrated in ethanol and embedded in LRWhite resin that was polymerized using heat. The embedded cells were separated from the coverslips after a short treatment with liquid nitrogen and cut parallel to the substrate using a Leica Ultracut ultramicrotome (Leica Microsystems, Vienna, Austria). The ultrathin sections were mounted on Formvar/carbon-coated nickel grids and stained with aqueous uranyl acetate and lead citrate. The grids were examined using a Tecnai G2Sphera 20 electron microscope (FEI Company, Hillsboro, OR, USA) equipped with a LaB6 gun. The images were recorded using an accelerating voltage of 120 kV with a GatanUltraScan 1000 slow scan CCD camera (Gatan, Pleasanton, CA, USA).

Survival Testing with Zebrafish *in Vivo*. The microinjection protocol that was used was adapted from the work of Cosma and colleagues.[26] At 2 days postfertilization, the zebrafish embryos (n = 19–24) were infected with DsRed-expressing *M. marinum* suspended in a 1% Tween 80 solution. Five nanoliters of the bacterial suspension, containing approximately 160 CFU, was injected into the posterior cardinal vein. The embryos were allowed to recover overnight before being injected with free RIF, the RIF-loaded nanoparticles contained in MPEO$_{113}$-*b*-PCL$_{33}$ (**P4-RIF**) or blank nanoparticles (**P4**; as a control). The administration of the

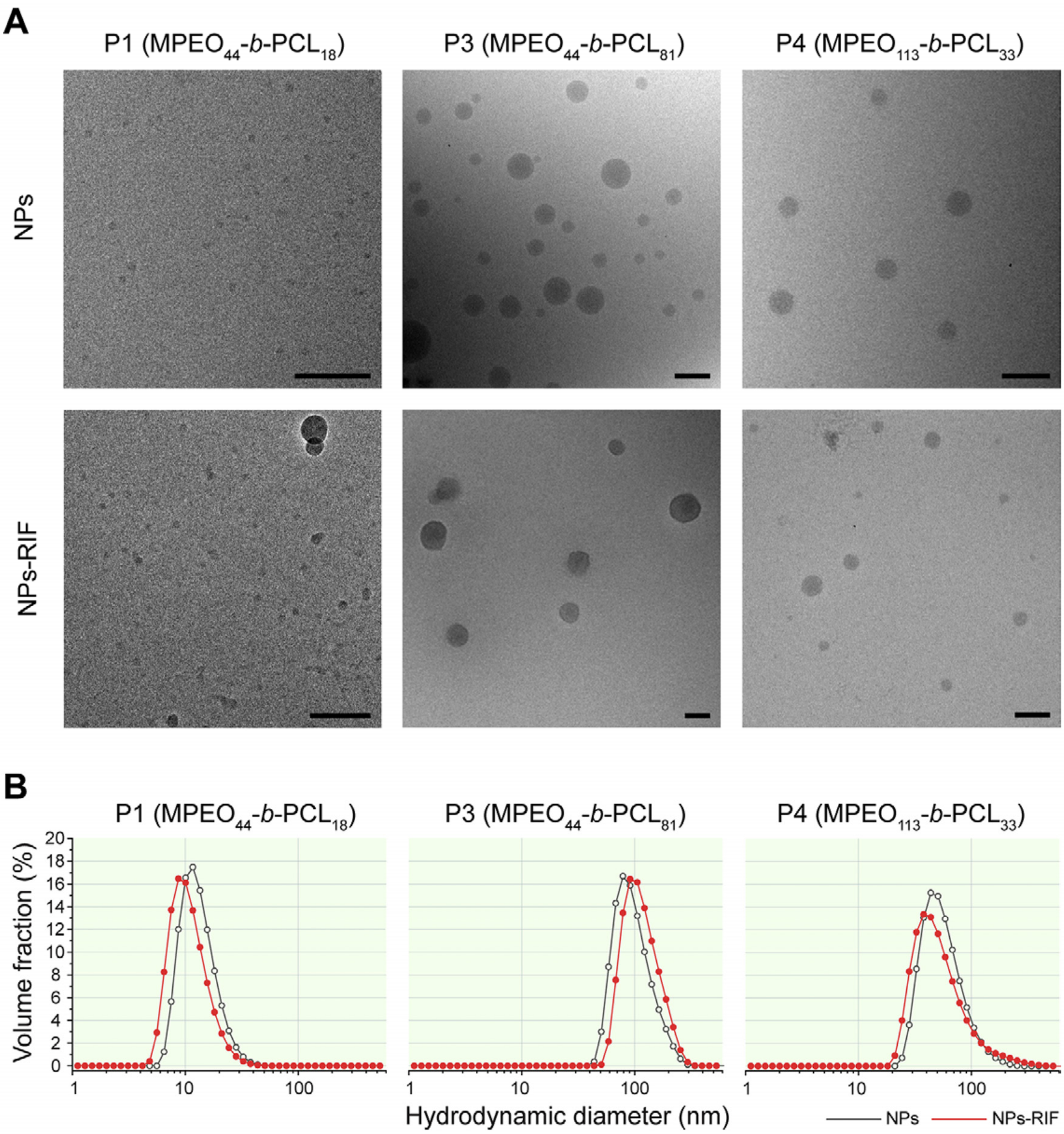

Figure 2. Morphology and size distribution of the chosen MPEO-*b*-PCL formulations. (A) Cryo-TEM images of blank and RIF-loaded NPs. Scale bars: 100 nm. See Figure S4 and Figure S5 for a better resolution images of **P1**-based NPs. (B) Corresponding DLS results shown as distribution functions. Both blank NPs (gray line) and RIF-loaded NPs (red line) are shown.

formulations was made via the caudal vein. The injection volume was 10 nL, which corresponds to a therapeutic dose of 10 mg/kg, assuming that an average zebrafish embryo has a body mass of approximately 1 mg.[16] The different treatment groups were separated from one another by being placed in 10 cm Petri dishes filled with zebrafish egg water[26] supplemented with PTU. A fish was considered dead when its heart stopped beating.

Experiments were conducted in agreement with the ethical provisions enforced by the Norwegian national animal research authority (NARA).

Imaging of Nanoparticles *in Vivo*. At 2 days postfertilization, Tg(*fli1*a:EGFP) zebrafish embryos possessing green fluorescent vasculature,[27] were administered TMR-labeled NPs via injection into the caudal vein; the injection volume was 5 nL. Two hours postinjection, the embryos were imaged using a Leica M205 FA stereomicroscope and the imaging software LAS AF (Leica Microsystems, Wetzlar, Germany). The embryos were sedated by immersion in a 230 μg/mL tricaine bath.

Subsequently, the embryos were imaged using confocal laser scanning microscopy. For this purpose, the sedated embryos were placed on a glass-bottomed dish and immersed in low melting point agarose that, once hardened, was covered with egg water. Images were obtained using an Olympus FluoView 1000 confocal laser scanning microscope BX61WI and subsequently analyzed and processed using Imaris Image Analysis Software (Bitplane, Belfast, United Kingdom).

Data Analysis. The results are expressed in the form of the mean ± SD and were analyzed by analysis of variance (ANOVA). Differences were considered significant at * $p \leq 0.05$, ** $p \leq 0.01$ and *** $p \leq 0.001$.

RESULTS AND DISCUSSION

MPEO-*b*-PCL Synthesis and Characterization. The matrix was prepared by way of a metal-free ring-opening polymerization (ROP) of CL initiated by MPEO, in the presence of HCl as the catalyst, at room temperature (Figure 1A). Typically, stannous octoate is used for conventional ROP of cyclic esters. For biomedical applications, however, such an organometallic catalyst may be difficult to remove from the products, and the resulting contamination of the polymer matrix may potentially affect the human body and cell

P1

Table 1. Nanoparticles Characterization Results[a]

Formulation (Assembled matrix)	H/H ratio[b]	NPs without RIF D_h[c]	PDI	D_g[d]	M_w	RIF-loaded NPs D_h	PDI	D_g	M_w	DL[e]	EE
P1 (MPEO$_{44}$-*b*-PCL$_{18}$)	5:5	19 ± 0.2	0.23 ± 0.01	[f]	0.13×10^7	16 ± 0.4	0.21 ± 0.01	[f]	0.78×10^6	23.4 ± 0.3	29.9 ± 0.3
P2 (MPEO$_{44}$-*b*-PCL$_{27}$)	4:6	24 ± 0.3	0.22 ± 0.01	35	0.77×10^7	78 ± 0.7	0.28 ± 0.01	77	1.42×10^7	21.4 ± 0.6	25.2 ± 0.9
P3 (MPEO$_{44}$-*b*-PCL$_{81}$)	2:8	109 ± 0.2	0.11 ± 0.02	77	10.1×10^7	124 ± 0.8	0.10 ± 0.01	[f]	[f]	17.8 ± 0.8	22.4 ± 1.1
P4 (MPEO$_{113}$-*b*-PCL$_{33}$)	6:4	75 ± 0.2	0.16 ± 0.01	51	1.81×10^7	85 ± 0.9	0.23 ± 0.01	53	2.23×10^7	10.9 ± 1.1	14.6 ± 1.7
P5 (MPEO$_{113}$-*b*-PCL$_{113}$)	3:7	95 ± 0.8	0.26 ± 0.01	115	3.41×10^7	83 ± 0.9	0.23 ± 0.01	74	5.35×10^7	17.0 ± 1.2	22.4 ± 1.1

[a] Mean values with standard deviation are shown. [b] Hydrophilic/hydrophobic ratio. [c] Dynamic light scattering experiments measured the z-average of hydrodynamic diameter (D_h, nm) and polydispersity index (PDI). [d] Asymmetrical flow field-flow fractionation investigations measured the z-average of diameter of gyration (D_g, nm) and molecular weight (M_w, Da). [e] The efficiency of RIF encapsulation is expressed as drug loading percentage (DL, %) and entrapment efficiency (EE, %) values. [f] Values could not be estimated due to very small particle size (sample **P1**) or the formulations' tendency to aggregate (sample **P3-RIF**).

cultures, as was noted by Hyun and colleagues,[20,28] the researchers who pioneered this HCl-based method.

To synthesize MPEO-*b*-PCL conjugates with fluorescent dyes, we employed an existing method for the one-step conjugation (Figure 1B) of both 7-(diethylamino)coumarin-3-carbonyl azide (DACCA, blue fluorescence) and tetramethylrhodamine-5-carbonyl azide (TMR, red fluorescence) to the end of the hydrophobic PCL block.[21,29] Several diblock copolymers were prepared with various compositions, as listed in Table SI, Supporting Information.

The ^{1}H NMR spectrum of the prepared copolymer is shown in Figure S1A. GPC investigations of the prepared copolymers showed monomodal distributions, as is shown by the overlap of the normalized GPC curves (Figure S1B). As is evident from the results of ^{1}H NMR, GPC, and critical aggregation concentration (CAC) determination (Table SI, Figure S2), most of the physicochemical characteristics can be described depending upon the blocks length.

Nanoparticles Preparation and Physicochemical Characterization. The nanoparticles were prepared using a nanoprecipitation method described in detail in the Materials and Methods section and the physicochemical characterization was carried out using dynamic light scattering (DLS), asymmetrical flow field-flow fractionation (AFFFF) and cryo-transmission electron microscopy (cryo-TEM).

MPEO-*b*-PCL nanobeads in water are characterized by an insoluble core composed of the hydrophobic PCL block, allowing encapsulation of hydrophobic compounds.[30,31] Several architectures are possible, depending on the hydrophobic/hydrophilic ratio (i.e., number of hydrophobic PCL monomer units/number of hydrophilic PEO monomer units). However, if the solvent switch is fast, block copolymers tend to form spherical assemblies instead of cylindrical or planar ones, since this is the fastest way to reduce their interfacial area. The spherical assemblies are therefore found also for high hydrophobic fractions (where cylindrical particles and vesicles/flat bilayers are expected as the most stable equilibrium structures) as metastable, kinetically relatively preserved structures with substantial lifetimes. Within this study, the NPs' morphology was inspected using cryo-TEM, allowing for the direct observation of samples in the vitrified, frozen-hydrated state. The morphology of the nanoparticles can be seen in Figure 2A. Those microphotographs directly confirm that the studied MPEO-*b*-PCL matrix was successfully assembled into defined polymeric nanoparticles. The investigated samples were found to be spherical (Figure 2); this finding is in line with the above-mentioned reasoning as well as with earlier studies of MPEO-*b*-PCL-based assemblies.[18,31] Differences between blank particles and RIF-loaded nanoparticles were observed within the sample derived from MPEO$_{44}$-*b*-PCL$_{81}$ (**P3** and **P3-RIF**). Within this pair of formulations, **P3-RIF** formulations contained more contrasting structures with slight nonsphericity.

For all the copolymers, the DLS distribution function is portrayed as a relatively narrow peak, with a hydrodynamic diameter in the range of 20−110 nm (Figure 2B), and the copolymers are assembled in a blocks length-dependent manner (Table 1).

As it is known that DLS investigations in most situations cannot reveal the actual size distributions of particles and the averages that are obtained usually overestimate the sizes of the particles,[32,33] the DLS-based results were verified using AFFFF experiments. These measurements provided the actual size and the molar mass distributions, which appeared to be rather narrow in most cases (Figure S3). Another advantage of AFFFF is its ability to monitor the content of noncomplexed (unassembled) polymer in the presence of nanoparticles. The AFFFF experiments showed that the assembling process of the copolymers that were examined reached almost 100%, as no free polymer was found in the samples.

The results from DLS and AFFFF are summarized in Table 1. In general, the DLS and AFFFF results were in mutual agreement and together with the cryo-TEM investigations provided insight into the NPs' structure. The first indication is the size of the NPs, which cannot be so high that the system would be a micelle, as often stated in the literature.[30,34,35] Another proof is the AFFFF-estimated molecular weight of the NPs (Table 1), which indicates that approximately 200−5 000 polymer chains comprise one nanoparticle, while a micelle contains approximately 10−100 polymer chains.[36]

When comparing DLS and AFFFF data in detail, it should be kept in mind that the geometrical dimensions (diameters) of particles calculated based on the diameters of gyration D_g are $D = 1.29\ D_g$, assuming both spherical geometry and that the samples were filtered slightly differently prior to DLS and AFFFF measurements. The apparent structural density ρ of

DOI: 10.1021/acs.biomac.9b00214

P1

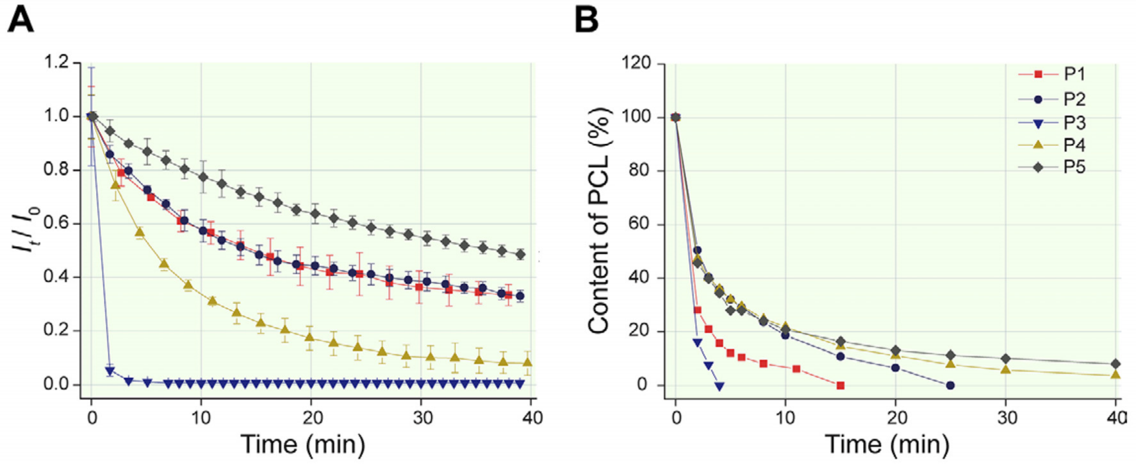

Figure 3. Enzymatic degradation of MPEO-*b*-PCL NPs. (A) Dependence of DLS intensity given as the ratio I_t/I_0 of prepared NPs (0.91 mg/mL), based on degradation time at 37 °C and pH 7.4 (0.01 M PBS) in the presence of lipase from *Pseudomonas* sp. (0.36 U/mL); the subscripts 0 and t represent time points during degradation $t = 0$ and $t = t$, respectively. (B) Enzymatic degradation of PCL blocks in NPs, based on decrease of the intensity of the OCH_2 "g" signal. Note the extremely fast degradation rate for formulation $MPEO_{44}$-*b*-PCL_{81} (**P3**).

particles was calculated as an equivalent average density from the weight-average of molecular weight M_w using the model of a sphere with the diameter D, with no correction for poly dispersity; $\rho = 6M_w/\pi N_A D^3$. The density of the nanoparticles was found to be reasonably low (values ranging from $\rho = 0.15$ to 0.30 g/mL), suggesting that the polymeric nanoparticles are probably porous and water-swollen.

The AFFFF analysis further demonstrated that formulations containing spherical particles can be affected by aggregation or restructuring (slow transition to the equilibrium most stable architecture), but this finding was observed only after substantial aging of the formulations (Figure S6).

In regards to the prediction of biological activity, the size range of the obtained NPs should be suitable for delivery via inhalation into the trachea-bronchial and alveolar region,[37] which represents one of the most promising methods of delivery for tuberculosis treatment.[38] In addition, particles within the obtained size range are suitable for internalization into Mϕ,[39] supporting the hypothesis that this RIF delivery system should possess high activity against invading mycobacteria within Mϕ.

Enzymatic Degradability. The fabricated MPEO-*b*-PCL copolymer is known for its biocompatibility as well as its biodegradability, which is defined as the gradual breakdown of a material mediated by a specific biological activity. Biodegradable polymers are polymers with the ability to function for a predefined period, with subsequent degradation by way of a controlled mechanism.[40] To this end, we focused on the examination of the degradation of the fabricated NPs. To achieve this goal, enzyme-catalyzed degradation of NPs was investigated using both DLS and ^{1}H NMR. As it is commonly regarded as a model of lipase activity, bacterial lipase isolated from *Pseudomonas* sp. was used; also, this type of lipase demonstrates higher activity and better efficiency compared to mammalian lipases such as lipase derived from the porcine pancreas.[18,41]

During the DLS experiment, degradation was observed as a decrease in the light scattering intensity for all of the tested formulations, whereas during the ^{1}H NMR spectroscopy experiment, degradation was observed as a decrease in the intensity of the OCH_2 signal.

As is evident in Figure 3A, all of the tested formulations underwent enzymatic degradation that was observable as a gradual decrease of the light scattering intensity. The fastest and slowest degradation rates were found for formulations **P3** ($MPEO_{44}$-*b*-PCL_{81}) and **P5** ($MPEO_{113}$-*b*-PCL_{113}), respectively.

Enzymatic hydrolysis is known to be a heterogeneous process affected by the mode of interaction between the lipase and the polymeric chains, and it typically utilizes four steps:[42] (1) diffusion of the enzyme to the solid surface; (2) adsorption of the enzyme to the substrate (NPs, in our case); (3) catalysis of the degradation process; and (4) diffusion of the degradation products from the solid substrate. In terms of the substrate's physicochemical properties, the adsorption and rate of degradation are affected by molecular weight, chemical composition, crystallinity, and surface area. Thus, the dependence of the degradation kinetics on the properties of the NPs, such as size and surface area, differs within the studied sample set.

For the quantitative characterization of the enzymatic degradation of the PCL blocks, the time dependence of PCL consumption was calculated for all the measured samples. The integral intensity of signal marked as "e" (Figure S7) was defined as 2 (there are two equivalent protons) and was used as an internal standard for monitoring of degradation within all the spectra. Subsequently, the integral intensity of signal "g" (Figure S7) was used for calculation of the percent of PCL blocks according to the relationship $[(I_t^g/I_0^g) \times 100]$, where the subscripts 0 and t represent the time points during degradation $t = 0$ (i.e., before lipase addition) and $t = t$ (i.e., after lipase addition), respectively. The results obtained are shown in Figure 3B; similar to that obtained from DLS, the fastest degradation was observed for sample **P3** and was slowest for sample **P5**, whereas the degradation rates for the remaining samples differed from those measured during DLS.

Figure S7 shows the ^{1}H NMR spectra of **P2**-based NPs that were measured in deuterated PBS at 37 °C before (Figure S7A) and after (Figure S7B,C) lipase addition. The chemical structures and signal assignments are presented in the same figure. The comparison between the spectra was recorded in a solvent suitable for all the blocks (deuterated chloroform, cf. Figure S1A) and PBS (Figure S7), showing that the broader

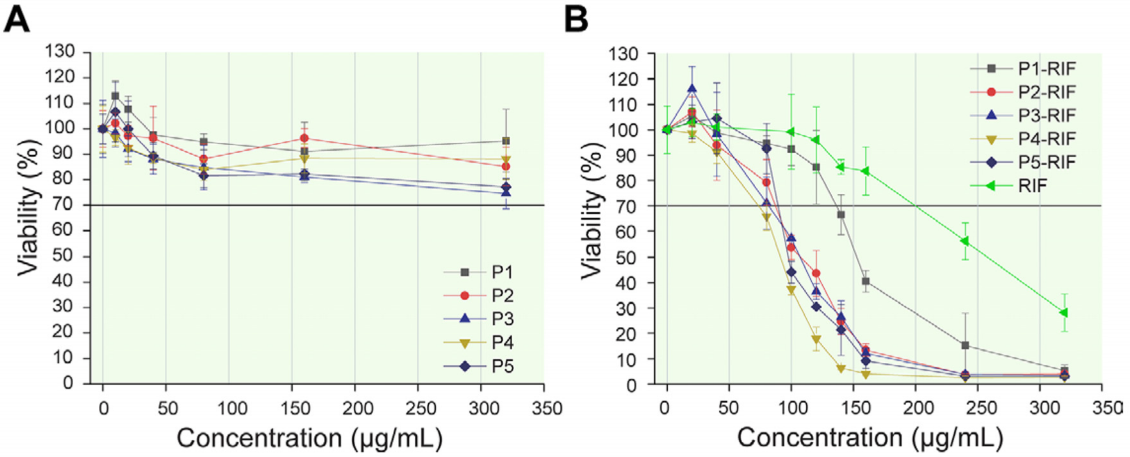

Figure 4. Viability of Raw 264.7 cells as detected by MTT assay. Cells were incubated with different concentrations of NPs, NPs-RIF or RIF for 24 h and their viability was assessed via measurement of the concentration of metabolically produced formazan. (A) Effect of different RIF-free MPEO-*b*-PCL nanoparticles. There was no cytotoxic effect for blank NPs. (B) Effect of different RIF-loaded MPEO-*b*-PCL nanoparticles. Note the higher toxicity of RIF-loaded formulations compared to free RIF, suggesting more efficient targeting of the carrier to M*ϕ*. The horizontal lines in the panels indicate the level at which, in terms of cell viability, the distinction between cytotoxicity (above) and noncytotoxicity (below) was made.

signals obtained from the hydrophobic PCL block and the strong signals obtained from the hydrophilic MPEO demonstrate the presence of a core−shell formation in the deuterated PBS system. These results demonstrate that the PCL protons are restricted in mobility in the moderately hydrated solid-like core of NPs, while MPEO blocks create a liquid-like shell. After the addition of lipase, the intensity of the side methyl signals from the PCL monomer unit ("c" and "g", see Figure S7B) decreases, while the singlets related to the "d" and "f" protons split and the MPEO signals ("a", "b") remain unchanged. The second effect observed in this spectrum is the appearance of new signals related to the degradation products, in particular, two signals for "c" and "g". One pair of the signals "g'", "c'", was identified as representing the $-$ CH_2OH and $C(O)CH_2$ groups of 6-hydroxyhexanoic acid, respectively (Figure S7D).

Drug Loading and Release. In order to induce the desired pharmacological effect, noncovalent RIF encapsulation was carried out and allowed by following aspects. As MPEO-*b*-PCL-based nanocarriers are characterized by an insoluble core composed of the hydrophobic PCL block,[30] rifampicin, a nonpolar drug ($\log p = 3.7$),[43] allows the hydrophobic forces-based encapsulation. For our system, drug loading and entrapment efficiency values ranged from 21 to 42% and from 15 to 30%, respectively (Table 1).

No less questionable aspect is the RIF release mechanism. In general, encapsulated drugs can be released from nanocarriers via diffusion through the polymeric matrix or water-filled pores or after an erosion of the polymeric particle.[44] Since nanocarrier was found to by enzymatically degradable by DLS, ^1H NMR and flow cytometry (see below), erosion-controlled RIF release is highly foreseeable. Hence, we performed a common dialysis-based study of RIF release without and in the presence of bacterial lipase. Surprisingly, as is evident from Figure S8, no increased release was observed when the release experiment was carried out in the presence of lipase. Of note that this finding is in line with our previous work dealing with RIF-loaded MPEO-*b*-PCL nanocarriers.[18] For this, we suggest two possible explanations. First, the RIF release might be controlled by diffusion, despite the fact that we found that the NPs are enzymatically degradable. The second possible explanation is that the approach used (i.e., the dialysis-based method) is not able to evaluate the lipase-controlled drug release, as the RIF transport through the dialysis tube might be the major RIF release-controlling factor. This hypothesis is supported by several reports[45,46] that indicate the dialysis-based method as providing misleading data.

Biocompatibility and Cytotoxicity. In the context of biorelevant analysis, we studied the effect of the prepared formulations in terms of possible cytotoxicity. For this purpose, the toxicity of NPs was investigated using the MTT method, after a 24 h incubation of Raw 264.7 cells' with each formulation. The goal of these *in vitro* experiments was not only to answer the question of whether or not our nanoparticles are safe but also whether or not the targeting of RIF to M*ϕ* is efficient. It is known that NPs are preferentially taken up by M*ϕ*, which further enhances their targeting.[1] Raw 264.7 cell line we used for this study is a monocyte-macrophage cell line.[47] Given a logical assumption that the more efficient the targeting is, the more of the drug is delivered, we suggest that the increased level of a drug within a cell correlates with cell viability observed. Hence, we assume that comparison of the RIF-loaded nanoparticles' toxic effects is an indirect comparison of their targeting efficiency, as we discussed in our previous study.[18]

In the case of blank nanoparticles (samples **P1**, **P2**, **P3**, **P4** and **P5**), the cell viability was influenced very little, even during treatment with a high concentration (320 μg/mL, corresponding to 1.6 g nanoparticles per 5 L of blood), suggesting that such copolymers are truly safe and well-tolerated for Raw 264.7 M*ϕ*, even when administered *in vivo* (see below). Despite the fact that nanoformulations **P3** ($MPEO_{44}$-*b*-PCL_{81}) and **P5** ($MPEO_{113}$-*b*-PCL_{113}) exhibited slightly higher toxicity (nonsignificant), we can conclude that all of the tested blank NPs are noncytotoxic (Figure 4A).

In contrast, as is evident from Figure 4B, RIF encapsulation leads to a dramatic increase of cytotoxicity in M*ϕ* even when compared to a nonencapsulated form of the drug, suggesting a higher efficiency in RIF-targeting to the cells. As is evident from Figure 4B and the calculated values of IC_{50} (see below, Table SII), the most cytotoxic formulation is **P4-RIF**, which is

P1

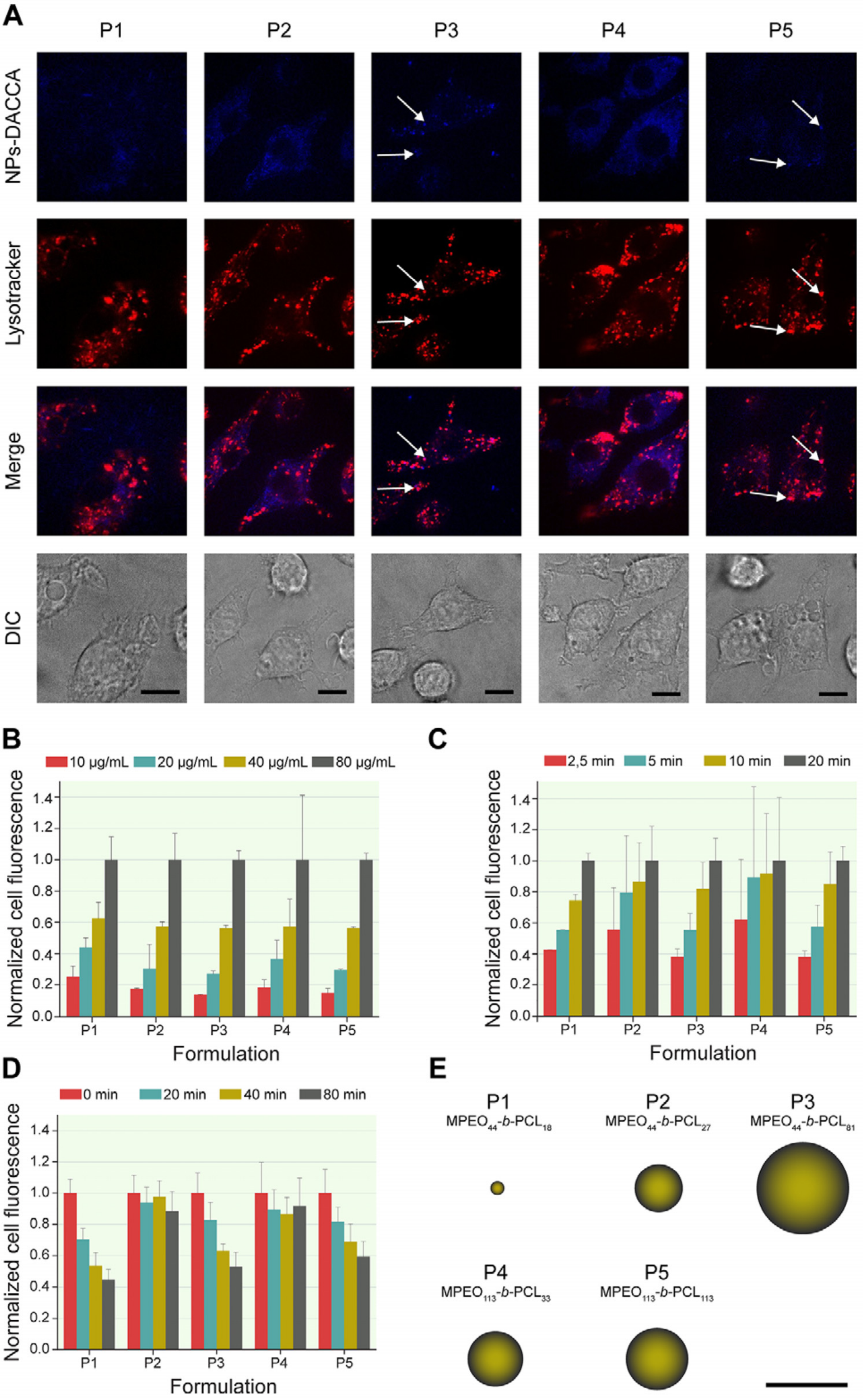

Figure 5. Study of cellular uptake and fate of NPs. (A) Confocal microscopic images of Raw 264.7 cells 20 min after addition of DACCA-labeled MPEO-*b*-PCL formulations (40 *μ*g/mL). Scale bars: 10 *μ*m. (B) Effect of NPs' concentration on cellular uptake based on analysis of flow cytometric data. (C) Time course of cell-associated fluorescence after the addition of 40 *μ*g/mL of DACCA-labeled formulations, based on analysis of flow cytometric data. (D) Time course of NPs' degradation observed after the monolayers were incubated with 40 *μ*g/mL of DACCA-labeled formulations for 20 min, based on analysis of flow cytometric data. (E) Size characterization and marking of fabricated NPs. Scale bar: 100 nm.

based on assembled copolymer MPEO$_{113}$-*b*-PCL$_{33}$. Formulations **P2-RIF**, **P3-RIF** and **P5-RIF** showed slightly weaker effects, whereas formulation **P1-RIF** was found to have the lowest toxicity to Raw 264.7 cells. Since the IC$_{50}$ values were (130.8 ± 4.1), (110.1 ± 11.9), (114.4 ± 12.6), (91.0 ± 2.5), (93.8 ± 6.6) and (295.9 ± 0.7) *μ*g of RIF per mL for **P1-RIF**, **P2-RIF**, **P3-RIF**, **P4-RIF**, **P5-RIF** and free RIF, respectively, we can conclude that all the tested RIF-loaded formulations were more toxic than the free form of RIF and were not toxic for M*ϕ* at the concentrations used for the infected macrophage treatment study (see below). Additionally, based on these results, formulation **P4-RIF** was chosen as the best candidate in terms of RIF-targeting to Mϕ.

During the hemolytic study, none of the tested formulations induced any hemolysis when used within the tested concentration range (100−800 μg/mL) after 4 and 8 h of incubation at 37 °C, suggesting excellent biocompatibility.

Internalization and Intracellular Degradation. To localize the NPs within Raw 264.7 Mϕ, we investigated the uptake of DACCA-labeled NPs into cells by live-cell imaging using confocal spinning disc microscopy. The cells were seeded on Petri dishes with glass bottoms. Then, the DACCA-labeled formulations and LysoTracker Deep Red, which is a marker that is a weak base that allows labeling and tracking of acidic organelles, were added and images were acquired after 20 min of incubation.

As shown in Figure 5A, the microscopic investigations revealed differences between the tested formulations. The formulation based on **P3** nanoparticles (approximately 110 nm in diameter, according to DLS) exhibited cytosolic and bright vesicular localization and clear colocalization with Lysotraker-positive cellular vesicles (white arrows). In contrast, **P2** (approximately 25 nm) and **P4** (ca. 80 nm) exhibited bright cytosolic localization, with a fluorescent structure adjacent to the cellular membrane and a vesicular structure in the cytoplasm. Colocalization with LysoTracker-positive structures (i.e., low pH compartments, presumably lysosomes) was only partial. The fluorescence intensity of cells was poor in the case of **P1** (approximately 20 nm), but showed partial colocalization with low pH compartments. Finally, nanoformulation **P5** (approximately 100 nm) showed clear colocalization with low pH compartments (white arrows) and in the cytosol.

Subsequent to microscopy, flow cytometry was carried out to evaluate the fate of DACCA-labeled NPs in terms of the effect of their concentration, their time-dependent effects and the degradation kinetics of NPs. All of the obtained data were normalized to the maximum cell-associated fluorescence values to ensure the comparability of results determined from samples with variable total cell fluorescence intensities.

As is evident from the cell-associated fluorescence data, fabricated NPs are successfully taken up by Raw 264.7 cells in a concentration-dependent manner (Figure 5B) and with a maximal cell fluorescence intensity after 20 min of incubation (Figure 5C). Internalization half-lives were calculated based on the internalization time course by curve fitting of the data using the equation:

$$F(t) = F_0 + F_{\max}(1 - e^{-t/k}) \qquad (5)$$

where $F(t)$ is the cell fluorescence signal at time t, F_0 and $F_{\max}$ are the initial fluorescence signal and the maximal signal, respectively, and k is the internalization rate constant (Table SIII). Formulations exhibiting the fastest cell uptake were revealed to contain **P4** and **P2** NPs, with internalization half-lives of 2.4 and 6.2 min, respectively. The remaining formulations, **P5**, **P3** and **P1**, had internalization half-lives of 9.4 min, 11.4 and 21.0 min, respectively. Interestingly, these findings do not meet the size- or PDI-related trends observed (see above), despite the fact that the NPs' size is known as one of the main physicochemical aspects that influence the cellular uptake. Among this factor, the hydrophilic/hydrophobic ratio of the copolymers assembled is also an important parameter in terms of cellular internalization.[35,48] In this regards, Zhang and colleagues[35] studied the same diameter- and different hydrophilic/hydrophobic ratios-possessing MPEO-*b*-PCL NPs and their uptake by HUVEC and HepG2 cell lines. MPEO-*b*-PCL NPs with higher hydrophilicity were taken up by the cells more easily. This is in line with our results; except the highest internalization half-live value-revealing formulation **P1** (MPEO$_{44}$-*b*-PCL$_{18}$), the internalization half-lives decrease with increasing hydrophilicity (see the above-mentioned internalization half-lives and Table 1). In other words, NPs with the highest hydrophilicity may be covered by the least amount of proteins and are taken up by the cells more easily, as properties of the protein corona has a significant effect on NPs internalization.[49]

Since differences in the rates of cellular uptake and cellular fates were observed that depended upon the investigated nanoparticles' properties, the experiments focused on the study of the degradation kinetics of NPs were also conducted (Figure 5D, Table SIII). For this purpose, the cells were incubated with DACCA-labeled formulations with subsequent washes, after which the cell-associated fluorescence was measured at different time points. Degradation half-life values were determined by fitting the data to single exponential decay. This approach was possible due to the fact that enzymatic degradation of the DACCA-labeled matrix leads to quenching of fluorescence.[18]

During these investigations, the sharpest decrease in fluorescence was found for the MPEO$_{44}$-*b*-PCL$_{18}$-based formulation **P1**, which possessed the smallest particle size. The degradation half-life for this formulation was found to be 51.6 min. Formulations **P3** and **P5** had degradation half-life values of 90.0 and 91.2 min, respectively. Evaluation of either formulation **P2** or **P4** did not produce a favorable fit, as the corresponding data were subject to high uncertainty. Despite this, the degradation half-life for these formulations was estimated to be approximately 20 h. This seems to be in line with the results from fluorescence microscopy investigations, as both formulations **P2** and **P4** exhibited bright cytosolic localization (see above, Figure 5A) and no colocalization with LysoTracker-positive structures, i.e., presumably lysosomes, organelles that degrade extra/intra cellular material. Additionally, with respect to the above-mentioned aspects of lipase-based degradation, the intracellular degradation-related results obtained may be due to a combination of several factors (e.g., hydrophilicity/hydrophobicity ratio, size, surface, etc.) affecting adsorption of the lipases to the NPs. Moreover, the enzymatic degradation kinetics exhibited within living cells differ strongly from those produced during the degradation studies performed using DLS or NMR (see above) in solution.

Most Promising Formulation. Considering the bio-relevant analysis, we concluded that the most promising formulation for subsequent antituberculotic testing was the MPEO$_{113}$-*b*-PCL$_{33}$-based formulation **P4**, which demonstrated the highest cytotoxicity. Again, this conclusion was based on the assumption that the more efficient the targeting is, the more of the drug is delivered. In other words, an increased level of a drug within a cell possibly correlates with cell viability observed, as we discussed above. Not surprisingly, using three different approaches (i.e., DLS, ^{1}H NMR, and flow cytometry investigation), the **P4**-based nanoparticles were found to be enzymatically degradable, similarly as all the nanoformulations tested. In addition, the enzymatic degrad-

P1

ability suggests favorable behavior *in vivo*, as the MPEO-*b*-PCL copolymers undergo degradation to MPEO and 6-hydroxyhexanoic acid, the degradation product of PCL (see the discussion above). Both $MPEO_{44}$ (2 000 Da) and $MPEO_{113}$ (5 000 Da) do not exceed the threshold for renal filtration of polymers 30−50 kDa[50] whereas the biocompatible 6-hydroxyhexanoic is converted to adipic acid by ω-oxidation in the endoplasmic reticulum of liver and kidney cells *in vivo*. The adipic acid is then metabolized by β-oxidation and Krebs cycle to carbon dioxide and water.[51]

In addition to the biorelevant analysis, the chosen formulation based on **P4** revealed the fastest cell internalization, and, finally, the slowest intracellular degradation, suggesting a protracted elimination within the infected cells.

No less questionable aspect related to the **P4**-based formulations is their stability. It is known that NP's colloidal stability and NPs-proteins interactions in the biological fluids control the cell adhesion, and consequently the uptake.[52] In general, this phenomenon represents an experimental difficulty to investigating, as mammal plasma has over 3 700 proteins.[53] The fouling properties of NPs have been studied by placing them in contact with proteins such as bovine serum albumin (BSA),[54] lysozyme,[55,56] and fibrinogen.[57] An interaction of MPEO-*b*-PCL-based NPs with BSA was studied by the groups of Li[54] and Murthy,[34] for instance. Li group found that all the formulations tested (i.e., $MPEO_{44}$-*b*-PCL_{18}, $MPEO_{44}$-*b*-PCL_{31}, $MPEO_{44}$-*b*-PCL_{45}, $MPEO_{113}$-*b*-PCL_{44}, $MPEO_{113}$-*b*-PCL_{61}, and $MPEO_{113}$-*b*-PCL_{88}), except $MPEO_{44}$-*b*-PCL_{18}, remained stable over a period of 24 h with a maximum increase of 15 nm in the NPs' size after 48 h of incubation with BSA. Given these results, it could be assumed that the **P4**-based formulations we choose for the antibacterial testing *in vitro* and *in vivo* should not lead to aggregation.

Antibacterial Properties. Several bacterial strains were used for the basic characterization of the formulations' antibacterial properties. For this purpose, a broth microdilution assay was carried out. As is evident from Table 2, the minimal inhibitory concentration (MIC) of RIF was reduced for all tested species in the presence of the copolymers, suggesting that the prepared surfactant-like MPEO-*b*-PCL copolymers, similarly to some nonionic surfactants,[58,59] increase the permeability of the cell wall for RIF. In contrast, RIF-free formulations did not lead to any growth inhibition even when incubation was carried out with a very high concentration (1 000 μg/mL) of the polymer (data not shown).

Table 2. Minimal Inhibitory Concentrations for Free RIF and Its Encapsulated Form

Bacterial strain	RIF (μg/mL)	NPs-RIF (μg/mL)[a]	Decrease[b]
Escherichia coli	6	1−1.5	4−6
Mycobacterium fortuitum	8	−[c]	−
Mycobacterium phlei	0.25	0.047−0.064	3.9−5.3
Mycobacterium smegmatis	32	24	1.3
Mycobacterium sp.	8	3−4	2−2.7
Staphylococcus aureus subsp. *aureus*	0.125	0.032−0.064	2−3.9

[a] A broth microdilution assay provided the same MIC values for all of the prepared formulations. [b] Number of times of decrease. [c] Not estimated.

In order to investigate the bacterial inactivation mechanism of the manufactured formulations, we performed a common time-kill curve analysis with *M. fortuitum* clinical isolate as a model fast-growing mycobacterial strain. This assay was performed with both free RIF and **P4**-based NPs loaded with RIF in the presence of 3 antimicrobial concentrations ranging from 1 × MIC to 16 × MIC estimated for the free RIF (i.e., 8 μg/mL). Figure S9 shows the time-kill curves obtained. As is evident, both samples tested shared similar characteristics and a concentration-dependent effect. During the free RIF and **P4-RIF** NPs exposure, bactericidal activity was observed after 24−48 h, however, regrowth occurred after the initial killing and was noticeable for both the 1 × MIC and 4 × MIC exposures. Maximum decrease in bacterial population size was observed at 120 h at the highest concentration (i.e., 16 × MIC). These findings seem to be in line with the fact that *M. fortuitum* was found to be, similarly as most of the nontuberculous mycobacteria, naturally RIF-resistant.[60] Despite this, time-kill curves for *M. fortuitum* exposed to **P4-RIF** NPs revealed a higher decrease in bacterial population size than those observed for *M. fortuitum* when exposed to the free RIF. This is in line with the above-mentioned decrease of MIC values observed after RIF encapsulation.

Macrophages Infection and Treatment. One of the most important tasks was to assess the antituberculotic efficacy within mycobacteria-infected Mϕ. During the initial experiments, we compared three selected RIF-loaded nanoparticles (i.e., **P1** and **P3**, which had the smallest and largest particle sizes, respectively, and **P4**, which was the most efficient). For this purpose, we infected murine Raw 264.7 Mϕ monolayers with the virulent *M. tuberculosis* H37Rv strain at a multiplicity of infection (MOI) of 2.5 and treated them with free RIF or the equivalent amount encapsulated in NPs for 48 h. Because of rapid Raw 264.7 Mϕ division, the amount of FBS in the media was 5% instead of 10% for all of the infection-based experiments.

The concentration of RIF used during this testing was 20 μg/mL, a clinically relevant concentration[61] which also did not have any toxic effects on Mϕ (see above; cf. Table SII). RIF-free NPs were also used for treatment.

As shown in Figure 6A, all of the tested nanoformulations were more efficient compared to a free form of RIF within 48 h of treatment. This is in line with many earlier antituberculotic delivery-focused studies of both *M. tuberculosis* and *M. bovis* Bacillus Calmette−Guérin (BCG).[13,15,62−64] Additionally, variable effects of the tested formulations were observed, suggesting that robust metabolic testing of drug carrier cytotoxicity (e.g., MTT assay) may be useful as an indirect screening approach for the analysis of targeting efficacy, as our MTT-based results suggest similar behavior compared with infection/treatment-based results. In other words, for example, the formulation **P1-RIF** revealed both the lowest cytotoxicity and lower efficacy in terms of the killing of intracellular mycobacteria.

Finally, we focused on the treatment of infected Mϕ for a longer period. Figure 6B shows an experiment in which the cells were incubated with **P4-RIF** NPs (20 μg/mL) for 5 days, leading to a significant killing effect. In other words, no *M. tuberculosis* colonies grew on the Löwenstein−Jensen medium after the nondiluted cell lysate was seeded. In contrast, after 5 days of monotherapy with free RIF, the infection still persisted (Figure 6B). Surprisingly, as is evident from these results, RIF-

DOI: 10.1021/acs.biomac.9b00214

P1

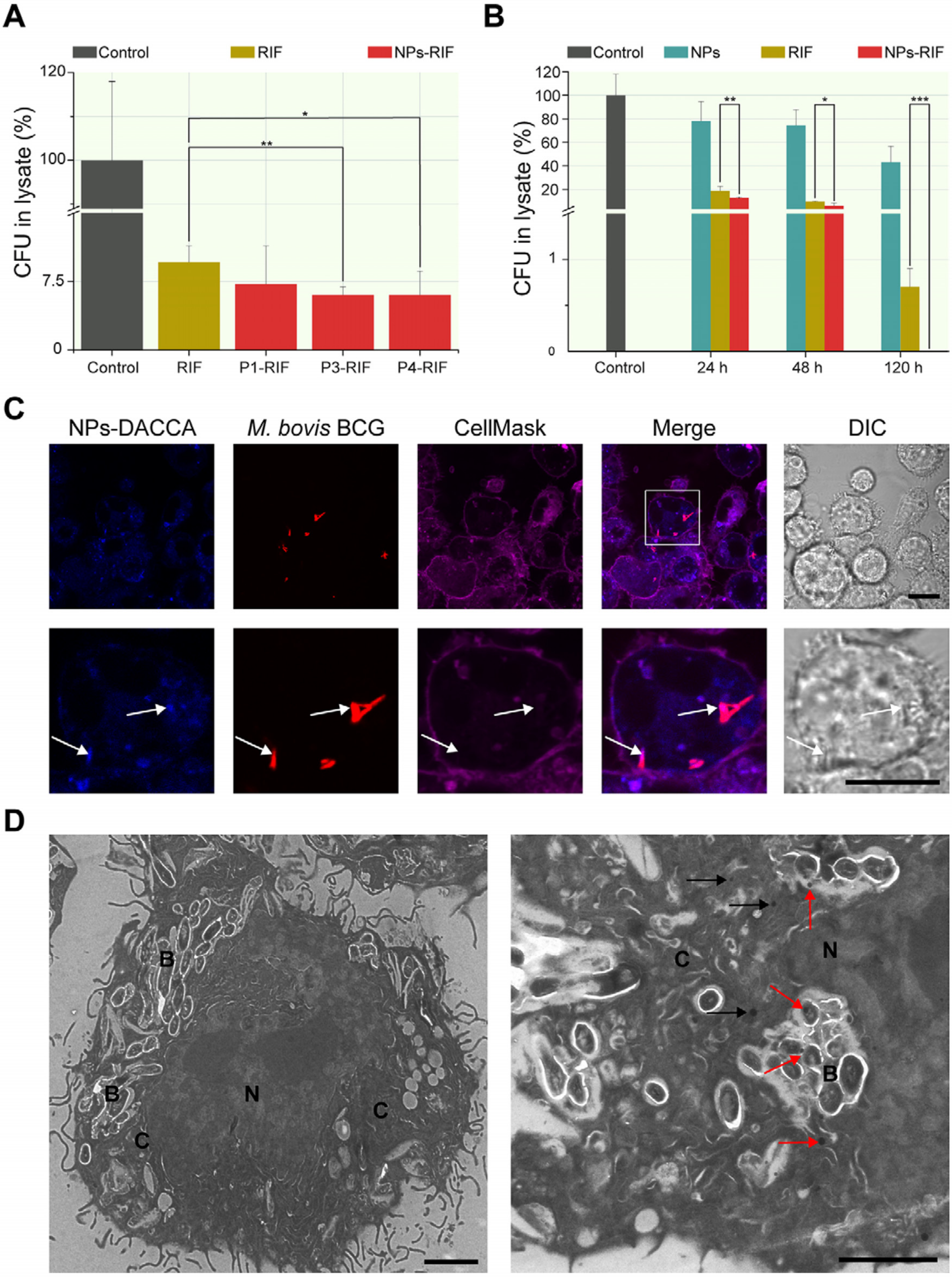

Figure 6. Infection and treatment of Raw 264.7 cells. (A) Comparison of three different RIF-loaded formulations, MPEO$_{44}$-*b*-PCL$_{18}$ (**P1-RIF**), MPEO$_{44}$-*b*-PCL$_{81}$ (**P3-RIF**) and MPEO$_{113}$-*b*-PCL$_{33}$ (**P4-RIF**), after a two-day treatment procedure. (B) Killing effects of the most promising drug candidate, MPEO$_{113}$-*b*-PCL$_{33}$ (**P4-RIF**), that was loaded with RIF and used during a five-day treatment procedure. Note the higher efficiency of RIF-loaded nanoparticles, as well as the surprising effect of blank NPs, in terms of the decrease in the number of tubercle bacilli. (C) Corresponding images from confocal laser scanning microscopy of Raw 264.7 cells after infection by DsRed-expressing *M. bovis* BCG and 1 day of treatment with MPEO$_{113}$-*b*-PCL$_{33}$-DACCA NPs (**P4**). Note the increased NP-related signal within the location of mycobacteria persistence (white arrows). Scale bars: 10 μm. See Figure S10 for a better resolution image. (D) Corresponding images from TEM. Examples are from a mycobacteria-infected cell that was treated with **P4** NPs overnight. Conventional TEM demonstrated the occurrence of bacteria in the cytoplasm, as well as their frequent association with NPs (red arrows). NPs distributed freely in the cytoplasm are marked with black arrows. B, bacteria; C, cytoplasm; N, nucleus. Scale bars: 2 μm.

free NPs also affected the invading bacteria, which supports the hypothesis that the surfactant-like behavior of the fabricated copolymers affects the mycobacterial cell wall permeability. Thus, the mycobacteria are probably more

DOI: 10.1021/acs.biomac.9b00214
Biomacromolecules 2019, 20, 1798−1815

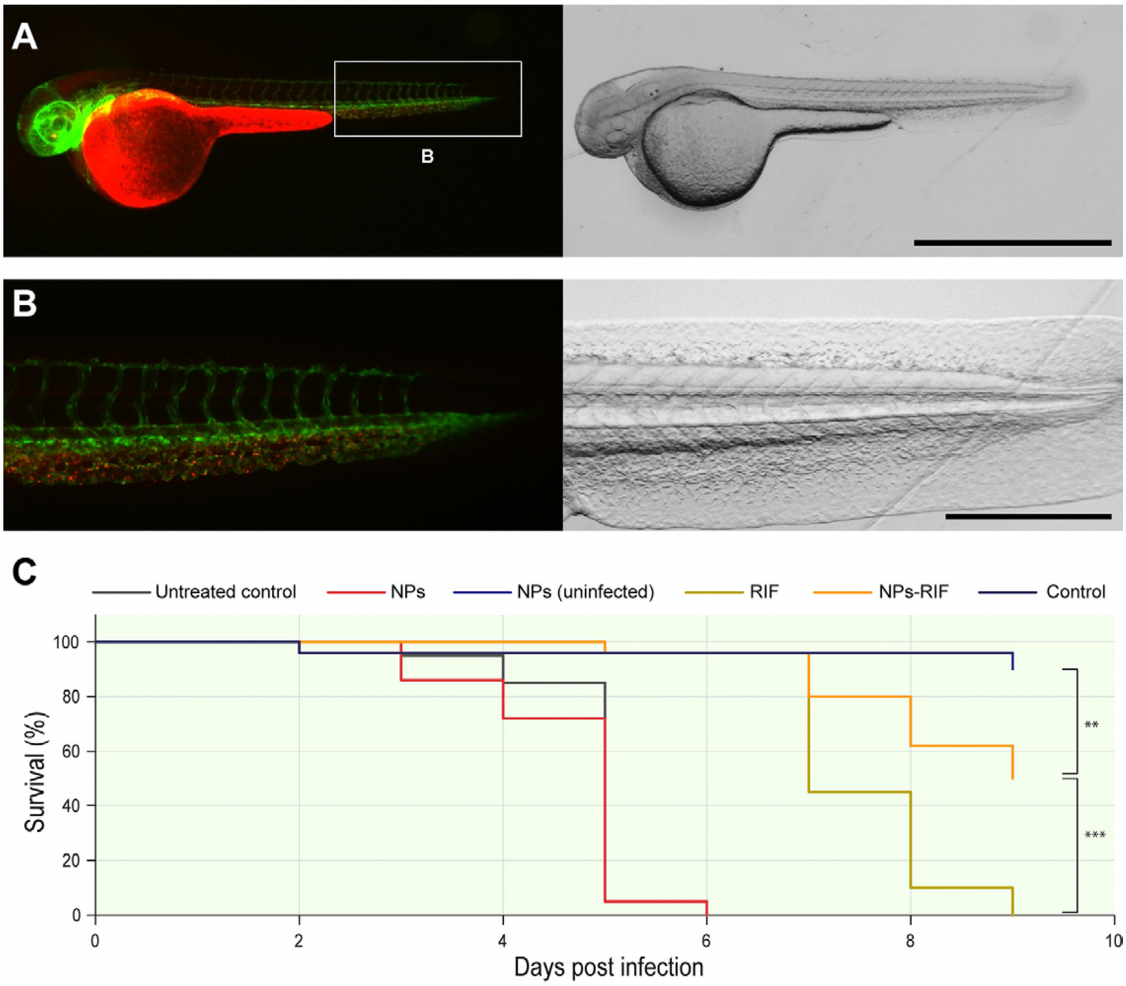

Figure 7. Testing of antituberculotic nanoparticles *in vivo*. (A) Stereomicroscopy of Tg(*fli*1a:EGFP) zebrafish embryos injected with red fluorescent NPs. Images obtained at 30× and 120× magnification. Green channel, blood vessels; red channel, TMR-labeled NPs (**P4**), in addition to autofluorescence from the yolk sack. Scale bar: 1 mm. (B) Enlargement of the area demarcated by the white rectangle, showing the fluorescent image of the tail area. The NPs, in red, clearly colocalize with the endothelial cells, causing the majority to no longer circulate in the bloodstream. Scale bar: 300 μm. (C) Cumulative mortality of infected zebrafish larvae treated with 10 mg/kg free form RIF, RIF-loaded **P4** ($MPEO_{113}$-*b*-PCL_{33}) nanoparticles (NPs-RIF) and blank nanoparticles (NPs).

sensitive to the elimination mechanisms possessed by macrophages. Such a hypothesis, however, must be investigated in more detail in order to come to any specific conclusions in terms of the impact of the drug delivery systems on mycobacteria.

To fully carry out the biorelevant analysis of the NPs, we also addressed the question of whether or not the NPs are localized close to the invading bacteria. In several studies, fluorescent protein-expressing mycobacteria were found to be an elegant tool for use in the biorelevant analysis of antituberculotic delivery systems.[65] Thus, to elucidate the treatment procedure and confirm that MPEO-*b*-PCL NPs can be adapted into a platform for delivering antituberculotics into infected Mϕ, DACCA-labeled NPs (**P4**) were incubated with DsRed-expressing *M. bovis* BCG-infected Raw 264.7 cells. Subsequently, we used confocal laser scanning microscopy to determine the intracellular fate of fluorescently labeled NPs.

Not surprisingly, the results proved that MPEO-*b*-PCL NPs, similarly to other types of antituberculotic drug delivery systems,[15,66] can be internalized efficiently by Mϕ when the macrophages are either uninfected (Figure 5A) or infected (Figure 6C). Additionally, when the Raw 264.7 cells were infected with red *M. bovis* BCG and were allowed to internalize the DACCA-labeled NPs, these cells showed increased NP-related signaling at the location where *M. bovis* persisted (Figure 6C, white arrows). Thus, we next performed conventional TEM of ultrathin sections of aldehyde-fixed cells to further substantiate the results of the confocal laser scanning microscopy of the intracellular locations of both NPs and mycobacteria.

Figure 6D (left) shows a macrophage infected with bacteria, which have accumulated in the endosomal region of the cytoplasm. Surprisingly, as is evident in the image at higher magnification (Figure 6D, right), the administered NPs are very often localized adjacent to the invading bacteria, directly within the same endosomal compartment (red arrows). This result is in agreement with the conclusions of de Faria and colleagues[67] who described that NPs based on poly(lactic-*co*-glycolic acid) (PLGA) NPs carrying an isoniazid derivative directly interacts with the *M. bovis* BCG phagosomes in Mϕ. However, this is at odds with the findings of the Griffiths[15] and Heifets[62] groups. They showed that PLGA or poly(butyl cyanoacrylate) NPs remain in separate compartments, as bacteria-NPs colocalization was not observed. Nevertheless, the quantitative evaluation of 20 images taken with a CCD camera, which contained clearly visible and intracellularly localized NPs, showed that more than 50% of the NPs (57 out of 111) were associated with cellular compartments containing bacteria.

Importantly, as is evident in Figure 6D (right), both the morphology and size of administered NPs are very similar to that of uncut NPs visualized by cryo-TEM (see Figure 2A), even after cellular uptake and overnight incubation in culture.

***In Vivo* Testing with Zebrafish.** The final step of this study was to perform biorelevant analysis *in vivo*. We used the zebrafish embryo as a model system[16] for use in noninvasive imaging and in the simultaneous testing of the antitubercular properties of our RIF-containing nanoparticles. To ensure that our drug delivery system is also safe and noncytotoxic also for nonmammalian organisms, we conducted the cytotoxicity testing using zebrafish embryonic fibroblast ZF4 cells.[24] As is evident from Figure S11, blank NPs (**P4**) revealed no cytotoxic effects, even after 48 h of incubation, confirming that the fabricated material is safe. In contrast, the NPs-RIF (**P4-RIF**) formulation demonstrated increased cytotoxicity compared to free RIF in a pattern similar to that described above, confirming that both the encapsulation of RIF leads to an increase in its bioavailability and that the targeting of the drug is more efficient even within zebrafish fibroblasts (Table SII).

To image the nanoparticles *in vivo*, we injected Tg-(*fli1*a:EGFP) zebrafish embryos possessing vasculature visible by way of green fluorescence with a TMR-labeled version of our most promising candidate, $MPEO_{113}$-*b*-PCL_{33} (**P4**), in the caudal vein.

As shown in Figure 7A,B, the majority of the TMR-labeled NPs colocalized with the endothelial cells within two h of injection into the bloodstream. Additionally, confocal microscopy demonstrated that the NPs were taken up by the endothelial cells, whereas only a minor fraction of the nanoparticles was still circulating in the bloodstream (Video SV1).

The final task was to establish whether the system we had developed for encapsulating RIF facilitated therapeutic effects *in vivo*. To evaluate this using a zebrafish model of tuberculosis, we infected zebrafish larvae with *M. marinum*, the causative agent of tuberculosis in ectotherms, including fish. We know from previous studies that this type of infection results, similarly to human tuberculosis, in uptake by macrophages that in time aggregate forming granulomas and even undergoing epithelioid transformation;[68,69] late stage infection also shows typical features of the human pathology being characterized by extensive necrosis and neutrophil infiltration.[70] Here, we have injected about 160 CFU of *M. marinum* which are typically associated with a chronic infection of zebrafish embryos leading to an early death approximately 10−11 days after bacterial challenge.[68] One day after infection, the larvae received an injection containing 10 ng of RIF in either free form or encapsulated in NPs, with the dose amounting to 10 mg/kg for an embryo weighing 1 mg, which is equivalent to the amount of the drug given to mice.[71] As a control, we injected RIF-free NPs, as well.

During the survival study, RIF in its free form was shown to have a protective effect against the *M. marinum* infection, delaying mortality for approximately 3 days. In contrast, despite the fact that the majority of the TMR-labeled NPs were colocalized with the endothelial cells, which are not the primary sites of persistence for tubercle bacilli, administration of RIF-loaded NPs to zebrafish larvae significantly improved the outcome of treatment; when treated with RIF that was encapsulated in NPs, 50% of the larvae were still alive at day 9 postinfection (Figure 7C). Similar results were obtained by the Griffiths group[16] during their study of the effect of RIF-loaded PLGA NPs (approximately 230 nm in diameter) during the treatment of *M. marinum*-infected zebrafish embryos. However, the therapeutic effect of these PLGA-based formulations was plagued by a slightly higher mortality rate compared to the MPEO-*b*-PCL-based formulation used in this study, even when administered at a dose of 12 mg/kg.

Overall, the increased efficacy of our formulation compared to that containing a free form of the drug could reflect a combination of several factors. Prolonged release and delayed clearance of RIF due to the encapsulation of the drug in NPs could have resulted in improved pharmacokinetics. In other words, our RIF-containing nanoformulation allows the drug to remain in the zebrafish embryo for a longer period of time and to be released more slowly compared to the free form of the drug, which is rapidly excreted. Despite the observation of the weak colocalization of NPs and fluorescent *M. marinum* (data not shown), direct uptake of a minor fraction of the nanoparticles by *M. marinum*-infected M*ϕ*, leading to the release of RIF inside these cells, cannot be disproved. Moreover, it was shown that an enhanced permeability and retention (EPR)-like process allows NPs to extravasate from the vasculature to reach granulomas.[70] This suggests NPs' accumulation in the granulomas. Finally, empty NPs, by themselves, had no effect on either the uninfected or infected larvae, suggesting that the NPs are well-tolerated by the zebrafish larvae.

Last but not least, considering a clinical circumstance, the MPEO-*b*-PCL-based system we have described suggests increased antituberculotic efficacy both when administered intravenously or by the inhalation route. In other words, less than 600 mg of orally administered rifampicin, i.e. current pharmaceutical dosage,[43] would be required for at least two reasons. First, smaller total doses are generally required for localized therapy of the target organ, in order to achieve clinically effective results.[72] Second, intravenously administered NPs are able to accumulate in the granulomas, as the above-mentioned EPR-like effect allows NPs to extravasate from the vasculature.

■ CONCLUSIONS

The aim of this work was to robustly describe, to fundamentally characterize and to perform a biorelevant analysis of a biocompatible and biodegradable nanocarrier, which would hopefully serve as a subject of more in-depth study in the future. The MPEO-*b*-PCL-based nanocarrier that was described in this study was able to encapsulate RIF, a first-line antituberculotic agent, and it provided very good drug loading values and excellent properties in terms of cytotoxicity, cell uptake and antimycobacterial activity both *in vitro* and *in vivo*.

This study provides a generalizable strategy for the future improvement of polymer-based treatments for intracellularly persisting, bacterially caused infections. Moreover, this study highlights the need for more in-depth study of the interaction of nanomaterials with both macrophage-like and bacterial cells as well as with relevant model organisms to allow for the development of more efficient nanocarriers for use in drug delivery.

■ ASSOCIATED CONTENT

Ⓢ Supporting Information

The Supporting Information is available free of charge on the ACS Publications website at DOI: 10.1021/acs.biomac.9b00214.

> Results from physicochemical and biorelevant characterization of prepared MPEO-*b*-PCL copolymers, ^{1}H NMR spectra, results from AFFFF analysis of chosen MPEO-*b*-PCL formulation, cryo-TEM images of **P1**-based NPs at higher magnification, confocal laser scanning microscopy images of infected Raw 264.7 cells at higher magnification, ZF4 cells viability results (PDF)
>
> The tail area of zebrafish embryo (AVI)

■ AUTHOR INFORMATION

Corresponding Authors

*M.H. (mhruby@centrum.cz).

*J.T. (jiri.trousil@centrum.cz).

ORCID

Marián Sedlák: 0000-0003-2951-2846

Federico Fenaroli: 0000-0002-9060-8786

Petr Štěpánek: 0000-0003-1433-678X

Martin Hrubý: 0000-0002-5075-261X

Funding

Charles University (project no. SVV260440), Czech Science Foundation (grant no. 17-07164S and no. 17-09998S), Scientific Grant Agency VEGA (project no. 2/0177/17), Slovak Research and Development Agency (project no. 16-0550).

Notes

The authors declare no competing financial interest.

■ ACKNOWLEDGMENTS

J.T. acknowledges the support from Charles University (project no. SVV260440) and thanks Dr. Olga Janoušková for her kindness in assisting with the instrumentation necessary for some of the biological experiments, and thanks Prof. Gareth Griffiths for providing the DsRed-expressing *M. bovis* BCG strain and for his critical reading of the paper, and thanks Dr. Malgorzata Cebrat for providing the ZF4 cell line. P.Š., I.R., Z.S. and D.C. acknowledge the Czech Science Foundation (grant no. 17-07164S). M.H. acknowledges the Czech Science Foundation (grant no. 17-09998S). D.R. and M.S. acknowledge support from the Scientific Grant Agency VEGA and the Slovak Research and Development Agency (project no. 2/0177/17 and no. 16-0550). Z.S. thanks Dr. Jozef Janda for his expert cytometry advice. The cytometry measurements were performed at the Laboratory of Cytometry (Faculty of Science, Charles University, Prague, Czech Republic). E.P. thanks Na'ama Koifman at the Technion–Israel Institute of Technology (Haifa, Israel) for her kindness in assisting with the cryo-TEM investigations of the smallest particles.

■ ABBREVIATIONS

AFFFF,asymmetric flow field-flow fractionation; CAC,critical aggregation concentration; CL,ε-caprolactone; DACCA,7-(diethylamino)coumarin-3-carbonyl azide; DL,drug loading; DMEM,Dulbecco's Modified Eagle Medium; EL,entrapment efficiency; Et$_2$O,diethyl ether; MDR-TB,multidrug-resistant tuberculosis; MPEO,α-methoxy-ω-hydroxy poly(ethylene oxide); MTT,methylthiazolyldiphenyl-tetrazolium bromide; Mϕ,macrophages; NPs,nanoparticles; PTU,*N*-phenylthiourea; RBCs,red blood cells; RIF,rifampicin; TB,tuberculosis; THF,tetrahydrofuran; XDR-TB,extensively drug-resistant tuberculosis.

■ REFERENCES

(1) Gelperina, S.; Kisich, K.; Iseman, M. D.; Heifets, L. The Potential Advantages of Nanoparticle Drug Delivery Systems in Chemotherapy of Tuberculosis. *Am. J. Respir. Crit. Care Med.* **2005**, *172* (12), 1487–1490.

(2) Sosnik, A.; Carcaboso, Á. M.; Glisoni, R. J.; Moretton, M. A.; Chiappetta, D. A. New old challenges in tuberculosis: Potentially effective nanotechnologies in drug delivery. *Adv. Drug Delivery Rev.* **2010**, *62* (4), 547–559.

(3) Aristoff, P. A.; Garcia, G. A.; Kirchhoff, P. D.; Hollis Showalter, H. D. Rifamycins – Obstacles and opportunities. *Tuberculosis* **2010**, *90* (2), 94–118.

(4) Costa, A.; Pinheiro, M.; Magalhães, J.; Ribeiro, R.; Seabra, V.; Reis, S.; Sarmento, B. The formulation of nanomedicines for treating tuberculosis. *Adv. Drug Delivery Rev.* **2016**, *102*, 102–115.

(5) Trousil, J.; Hrubý, M. Novel nanoparticle delivery systems for rifampicin: an effective strategy against tuberculosis? *Nanomedicine (London, U. K.)* **2017**, *12* (12), 1359–1361.

(6) Wilson, J. W.; Tsukayama, D. T. Extensively Drug-Resistant Tuberculosis: Principles of Resistance, Diagnosis, and Management. *Mayo Clin. Proc.* **2016**, *91* (4), 482–495.

(7) De Matteis, L.; Jary, D.; Lucía, A.; García-Embid, S.; Serrano-Sevilla, I.; Pérez, D.; Ainsa, J. A.; Navarro, F. P.; M. de la Fuente, J. New active formulations against M. tuberculosis: Bedaquiline encapsulation in lipid nanoparticles and chitosan nanocapsules. *Chem. Eng. J.* **2018**, *340*, 181–191.

(8) Hwang, J.; Son, J.; Seo, Y.; Jo, Y.; Lee, K.; Lee, D.; Khan, M. S.; Chavan, S.; Park, C.; Sharma, A.; Gilad, A. A.; Choi, J. Functional silica nanoparticles conjugated with beta-glucan to deliver anti-tuberculosis drug molecules. *J. Ind. Eng. Chem.* **2018**, *58*, 376–385.

(9) Patil, K.; Bagade, S.; Bonde, S.; Sharma, S.; Saraogi, G. Recent therapeutic approaches for the management of tuberculosis: Challenges and opportunities. *Biomed. Pharmacother.* **2018**, *99*, 735–745.

(10) Griffiths, G.; Nyström, B.; Sable, S. B.; Khuller, G. K. Nanobead-based interventions for the treatment and prevention of tuberculosis. *Nat. Rev. Microbiol.* **2010**, *8* (11), 827–834.

(11) Vieira, A. C. C.; Chaves, L. L.; Pinheiro, S.; Pinto, S.; Pinheiro, M.; Lima, S. C.; Ferreira, D.; Sarmento, B.; Reis, S. Mucoadhesive chitosan-coated solid lipid nanoparticles for better management of tuberculosis. *Int. J. Pharm.* **2018**, *536* (1), 478–485.

(12) Leidinger, P.; Treptow, J.; Hagens, K.; Eich, J.; Zehethofer, N.; Schwudke, D.; Oehlmann, W.; Lünsdorf, H.; Goldmann, O.; Schaible, U. E.; Dittmar, K. E. J.; Feldmann, C. Isoniazid@Fe2O3 Nanocontainers and Their Antibacterial Effect on Tuberculosis Mycobacteria. *Angew. Chem., Int. Ed.* **2015**, *54* (43), 12597–12601.

(13) Hwang, A.; Lee, B.-Y.; Clemens, D. L.; Dillon, B. J.; Zink, J. I.; Horwitz, M. A. pH-Responsive Isoniazid-Loaded Nanoparticles Markedly Improve Tuberculosis Treatment in Mice. *Small* **2015**, *11* (38), 5066–5078.

(14) Upadhyay, S.; Khan, I.; Gothwal, A.; Pachouri, P. K.; Bhaskar, N.; Gupta, U. D.; Chauhan, D. S.; Gupta, U. Conjugated and Entrapped HPMA-PLA Nano-Polymeric Micelles Based Dual Delivery of First Line Anti TB Drugs: Improved and Safe Drug Delivery against Sensitive and Resistant Mycobacterium Tuberculosis. *Pharm. Res.* **2017**, *34* (9), 1944–1955.

(15) Kalluru, R.; Fenaroli, F.; Westmoreland, D.; Ulanova, L.; Maleki, A.; Roos, N.; Paulsen Madsen, M.; Koster, G.; Egge-Jacobsen, W.; Wilson, S.; Roberg-Larsen, H.; Khuller, G. K.; Singh, A.; Nyström, B.; Griffiths, G. Poly(lactide-co-glycolide)-rifampicin nanoparticles efficiently clear Mycobacterium bovis BCG infection in

macrophages and remain membrane-bound in phago-lysosomes. *J. Cell Sci.* **2013**, *126* (14), 3043−3054.

(16) Fenaroli, F.; Westmoreland, D.; Benjaminsen, J.; Kolstad, T.; Skjeldal, F. M.; Meijer, A. H.; van der Vaart, M.; Ulanova, L.; Roos, N.; Nystrom, B.; Hildahl, J.; Griffiths, G. Nanoparticles as drug delivery system against tuberculosis in zebrafish embryos: direct visualization and treatment. *ACS Nano* **2014**, *8* (7), 7014−26.

(17) Silveira, N.; Longuinho, M. M.; Leitão, S. G.; Silva, R. S. F.; Lourenço, M. C.; Silva, P. E. A.; Pinto, M. d. C. F. R.; Abraçado, L. G.; Finotelli, P. V. Synthesis and characterization of the antitubercular phenazine lapazine and development of PLGA and PCL nanoparticles for its entrapment. *Mater. Sci. Eng., C* **2016**, *58*, 458−466.

(18) Trousil, J.; Filippov, S. K.; Hrubý, M.; Mazel, T.; Syrová, Z.; Cmarko, D.; Svidenská, S.; Matějková, J.; Kováčik, L.; Porsch, B.; Konefał, R.; Lund, R.; Nyström, B.; Raška, I.; Štěpánek, P. System with embedded drug release and nanoparticle degradation sensor showing efficient rifampicin delivery into macrophages. *Nanomedicine* **2017**, *13* (1), 307−315.

(19) Kim, M. S.; Seo, K. S.; Khang, G.; Lee, H. B. Ring-Opening Polymerization of ε-Caprolactone by Poly(ethylene glycol) by an Activated Monomer Mechanism. *Macromol. Rapid Commun.* **2005**, *26* (8), 643−648.

(20) Hyun, H.; Park, H. S.; Kwon, Y. D.; Khang, G.; Lee, B. H.; Kim, S. M. Thermo-Responsive Injectable MPEG-Polyester Diblock Copolymers for Sustained Drug Release. *Polymers* **2014**, *6* (10), 2670.

(21) Luo, L.; Tam, J.; Maysinger, D.; Eisenberg, A. Cellular Internalization of Poly(ethylene oxide)-b-poly(ε-caprolactone) Diblock Copolymer Micelles. *Bioconjugate Chem.* **2002**, *13* (6), 1259−1265.

(22) Bauer, M.; Lautenschlaeger, C.; Kempe, K.; Tauhardt, L.; Schubert, U. S.; Fischer, D. Poly(2-ethyl-2-oxazoline) as alternative for the stealth polymer poly(ethylene glycol): comparison of in vitro cytotoxicity and hemocompatibility. *Macromol. Biosci.* **2012**, *12* (7), 986−98.

(23) Raschke, W. C.; Baird, S.; Ralph, P.; Nakoinz, I. Functional macrophage cell lines transformed by abelson leukemia virus. *Cell* **1978**, *15* (1), 261−267.

(24) Driever, W.; Rangini, Z. Characterization of a cell line derived from zebrafish (brachydanio rerio) embryos. *In Vitro Cell. Dev. Biol.* **1993**, *29* (9), 749.

(25) ISO. *Biological evaluation of medical devices*; ISO 10993-5; ISO, 2009.

(26) Cosma, C. L.; Swaim, L. E.; Volkman, H.; Ramakrishnan, L.; Davis, J. M. Zebrafish and frog models of Mycobacterium marinum infection. *Curr. Protoc. Microbiol.* 2006; Chapter 10, Unit 10B.2.

(27) Lawson, N. D.; Weinstein, B. M. In vivo imaging of embryonic vascular development using transgenic zebrafish. *Dev. Biol.* **2002**, *248* (2), 307−18.

(28) Kim, M. S.; Hyun, H.; Seo, K. S.; Cho, Y. H.; Won Lee, J.; Rae Lee, C.; Khang, G.; Lee, H. B. Preparation and characterization of MPEG−PCL diblock copolymers with thermo-responsive sol−gel−sol phase transition. *J. Polym. Sci., Part A: Polym. Chem.* **2006**, *44* (18), 5413−5423.

(29) Balestrieri, C.; Camussi, G.; Giovane, A.; Iorio, E. L.; Quagliuolo, L.; Servillo, L. Measurement of Platelet-Activating Factor Acetylhydrolase Activity by Quantitative High-Performance Liquid Chromatography Determination of Coumarin-Derivatized 1-O-Alkyl-2-sn-lysoglyceryl-3-phosphorylcholine. *Anal. Biochem.* **1996**, *233* (2), 145−150.

(30) Ianiro, A.; Patterson, J.; Gonzalez García, Á.; van Rijt, M. M. J.; Hendrix, M. M. R. M.; Sommerdijk, N. A. J. M.; Voets, I. K.; Esteves, A. C. C.; Tuinier, R. A roadmap for poly(ethylene oxide)-block-poly-ε-caprolactone self-assembly in water: Prediction, synthesis, and characterization. *J. Polym. Sci., Part B: Polym. Phys.* **2018**, *56* (4), 330−339.

(31) Dionzou, M.; Morere, A.; Roux, C.; Lonetti, B.; Marty, J. D.; Mingotaud, C.; Joseph, P.; Goudouneche, D.; Payre, B.; Leonetti, M.; Mingotaud, A. F. Comparison of methods for the fabrication and the characterization of polymer self-assemblies: what are the important parameters? *Soft Matter* **2016**, *12* (7), 2166−2176.

(32) Domingos, R. F.; Baalousha, M. A.; Ju-Nam, Y.; Reid, M. M.; Tufenkji, N.; Lead, J. R.; Leppard, G. G.; Wilkinson, K. J. Characterizing Manufactured Nanoparticles in the Environment: Multimethod Determination of Particle Sizes. *Environ. Sci. Technol.* **2009**, *43* (19), 7277−7284.

(33) Zölls, S.; Tantipolphan, R.; Wiggenhorn, M.; Winter, G.; Jiskoot, W.; Friess, W.; Hawe, A. Particles in Therapeutic Protein Formulations, Part 1: Overview of Analytical Methods. *J. Pharm. Sci.* **2012**, *101* (3), 914−935.

(34) Ukawala, M.; Rajyaguru, T.; Chaudhari, K.; Manjappa, A. S.; Pimple, S.; Babbar, A. K.; Mathur, R.; Mishra, A. K.; Murthy, R. S. Investigation on design of stable etoposide-loaded PEG-PCL micelles: effect of molecular weight of PEG-PCL diblock copolymer on the in vitro and in vivo performance of micelles. *Drug Delivery* **2012**, *19* (3), 155−67.

(35) Zhang, Z.; Qu, Q.; Li, J.; Zhou, S. The effect of the hydrophilic/hydrophobic ratio of polymeric micelles on their endocytosis pathways into cells. *Macromol. Biosci.* **2013**, *13* (6), 789−98.

(36) Kolouchova, K.; Sedlacek, O.; Jirak, D.; Babuka, D.; Blahut, J.; Kotek, J.; Vit, M.; Trousil, J.; Konefal, R.; Janouskova, O.; Podhorska, B.; Slouf, M.; Hruby, M. Self-Assembled Thermoresponsive Polymeric Nanogels for (19)F MR Imaging. *Biomacromolecules* **2018**, *19* (8), 3515−3524.

(37) Oberdörster, G.; Oberdörster, E.; Oberdörster, J. Nanotoxicology: An Emerging Discipline Evolving from Studies of Ultrafine Particles. *Environ. Health Perspect.* **2005**, *113* (7), 823−839.

(38) Pham, D. D.; Fattal, E.; Tsapis, N. Pulmonary drug delivery systems for tuberculosis treatment. *Int. J. Pharm.* **2015**, *478* (2), 517−29.

(39) Gustafson, H. H.; Holt-Casper, D.; Grainger, D. W.; Ghandehari, H. Nanoparticle Uptake: The Phagocyte Problem. *Nano Today* **2015**, *10* (4), 487−510.

(40) Williams, D. F.; Zhong, S. P. Biodeterioration/biodegradation of polymeric medical devices in situ. *Int. Biodeterior. Biodegrad.* **1994**, *34* (2), 95−130.

(41) Gan, Z.; Liang, Q.; Zhang, J.; Jing, X. Enzymatic degradation of poly(ε-caprolactone) film in phosphate buffer solution containing lipases. *Polym. Degrad. Stab.* **1997**, *56* (2), 209−213.

(42) Rahmouni, M.; Chouinard, F.; Nekka, F.; Lenaerts, V.; Leroux, J. C. Enzymatic degradation of cross-linked high amylose starch tablets and its effect on in vitro release of sodium diclofenac. *Eur. J. Pharm. Biopharm.* **2001**, *51* (3), 191−198.

(43) Rifampin. *Tuberculosis* **2008**, *88* (2), 151−154,.

(44) Grossen, P.; Witzigmann, D.; Sieber, S.; Huwyler, J. PEG-PCL-based nanomedicines: A biodegradable drug delivery system and its application. *J. Controlled Release* **2017**, *260*, 46−60.

(45) Moreno-Bautista, G.; Tam, K. C. Evaluation of dialysis membrane process for quantifying the in vitro drug-release from colloidal drug carriers. *Colloids Surf., A* **2011**, *389* (1), 299−303.

(46) Zambito, Y.; Pedreschi, E.; Di Colo, G. Is dialysis a reliable method for studying drug release from nanoparticulate systems?—A case study. *Int. J. Pharm.* **2012**, *434* (1), 28−34.

(47) Raschke, W. C.; Baird, S.; Ralph, P.; Nakoinz, I. Functional macrophage cell lines transformed by Abelson leukemia virus. *Cell* **1978**, *15* (1), 261−7.

(48) Behzadi, S.; Serpooshan, V.; Tao, W.; Hamaly, M. A.; Alkawareek, M. Y.; Dreaden, E. C.; Brown, D.; Alkilany, A. M.; Farokhzad, O. C.; Mahmoudi, M. Cellular uptake of nanoparticles: journey inside the cell. *Chem. Soc. Rev.* **2017**, *46* (14), 4218−4244.

(49) Lesniak, A.; Campbell, A.; Monopoli, M. P.; Lynch, I.; Salvati, A.; Dawson, K. A. Serum heat inactivation affects protein corona composition and nanoparticle uptake. *Biomaterials* **2010**, *31* (36), 9511−9518.

(50) Fox, M. E.; Szoka, F. C.; Fréchet, J. M. J. Soluble polymer carriers for the treatment of cancer: the importance of molecular architecture. *Acc. Chem. Res.* **2009**, *42* (8), 1141−1151.

(51) Orchel, A.; Jelonek, K.; Kasperczyk, J.; Dzierzewicz, Z. Growth of human fibroblasts in the presence of 6-hydroxyhexanoic acid. *Acta Polym. Pharm.* **2010**, *67* (6), 710−712.

(52) Giacomelli, F. C.; Stepánek, P.; Schmidt, V.; Jäger, E.; Jäger, A.; Giacomelli, C. Light scattering evidence of selective protein fouling on biocompatible block copolymer micelles. *Nanoscale* **2012**, *4* (15), 4504−4514.

(53) Lynch, I.; Cedervall, T.; Lundqvist, M.; Cabaleiro-Lago, C.; Linse, S.; Dawson, K. A. The nanoparticle−protein complex as a biological entity; a complex fluids and surface science challenge for the 21st century. *Adv. Colloid Interface Sci.* **2007**, *134−135*, 167−174.

(54) Wan, Y.; Gan, Z.; Li, Z. Effects of the surface charge on the stability of PEG-b-PCL micelles: simulation of the interactions between charged micelles and plasma components. *Polym. Chem.* **2014**, *5* (5), 1720−1727.

(55) Chakraborti, S.; Chatterjee, T.; Joshi, P.; Poddar, A.; Bhattacharyya, B.; Singh, S. P.; Gupta, V.; Chakrabarti, P. Structure and Activity of Lysozyme on Binding to ZnO Nanoparticles. *Langmuir* **2010**, *26* (5), 3506−3513.

(56) Roy, S.; Saxena, S. K.; Mishra, S.; Yogi, P.; Sagdeo, P. R.; Kumar, R. Ecofriendly gold nanoparticles − Lysozyme interaction: Thermodynamical perspectives. *J. Photochem. Photobiol., B* **2017**, *174*, 284−290.

(57) Zhang, H.; Wu, P.; Zhu, Z.; Wang, Y. Interaction of γ-Fe2O3 nanoparticles with fibrinogen. *Spectrochim. Acta, Part A* **2015**, *151*, 40−47.

(58) Piddock, L. J. V.; Williams, K. J.; Ricci, V. Accumulation of rifampicin by Mycobacterium Aurum, Mycobacterium smegmatis and Mycobacterium tuberculosis. *J. Antimicrob. Chemother.* **2000**, *45* (2), 159−165.

(59) Hui, J.; Gordon, N.; Kajioka, R. Permeability barrier to rifampin in mycobacteria. *Antimicrob. Agents Chemother.* **1977**, *11* (5), 773−779.

(60) Woodley, C. L.; Kilburn, J. O.; David, H. L.; Silcox, V. A. Susceptibility of Mycobacteria to Rifampin. *Antimicrob. Agents Chemother.* **1972**, *2* (4), 245−249.

(61) Garnham, J. C.; Taylor, T.; Turner, P.; Chasseaud, L. F. Serum concentrations and bioavailability of rifampicin and isoniazid in combination. *Br. J. Clin. Pharmacol.* **1976**, *3* (5), 897−902.

(62) Kisich, K. O.; Gelperina, S.; Higgins, M. P.; Wilson, S.; Shipulo, E.; Oganesyan, E.; Heifets, L. Encapsulation of moxifloxacin within poly(butyl cyanoacrylate) nanoparticles enhances efficacy against intracellular Mycobacterium tuberculosis. *Int. J. Pharm.* **2007**, *345* (1), 154−162.

(63) Yoshida, A.; Matumoto, M.; Hshizume, H.; Oba, Y.; Tomishige, T.; Inagawa, H.; Kohchi, C.; Hino, M.; Ito, F.; Tomoda, K.; Nakajima, T.; Makino, K.; Terada, H.; Hori, H.; Soma, G.-I. Selective delivery of rifampicin incorporated into poly(DL-lactic-co-glycolic) acid microspheres after phagocytotic uptake by alveolar macrophages, and the killing effect against intracellular Mycobacterium bovis Calmette−Guérin. *Microbes Infect.* **2006**, *8* (9), 2484−2491.

(64) Hirota, K.; Hasegawa, T.; Nakajima, T.; Inagawa, H.; Kohchi, C.; Soma, G.-I.; Makino, K.; Terada, H. Delivery of rifampicin−PLGA microspheres into alveolar macrophages is promising for treatment of tuberculosis. *J. Controlled Release* **2010**, *142* (3), 339−346.

(65) Trousil, J.; Ulmann, V.; Hrubý, M. Fluorescence & Bioluminiscence in the Quest for Imaging, Probing & Analysis of Mycobacterial Infections. *Future Microbiol.* **2018**, *13*, 933−951.

(66) Clemens, D. L.; Lee, B.-Y.; Xue, M.; Thomas, C. R.; Meng, H.; Ferris, D.; Nel, A. E.; Zink, J. I.; Horwitz, M. A. Targeted Intracellular Delivery of Antituberculosis Drugs to Mycobacterium tuberculosis-Infected Macrophages via Functionalized Mesoporous Silica Nanoparticles. *Antimicrob. Agents Chemother.* **2012**, *56* (5), 2535−2545.

(67) de Faria, T. J.; Roman, M.; de Souza, N. M.; De Vecchi, R.; de Assis, J. V.; dos Santos, A. L. G.; Bechtold, I. H.; Winter, N.; Soares, M. J.; Silva, L. P.; De Almeida, M. V.; Báfica, A. An Isoniazid Analogue Promotes Mycobacterium tuberculosis-Nanoparticle Interactions and Enhances Bacterial Killing by Macrophages. *Antimicrob. Agents Chemother.* **2012**, *56* (5), 2259−2267.

(68) Davis, J. M.; Clay, H.; Lewis, J. L.; Ghori, N.; Herbomel, P.; Ramakrishnan, L. Real-Time Visualization of Mycobacterium-Macrophage Interactions Leading to Initiation of Granuloma Formation in Zebrafish Embryos. *Immunity* **2002**, *17* (6), 693−702.

(69) Cronan, M. R.; Beerman, R. W.; Rosenberg, A. F.; Saelens, J. W.; Johnson, M. G.; Oehlers, S. H.; Sisk, D. M.; Jurcic Smith, K. L.; Medvitz, N. A.; Miller, S. E.; Trinh, L. A.; Fraser, S. E.; Madden, J. F.; Turner, J.; Stout, J. E.; Lee, S.; Tobin, D. M. Macrophage Epithelial Reprogramming Underlies Mycobacterial Granuloma Formation and Promotes Infection. *Immunity* **2016**, *45* (4), 861−876.

(70) Fenaroli, F.; Repnik, U.; Xu, Y.; Johann, K.; Van Herck, S.; Dey, P.; Skjeldal, F. M.; Frei, D. M.; Bagherifam, S.; Kocere, A.; Haag, R.; De Geest, B. G.; Barz, M.; Russell, D. G.; Griffiths, G. Enhanced Permeability and Retention-Like Extravasation of Nanoparticles from the Vasculature into Tuberculosis Granulomas in Zebrafish and Mouse Models. *ACS Nano* **2018**, *12* (8), 8646−8661.

(71) de Steenwinkel, J. E. M.; Aarnoutse, R. E.; de Knegt, G. J.; ten Kate, M. T.; Teulen, M.; Verbrugh, H. A.; Boeree, M. J.; van Soolingen, D.; Bakker-Woudenberg, I. A. J. M. Optimization of the Rifampin Dosage to Improve the Therapeutic Efficacy in Tuberculosis Treatment Using a Murine Model. *Am. J. Respir. Crit. Care Med.* **2013**, *187* (10), 1127−1134.

(72) Smola, M.; Vandamme, T.; Sokolowski, A. Nanocarriers as pulmonary drug delivery systems to treat and to diagnose respiratory and non respiratory diseases. *Int. J. Nanomed.* **2008**, *3* (1), 1−19.

PUBLICATION P2

Trousil J., Pavliš O., Kubíčková P., Dai Y.-S., Škorič M., Marešová V., Knudsen D. K., Pavlova E., Fang J.-Y., Zimmerman M., Dartois V., Hrubý M. *Journal of Controlled Release*. 2020. 321, 312–323. IF = 7.90

J.T. synthesized the polymer, carried out the physicochemical characterizations, the cytotoxicity, and confocal microscopy experiments, conceptualized all the *in vivo* experiments, analyzed biological data, and wrote the paper. O.P. and P.K. were responsible for the infection experiments *in vivo* and contributed to the final version of the paper. Y.-S.D. carried out the bioimaging experiments. M.Š. carried out the histopathological examinations and contributed to the final version of the paper. V.M. and M.Z. carried out HPLC analyses. K.D.K. carried out the SANS analysis and contributed to the final version of the paper. E.P. performed the cryo-TEM investigation. J.-Y.F. supervised the bioimaging experiments. V.D. contributed to the pharmacokinetics-related part of the paper and supervised part of the HPLC. M.H. read the manuscript critically and contributed to the final version.

Journal of Controlled Release 321 (2020) 312–323

Contents lists available at ScienceDirect

Journal of Controlled Release

journal homepage: www.elsevier.com/locate/jconrel

Antitubercular nanocarrier monotherapy: Study of *In Vivo* efficacy and pharmacokinetics for rifampicin

Jiří Trousil[a,b,*], Oto Pavliš[c], Pavla Kubíčková[c], Miša Škorič[d], Věra Marešová[e], Ewa Pavlova[a], Kenneth D. Knudsen[f], You-Shan Dai[g], Matthew Zimmerman[h], Véronique Dartois[h], Jia-You Fang[g], Martin Hrubý[a,*]

[a] *Institute of Macromolecular Chemistry, Czech Academy of Sciences, Heyrovského náměstí 2, 162 00 Prague 6, Czechia*
[b] *Department of Analytical Chemistry, Faculty of Science, Charles University, Hlavova 8, 128 43 Prague 2, Czechia*
[c] *Center of Biological Defense, Military Health Institute, Military Medical Agency, 561 66 Těchonín, Czechia*
[d] *Department of Pathology and Parasitology, Faculty of Veterinary Medicine, University of Veterinary and Pharmaceutical Sciences Brno, Brno, Czechia*
[e] *Institute of Forensic Medicine and Toxicology, First Faculty of Medicine, Charles University in Prague and General University Hospital, Ke Karlovu 2, 121 08 Prague 2, Czechia*
[f] *Department of Physics, Institute for Energy Technology, P. O. Box 40, N-2027 Kjeller, Norway*
[g] *Pharmaceutics Laboratory, Graduate Institute of Natural Products, Chang Gung University, Taoyuan 333, Taiwan*
[h] *Public Health Research Institute, New Jersey Medical School, Rutgers, The State University of New Jersey, Newark, NJ 07103, USA*

ARTICLE INFO

Keywords:
Tuberculosis
Nanoparticles
Drug delivery system
Rifampicin
BALB/c mice
Pharmacokinetics
Histopathology

ABSTRACT

Tuberculosis represents a major global health problem for which improved approaches are needed to shorten the course of treatment and to combat the emergence of resistant strains. The development of effective and safe nanobead-based interventions can be particularly relevant for increasing the concentrations of antitubercular agents within the infected site and reducing the concentrations in the general circulation, thereby avoiding off-target toxic effects. In this work, rifampicin, a first-line antitubercular agent, was encapsulated into biocompatible and biodegradable polyester-based nanoparticles. In a well-established BALB/c mouse model of pulmonary tuberculosis, the nanoparticles provided improved pharmacokinetics and pharmacodynamics. The nanoparticles were well tolerated and much more efficient than an equivalent amount of free rifampicin.

1. Introduction

Tuberculosis (TB) represents a global health problem, although a potentially curative therapy has been available for approximately 50 years [1–3]. TB has killed millions of people over the past centuries and remains among the leading causes of infectious morbidity. This intracellular disease affects approximately 1 in 3 people worldwide, with over 10 million new cases per year and one death every three minutes [4].

TB can usually be treated with a 6- to 9-month course of combined therapy. Rifampicin (RIF), isoniazid, pyrazinamide and ethambutol are core drugs used for this purpose. However, the necessity of using a cocktail of anti-TB drugs and the long-term treatment schedules required for conventional therapy result in poor patient compliance; therefore, the risk of treatment failure and relapse is higher. Improved drug delivery strategies for the existing drugs can be exploited to shorten TB treatment duration and to avoid the selection of drug-resistant mutants [5].

Nanoparticle (NP) technology has emerged as one of the most promising approaches for overcoming the above-listed shortcomings associated with TB therapy thanks to the unique physicochemical properties of nanomaterials. These include their small size, allowing them to reach the intracellular level, and their ability to be modified to control their biorelevant behavior. Also note that nanobead-based interventions allow the improvement of aqueous solubility of drugs, drug protection, selective transport to the sites of infection and controlled release. [6] Utilizing nanocarriers for drug delivery into the lungs, which is the primary site of TB infection, offers an elegant way to circumvent the numerous difficulties associated with conventional therapy. [6–8] Within the sites of inflammation, the endothelium becomes permeable due to pathologic processes. Nanobead-based structures follow the route of particulate patterns, including intracellular pathogens, and they are preferentially taken up by phagocytes, which further enhance their targeting [1]. Thus, these approaches enhance the

---

* Corresponding authors at: Institute of Macromolecular Chemistry, Czech Academy of Sciences, Heyrovského náměstí 2, 162 00 Prague 6, Czechia.
E-mail addresses: trousil@imc.cas.cz (J. Trousil), hruby@imc.cas.cz (M. Hrubý).

https://doi.org/10.1016/j.jconrel.2020.02.026
Received 7 October 2019; Received in revised form 7 January 2020; Accepted 13 February 2020
Available online 14 February 2020
0168-3659/ © 2020 Elsevier B.V. All rights reserved.

therapeutic effectiveness and minimize the undesirable side effects of numerous antibacterial drugs [3,9].

In this context, several types of anti-TB nanoformulations, including solid lipid nanoparticles [6,10], inorganic nanoparticles [7,11,12], micelles [13], and polymeric nanoparticles [14–18], have been utilized. All of these "future medicines" for use in TB regimens, however, still require financial support and further preclinical studies to move on to the next developmental step and reach patients [19]. Despite the fact that handling both animals and pathogens requires specific facility and biosafety conditions, there are studies (*e.g.* [12,15,18,20–23],) describing the antitubercular activity *in vivo*. Most of these promising matrices are not, however, approved by regulatory authorities and, thus, have a lower chance of reaching clinical studies [19]. In this context, the toxicity studies required would increase the final cost of a novel intervention.

Recently, we described an intervention based on FDA-approved [24] biocompatible and biodegradable methoxy poly(ethylene oxide)-*block*-poly(ε-caprolactone) (MPEO-*b*-PCL) nanoparticles loaded with RIF, a cornerstone of modern antitubercular therapy. In these previous studies, we showed that the RIF-loaded nanoparticles were efficiently taken up by Raw 264.7 macrophage-like cells and efficiently killed the intracellularly persistent mycobacteria (nontuberculous *Mycobacterium* sp. as well as *M. tuberculosis* H37Rv). We also demonstrated in a zebrafish model of tuberculosis that the nanoparticles were well tolerated, had a curative effect and were significantly more efficient compared to a free form of RIF.

Considering these previous findings [17,18], we chose the most promising RIF-loaded nanoformulation, which was based on the MPEO_{5k}-*b*-PCL_{4k} copolymer, to test its biorelevant properties. We analyzed the pharmacokinetics and the effects of a RIF-loaded nanoformulation (**NPs-RIF**), a RIF-free nanoformulation (**NPs**), and free **RIF** on artificially induced tuberculous infection using a clinically relevant *in vivo* model.

2. Results and discussion

2.1. NP preparation and characterization

The MPEO_{5k}-*b*-PCL_{4k} copolymer was prepared by the previously described ring-opening polymerization of ε-caprolactone (CL) initiated by methoxy poly(ethylene oxide) (MPEO) (Fig. 1A) [25,26]. GPC and MALDI-TOF investigations showed molecular weights of M_n 8300 Da and 6500 Da and M_w 7200 and 6100 Da, respectively, while the ^{1}H NMR-determined M_n value was found to be 8800 Da.

The fabricated copolymer was subjected to NP preparation by nanoprecipitation from an acetone solution to prepare both the RIF-free and RIF-loaded nanoformulations. The DLS distribution functions of these formulations are portrayed as one mode (Fig. 1C) with z-average hydrodynamic diameter values of 75 nm (**NPs**) and 85 nm (**NPs-RIF**). Using cryo-TEM, these assemblies were found to be spherical (Fig. 1D) and, according to the image analysis (**Fig. S1**), the **NPs** and **NPs-RIF** revealed diameters (nm) of (35 ± 14) and (34 ± 15), respectively. The latter values are close to the peaks seen at *ca.* 45 nm in the DLS distributions (*cf.* Fig. 1C). These peaks represent the particle sizes with the highest volume fraction in the sample, which were the main contributors in the image analysis due to the limited particle number inspected there. Furthermore, the presence of attached water (see below) will also contribute to the sizes from DLS being larger than those extracted from image analysis.

The shape of the NPs was studied by means of small-angle neutron scattering (SANS). The SANS data for the **NPs** and **NPs-RIF** samples (Fig. 1B) showed some differences in the low-*q* range, and the model fits (Fig. 1B, inset) of the data gave a slightly different average diameter for the two samples, 54 nm for the blank **NPs** and 48 nm for the **NPs-RIF** particles. These values are, however, in line with our previous study [18], in which asymmetric flow field flow fractionation (AFFFF) analysis of MPEO_{5k}-*b*-PCL_{4k}-based **NPs** and **NPs-RIF** formulations provided diameter of gyration values of 51 nm and 53 nm, respectively. Note that these diameter values are lower than the average values reported by DLS, which is expected because DLS also effectively measures the non-free water in proximity to the particle surface. Additionally, the SANS data show complete overlap at high *q* (corresponding to length scales roughly below 20 nm), demonstrating that the polymer structure inside the particles does not change when they are loaded with RIF. At the same time, the patterns indicate that the **NPs-RIF** particles have a slightly different density profile than the **NPs.** This may be related to the presence of a gradient in the RIF concentration within the particles. Finally, there is no difference in the SANS data collected at 25 °C and at 37 °C, which is a clear demonstration of the very good temperature stability of these particles, both unloaded and when loaded with RIF. This means that there is no significant dehydration upon temperature change, which could otherwise reduce the loading capacity.

2.2. Cytotoxicity assays

Before the *in vivo* experiments, we performed robust cytotoxicity testing based on MTT. The assay is based on the cleavage of the yellow tetrazolium salt MTT to purple formazan crystals by metabolically active cells. The MTT assays were performed with the mouse ascites-based macrophage J744A.1 cell line, the mouse peritoneal macrophage IC-21 cell line, the mouse alveolar macrophage MH-S cell line, and the human lung epithelium BEAS-2B cell line.

MPEO-*b*-PCL is an FDA-approved copolymer that was shown to possess no or only minor toxic effects on the viability of different cell lines. Hence, it was not surprising that blank MPEO_{5k}-*b*-PCL_{4k} **NPs** did not reveal any significant toxicity [27]. In contrast, **NPs-RIF** revealed increased cytotoxicity compared to **RIF** (**Fig. S2B** & **C**). In terms of drug delivery, this finding is somewhat unusual; however, it is in line with our previous studies dealing with RIF-loaded MPEO-*b*-PCL nanoformulations [17,18]. We hypothesize that it was caused by the fact that the NP-mediated RIF delivery is more efficacious. Thus, more of the drug is delivered. This issue was not, however, addressed further.

The IC_{50} (μg/mL) values for the **NPs-RIF** formulation were found to be (238 ± 27), (134 ± 5), (157 ± 6) and (273 ± 20) for the IC-21, J774A.1, MH-S and BEAS-2B cell lines, respectively. The estimated IC_{50} values are approximately ten times higher than clinically relevant concentrations of rifampicin (see below), suggesting that the above-mentioned phenomenon should not lead to significant toxic effects *in vivo*.

2.3. Bioimaging of the NPs after intraperitoneal injection

In our previous studies [17,18], the RIF-loaded MPEO-*b*-PCL nanocarriers were described in terms of physicochemical properties: drug loading and release, hemolytic activity, interaction with Raw 264.7 macrophage-like cells and impact on mycobacterial infection in zebrafish embryos. Hence, to obtain a more detailed picture of this system, the main aim of this work was to assess the biorelevant properties, such as the pharmacokinetics or antitubercular efficacy in a mouse model.

To evaluate the biodistribution of our NPs and to acquire a deeper understanding of their fate, we performed *in vivo* and *ex vivo* imaging of Dyomics 700-labeled NPs (**NPs-Dy**) after a single intraperitoneal administration to mycobacteria-free BALB/c mice at a dose of 10 mg/kg, an amount that corresponds to the dose used for all the mouse experiments (see below).

Fig. 2A depicts the NIR signal of **NPs-Dy** and free **Dy** (administered at a corresponding concentration of 55 μg/mL) as a function of time *in vivo*. The maximum whole body NIR signal was reached within 1–2 h after the administration of both **NPs-Dy** and **Dy**. In both cases, a subsequent decrease in the NIR signal was observed. The free dye, which is a low molecular weight compound, showed a faster clearance, while the decay of the **NPs-Dy** signal was slower, as was evident from the NIR

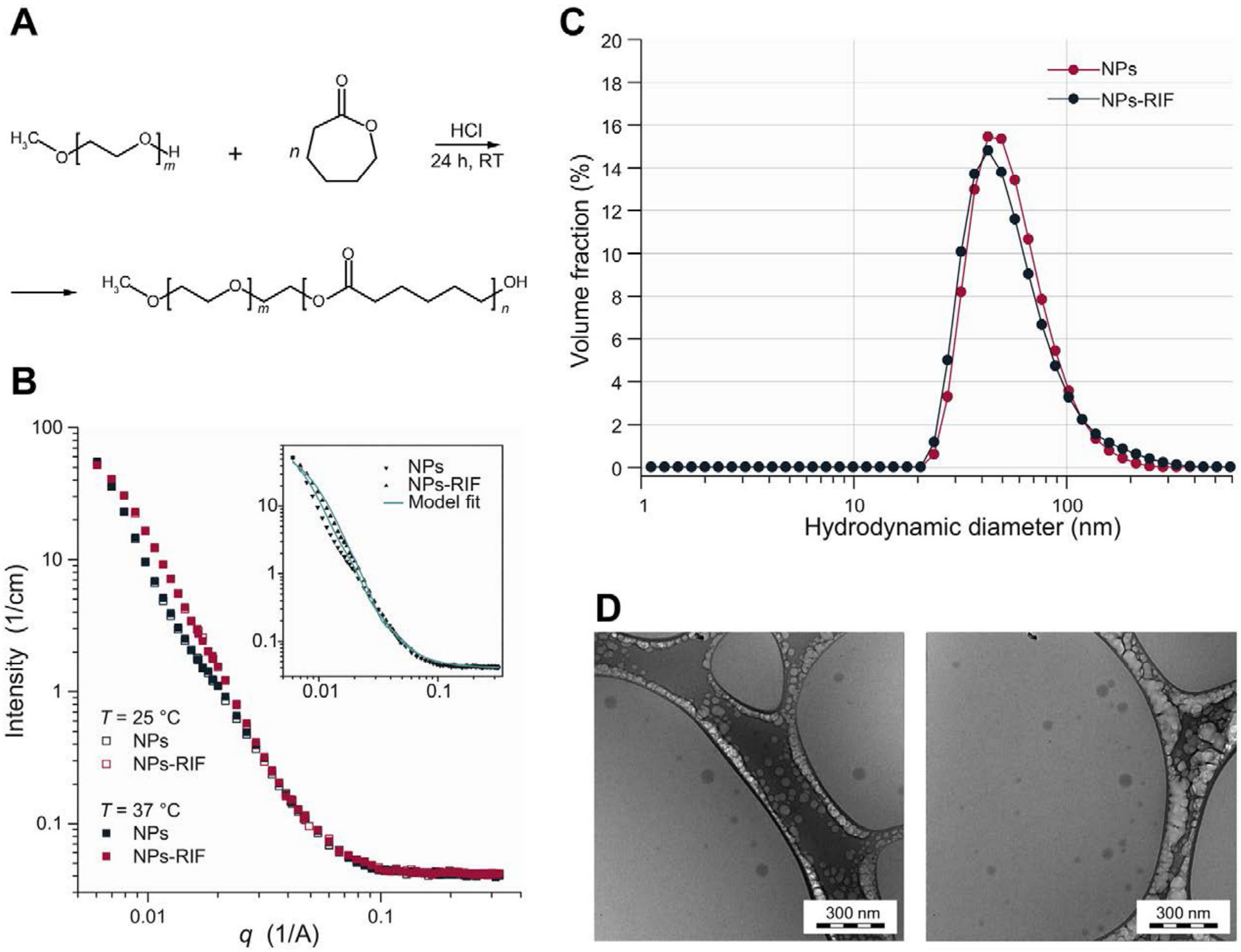

Fig. 1. NP preparation and physicochemical characterization. (**A**) Scheme of MPEO-*b*-PCL synthesis. (**B**) Small-angle neutron scattering (SANS) patterns. (**C**) Corresponding volume-weighted size distribution was obtained from the dynamic light scattering (DLS) investigation. (**D**) Cryo-TEM images of **NPs** (left) and **NPs-RIF** (right) formulations.

data quantification (Fig. 2B). These data suggest that the major fraction of both the **NPs-Dy** and free **Dy** was eliminated within 24 h of the experiment. Regarding the fate of the NPs, the *in vivo* imaging also revealed that the NPs were found mainly in the liver, intestinal tissue, *i.e.*, organs of the mononuclear phagocyte system (MPS). This result was confirmed by an additional evaluation of the NIR signal from the different organs *ex vivo* 6 h after injection (Fig. 2C). Higher mean signal was recovered from the liver and stomach/intestine for **NPs-Dy** than for **Dy** itself. Both *in vivo* and *ex vivo*, fluorescence could be observed in the blank intestinal tissue, probably arising from autofluorescent food [28]. The other organs inspected (*i.e.*, brain, heart, lung, spleen, bladder/ovary, and kidney) did not reveal any signal that could be distinguished from the noise.

Based on the results shown, it can be suggested that both liver and intestinal tissue are involved in the NP elimination and that the polymeric carrier is cleared though both the MPS and hepatobiliary system [29].

2.4. Pharmacokinetics and pharmacodynamics of rifampicin

Since the bioimaging depicts only the polymeric nanocarrier fate and does not provide any detailed information about the drug-loaded nanobead-based intervention, we focused on the study of RIF pharmacokinetics. Using mycobacteria-infected BALB/c mice, the pharmacokinetic parameters of **NPs-RIF** were compared with those of free rifampicin (**RIF**). A single dose of **NPs-RIF** at 10 mg/kg or 10 mg/kg of free **RIF** was administered intraperitoneally; the dose used corresponds to a standard dose of RIF when considering the copolymer–drug ratio used for the nanoprecipitation. The pharmacokinetics were then investigated using liquid chromatography. Blood and lungs were collected at various time points (2, 4, 6, 8, 12, 24, 48, and 72 h).

Both serum and lung homogenate analysis revealed that **NPs-RIF** showed a sustained release compared to free **RIF** (Fig. 3). This observation appears to be in line with the above-described prolonged retention proven by the bioimaging (Fig. 2) and thus suggests improved pharmacokinetics. Consistent with these findings, rifampicin released from the nanobead-based intervention had significantly higher AUCs for serum and lung tissue compared with free **RIF** (Table 1), suggesting better bioavailability, a phenomenon that was also observed for the previously described NP-based antibacterial formulations [30,31].

The critical **NPs-RIF** pharmacokinetic parameters were improved compared to those orally administered at a single dose of 10 mg/kg, which corresponds to a human daily dose of 600 mg (the WHO-recommended dose). For instance, Bruzzese and colleagues [32] found the $AUC_{0-24\ h}$ for plasma and lungs to be 106.6 µg·h/mL and 44.7 µg·h/g, respectively, when free RIF was orally administered to CD1 mice. Similarly, the $AUC_{0-24\ h}$ for plasma when RIF was orally administered to BALB/c mice was 122.4 µg·h/mL (*cf.*, **Table I**) [33].

The pharmacodynamics were also evaluated in terms of the $AUC_{0-24\ h}$/MIC and C_{max}/MIC ratios, and whether the RIF level was above or below the MIC for RIF in treating *M. tuberculosis* H37Rv (*i.e.*, 0.2 µg/mL [34]) was considered. However, as the MIC refers to the minimal concentration of an antibiotic that prevents visible growth in a liquid suspension (*e.g.*, broth or plasma), the volume distribution of RIF (0.85 L/kg [35]) was used to convert the MIC value to a more lung tissue-relatable parameter (0.17 µg/g) [30].

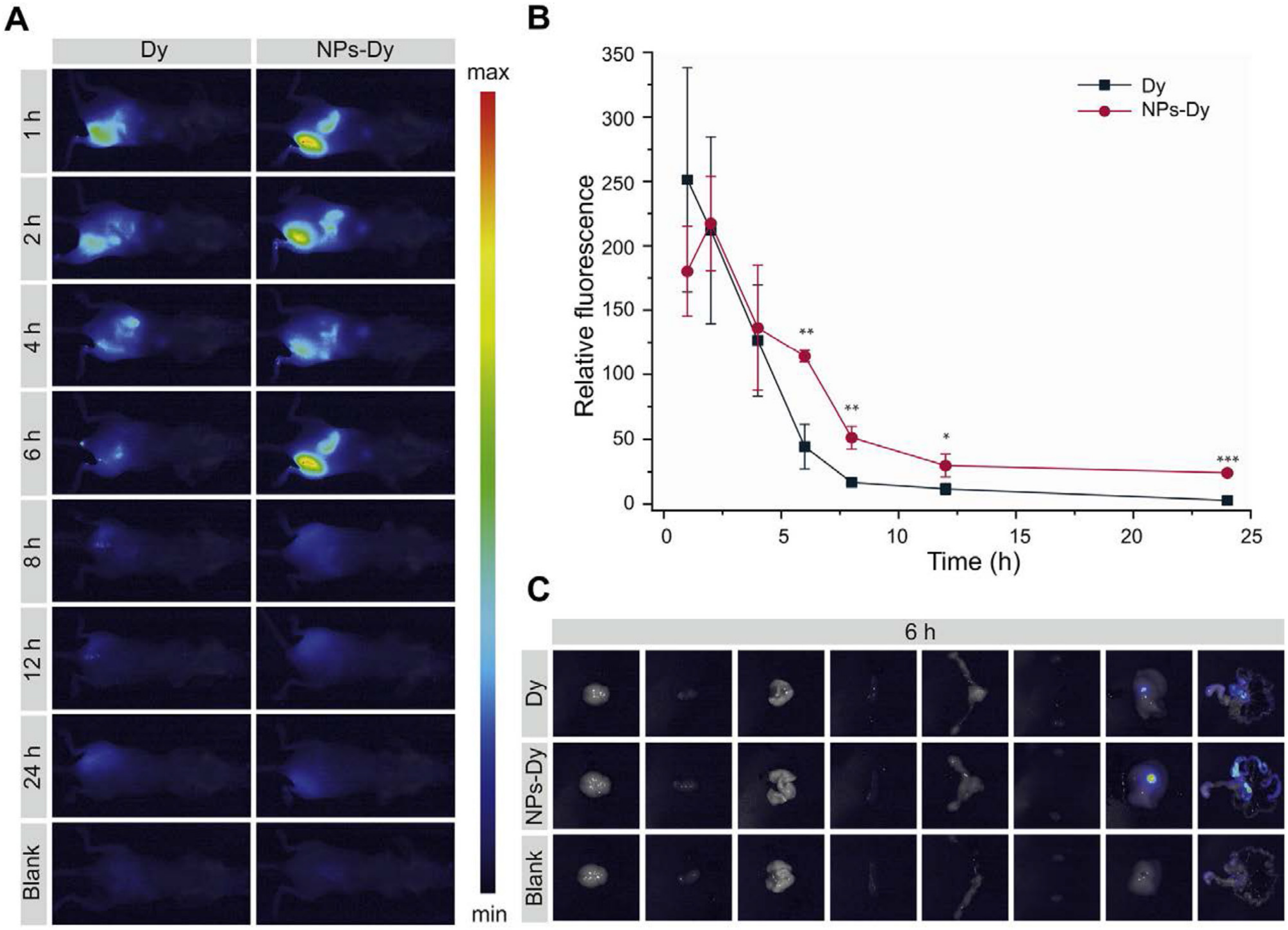

Fig. 2. Bioimaging of MPEO-*b*-PCL NPs in BALB/c mice after intraperitoneal administration. (**A**) Real-time imaging within 24 h after administration. (**B**) Whole body NIR fluorescence data quantification ($n = 3$). Note the prolonged elimination of the NP-based intervention (**NPs-Dy**) compared to the free Dyomics 700 (**Dy**). (**C**) *Ex vivo* imaging of brain, heart, lung, spleen, bladder/ovary, kidney, liver, and stomach/intestine (from left to right) at 6 h after administration. Liver-related fluorescence intensities were 1.7 ± 1.5 and 12.9 ± 5.6 for **Dy** and **(NPs-Dy)**, respectively, whereas intestinal tissue revealed fluorescence intensities of 8.8 ± 0.3 and 40.8 ± 15.0 for **Dy** and (**NPs-Dy**), respectively. The results are expressed as the means ± SD and were analyzed by ANOVA; for the bioimaging, three mice were used for each time point.

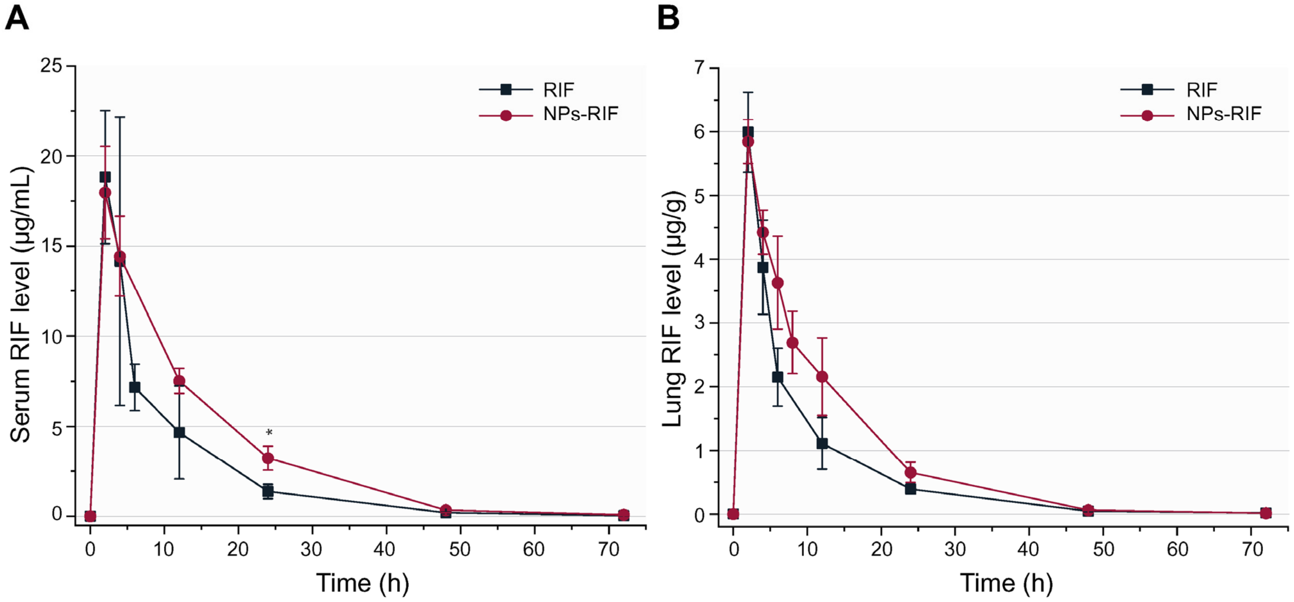

Fig. 3. Pharmacokinetics of rifampicin. NP-encapsulated RIF (**NPs-RIF**) and free **RIF** were administered intraperitoneally to mice at a dose of 10 mg/kg of rifampicin. The animals were euthanized at various time points to determine the rifampicin pharmacokinetics in the serum (**A**) and lungs (**B**). The data represent mean values ± SD ($n = 3$ or 2 for lung or serum analysis, respectively).

Table 1
Summary of critical pharmacokinetic and pharmacodynamic values for free and encapsulated rifampicin.

Organ	Therapy	$AUC_{0–24\ h}$	AUC_{total}	C_{max}	T_{max} (h)	$T_{1/2}$ (h)	C_{max}/MIC	$AUC_{0–24\ h}$/MIC (h)
Serum	RIF	144.8	163.5	18.8	2	3.8	94	724
	NPs-RIF	202.7	250.5	18.0	2	8.3	90	1013.5
Lung	RIF	40.7	46.6	6.0	2	3.2	35.2	239.4
	NPs-RIF	57.1	66.6	5.8	2	6.4	34.1	335.9

Definition of abbreviations: $AUC_{0–24\ h}$, area under the concentration–time curve from 0 to 24 h after dose, units are µg·h/mL or µg·h/g for serum or lung tissue, respectively; AUC_{total}, area under the concentration–time curve from 0 to 72 h after administration; C_{max}, maximum concentration in serum or lung tissue (µg/mL or µg/g, respectively); T_{max}, time to maximum concentration; $T_{1/2}$, elimination half-life; MIC, minimal inhibitory concentration. The results obtained are based on sampling at 2, 4, 6, 8, 12, 24, 48, and 72 h after a single intraperitoneal dose (10 mg/kg).

The C_{max}/MIC ratios were found to be almost the same for both **NPs-RIF** and free **RIF** (Table 1). However, the pharmacodynamics of RIF, as expressed by the ratio of the RIF concentration to the MIC, were found to be improved in both serum and lung tissue when **NPs-RIF** was administered (**Fig. S3**). In other words, the level of RIF released from the nanobead-based intervention in both serum and lungs was greater than that of free RIF, and hence the nanobead-based intervention-related T > MIC values (*i.e.*, the time during which the drug level is above the MIC) were greater in both serum and lungs.

Similarly, in both serum and lungs, the **NPs-RIF**-related $AUC_{0–24\ h}$/MIC ratios were greater compared to those estimated for free **RIF** (Table 1). This is promising, as the AUC/MIC ratio was found to be the pharmacodynamic parameter that best correlates with a reduction in bacterial counts [36]. Thus, the $AUC_{0–24\ h}$/MIC ratios suggest a successful treatment outcome, which is consistent, for instance, with the finding of Jayaram and colleagues [36] who found that an AUC/$MIC_{0–24\ h}$ of 271 is required for a 1 log CFU reduction *in vivo*.

Several clinical trials are currently evaluating the efficacy of high-dose RIF for pulmonary TB (900 to 1200 mg daily, approximately corresponding to 20 mg/kg in mice), as well as for TB meningitis at doses up to 35 mg/kg in patients. Overall, these high doses have been well tolerated, indicating that **NP-RIF** could be administered at higher doses as well, further improving efficacy [37,38].

2.5. *Mouse infection and treatment*

To evaluate the pharmacokinetics- and pharmacodynamics-suggested potential of the fabricated nanobead-based intervention, we focused on the efficacy of our $MPEO_{5k}$-*b*-PCL_{4k} nanoparticles loaded with RIF (**NPs-RIF**) in a mouse model of pulmonary tuberculosis.

We infected BALB/c mice with a virulent *M. tuberculosis* H37Rv strain by intranasal administration of a suspension containing 250–900 viable bacilli. Over the ensuing four weeks, well-defined lung granulomas in the infected animals were noted (Fig. 4**A**), and the mycobacteria grew *ca.* 3 logs to *ca.* 3×10^5 CFU per lung and 2 logs to *ca.* 4×10^4 CFU per spleen (Fig. 4B, C). Notably, histopathological examination of the spleen (four weeks post infection) revealed no granulomatous infection (images not shown) despite hematogenic/lymphogenic dissemination proven by spleen homogenate cultivation.

Four weeks after infection, the mice were treated with blank **NPs**, free **RIF** and **NPs-RIF** *via* the intraperitoneal route at 10 mg/kg, an amount that has been equated to the clinically tolerated dose for rifampin in humans, 5 days per week. Control groups containing both healthy and infected animals were included.

As is evident in Fig. 4B & C, the tubercle burden in mice treated with **NPs-RIF**, compared to untreated mice was significantly reduced in the lungs after both 4 and 8 weeks of therapy. More importantly, these observed reductions in colony-forming units (CFU) in lung tissue achieved by the **NPs-RIF** formulation were significantly greater than those achieved by an equivalent amount of free **RIF** after both 4 and 8 weeks of therapy ($p < .01$ and $p < .001$, respectively). The treatment with blank NPs did not reveal any notable effect on the reduction of pulmonary infection.

The reductions in CFU in spleens achieved by **NPs-RIF** were similar to those in the lungs and were significantly greater compared to those achieved by free **RIF** after both the 4- and 8-week treatment sessions ($p < .01$ and $p < .05$, respectively).

All of these findings were also confirmed and clearly visualized by detailed histopathological examinations. Despite the fact that no gross pathology (Fig. 5) was observed in any of the examined lungs, after 12 weeks post infection (*i.e.*, 8 weeks of treatment), the untreated mice developed chronic inflammation with lung parenchyma-localized nodular granulomatous reaction characterized by macrophage and lymphocyte infiltration (Fig. 5), numerous acid-fast bacilli and collagen deposition. Identically, lungs from the blank **NP**-treated animals revealed the same granulomas, with fibrosis and cellular infiltrate (Fig. 5). Notably, the spleens did not show signs of granulomatous infection or inflammation, which is in accordance with, for example, Irwin et al. [39], who observed no spleen-localized granulomas 7 weeks post infection in BALB/c mice, even though (as in our case) mycobacteria were detectable by cultivation.

In contrast, both **RIF**- and **NPs-RIF**-treated mice presented lungs with a reduced number of granulomas and decreased collagen deposition, suggesting the suppression of nodular chronic inflammation. Note the *ex vivo* examination demonstrated that **NPs-RIF** improved the treatment efficacy, as it led to a significant reduction in the number of granulomas compared to free **RIF**. Treated mice also revealed negative ZN staining (Fig. 5). This finding, however, does not necessarily mean that those lesions were sterilized, as the sensitivity of the ZN staining is reduced by the effects of the fixative fluid and/or organic solvent [40]. Notably, as discussed above, CFU counting revealed an infection with a significantly reduced number of viable mycobacteria (Fig. 4B, C) within both the spleen and lungs.

2.6. *Mechanism of the described antitubercular intervention*

The mechanism behind the observed improvement caused by this therapy is also important to discuss. Given the results presented here, we suggest three synergic effects that could lead to increased antitubercular efficacy *in vivo*.

First, it is likely that the increased efficacy of NPs carrying RIF is due to the improved critical pharmacokinetic and pharmacodynamic parameters estimated in both serum and lungs. This improvement may reflect delayed drug clearance, prolonged drug release by virtue of RIF being entrapped in these polymeric NPs and increased bioavailability.

Second, it is known that nanobead-based structures can be taken up by uninfected macrophages that subsequently migrate to the site of tubercle infection, including the lungs. Fenaroli and colleagues [15] described that poly(lactic-*co*-glycolic acid) (PLGA) nanoparticles administered to *M. marinum*-infected zebrafish larvae were taken up by macrophages that rapidly migrated into the granulomas. Similarly, Dannenberg [41] described the dynamic influx of macrophages into *M. bovis* BCG granulomas in rabbits. After intraperitoneal injection, the nanoformulation is subjected to the major cell type of peritoneal

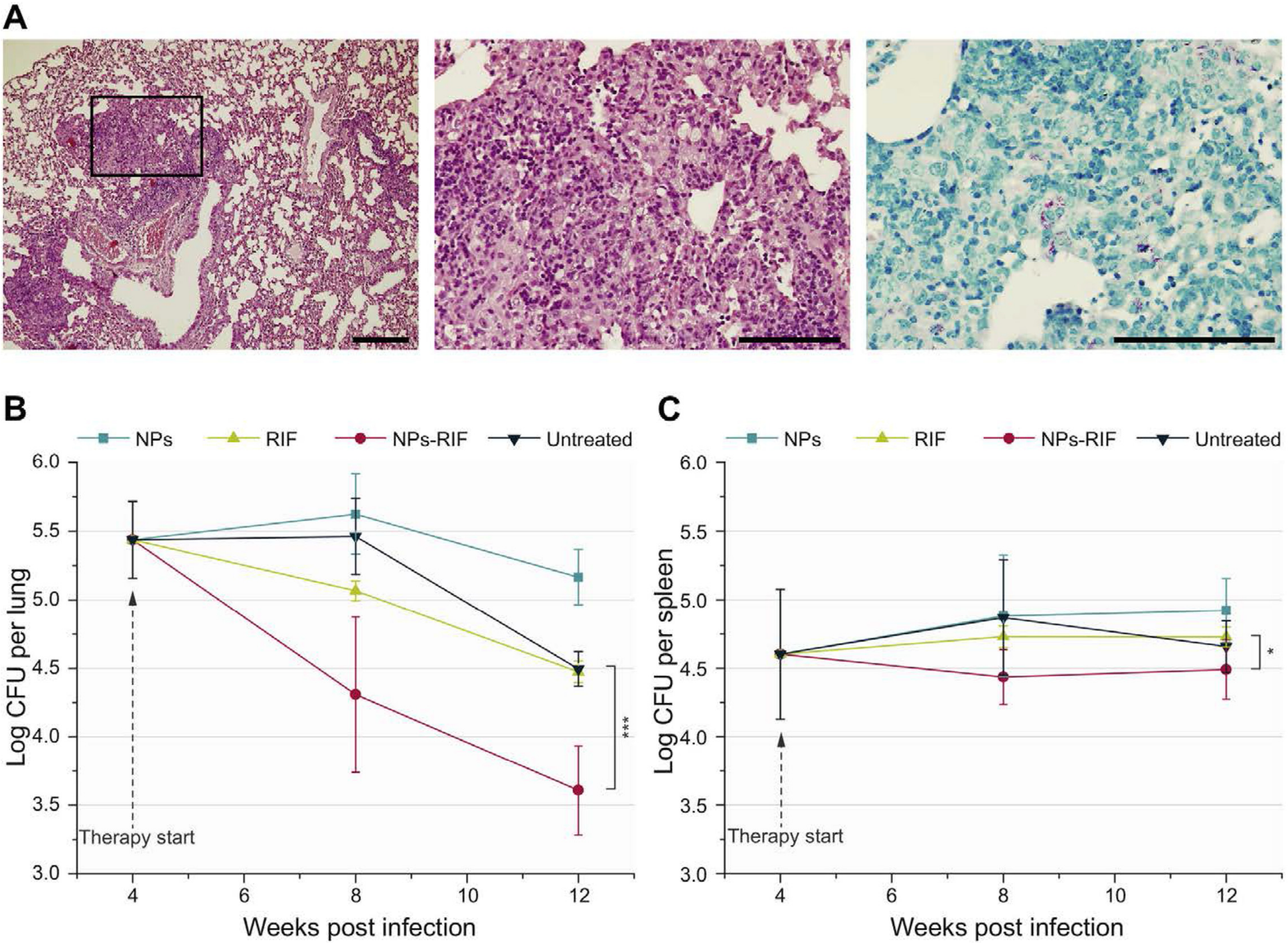

Fig. 4. *In vivo* testing of the fabricated formulations. Mice were infected with viable *M. tuberculosis* H37Rv bacilli by the intranasal route. (**A**) *Ex vivo* histopathological examination demonstrating pulmonary granulomas as a result of TB infection induction. Lung tissues obtained from BALB/c mice 4 weeks after infection with *M. tuberculosis* H37Rv before the subsequent treatment are shown. Hematoxylin and eosin (H&E) staining revealed a lung parenchyma-localized granulomatous inflammatory reaction, characterized by multifocal nodular infiltrate with macrophages (light cytoplasm and round or irregular nucleus) and lymphocytes. A high-power view of the inset is shown in the middle. Ziehl–Nielsen (ZN, right) staining showed numerous acid-fast bacilli (red) in the lesions. During the subsequent treatment, mycobacterial burdens were monitored throughout the course of infection in the lungs (**B**) and spleens (**C**). The effect of the tested formulation (*i.e.*, **NPs**, **RIF**, and **NPs-RIF**) treatments was determined by assaying the mycobacteria CFUs 4, 8, and 12 days post infection. Formulations were administered at 10 mg/kg. The RIF amount was equivalent to those of both the **RIF** and **NPs-RIF** formulations. Scale bars: 200 μm, 100 μm, and 50 μm. The results are expressed as the means ± SD and were analyzed by ANOVA. (For interpretation of the references to colour in this figure legend, the reader is referred to the web version of this article.)

cells—peritoneal macrophages. It could be that peritoneal macrophages are able to take up the nanobeads and migrate to the site of infection, as mentioned above. To confirm this, we carried out a simple experiment focused on the uptake of fluorescently labeled NPs using IC-21 peritoneal macrophages. **Fig. S4** depicts the trafficking, which was studied using confocal laser scanning microscopy, and it is evident that it is a fast process, even though the experiment was carried out at relatively low concentration (40 μg/mL). IC-21 macrophages took up the NPs within a few minutes of incubation. Recently, we described that MPEO-*b*-PCL NPs are able to be taken up by monocyte-macrophage cells in a concentration-dependent manner [18]. Considering this, one may hypothesize that the internalization *in vivo* is even faster than in the *in vitro* uptake experiment, as the concentration of NPs injected was 1000 μg/mL. The *in vivo* bioimaging results revealed that the majority of the **NPs-Dy** were in the liver and intestinal tissue, which are macrophage-rich organs. Altogether, the concept that uninfected macrophages from distant sites may carry nanobead-based structures into infected granulomatous tissue is one of the possible aspects reflecting the improved treatment we observed. In addition, drug-loaded NPs may protect macrophages that are not yet infected.

Recently, the Griffiths group [42] found that an enhanced permeability and retention (EPR)-like process occurs, allowing nanobeads to extravasate from the vasculature to reach granulomas assembled during TB infection. Because NPs that are cleared from the peritoneal cavity end up in the systemic circulation after passing through the lymph nodes and ducts following an i.p. injection [43], this is a third possible explanation for the improved treatment. One may note that the *in vivo* and *ex vivo* imaging cannot support this hypothesis, since these experiments were carried out with noninfected mice. The pharmacokinetics study carried out with mycobacteria-infected mice, however, revealed increased levels of RIF within the lungs (Fig. 3B). For example, at 4 h, the total drug content in the lung tissue was 815 and 683 ng for **NPs-RIF** and **RIF**, respectively. Similarly, at 12 h, the antibiotic content was 382 and 233 ng, respectively, making the EPR-like effect a highly possible explanation.

2.7. Final remarks and future prospects

As indicated above, the aim of this study was to comprehensively analyze the effects of a fabricated RIF-loaded MPEO-*b*-PCL

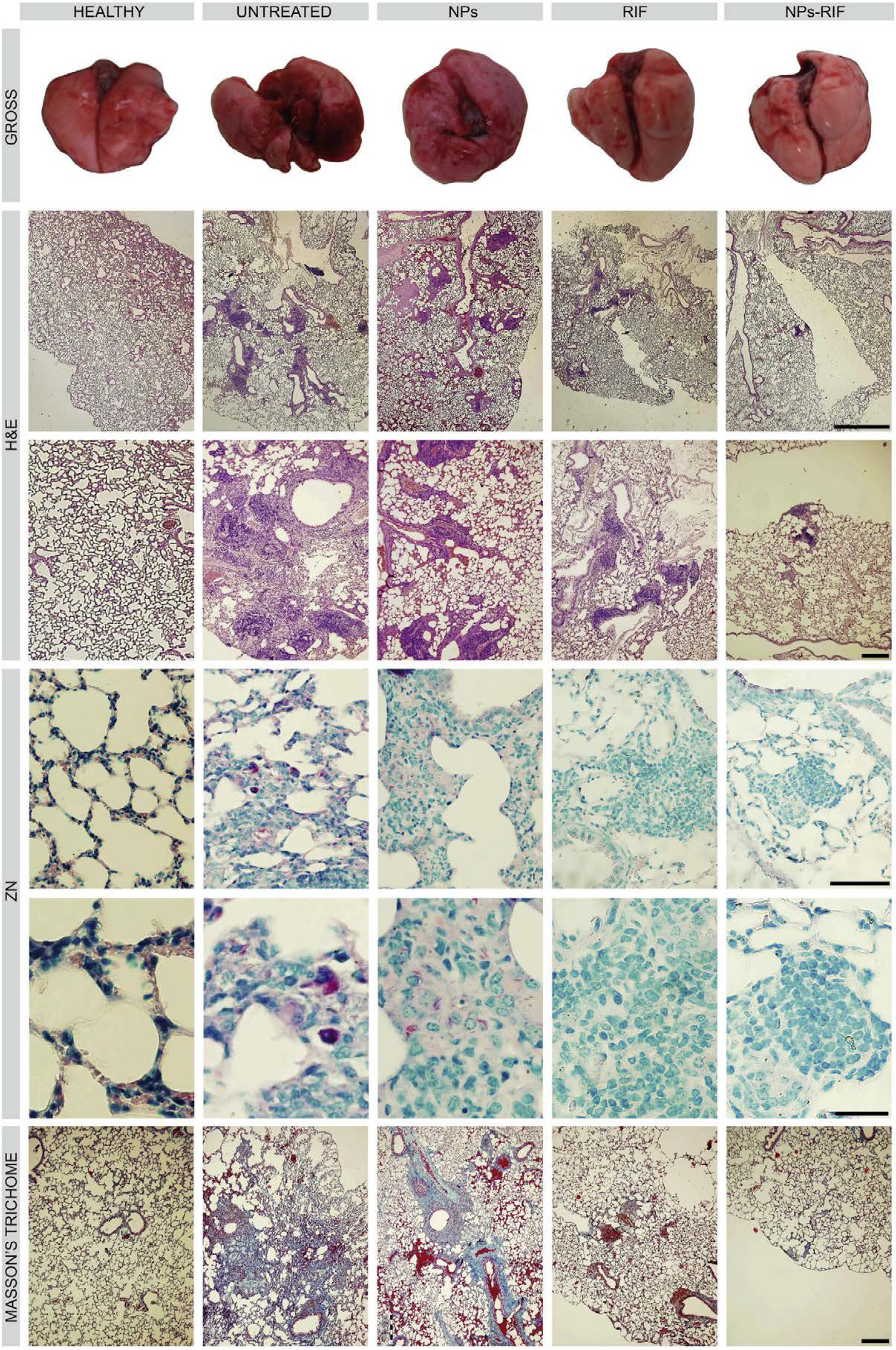

(caption on next page)

P2

Fig. 5. *Ex vivo* examination of lungs dissected from treated, untreated and healthy mice. Lung tissues obtained from BALB/c mice 12 weeks after infection, *i.e.*, 8 weeks of treatment. Macroscopic examination revealed no gross pathology. In contrast, hematoxylin and eosin (H&E) staining revealed clear changes in lung parenchyma-localized granulomas as a response to the treatment. The lung tissues demonstrated a marked response to **RIF** and **NPs-RIF** therapy as a clear decrease in collagen deposition (Masson's trichrome staining, blue) and no presence of acid-fast bacilli (ZN staining), whereas lungs dissected from both untreated and **NPs**-treated animals revealed gross fibrosis and numerous acid-fast tubercle bacilli. Scale bars: 1 mm, 200 μm, 50 μm, 25 μm, and 200 μm. (For interpretation of the references to colour in this figure legend, the reader is referred to the web version of this article.)

nanoformulation on infected mice in order to contribute to the field of antitubercular drug delivery systems. The intervention conducted as monotherapy revealed an interesting efficacy. Considering the safety, we suggest that the fabricated nanoformulation is well tolerated with repeated i.p. administration, as *ex vivo* histopathological examination of H&E-stained liver, kidney, and brain sections revealed no morphological differences from the untreated healthy mice. These organs were without any dystrophic, necrotic or inflammatory changes, suggesting that all administered formulations (*i.e.*, **NPs**, **RIF** and **NPs-RIF**) were well tolerated by the infected mice. Furthermore, the body weights of all treated animals were maintained over the course of treatment (data not shown).

As mentioned above, some studies have described the testing of anti-TB nanoformulations *in vivo*. The *in vivo* models used, however, differ from study to study in terms of the animal, mycobacterial load, and treatment regimen, *etc.* These differences complicate the comparison and critical discussion of such studies. Demonstrations by us or other groups showing that nanobead-based interventions have greater *in vitro* and *in vivo* therapeutic efficacy than the free drug is an important proof of principle. However, studies of additional drug incorporation and rational design features have the potential for even greater improvements in efficacy for the treatment of different types of persistent intracellular bacterial infections. Moreover, there are still essential questions related to this issue that are not fully answered or managed. For instance, comprehensive studies focused on the corona modification effects of NPs, different stimuli responsivities and their effect on intracellular infections, and the comparison of drug entrapment methods (encapsulated *vs.* conjugated antibiotics) are needed, and they may be expected to further enhance the efficacy of novel antibacterial interventions based on nanomedicines. The study of combination therapies using nanomedicines should also be comprehensively conducted. This is due to the necessity of including such interventions in a multidrug regimen to reduce the population of mycobacteria to undetectable levels and to avoid the selection of resistant strains, even though *in vivo* testing reveals an improved efficacy.

3. Conclusions

In summary, we demonstrate here, for the first time, the effect of MPEO-*b*-PCL-based nanoparticles carrying rifampicin—a cornerstone of modern antitubercular therapy—on lung tuberculosis in mice. We show that this nanobead-based intervention is well-tolerated and that it is significantly more efficacious than an equivalent amount of free rifampicin.

Finally, we believe that this study highlights the need for more in-depth analyses of the biorelevant characteristics of anti-TB drug delivery systems and their impact on infection models to advance this emerging field and to obtain nanocarriers that will facilitate marked improvement of TB treatment.

4. Materials and methods

4.1. Ethics statement

All animal studies were conducted with approval from the Institutional Animal Care and Use Committee of Chang Gung University and according to the Czech law No. 246/1992 Sb. on animal protection against brutalization.

4.2. Materials

Amphotericin B (250 μg/mL), Dulbecco's modified Eagle's medium (DMEM, high glucose, GlutaMAX™), fetal bovine serum (FBS, heat inactivated), penicillin–streptomycin solution, and Roswell Park Memorial Institute medium (RPMI 1640, ATCC modification) were purchased from Life Technologies Czech Republic Ltd. (Prague, Czechia). Dyomics (Dy) 700 NHS-ester was purchased from Dyomics GmbH (Jena, Germany).

Löwenstein–Jensen medium supplemented with ampicillin (25 μg/mL) was purchased from LabMediaServis Ltd. (Jaroměř, Czechia).

Other reagents and solvents were purchased from Sigma–Aldrich Ltd. (Prague, Czechia).

4.3. Synthesis of the MPEO-b-PCL copolymer

The MPEO-*b*-PCL copolymer was prepared as previously described [25,44]. Azeotropically dried MPEO (1 eq.) and dried CL were added to a glass tube containing 10 mL of dry CH_2Cl_2 and a magnetic stirrer, which was connected to a vacuum system. An exhaust-refilling process with argon was repeated multiple times. The copolymerization was then initiated by the addition of a 2.0 M HCl solution (2 eq., in diethyl ether) at 25 °C, and the reaction mixture was stirred overnight. The resulting copolymers were precipitated in cool diethyl ether and filtered. The filtrate was washed with cool diethyl ether and dried at room temperature under reduced pressure.

The yield was 93%. DSC: melting temperature 56.4 °C. ^1H NMR (300 MHz, $CDCl_3$, δ): peak a (δ = 3.37 ppm, $\mathbf{CH_3}$–O–), peaks b + c (δ = 3.63 ppm, PEO repeating unit: $-\mathbf{CH_2}-\mathbf{CH_2}-O-$), peak d ($\delta$ = 4.21 ppm, $-O-CH_2-\mathbf{CH_2}-$), peak e (δ = 2.29 ppm, CL repeating unit: $-CO-\mathbf{CH_2}-CH_2-CH_2-CH_2-CH_2-O-$), peaks f + h ($\delta$ = 1.64 ppm, CL repeating unit: $-CO-CH_2-\mathbf{CH_2}-CH_2-\mathbf{CH_2}-CH_2-O-$), peak g ($\delta$ = 1.37 ppm, CL repeating unit: $-CO-CH_2-CH_2-\mathbf{CH_2}-CH_2-CH_2-O-$), peak i ($\delta$ = 4.05 ppm, CL repeating unit: $-CO-CH_2-CH_2-CH_2-CH_2-\mathbf{CH_2}-O-$) and peak j ($\delta$ = 2.54 ppm, $-\mathbf{OH}$).

Dy 700 NHS-ester was used for the fluorescent MPEO-*b*-PCL conjugate preparation. An NH_2-terminated MPEO-*b*-PCL (MPEO-*b*-PCL-NH_2) copolymer was prepared as previously described [17]. Dy 700 NHS-ester (3 eq.) was dissolved in a small amount of dimethyl sulfoxide (DMSO) in a vial. Next, 1 eq. of MPEO-*b*-PCL-NH_2 and 3 eq. of trimethylamine in DMSO were added. The reaction was maintained upon magnetic stirring at 25 °C for 48 h. Labeling with 7-(diethyl amino) coumarin-3-carbonyl azide (DACCA) was carried out according to a previously described method [18].

In both cases, the free dye was removed by gel filtration (Sephadex LH-20 with DMSO elution). UV/VIS (Synergy H1 Hybrid Reader, BioTek, Winooski, WT, USA) and fluorescence spectroscopy (Aminco Bowman Series 2 spectrofluorometer, Aminco, Lake Forest, CA, USA) were used to confirm covalent bonding of the dye to the polymer backbone (data not shown). The labeling efficacy, expressed as the ratio of the determined amount of the dye to the theoretical amount of dye, was measured by spectrophotometry and was found to be 70–80%.

4.4. Characterization of the MPEO-b-PCL copolymer

Proton nuclear magnetic resonance (^1H NMR) was used to confirm the structure of the prepared MPEO-*b*-PCL copolymer. ^1H NMR spectra were recorded with a Bruker Avance DPX 300 spectrometer (Bruker

Daltonik GmbH, Bremen, Germany) operating at 300.1 MHz. All NMR spectra were measured on samples in 5 mm NMR tubes using $CDCl_3$ as the solvent at 25 °C. The chemical shifts were relative to TMS using hexamethyldisiloxane (HMDSO, $\delta = 0.05$ ppm from TMS) as the internal standard. The typical conditions for the spectra collection were as follows: π/2 pulse width, 15.6 μs (10 μs); relaxation delay, 10 s; spectral width, 6.6 kHz; acquisition time, 4.95 s (2.18 s).

Gel permeation chromatography (GPC) was used to determine the M_w, M_n and M_w/M_n (dispersity, $Đ$) and for molar mass distribution control. GPC separations were performed using a Deltachrom pump (Watrex Ltd., Prague, Czechia), a Midas Spark autosampler (DataApex Ltd., Prague, Czechia) and two PLgel MIXED-B-LS columns (30 × 1 cm, particle size 10 μm) for separation in the molecular weight range of approximately 400–10 000 000 Da. Tetrahydrofuran (THF) was used as the mobile phase. The detector was a PL ELS-1000 evaporative light scattering detector (Polymer Laboratories, Varian Inc., Amherst, USA). The data were accumulated and processed using Clarity software version 6.0.0.295 (DataApex Ltd.). The injection volume of the GPC system was 0.1 mL. Separations were performed at a mobile phase (THF) flow rate of 1 mL/min. Evaluation of the chromatograms was based on a polystyrene (PS) standard calibration.

Matrix-assisted laser desorption/ionization with time of flight detection (MALDI-TOF) was used to confirm the GPC-based results. The MPEO-*b*-PCL sample was prepared by the dried droplet method: solutions of sample (10 mg/mL) and DCTB (trans-2-[3-(4-t-butyl-phenyl)-2-methyl-2-propenylidene]malonitrile 10 mg/mL, as a matrix in DMF) were mixed in a volume ratio of 4:20. Subsequently, the mixture (1 μL) was deposited on the ground-steel target plate. The drop was dried in an ambient atmosphere.

MALDI-TOF MS mass spectra were acquired with an UltrafleXtreme (Bruker Daltonics, Bremen, Germany) in the positive ion reflectron mode. The spectra were the sum of 25 000 shots with a DPSS, Nd:YAG laser (355 nm, 1000 Hz). Delayed extraction and external calibration were used.

The thermal properties of the copolymer were characterized by differential scanning calorimetry (DSC) using a Q2000 calorimeter (TA Instruments, New Castle, USA) with nitrogen purge gas (20 mL/min). The instrument was calibrated for temperature and heat flow using indium as a standard. Samples of approximately 5 mg were encapsulated in T-zero aluminum pans. The analysis was performed in cycles of heating–cooling–heating, from −90 °C to 90 °C at 5 °C/min. The heat of fusion of copolymers was calculated from the first heating endotherms.

4.5. Preparation and characterization of nanoparticles

The nanoformulations were prepared by the nanoprecipitation method as previously described [17]. Briefly, 10 mg of the copolymer was dissolved in 2.5 mL of acetone. The resulting solution was then subjected to quick addition of 10 mL of PBS with continuous stirring (200 rpm). RIF-loaded NPs were prepared in the presence of RIF by the same method. Subsequently, the acetone was removed by evaporation under reduced pressure (40 °C) in both cases. The prepared formulations were filtered through a 0.22 μm PVDF filter for all experiments.

The nanoparticle size was investigated by dynamic light scattering (DLS). DLS experiments were carried out using a Nano-ZS instrument, Model ZEN3600 (Malvern Instruments Ltd., UK) at an angle of 173°. A He—Ne 4.0 mW laser operating at 633 nm was used. The data were analyzed using the DTS (Nano) program (Malvern Instruments Ltd., UK).

The mean positions of the peaks in the intensity–hydrodynamic diameter (D_h) distributions were used to represent the data. The D_h values of the particles were calculated from the diffusion coefficient using the Stokes–Einstein equation:

$$D = \frac{k_B T}{3\pi\eta D_h}, \tag{1}$$

where T is the absolute temperature, η is the viscosity of the solvent and k_B is the Boltzmann constant.

The nanoparticle morphology was studied using cryogenic transmission electron microscopy (cryo-TEM). For this purpose, 4 μL of the sample was applied to an electron microscopy grid covered with a holey carbon supporting film (400 mesh, Cu, Agar Scientific, UK) after hydrophilization by glow discharge (Expanded Plasma Cleaner, Harrick Plasma, USA). A piece of filter paper was used to absorb the excess solution. Subsequently, the grid was immediately plunged into liquid ethane held at −182 °C, and the vitrified sample was immediately transferred without rewarming into the microscope and observed at −173 °C.

A Tecnai G2 Spirit Twin 120 kV microscope (FEI, Czechia) equipped with a cryo-holder (Gatan, cryo-specimen holder) was used for the investigations using the bright field imaging mode at an accelerating voltage of 120 kV. Size distribution analysis was performed using ImageJ software. For each system, more than one hundred particles in the cryo-TEM micrographs were measured.

The shape and size of the particles were also investigated in the liquid state by small-angle neutron scattering (SANS). The experiments were carried out at the SANS installation at the JEEP-II reactor in Norway. The wavelength was set with a velocity selector (Dornier) using a wavelength resolution (Δλ/λ) of 10%. Each complete scattering curve was composed of three independent measurements using different wavelength–distance combinations (5 Å/1 m, 5 Å/3.4 m, and 10 Å/3.4 m). The resulting q-range for the experiment was 0.006–0.3 $Å^{-1}$. The solutions were filled into 5 mm quartz cuvettes, which were placed in a copper casing for good thermal contact before being mounted on the sample stage. The temperature was controlled by a water circulator, maintaining the set value to within ± 0.1 °C. Deuterium oxide (D_2O) was used as a solvent instead of H_2O to obtain good contrast and low background for the neutron scattering experiments. Standard reductions of the scattering data, including transmission corrections, were conducted by incorporating data collected from the empty cell and the blocked-beam background. All data were finally transformed to an absolute scale, *i.e.*, coherent differential cross section (dΣ/dΩ).

The SANS data were fitted to a spherical core-corona particle model as previously described [45] using the SasView program (www.sasview.org). The fitted particle diameter consists of a core composed mainly of PCL and a corona of MPEO. The theoretical values for the scattering length density (SLD) of PCL (0.85×10^{-6} $Å^{-2}$) and PEO (0.57×10^{-6} $Å^{-2}$) were employed in the fitting.

4.6. Cell culture and bacteria

BEAS-2B, J774A.1 and MH-S cell lines were purchased from Sigma–Aldrich Ltd. (Prague, Czechia). The IC-21 cell line was kindly provided by Dr. Jaroslava Lieskovská (Department of Medical Biology, Faculty of Science, University of South Bohemia in České Budějovice, Czechia). The BEAS-2B, IC-21, and MH-S cell lines were maintained in RPMI 1640 supplemented with FBS (10%), penicillin (100 U/mL), streptomycin (100 μg/mL), amphotericin B (2.5 μg/mL), and 2-mercaptoethanol (0.05 mM) in a humidified atmosphere containing 5% CO_2 at 37 °C. The J774A.1 cells were maintained in DMEM supplemented with FBS (10%), penicillin (100 U/mL), streptomycin (100 μg/mL) and amphotericin B (2.5 μg/mL) in a humidified atmosphere containing 5% CO_2 at 37 °C.

The culture of *M. tuberculosis* H37Rv (ATCC 27294) was originally obtained from the Public Health England Culture Collection (Salisbury, UK) and was maintained on Löwenstein–Jensen slants in a humidified atmosphere containing 5% CO_2 at 35 °C for 2–3 weeks. Subsequently, mycobacterial stocks (*ca.* 1×10^7 CFU/mL) were prepared and stored at −196 °C prior to the infections.

4.7. Cytotoxicity study

Cytotoxicity was examined using an MTT assay. For this purpose, BEAS-2B, IC-21, J774A.1, and MH-S cells were seeded into 96-well plates at a density of 15 000 cells per well. The cells were then incubated overnight at 37 °C in 5% CO_2 with subsequent replacement of the cell culture medium (100 µL of fresh culture medium containing the tested formulations). After 24 h of incubation, 10 µL of MTT solution (5 mg/mL, PBS) was added to each well. Subsequently, the plates were incubated for 2–4 h prior to aspiration of the medium and isopropanol addition (100 µL). After 15 min of blue formazan solubilization (37 °C), a Synergy H1 Hybrid Reader instrument (BioTek) was used to assess cell viability by spectrophotometry at 570 nm. The results of the MTT assay were expressed as a percentage of the control (cells in control medium), which was considered to be 100%. Reduction of cell viability by more than 30% is considered a cytotoxic effect, according to the ISO 10993-5. The tests were performed with at least three separate experiments.

4.8. Nanoparticles uptake study

The cellular uptake was studied using confocal laser scanning microscopy. For this purpose, IC-21 cells were seeded at the bottom of ibidi µ–Dishes (ibidi GmbH, Planegg/Martinsried, Germany) and left to adhere overnight. The next day, the medium was replaced with RPMI containing DACCA-labeled nanobeads (40 µg/mL). At different time points of the incubation (2, 5, 10, 20, and 40 min), the cells were washed using PBS and then fixed (4% paraformaldehyde in PBS). Visualization of the fixed cells was carried out using an Olympus FV 10 confocal laser scanning microscope (Olympus Czech Group Ltd., Prague, Czechia) using a 60× oil objective. Signal detection was observed in a channel of exc. 405 nm and em. 425–475 nm; fluorescence quantification was performed using ImageJ software. For this purpose, within three separate experiments, ten fields were used for the quantification.

4.9. Bioimaging experiments

The NP fate was assessed by *in vivo* bioimaging. Female BALB/c mice between the ages of 4 and 6 weeks were randomly divided into 2 groups with 3 animals in each and a control group containing 2 mice. The first group received a single intraperitoneal dose (10 mg/kg) of Dyomics 700-labeled NPs (**NPs−Dy**, 1 mg/mL, PBS). The second group received the same dose of PBS solution containing free Dyomics 700 (**Dy**) at a corresponding concentration. The control group received a corresponding volume of PBS (200 µL). The bioimaging was carried out under anesthesia with an intraperitoneal injection (50 mg/kg) of Zoletil® 50 (Virbac, Carros, France) using a Pearl® Impulse system (Li-Cor, Lincoln, NE, USA). Fluorescence images were acquired at 1, 2, 4, 6, 8, 12, and 24 h. To visualize the *ex vivo* fluorescence in different organs (brain, heart, lung, spleen, kidney, bladder/ovary, liver, and stomach/intestine), an additional imaging experiment was carried out. For this purpose, the mice were euthanized at 6 h ($n = 3$ mice per group) after injection.

4.10. Pharmacokinetic assessment

The pharmacokinetics of NP-encapsulated RIF and free RIF were assessed in mycobacteria-infected mice. For this purpose, specific pathogen-free female BALB/c mice (Velaz Ltd., Prague, Czechia) between the ages of 4 and 6 weeks were housed at five animals per cage in HEPA-filtered racks (Tecniplast S.p.A., Buguggiate VA, Italy) in certified animal biosafety level three (BSL 3) laboratories and were rested for 4 weeks before testing.

The BALB/c mice were anaesthetized with xylazine (8 mg/kg, i.p.) and ketamine (80 mg/kg, i.p.) and were intranasally infected with *ca.* 1×10^2 CFU of *M. tuberculosis* H37Rv (50 µL per mouse). One day later, seven mice were euthanized to determine the initial number of bacteria delivered to their lungs. Four weeks post infection, seven mice were euthanized to determine the number of bacteria in the lungs and spleens prior to the subsequent experiments.

NP-encapsulated RIF and free RIF were administered intraperitoneally in a single dose of 10 mg/kg; the mice were then sacrificed at time points of 2, 4, 6, 8, 12, 24, 48, and 72 h. At each time point, a terminal blood collection was carried out by way of axilla incision. The blood was collected using a sterile Pasteur pipette, placed into sterile Eppendorf tubes and stored at 4 °C prior to liquid chromatography analysis. To determine the RIF concentrations in the lung tissue, lungs were obtained from each animal at each time point, weighed, snap-frozen and stored at −80 °C prior to the analysis.

Pharmacokinetic parameters for both NP-encapsulated RIF and free **RIF** were assessed with Origin 2019 software (OriginLab Corporation, Wellesley Hills, MA, USA). The highest serum or lung concentrations were defined as $C_{\max}$, with the corresponding times as $T_{\max}$. The area under the time–concentration curves up to 24 h (AUC_{0-24}) and up to 72 h (AUC_{total}) after the dose were calculated by integration from zero up to 24 h and 72 h, respectively. The elimination half-lives were calculated based on the time–concentration course by curve fitting of the data using the equation:

$$C_t = C_0 \bullet e^{-kt}, \tag{2}$$

where C_t is the serum or lung concentration at time t, C_0 is the concentration at $t = 0$, and k is the elimination constant. The elimination half-life $T_{1/2}$ is then:

$$T_{1/2} = \ln 2/k. \tag{3}$$

4.11. Liquid chromatography analysis of serum and lung tissue

RIF determination in serum was carried out as follows. The blood samples were centrifuged at 4 200 rpm for 2 min. The serum (0.2 mL) was collected and mixed with probenecid (10 µg/mL) as an internal standard. Thereafter, 1 mL of acetonitrile was added, and the tubes were vortexed vigorously to allow for maximal protein precipitation. The samples were centrifuged (5 min, 13 400 rpm), and 300 µL of the supernatant was diluted with 100 µL of deionized water and transferred to clean glass autosampler vials for LC-MS/MS analysis.

Sample analysis was performed using a Nexera X2 HPLC chromatography system (Schimadzu, Nakagyo-ku, Kyoto, Japan) coupled to an AB Sciex Qtrap 5500 triple quadrupole mass spectrometer (Sciex, Foster City, CA, USA) equipped with an electrospray ionization (ESI) TurboIonSpray source. Chromatographic separation was carried out on a Zorbax Eclipse C18 column (4.6 × 50 mm, 1.8 µm) protected by a C18 security guard cartridge (4 × 2 mm) at 30 °C. An isocratic elution operating at a flow rate of 0.5 mL/min was used. The mobile phase consisted of a combination of phase A (10 mM ammonium formate supplemented with 0.2% formic acid) and B (acetonitrile) at a ratio of 30:70. The autosampler was maintained at 15 °C; the injection volume was 1 µL. For data acquisition, mass spectrometry was performed in multiple reaction monitoring (MRM) at unit resolution in positive scan mode. The protonated molecular ions were selected as precursors. The following transitions were monitored: m/z 823.4 → 791.3 and m/z 286.2 → 244.1 for RIF and probenecid, respectively. Analyst® software (version 1.6.3, Sciex, Foster City, CA, USA) was used for quantitative data analysis.

For the RIF determination in lung tissue, dissected lungs were mixed with PBS at a ratio of 1:4, and the samples were pulverized for 2–4 cycles (45 s, 6 000 rpm) in a bead beat sample preparation tube. Subsequently, 20 µL of the prepared homogenate was mixed with 200 µL of acetonitrile/methanol (1:1) containing rifampicin-d8 (20 ng/mL) in 1.5 mL screw-top centrifuge tubes. The samples were centrifuged

(5 min, 4 000 rpm), and the upper layer was used for the analysis. RIF lung levels were determined using an Agilent 1260 chromatographic system coupled to an AB Sciex Qtrap 4000 triple quadrupole mass spectrometer (Sciex). The separation was carried out on an Agilent SB-C8 column (2.1 × 30 mm, 3.5 μm). The mobile phase consisted of a combination of phase A (0.1% formic acid in water) and B (0.1% formic acid in acetonitrile). Elution was carried out with a gradient elution (2.5 min linear gradient from 90:10 to 5:95 (A:B), a 1.5 min isocratic elution with 5:95, followed by an additional period of 1 min isocratic elution at the initial conditions of 90:10. The flow rate was 0.7 mL/min, and the injection volume was 3 μL. For the data acquisition, mass spectrometry was performed by multiple reaction monitoring (MRM) in positive scan mode. The following transitions were monitored: m/z 823.5 → 791.6 and m/z 831.5 → 799.6 for RIF and RIF-d8, respectively. The data processing was performed using Analyst software (version 1.6.2; Applied Biosystems Sciex).

4.12. Assessment of treatment efficacy

Similarly, as in the pharmacokinetics-focused experiments, the treatment efficiency study was performed with *M. tuberculosis* H37Rv-infected specific-pathogen-free BALB/c mice (Velaz Ltd.) between the ages of 4 and 6 weeks with continuous control of the mycobacterial burden (as mentioned above). The treatment efficiency study was based on 4- and 8-week therapies and was performed as follows. Treated mice received specific formulations, *i.e.*, **NPs** (MPEO$_{5k}$-*b*-PCL$_{4k}$ NPs, 1 mg/mL, PBS), **NPs-RIF** (MPEO$_{5k}$-*b*-PCL$_{4k}$ NPs loaded with RIF, 1 mg/mL, PBS), and free **RIF** (1 mg/mL, PBS supplemented with 5% DMSO), intraperitoneally administered once per day (5 days per week). The dose was 10 mg/mL (200 μL per mouse) for all formulations.

All tested formulations were aseptically filtered through a sterile 0.22 μm PVDF syringe filter and adjusted in flame-sealed glass ampoules in a biosafety cabinet prior to testing *in vivo*. The sealed formulations were stored at room temperature in the dark and were administered, at the latest, one week after preparation.

After completion of the 4- and 8-week therapies, the mice were sacrificed by CO$_2$ inhalation, and the organs (lung, spleen, liver, kidneys, and brain) were aseptically removed. To determine the CFU in the lungs and spleens, these organs were homogenized in tea strainers with sterile saline, and serially diluted homogenates were incubated on Löwenstein–Jensen plates supplemented with ampicillin (25 μg/mL) in a humidified atmosphere containing 5% CO$_2$ at 35 °C for 2–3 weeks. One mouse from each group was taken for histopathological examination. The organs were photodocumented and collected from specimens with fixation solution.

4.13. Histopathological examination

The organs of mice (lung, spleen, liver, kidneys, and brain) were collected after euthanasia and fixed in buffered 10% neutral formalin, dehydrated, embedded in paraffin wax, and sectioned on a microtome at a thickness of 4 μm. Tissue sections from the organs of all mice were stained with hematoxylin and eosin (H&E) and Ziehl–Neelsen (ZN) stain. Lung tissue sections were subjected to Masson's trichrome staining as well.

4.14. Data analysis

The results are expressed as the means ± SD and were analyzed by ANOVA. Differences were considered significant at * $p \le .05$, ** $p \le .01$, and *** $p \le .001$.

Acknowledgments

J.T. acknowledges support from Charles University (project No. SVV260440) and thanks Dr. Olga Šebestová Janoušková (Institute of Macromolecular Chemistry CAS) for allowing work on cell culture experiments in her lab. Thanks to Ms. Zuzana Walterová (Institute of Macromolecular Chemistry CAS) for the MALDI-TOF analysis. Thanks to Dr. Jakub Hraníček (Department of Analytical Chemistry, Faculty of Science, Charles University) for his kindness in assisting with the instrumentation necessary for the fluorescence spectra measuring, and thanks to Prof. Gareth Griffiths (Department of Biosciences, University of Oslo) for his critical reading of the manuscript. J.T. and M.H. acknowledge the Czech Science Foundation (grants Nos. 17-07164S and 17-09998S) and the Ministry of Education, Youth and Sports of the Czech Republic, National sustainability program I (grant No. POLYMAT LO1507). K.D.K. acknowledges funding from the Research Council of Norway (project 245942/F50). The Czech-Taiwanese collaboration was supported by the Czech Academy of Sciences (projects Nos. TWN-18-10 and VAJVA-19-55).

Appendix A. Supplementary data

Supplementary data to this article can be found online at https://doi.org/10.1016/j.jconrel.2020.02.026.

References

[1] S. Gelperina, K. Kisich, M.D. Iseman, L. Heifets, The potential advantages of nanoparticle drug delivery Systems in Chemotherapy of tuberculosis, Am. J. Respir. Crit. Care Med. 172 (2005) 1487–1490.

[2] A. Sosnik, Á. Carcaboso, R.J. Glisoni, M.A. Moretton, D.A. Chiappetta, New old challenges in tuberculosis: potentially effective nanotechnologies in drug delivery, Adv. Drug Deliv. Rev. 62 (2010) 547–559.

[3] J. Trousil, M. Hrubý, Novel nanoparticle delivery systems for rifampicin: an effectivc stratcgy against tubcrculosis? Nanomcdicinc (London) 12 (2017) 1359–1361.

[4] WHO, Global Tuberculosis Report 2016, WHO, 2017.

[5] A. Zumla, P. Nahid, S.T. Cole, Advances in the development of new tuberculosis drugs and treatment regimens, Nat. Rev. Drug Discov. 12 (2013) 388.

[6] L. De Matteis, D. Jary, A. Lucía, S. García-Embid, I. Serrano-Sevilla, D. Pérez, J.A. Ainsa, F.P. Navarro, J.M. de la Fuente, New active formulations against M. tuberculosis: Bedaquiline encapsulation in lipid nanoparticles and chitosan nanocapsules, Chem. Eng. J. 340 (2018) 181–191.

[7] J. Hwang, J. Son, Y. Seo, Y. Jo, K. Lee, D. Lee, M.S. Khan, S. Chavan, C. Park, A. Sharma, A.A. Gilad, J. Choi, Functional silica nanoparticles conjugated with beta-glucan to deliver anti-tuberculosis drug molecules, Ind. Eng. Chem. Res. 58 (2018) 376–385.

[8] K. Patil, S. Bagade, S. Bonde, S. Sharma, G. Saraogi, Recent therapeutic approaches for the management of tuberculosis: challenges and opportunities, Biomed. Pharmacother. 99 (2018) 735–745.

[9] G. Griffiths, B. Nyström, S.B. Sable, G.K. Khuller, Nanobead-based interventions for the treatment and prevention of tuberculosis, Nat. Rev. Microbiol. 8 (2010) 827–834.

[10] A.C.C. Vieira, L.L. Chaves, S. Pinheiro, S. Pinto, M. Pinheiro, S.C. Lima, D. Ferreira, B. Sarmento, S. Reis, Mucoadhesive chitosan-coated solid lipid nanoparticles for better management of tuberculosis, Int. J. Pharm. 536 (2018) 478–485.

[11] P. Leidinger, J. Treptow, K. Hagens, J. Eich, N. Zehethofer, D. Schwudke, W. Oehlmann, H. Lünsdorf, O. Goldmann, U.E. Schaible, K.E.J. Dittmar, C. Feldmann, Isoniazid@Fe2O3 Nanocontainers and their antibacterial effect on tuberculosis mycobacteria, Angew. Chem. Int. Ed. 54 (2015) 12597–12601.

[12] A. Hwang, B.-Y. Lee, D.L. Clemens, B.J. Dillon, J.I. Zink, M.A. Horwitz, pH-responsive isoniazid-loaded nanoparticles markedly improve tuberculosis treatment in mice, Small 11 (2015) 5066–5078.

[13] S. Upadhyay, I. Khan, A. Gothwal, P.K. Pachouri, N. Bhaskar, U.D. Gupta, D.S. Chauhan, U. Gupta, Conjugated and entrapped HPMA-PLA Nano-polymeric micelles based dual delivery of first line anti TB drugs: improved and safe drug delivery against sensitive and resistant Mycobacterium tuberculosis, Pharm. Res. 34 (2017) 1944–1955.

[14] R. Kalluru, F. Fenaroli, D. Westmoreland, L. Ulanova, A. Maleki, N. Roos, M. Paulsen Madsen, G. Koster, W. Egge-Jacobsen, S. Wilson, H. Roberg-Larsen, G.K. Khuller, A. Singh, B. Nyström, G. Griffiths, Poly(lactide-co-glycolide)-rifampicin nanoparticles efficiently clear Mycobacterium bovis BCG infection in macrophages and remain membrane-bound in phago-lysosomes, J. Cell Sci. 126 (2013) 3043–3054.

[15] F. Fenaroli, D. Westmoreland, J. Benjaminsen, T. Kolstad, F.M. Skjeldal, A.H. Meijer, M. van der Vaart, L. Ulanova, N. Roos, B. Nystrom, J. Hildahl, G. Griffiths, Nanoparticles as drug delivery system against tuberculosis in zebrafish embryos: direct visualization and treatment, ACS Nano 8 (2014) 7014–7026.

[16] N. Silveira, M.M. Longuinho, S.G. Leitão, R.S.F. Silva, M.C. Lourenço, P.E.A. Silva, M.D.C.F.R. Pinto, L.G. Abraçado, P.V. Finotelli, Synthesis and characterization of the antitubercular phenazine lapazine and development of PLGA and PCL nanoparticles for its entrapment, Mater. Sci. Eng. C 58 (2016) 458–466.

[17] J. Trousil, S.K. Filippov, M. Hrubý, T. Mazel, Z. Syrová, D. Cmarko, S. Svidenská, J. Matějková, L. Kováčik, B. Porsch, R. Konefał, R. Lund, B. Nyström, I. Raška,

P. Štěpánek, System with embedded drug release and nanoparticle degradation sensor showing efficient rifampicin delivery into macrophages, Nanomed. Nanotechnol. Biol. Med. 13 (2017) 307–315.

[18] J. Trousil, Z. Syrová, N.-J.D. Knudsen, D. Rak, R. Konefał, E.P. Pavlova, J. Matějková, D. Cmarko, P. Kubíčková, O. Pavliš, M. Sedlák, F. Fenaroli, I. Raška, P. Štěpánek, M. Hrubý, Rifampicin Nanoformulation enhances treatment of tuberculosis in Zebrafish, Biomacromolecules 20 (2019) 1798–1815.

[19] E. Grotz, N. Tateosian, N. Amiano, M. Cagel, E. Bernabeu, D.A. Chiappetta, M.A. Moretton, Nanotechnology in tuberculosis: state of the art and the challenges ahead, Pharm. Res. 35 (2018) 213.

[20] J. Costa-Gouveia, E. Pancani, S. Jouny, A. Machelart, V. Delorme, G. Salzano, R. Iantomasi, C. Piveteau, C.J. Queval, O.-R. Song, M. Flipo, B. Deprez, J.-P. Saint-André, J. Hureaux, L. Majlessi, N. Willand, A. Baulard, P. Brodin, R. Gref, Combination therapy for tuberculosis treatment: pulmonary administration of ethionamide and booster co-loaded nanoparticles, Sci. Rep. 7 (2017) 5390.

[21] A. Sharma, S. Sharma, G.K. Khuller, Lectin-functionalized poly (lactide-co-glycolide) nanoparticles as oral/aerosolized antitubercular drug carriers for treatment of tuberculosis, J. Antimicrob. Chemother. 54 (2004) 761–766.

[22] C.M. Johnson, R. Pandey, S. Sharma, G.K. Khuller, R.J. Basaraba, I.M. Orme, A.J. Lenaerts, Oral therapy using nanoparticle-encapsulated antituberculosis drugs in Guinea pigs infected with Mycobacterium tuberculosis, Antimicrob. Agents Chemother. 49 (2005) 4335–4338.

[23] E.L. Barrow, W.W. Barrow, D.C. Quenelle, L. Westbrook, G.A. Winchester, J.K. Staas, Efficacy of rifabutin-loaded microspheres for treatment of Mycobacterium avium-infected macrophages and mice, Drug Deliv. 14 (2007) 119–127.

[24] P. Grossen, D. Witzigmann, S. Sieber, J. Huwyler, PEG-PCL-based nanomedicines: a biodegradable drug delivery system and its application, J. Control. Release 260 (2017) 46–60.

[25] H. Hyun, H.S. Park, Y.D. Kwon, G. Khang, B.H. Lee, S.M. Kim, Thermo-responsive injectable MPEG-polyester diblock copolymers for sustained drug release, Polymers 6 (2014).

[26] M.S. Kim, H. Hyun, K.S. Seo, Y.H. Cho, J. Won Lee, C. Rae Lee, G. Khang, H.B. Lee, Preparation and characterization of MPEG–PCL diblock copolymers with thermo-responsive sol–gel–sol phase transition, J. Polym. Sci. A 44 (2006) 5413–5423.

[27] P. Grossen, D. Witzigmann, S. Sieber, J. Huwyler, PEG-PCL-based nanomedicines: a biodegradable drug delivery system and its application, J. Control. Release 260 (2017) 46–60.

[28] Y. Inoue, K. Izawa, S. Kiryu, A. Tojo, K. Ohtomo, Diet and abdominal autofluorescence detected by in vivo fluorescence imaging of living mice, Mol. Imaging 7 (2008) (7290.2008.0003).

[29] Y.-N. Zhang, W. Poon, A.J. Tavares, I.D. McGilvray, W.C.W. Chan, Nanoparticle–liver interactions: cellular uptake and hepatobiliary elimination, J. Control. Release 240 (2016) 332–348.

[30] J. Chen, F.Y. Su, D. Das, S. Srinivasan, H.N. Son, B. Lee, F. Radella 2nd, D. Whittington, T. Monroe-Jones, T.E. West, A.J. Convertine, S.J. Skerrett, P.S. Stayton, D.M. Ratner, Glycan targeted polymeric antibiotic prodrugs for alveolar macrophage infections, Biomaterials 195 (2019) 38–50.

[31] R. Pandey, S. Sharma, G.K. Khuller, Oral solid lipid nanoparticle-based antitubercular chemotherapy, Tuberculosis (Edinb.) 85 (2005) 415–420.

[32] T. Bruzzese, C. Rimaroli, A. Bonabello, G. Mozzi, S. Ajay, N.D. Cooverj, Pharmacokinetics and tissue distribution of rifametane, a new 3-azinomethyl-rifamycin derivative, in several animal species, Arzneimittelforschung 50 (2000) 60–71.

[33] V. Hosagrahara, J. Reddy, S. Ganguly, V. Panduga, V. Ahuja, M. Parab, J. Giridhar, Effect of repeated dosing on rifampin exposure in BALB/c mice, European journal of pharmaceutical sciences 49 (2013) 33–38.

[34] S. Chanwong, N. Maneekarn, L. Makonkawkeyoon, S. Makonkawkeyoon, Intracellular growth and drug susceptibility of Mycobacterium tuberculosis in macrophages, Tuberculosis (Edinb.) 87 (2007) 130–133.

[35] S. Chanwong, N. Maneekarn, L. Makonkawkeyoon, S. Makonkawkeyoon, Intracellular growth and drug susceptibility of Mycobacterium tuberculosis in macrophages, Tuberculosis 87 (2007) 130–133.

[36] R. Jayaram, S. Gaonkar, P. Kaur, B.L. Suresh, B.N. Mahesh, R. Jayashree, V. Nandi, S. Bharat, R.K. Shandil, E. Kantharaj, V. Balasubramanian, Pharmacokinetics-pharmacodynamics of Rifampin in an aerosol infection model of tuberculosis, Antimicrob. Agents Chemother. 47 (2003) 2118.

[37] C. Seijger, W. Hoefsloot, I. Bergsma-de Guchteneire, L. Te Brake, J. van Ingen, S. Kuipers, R. van Crevel, R. Aarnoutse, M. Boeree, C. Magis-Escurra, High-dose rifampicin in tuberculosis: experiences from a Dutch tuberculosis Centre, PLoS One 14 (2019) e0213718.

[38] R.E. Aarnoutse, G.S. Kibiki, K. Reither, H.H. Semvua, F. Haraka, C.M. Mtabho, S.G. Mpagama, J. van den Boogaard, I.M.S. Boer, C. Magis-Escurra, M. Wattenberg, J.G.M. Logger, L.H.M. Te Brake, M. Hoelscher, S.H. Gillespie, A. Colbers, P.P.J. Phillips, G.P. van Balen, M.J. Boeree, Pharmacokinetics, tolerability, and bacteriological response of rifampin administered at 600, 900, and 1,200 milligrams daily in patients with pulmonary tuberculosis, Antimicrob. Agents Chemother. 61 (2017) (01054–01017).

[39] S.M. Irwin, V. Gruppo, E. Brooks, J. Gilliland, M. Scherman, M.J. Reichlen, R. Leistikow, I. Kramnik, E.L. Nuermberger, M.I. Voskuil, A.J. Lenaerts, Limited activity of Clofazimine as a single drug in a mouse model of tuberculosis exhibiting Caseous necrotic granulomas, Antimicrob. Agents Chemother. 58 (2014) 4026–4034.

[40] H. Fukunaga, T. Murakami, T. Gondo, K. Sugi, T. Ishihara, Sensitivity of acid-fast staining for Mycobacterium tuberculosis in formalin-fixed tissue, Am. J. Respir. Crit. Care Med. 166 (2002) 994–997.

[41] A.M. Dannenberg, Macrophage turnover, division and activation within developing, peak and “healed” tuberculous lesions produced in rabbits by BCG, Tuberculosis 83 (2003) 251–260.

[42] F. Fenaroli, U. Repnik, Y. Xu, K. Johann, S. Van Herck, P. Dey, F.M. Skjeldal, D.M. Frei, S. Bagherifam, A. Kocere, R. Haag, B.G. De Geest, M. Barz, D.G. Russell, G. Griffiths, Enhanced permeability and retention-like extravasation of nanoparticles from the vasculature into tuberculosis granulomas in Zebrafish and mouse models, ACS Nano 12 (2018) 8646–8661.

[43] G. Bajaj, Y. Yeo, Drug delivery systems for intraperitoneal therapy, Pharm. Res. 27 (2010) 735–738.

[44] M.S. Kim, K.S. Seo, G. Khang, H.B. Lee, Ring-opening polymerization of ε-Caprolactone by poly(ethylene glycol) by an activated monomer mechanism, Macromol. Rapid Commun. 26 (2005) 643–648.

[45] J.S. Pedersen, Form factors of block copolymer micelles with spherical, ellipsoidal and cylindrical cores, J. Appl. Crystallogr. 33 (2000) 637–640.

PUBLICATION P3

Urbánek T., **Trousil J.**, Rak D., Gunár K., Konefał R., Šlouf M., Sedlák M., Šebestová J. O., Hrubý M. γ-Butyrolactone copolymerization with the well-documented polymer drug carrier poly(ethylene oxide)-*block*-poly(ε-caprolactone) to fine-tune its biorelevant properties. *Macromolecular Bioscience*. 2020, 1900408, IF = 3.85

T.U. synthesized the polymers, carried out the physicochemical characterizations of both the polymers and nanoparticles, and wrote the paper. J.T. carried out the cytotoxicity and confocal microscopy experiments, conceptualized the intracellular degradation investigations, and wrote the paper. D.R. performed the AFFFF experiments. K.G. performed the flow cytometry investigations. R.K. performed and evaluated the 1H NMR analysis. M.Š. supervised the TEM investigations. M.S. supervised the AFFFF experiments and evaluated the results. O.Š.J. supervised the flow cytometry investigations and cell-associated fluorescence data fitting. M.H. supervised the project and contributed to the final version of the paper.

P3

FULL PAPER

Macromolecular Bioscience
www.mbs-journal.de

γ-Butyrolactone Copolymerization with the Well-Documented Polymer Drug Carrier Poly(ethylene oxide)-*block*-poly(ε-caprolactone) to Fine-Tune Its Biorelevant Properties

*Tomáš Urbánek, Jiří Trousil, Dmytro Rak, Kristýna Gunár, Rafał Konefał, Miroslav Šlouf, Marián Sedlák, Olga Šebestová Janoušková, and Martin Hrubý**

Polymeric drug carriers exhibit excellent properties that advance drug delivery systems. In particular, carriers based on poly(ethylene oxide)-*block*-poly(ε-caprolactone) are very useful in pharmacokinetics. In addition to their proven biocompatibility, there are several requirements for the efficacy of the polymeric drug carriers after internalization, e.g., nanoparticle behavior, cellular uptake, the rate of degradation, and cellular localization. The introduction of γ-butyrolactone units into the hydrophobic block enables the tuning of the abovementioned properties over a wide range. In this study, a relatively high content of γ-butyrolactone units with a reasonable yield of $\approx$60% is achieved by anionic ring-opening copolymerization using 1,5,7-triazabicyclo[4.4.0]dec-5-ene as a very efficient catalyst in the nonpolar environment of toluene with an incorporated γ-butyrolactone content of $\approx$30%. The content of γ-butyrolactone units can be easily modulated according to the feed ratio of the monomers. This method enables control over the rate of degradation so that when the content of γ-butyrolactone increases, the rate of degradation increases. These findings broaden the application possibilities of polyester-polyether-based nanoparticles for biomedical applications, such as drug delivery systems.

1. Introduction

Amphiphilic polymeric nanoparticles (NPs) are nanomaterials generated by the self-association of polymeric amphiphiles above a critical aggregation concentration, and their use of intervention is based on their physicochemical properties and architecture; the array of hydrophilic and hydrophobic domains can vary.[1–3] A class of important biodegradable and/or biocompatible polymers, aliphatic polyesters, have been widely studied due to their large-scale accessibility by the ring-opening polymerization (ROP) of cyclic esters or lactones.[4] In contrast to the commonly used lactones or esters for the synthesis of aliphatic copolyesters, γ-butyrolactone (γBL) is a very promising monomer, as introduction of γBL into other aliphatic polyesters might modify the degradation rate to meet the desired application demand.[5–8] Notably, the biocompatibility of poly(γ-butyrolactone) (P4HB) has been shown to be better than that of poly(glycolic acid) and poly(lactide-*co*-glycolide), which are copolymers that have been widely studied in terms of drug delivery in vivo.[7,9] Given this, γBL has been suggested to be a suitable comonomer for drug delivery system tuning.

Although γBL seems to be the perfect choice as a monomer for polymers in medical applications, its thermodynamic parameters do not allow for it to undergo ROP to a sufficient extent.[10,11] In the 1930s, γBL was proclaimed as a nonpolymerizable substance[12] and the corresponding research slowed. Polymerization conditions have been considered the key factors that determine the polymerizability of a substance, and in the 1960s, γBL was successfully converted into low-molecular-weight polyester (1200–3500 g mol^{-1}) under extreme conditions (2 GPa, 165 °C);[13] the high-pressure homopolymerization of γBL has been reported several times, and the molecular weight was increased by acid catalysis.[14] Attempts were made to prepare high-molecular-weight P4HB under less extreme conditions, and in 2016, these attempts resulted in success when a lanthanum

---

T. Urbánek, J. Trousil, Dr. K. Gunár, Dr. R. Konefał, M. Šlouf,
Dr. O. Šebestová Janoušková, Dr. M. Hrubý
Institute of Macromolecular Chemistry
Czech Academy of Sciences
Heyrovského náměstí 2, 162 00 Prague 6, Czechia
E-mail: mhruby@centrum.cz

J. Trousil
Department of Analytical Chemistry
Charles University
Faculty of Science
Hlavova 8, 128 43 Prague 2, Czechia

Dr. D. Rak, Dr. M. Sedlák
Institute of Experimental Physics
Slovak Academy of Sciences
Watsonova 47, 040 01 Košice, Slovakia

The ORCID identification number(s) for the author(s) of this article can be found under https://doi.org/10.1002/mabi.201900408.

DOI: 10.1002/mabi.201900408

© 2020 WILEY-VCH Verlag GmbH & Co. KGaA, Weinheim

complex was employed as a catalyst.[15] However, currently, as biologic and electronic applications are at the forefront of interest, the purity of polymers is taken into account, and thus, nonmetallic catalysts are preferred.[16–21] A viable strategy for the incorporation of γBL into a polymeric chain is its copolymerization with thermodynamically favorable monomers.[8,22,23]

Amphiphilic diblock copolymers composed of hydrophobic biodegradable polyester blocks and hydrophilic polymer blocks are very suitable for the construction of micellar/nanoparticle drug delivery systems with core-corona structures because hydrophobic drugs can be encapsulated into micelle cores, while the hydrophobic portion can be degraded into low-molecular-weight fragments after drug release, allowing for elimination from the system of the organism while the hydrophilic corona-forming block protects the core from unwanted interactions in the organism. Among such copolymers, methoxy poly(ethylene oxide)-*block*-poly(ε-caprolactone) is very popular for the construction of drug delivery systems. However, the tuning of its properties is limited by the chemical properties of the polymer block from which it is composed.

In this work, we report the synthesis and characterization of an amphiphilic block copolymer composed of mPEO and poly(ε-caprolactone-*co*-γ-butyrolactone) (PCL-*co*-P4HB) possessing a favorable amount of P4HB. This copolymer undergoes self-association in an aqueous medium and forms spherical amphiphilic assemblies, as determined by cryo-transmission electron microscopy (cryo-TEM). This intervention was found to be enzymatically degradable by two different approaches (dynamic light scattering, DLS, and flow cytometry) and noncytotoxic. In addition, the low-molecular-weight hydrolytic products of the polyester block (6-hydroxyhexanoic acid and 4-hydroxybutyric acid) are fully metabolizable into carbon dioxide and water. The novel copolymerization of P4HB into the hydrophobic polyester block of mPEO-PCL block copolymers of this article was found to be an excellent tool for the adjustment of the properties critical for its use in drug delivery systems (NP behavior, cell uptake, biodegradation rate, and intracellular localization) over a very wide range, strongly increasing the variety of possible uses.

2. Experimental Section

2.1. Materials

γBL (≥99%) and ε-caprolactone (εCL, 97%) were purchased from Sigma-Aldrich Ltd. (Prague, Czechia), dried over calcium hydride for 24 h, subsequently distilled under reduced pressure, and stored under an inert atmosphere prior to use.

Benzyl alcohol (BA, ≥99%, Sigma-Aldrich Ltd.) was dried over calcium oxide for 24 h and subsequently distilled under reduced pressure twice and stored under an inert atmosphere prior to use. Poly(ethylene oxide) monomethyl ether, 2 and 5 kDa (mPEO_{45} and mPEO_{114}, Sigma-Aldrich Ltd.), were azeotropically dried with toluene prior to use.

3,5-Bis(trifluoromethyl)phenyl isothiocyanate (98%), 1-(4,5-dimethylthiazol-2-yl)-3,5-diphenylformazan (MTT, BioReagent), cyclohexylamine (≥99.9%), 1,8-diazabicyclo[5.4.0]undec-7-ene (DBU), diphenyl phosphate (DPP), hydrochloric acid (in diethyl ether, 2 M), lipase from *Pseudomonas* sp. (type XIII) (Sigma-Aldrich Ltd.), paraformaldehyde, 1,5,7-triazabicyclo[4.4.0]dec-5-ene (TBD, 98%), 7-(diethylamino)coumarin-3-carbonyl azide (DACCA), and γ-hydroxybutyric acid sodium salt were purchased from Sigma-Aldrich Ltd. and used as received.

7-Aminoactinomycin D (7AAD), amphotericin B (250 µg mL^{-1}), CellMask Deep Red, Dulbecco's modified Eagle medium (DMEM, high glucose, GlutaMAX), fetal bovine serum (FBS, heat-inactivated), LysoTracker Deep Red, penicillin-streptomycin solution (10 000 U mL^{-1}), and Triton X-100 solution (1%) were purchased from Life Technologies Ltd. (Prague, Czechia).

2.2. Synthesis of *N*-(3,5-bistrifluoromethyl)phenyl-*N′*-cyclohexylthiourea (TU)

Cyclohexylamine (210 µL, 1.84 mmol) was added to 10 mL of dry dichloromethane (DCM) under an argon atmosphere. This solution was cooled in an ice bath and 3,5-bis(trifluoromethyl) phenyl isothiocyanate (337 µL, 1.85 mmol) was added.[24] The reaction was maintained overnight (16 h) at room temperature. The product precipitated from the solution, the solvent was evaporated under reduced pressure and the product was purified by recrystallization from petroleum ether with a yield of 91%. The product was further used as a cocatalyst of DBU for the ROP of γBL with εCL.

2.3. Synthesis of Poly(ε-caprolactone-*co*-γ-butyrolactone) (PCL-*co*-P4HB)

Polymerization reactions (**Figure 1**A) were carried out in dry vessels under an argon atmosphere for 24 h. The desired amounts of initiator (BA), catalyst (HCl/Et_2O, DPP, TBD or DBU/TU), and solvent were added into the vessels equipped with magnetic stirring bars. The solutions were stirred while the monomers (εCL and γBL) were added. The feed ratios are listed in the Tables S1 and S2 in the Supporting Information. The products were washed with ice-cold Et_2O.

2.4. Synthesis of Poly[ethylene oxide-*block*-(ε-caprolactone-*co*-γ-butyrolactone)] [mPEO-*b*-(PCL-*co*-P4HB)]

Polymerization reactions (Figure 1B) were carried out in the same manner as the polymerization of PCL-*co*-P4HB. In this case, the poly(ethylene oxide) monomethyl ethers were used as the macroinitiators and only TBD was used as the catalyst. Feed amounts are listed in Table S3 in the Supporting Information.

2.5. Fluorescent Labeling of mPEO-*b*-(PCL-*co*-P4HB)

Chosen samples of the prepared copolymers were labeled with DACCA for biological analysis, synthesis scheme shown in Figure S12 in the Supporting Information. Each sample of 80 mg of mPEO-*b*-(PCL-*co*-P4HB) was dissolved in 10 mL of toluene, and 2 molar equivalents of DACCA were added to this

© 2020 WILEY-VCH Verlag GmbH & Co. KGaA, Weinheim

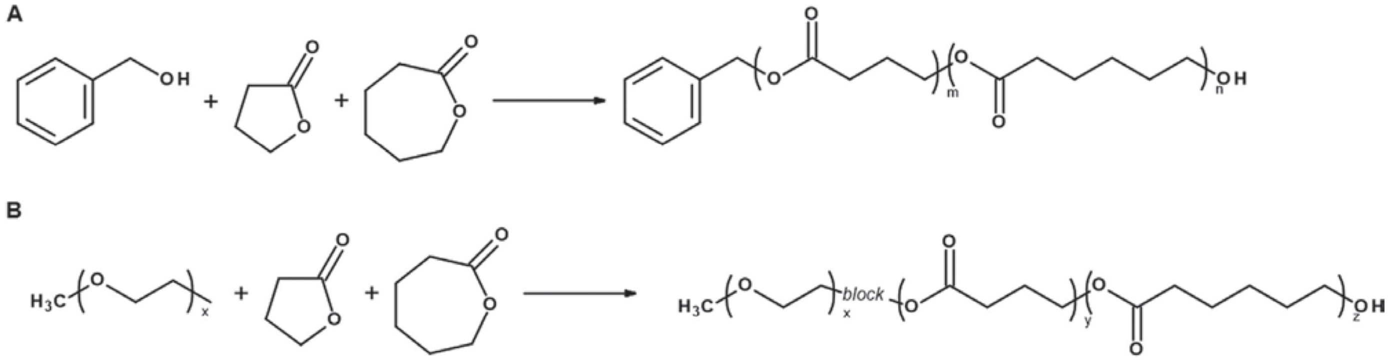

Figure 1. Synthesis scheme of A) copolymer PCL-*co*-P4HB and B) block copolymer mPEO-*b*-(PCL-*co*-P4HB).

solution. The reactions were maintained at 80 °C under an argon atmosphere for 24 h.[25] The products were purified by dialysis and freeze-dried. The UV–vis spectra were measured with a UV–vis spectrophotometer (Evolution 220 Spectrometer, Thermo Scientific, USA). Fluorescence spectra of the samples were recorded (90° angle geometry, 1 × 1 cm quartz cell) with an Aminco Bowman Series 2 spectrofluorometer (Aminco, Lake Forest, CA, USA) at an excitation wavelength of 420 nm and are shown in Figure S13 in the Supporting Information.

2.6. Preparation of Nanoformulations

Nanoparticles were prepared by the nanoprecipitation method. Samples of mPEO-*b*-(PCL-*co*-P4HB) (10 mg) were diluted in acetone (1 mL), and subsequently, an aqueous phase [distilled water or phosphate-buffered saline (PBS)] (10 mL) was rapidly added while stirring at 200 rpm. The excess acetone was evaporated under reduced pressure. The final concentrations of the samples were 1 mg mL^{-1}. Nanoformulations were always prepared fresh for each characterization.

2.7. Characterization of PCL-*co*-P4HB and mPEO-*b*-(PCL-*co*-P4HB)

Proton nuclear magnetic resonance (^{1}H NMR), size-exclusion chromatography (SEC), and Fourier transform infrared spectroscopy (FTIR) were used for fundamental characterization of the synthetized copolymer structures.

A Bruker AVANCE DPX 300 (and/or AVANCE III 600 MHz) spectrometer (Bruker Daltonik GmbH, Bremen, Germany) operating at 300.1 or 600.2 MHz was utilized for chemical structure determination. All samples were dissolved in deuterated chloroform at 25 °C. The chemical shifts were relative to tetramethylsilane (TMS) using hexamethyldisiloxane (HMDSO, δ = 0.05 ppm from TMS) as the internal standard.[26] ^{13}C NMR spectrum was recorded using Bruker AVANCE III 600 MHz operating at 150.9 MHz in deuterated chloroform at 25 °C. The chemical shift was relative to TMS using HMDSO (δ = 2.00 ppm from TMS) as the internal standard.

A Perkin Elmer PARAGON 1000 PC FTIR spectrometer was utilized for chemical structure confirmation. The spectrometer had a resolution of 4 cm^{-1}, 32 accumulated scams, and strong apodization. The reflective measurements were performed using an ATR-Specac MKII Golden Gate Single Reflection system with a diamond crystal and an angle of incidence of 45°. The samples were characterized in powder form.

Physical characterization of the synthetized copolymers was determined by SEC. Namely, the mass-average molar mass M_n, the number-average molar mass M_w, and their ratio M_w/M_n provided information about the chain length distribution–dispersity, *Đ*. The separation was carried out using a DeltaChrom pump (Watrex Ltd., Prague, Czechia), a Midas Spark autosampler (DataApex Ltd., Prague, Czechia), and two PLgel MIXED-B-LS columns. The samples were dissolved in tetrahydrofuran (THF), which served as the mobile phase in the chromatographic system with a flow rate of 1 mL min^{-1} at 25 °C. A PL ELS-1000 evaporative light scattering detector (Polymer Laboratories, Varian Inc., Amherst, USA) was used for the detection. The evaluation of the sample chromatograms was performed using Clarity Software Version 6.0.0.295 (DataApex Ltd.) with polystyrene standard calibration.[27]

2.8. Characterization of the Nanoparticles Prepared by mPEO-*b*-(PCL-*co*-P4HB)

Different techniques were used for the characterization of the nanoparticles. DLS measurements were carried out on a ZEN3600 Nano-ZS instrument (Malvern Instruments Ltd., UK) using an angle of 173°. A He–Ne laser (4.0 mW, operating at 633 nm) was used. The hydrodynamic diameter of the particles was calculated from the diffusion coefficient using the Stokes–Einstein equation.

Static light scattering (SLS) measurements were performed on an ALV-6010 instrument (ALV GmbH, Germany) equipped with a 22 mW He–Ne laser in the angular range of 30°–150°. The data were analyzed by using a Zimm plot. The dn/dc values were measured as described below.

The additional method for characterizing the prepared nanoparticles was asymmetric-flow field-flow fractionation (AF4). The instrument setup for AF4 consisted of an Eclipse 3+ separation system (Wyatt Technology Europe, Dernbach, Germany) coupled to a 1260 Infinity isocratic pump and degasser (Agilent Technologies, Santa Clara, CA, USA), a DAWN HELEOS II MALS detector with a 120 mW gallium-arsenide laser at a wavelength of 661 nm (Wyatt Technology, Santa Barbara, CA, USA), and an RI-101 RI detector (Shodex, Munich, Germany). Prepared nanoparticles in filtered

© 2020 WILEY-VCH Verlag GmbH & Co. KGaA, Weinheim

deionized water underwent measurements using a 275 mm long trapezoidal channel consisting of a 490 µm spacer and a regenerated cellulose membrane with a 5 kDa cutoff. Collected data were processed using ASTRA 6 software.

The measurements followed the established procedure in ref. [28]. As a result, the mass-average molar mass M_w and the diameter of gyration D_g were obtained.

The refractive index increment d*n*/d*c* of the solutions was measured with a BI-DNDCW differential refractometer (Brookhaven Instruments Corporation, USA). The d*n*/d*c* values were obtained using a potassium chloride calibration solution.

2.9. Morphology of the NPs

The nanoparticle morphology was observed by transmission electron microscopy. To characterize the morphology of the nanoparticles, 3 µL of sample solution was applied to a formvar-carbon electron microscopy grid. Samples were observed without staining at 100 kV using an FEI Morgagni TEM equipped with a MegaView III side-entry charge-coupled device camera. For cryo-TEM, where the hydrated samples were imaged without the perturbation generated by drying, the sample solution was applied to a carbon-covered polymer-grid supporting film (lacey-carbon grids, Electron Microscopy Sciences, Hatfield, USA) and glow discharged for 40 s with a 5 mA current. Most of the sample was removed by blotting and the grid was immediately plunged into liquid ethane at −183 °C. The sample was then transferred without rewarming into a Tecnai Sphera G20 electron microscope (FEI) using a Gatan 626 cryo-specimen holder (Gatan Inc., Pleasanton, CA, USA). Images were recorded at a 120 kV accelerating voltage using a Gatan UltraScan 1000 slow-scan charge-coupled device camera (achieving a final pixel size from 2 to 0.7 nm) in low-dose mode.

2.10. Enzymatic Degradation of NPs

The ^{1}H NMR and SEC measurements were used to determine the enzymatic degradation of the prepared nanoparticles and the procedure is described in ref. [28]. The degradation was studied in the presence of lipase from *Pseudomonas* sp. The appropriate amount of lipase (aqueous solution in PBS, 4 U mL^{-1}) was added to the nanoformulation (1 mg mL^{-1} in PBS) to initiate the degradation process, giving final concentrations of the copolymer and lipase of 0.98 mg mL^{-1} and 0.06 U mL^{-1}, respectively. The degradation was performed at 37 °C inside an NMR cuvette. In case of SEC measurements, the purification of the organic content was needed to be done after the degradation period. The PBS solution of the sample incubated with the lipase was poured into excess of cold diethyl ether, so the organic content precipitated. The precipitate was separated by centrifugation at 7000 rpm and 0 °C and dried. This material was dissolved in mobile phase of SEC and the analysis was performed.

2.11. Critical Aggregation Concentration (CAC) Determination

The NP formulations of the synthesized copolymers were prepared by the protocol described above. Series of concentrations reaching 10^{-6} mg mL^{-1} were obtained by serial dilution in PBS. A solution of Nile red in ethanol was added to each sample to obtain a final concentration of 10^{-6} mol L^{-1}. A Synergy H1 Hybrid Reader instrument (BioTek, Winooski, USA) was utilized to record the fluorescence of the samples. The excitation wavelength was 550 nm and the emission intensity was measured at 650 nm. The CACs were determined as the intersection points of the lines from two different parts of the graph of fluorescence intensity versus the negative logarithm of the concentrations, as seen in Figure S8 in the Supporting Information.[28]

2.12. Hemolysis assay

The determination of blood compatibility with the prepared NPs was carried out following the procedure in ref. [28]. Fresh human blood was collected for the analysis into heparin-coated vacutainers (Becton Dickinson Czechia Ltd., Prague, Czechia). Red blood cells (RBCs) were obtained by centrifugation of the blood at 3000 rpm for 10 min. The plasma was removed and RBCs were washed with PBS. The final concentration of RBCs in PBS for the hemolysis measurements was at a full blood dilution of 1:49.

To 0.3 mL of diluted RBCs, 1.2 mL of the appropriately diluted nanoformulation (in PBS) was added. With this procedure, several dilutions of NPs were prepared (100, 200, 400, and 800 µg mL^{-1}). Triton X-100 (1% in PBS) and PBS served as positive and negative controls, respectively.

After incubation at 37 °C for 8 h, the samples were centrifuged (3000 rpm, 10 min). Subsequently, the supernatants were collected and subjected to absorbance measurement at 541 nm on a Synergy H1 Hybrid Reader instrument (BioTek, Winooski, Vermont, USA). The percent hemolysis of RBCs in each sample was calculated by the following Equation (1)

$$\text{Hemolysis} = \frac{\text{sample absorbance} - \text{negative control}}{\text{positive control} - \text{negative control}} \times 100 \tag{1}$$

The results of the hemolysis assays were expressed as a percentage of the positive control (1% Triton X-100 in PBS), which was considered 100%. Hemoglobin release up to 2% was classified as nonhemolytic, according to the ASTM F756-08 standard.[29] The results of this assay are expressed as mean values of triplicate analysis.

2.13. Cell Culture

The murine monocyte-macrophage (Mϕ) cell line J774A.1[30] was purchased from Sigma-Aldrich Ltd. The cells were maintained in DMEM supplemented with FBS (10%), penicillin (100 U mL^{-1}), streptomycin (100 µg mL^{-1}), and amphotericin B (2.5 µg mL^{-1}) in a humidified atmosphere containing 5% CO$_2$ at 37 °C.

2.14. Cytotoxicity Study

Cytotoxicity was evaluated using the MTT assay. For this purpose, J774A.1 Mϕs were seeded in 96-well plates at a density of 5000 cells per well. The cells were then incubated overnight at 37 °C and 5%

© 2020 WILEY-VCH Verlag GmbH & Co. KGaA, Weinheim

CO$_2$ with subsequent replacement of the medium with 100 µL of fresh culture medium containing the tested formulations. After 24 h of incubation, the medium was replaced with 100 µL of MTT solution (0.5 mg mL^{-1} in PBS), and the plates were incubated for 2–4 h prior to aspiration of the medium and dimethyl sulfoxide addition (100 µL). After 15 min of blue formazan solubilization (37 °C), a Synergy H1 Hybrid Reader instrument (Biotek, Winooski, USA) was used to assess cell viability by spectrophotometry at 570 nm. The results of the MTT assay were expressed as a percent of the control (cells in control medium), which was considered 100 %. A reduction in cell viability by more than 30% was considered a cytotoxic effect according to the ISO 10993-5.[31] The tests were performed in at least three separate experiments.

2.15. Microscopic Investigation of Cellular Uptake

Confocal laser scanning microscopy (CLSM) was used to study cellular uptake and lysosome-nanoparticle colocalization. For the uptake study, J774A.1 cells were seeded at the bottom of ibidi µ-dishes (ibidi GmbH, Planegg/Martinsried, Germany) and left to adhere overnight. Subsequently, the medium was replaced with fresh medium (full DMEM) containing DACCA-labeled NPs (2.8 nmol mL^{-1}). After 40 min of incubation, the cells were washed with prewarmed PBS (37 °C) three times, stained with CellMask Deep Red according to the manufacturer's protocol for 10 min, washed with warm PBS, fixed using a paraformaldehyde solution (4% in PBS), and kept under PBS until subsequent analysis. Cells were visualized on an Olympus FV 10 confocal laser scanning microscope (Olympus Czech Group Ltd., Prague, Czech Republic) using a 60 × oil objective. Signal detection was observed in channels 1 (DACCA, exc. 405 nm, em. 425–475 nm) and 2 (CellMask Deep Red, exc. 650 nm, em. 655–750 nm).

Similarly, the lysosome-nanoparticle colocalization study was carried out using overnight-adhered macrophages (Mϕs). The medium was replaced with fresh DMEM containing DACCA-labeled NPs (2.8 nmol mL^{-1}) and LysoTracker (0.0125×10^{-6} M) and incubated for 40 min. Subsequently, the cells were washed and fixed as described above. Visualization was carried out using the same instrument under the same conditions. Before image analysis, the images were converted to eight-bit grayscale pictures, and the levels of colocalization were determined using ImageJ software. An image of the product of the differences from the mean (PDM), i.e., for each pixel: (blue intensity − mean blue intensity) × (red intensity – mean red intensity), was used to analyze the colocalization. In addition, Pearson correlation coefficient (PCC) values were calculated using the same software. For this purpose, at least six fields were used for the PCC calculation. PCC is a positive correlation between different channels that generates values ranging from –1 to 1. A value of 1 suggests a perfect positive linear correlation. Hence, in this case, a value of 1 would indicate total colocalization of the DACCA-labeled nanobead-based intervention with LysoTracker-positive compartments.

2.16. Flow Cytometry Investigations

Cellular internalization and intracellular degradation were studied by flow cytometry. Cell uptake of the fabricated DACCA-labeled NPs was measured via a BD FACSVerse flow cytometer (BD Biosciences, Franklin Lakes, NJ, USA). For this purpose, J774A.1 cells were incubated at 37 °C and 5% CO$_2$ in full DMEM. The overnight culture was seeded at a density of 200 000 cells per sample. NPs were added at a final concentration of 2 nmol mL^{-1} to the wells and incubated for 1, 5, 20, 40, 60, or 80 min. After washing with warm PBS, the cells were suspended in 0.5% bovine serum albumin (BSA, in PBS solution). Dead cells were stained with 7AAD according to the manufacturer's protocol. The measurement was repeated independently three times and in duplicate. Cell-associated fluorescence was analyzed using FlowJo 10.5.0 software (Tree Star Inc., Ashland, OR, USA).

Intracellular degradation estimation was based on a previously described method.[28] The overnight J774A.1 culture was seeded at a density of 200 000 cells per sample. NPs at a concentration of 2 nmol mL^{-1} were added to the appropriate wells and incubated for 60 min in full DMEM (37 °C, 5% CO$_2$). The incubation length was chosen according to the above-described internalization-related experiment, where the macrophages showed the maximum internalized NPs between 60 and 80 min of incubation. After washing with warm PBS, the cells were further incubated in particle-free full DMEM for 0, 10, 20, 30, 40, or 80 min. Cells were washed with PBS and suspended in 0.5% BSA (PBS solution); dead cells were stained with 7AAD and measured by BD FACSVerse. The measurement was repeated independently three times and in duplicate. Cell-associated fluorescence was analyzed using FlowJo 10.5.0 software.

3. Results and Discussion

3.1. Synthesis and Content of 4HB in PCL-*co*-P4HB

Previous studies that have focused on the polymerization of five-membered lactones have shown their unwillingness to undergo ring-opening polymerizations due to the low ceiling temperature.[10] However, this does not mean that the ring of five-membered lactones cannot be opened and that only the cyclic form is thermodynamically preferred. These rings do open, but there is no impetus to form high-molecular-weight polymers under normal conditions.[32,33] This is the reason why these compounds are difficult to homopolymerize but, on the other hand, are easy to incorporate into a polymer chain when copolymerization occurs with another appropriate heterocycle with a high ceiling temperature. Moreover, the extent of incorporation can also be tuned by the polymerization conditions.[10,34]

Hence, for the systematic investigation of incorporating γBL into polymer chains during copolymerization with εCL, a series of copolymerizations initiated by benzyl alcohol were performed (Figure 1A) with different copolymerization conditions. The polymerization parameters and resulting characterizations are given in Tables S1 and S2 in the Supporting Information. The data in Table S1 in the Supporting Information show the parameters depending on the feed ratio of monomers, whereas the data in Table 2 show the parameters depending on the nature of the catalyst and the solvent and the initial monomer concentrations. In total, four different catalytic systems were evaluated (structures shown in **Figure 2**A).

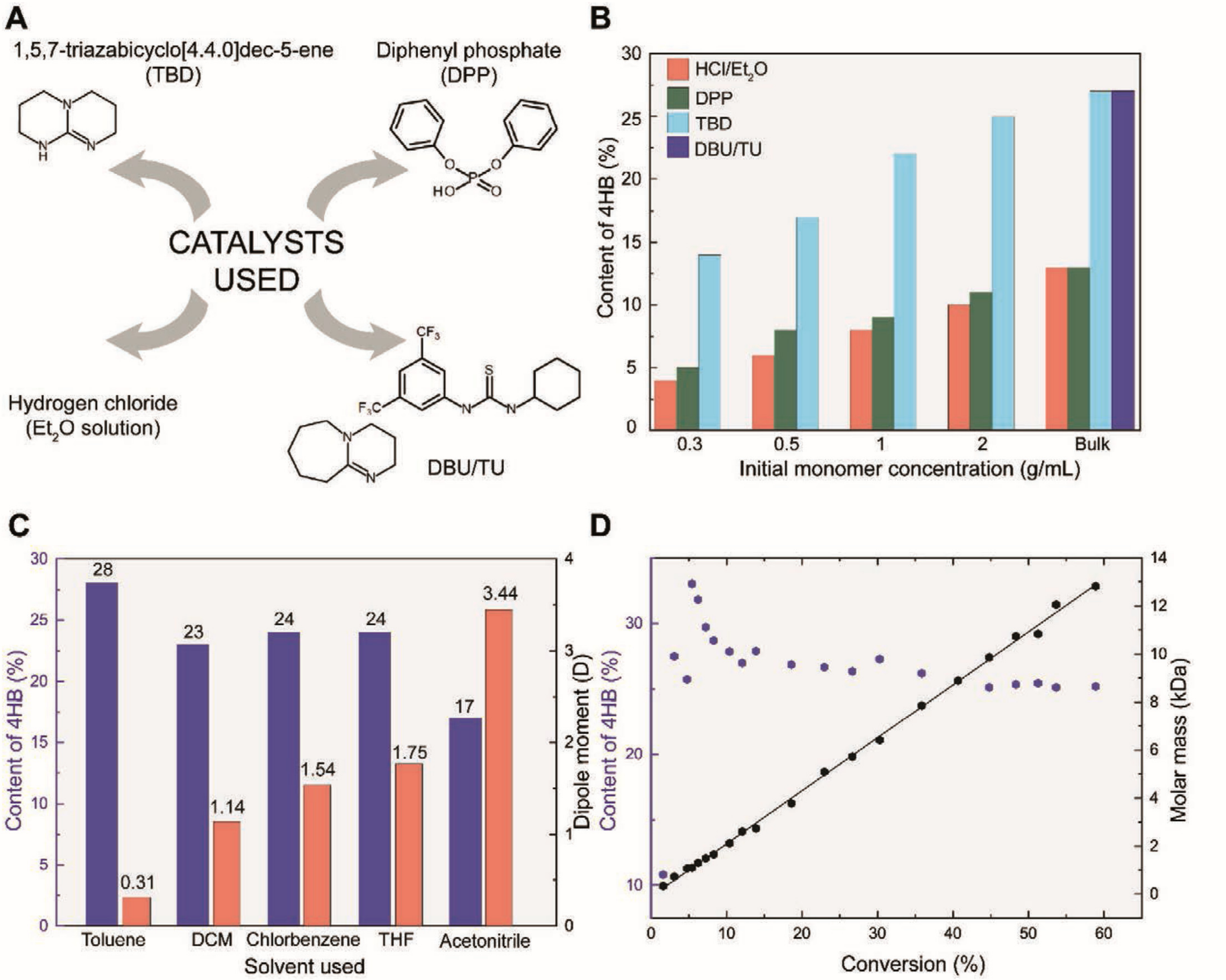

Figure 2. Copolymerization optimization. A) Different catalysts were used in subsequent studies of the content of 4HB in copolymers. B) Different initial monomer concentrations with DCM as the solvent as well as C) different solvents possessing various dipole moments were studied with TBD used the catalyst. D) The relationship between monomer consumption and the content of 4HB in the polymer chain and molar mass was studied. The εCL/γBL molar feed ratio was in all cases 1.15. Abbreviations: TBD, 1,5,7-triazabicyclo[4.4.0]dec-5-ene; DPP, diphenyl phosphate; Et_2O, diethyl ether; DBU, 1,8-diazabicyclo[5.4.0]undec-7-ene; TU, *N*-(3,5-bistrifluoromethyl)phenyl-*N′*-cyclohexylthiourea; DCM, dichloromethane; THF, tetrahydrofuran.

The data in Table S1 in the Supporting Information show the relationship between the monomer feed ratio and the amount of incorporated γBL. Not surprisingly, the higher the ratio of γBL in the feed, the more γBL was incorporated. The disadvantage of copolymerization with high amounts of γBL is its relatively low yield. The difference in the incorporated amount of γBL is remarkable when different catalysts were used (**P1–P4** catalyzed by HCl/Et2O and **P5–P8** by TBD).

The data schematically plotted in Figure 2B show a significant difference in the incorporated amount of γBL when different catalysts were used. A higher content of 4HB units in the prepared copolymers was observed when anionic catalysts (TBD and DBU/TU) were used compared to that observed in the copolymers prepared with cationic catalysts (HCl/Et_2O and DPP). This fact implies that different polymerization mechanisms significantly affect the amount of incorporated γBL.

The bulk copolymerization catalyzed by DBU/TU resulted in a yield of 39% and a copolymer containing 27% 4HB units but there was no high-molecular-weight copolymer formed when solution copolymerization was carried out at any concentration. TBD was identified as the most efficient and versatile catalytic system in this study. TBD is able to incorporate a relatively high amount of γBL at any initial monomer concentration. The trend of increasing incorporated γBL amount with increasing initial monomer concentration is evident in Figure 2B.

Solvent polarity is a considerable parameter when a certain amount of γBL incorporation is needed in the polymer chain. As shown in Figure 2C, there was a marked difference in 4HB content in the copolymer composition of PCL-*co*-P4HB when the nonpolar solvent toluene was used compared to the 4HB content when polar acetonitrile was used. It should be noted that TBD is a bifunctional catalyst, in which the base site works as a H-bonding acceptor to activate the alcohol initiator, while

© 2020 WILEY-VCH Verlag GmbH & Co. KGaA, Weinheim

the H-bonding donor component can activate the monomer via the coordination of the ester functionality. Thus, the noncoordinating solvent toluene enables higher incorporation of γBL in the evaluated copolymerization reaction.

The prepared copolymers were characterized by ^{1}H NMR and FTIR spectroscopy, and their structures were confirmed. The ^{1}H NMR spectra and FTIR spectra are shown in Figures S2 and S3 in the Supporting Information, respectively. The table of polymerization parameters and copolymer characteristics obtained by ^{1}H NMR spectroscopy and size exclusion chromatography can be found in Table S2 in the Supporting Information.

In addition, a ^{1}H NMR spectroscopic kinetic study was performed to understand the copolymerization behavior. TBD was used as the catalyst for this purpose and deuterated DCM was used as the solvent. The polymerization was performed in an NMR cuvette in situ and ^{1}H NMR spectra were taken periodically over time. The relative intensities of peaks corresponding to the γBL unit (δ 1.91 ppm) and the εCL unit (δ 1.33 ppm) were integrated and the following parameters were calculated. The resulting graph in Figure 2D shows the dependence of the content of 4HB and molar mass on the conversion. A moderate decrease in the content of 4HB units in the growing polymer chain with increasing conversion was observed, and the linear dependence of molar mass on conversion indicated the controlled manner of ring opening copolymerization. Additionally, the rate constants of the incorporation of γBL and εCL were determined. As the graphs in Figure S7 in the Supporting Information of the supplemental information show, εCL has been incorporated according to first-order kinetics with a rate constant of $k_{\varepsilon\mathrm{CL}} = 4.3 \times 10^{-5}\ \mathrm{s}^{-1}$, and the incorporation of γBL follows second-order kinetics with a rate constant of $k_{\gamma\mathrm{BL}} = 5.8 \times 10^{-6}\ \mathrm{dm}^3\ \mathrm{mol}^{-1}\ \mathrm{s}^{-1}$.

3.2. Synthesis of mPEO-*b*-(PCL-*co*-P4HB)

Many studies have shown that assemblies based on poly(ethylene oxide)-*block*-polycaprolactone can be successfully used as drug carriers for many medical applications.[35,36] Copolymerization with mPEO and other hydrophilic polymers ensures or enhances the solubility of these assemblies based on the copolymers and improves the biocompatibility/nonimmunogenicity of the whole system.[37] When mPEO is used for copolymerization, the assemblies do not show any toxicity at reasonable concentrations and are efficient when loaded with hydrophobic drugs,[27] suggesting an attractive polymeric matrix for drug delivery system preparation.

Thus, this work aimed to study the impact of 4HB disturbance on hydrophobic block regularity and on the biorelevant properties of mPEO-based assemblies. Given this, the most efficient conditions for incorporating γBL via the copolymerization initiated by BA were implemented (see above) and the copolymerization was conducted via ROP in the same manner and in the presence of the macroinitiator mPEO (Figure 1B). The macromolecular parameters of the prepared block copolymers are listed in **Table 1**. Samples **B2–B5** differ in hydrophobic ratio and macromolecular molar mass (i.e., mPEO) and in the molar mass of the samples themselves. The ^{1}H NMR spectrum of mPEO-*b*-(PCL-*co*-P4HB) with signal assignment is shown in Figure S6 in the Supporting Information. Moreover, the ^{13}C NMR spectrum in Figure S14 in the Supporting Information gave as detailed information about the copolymer microstructure. It proved that the distribution of CL and 4HB units along polyester block is very likely random.[38]

Sample mPEO$_{44}$-*b*-PCL$_{81}$ **B1** was synthesized in the absence of γBL for comparison of the properties with those of samples **B2** and **B3**. The critical aggregation concentrations were determined and the values are listed in Table 1. The CAC-related curves are shown in Figure S8 in the Supporting Information.

The one-step synthesis of labeled mPEO-*b*-(PCL-*co*-P4HB) with fluorescent dye was performed. DACCA was used for this purpose and the reaction scheme is shown in Figure S12 in the Supporting Information. The efficiencies of the reactions were determined by the standard addition method (free 7-(diethylamino)coumarin-3-carboxylic acid) and were found to be ≈45% by UV–vis spectroscopy. The absolute amounts of DACCA occurring in the polymeric matrices are listed in Table 1. The excitation and emission spectra at the excitation wavelength of 420 nm of free 7-(diethylamino)coumarin-3-carboxylic acid and samples of **B1–B5** are shown in Figure S13 in the Supporting Information.

3.3. Characterization of the Nanoparticles

The fabricated copolymers (**B1–B5**) were used for NP preparation. For this purpose, the nanoprecipitation method described

Table 1. Composition and characteristics of polymers initiated by poly(ethylene oxide) monomethyl ether (mPEO) using TBD as the catalyst.

No.	Copolymer	HH-ratio[a)]	Yield [%]	$f_{\gamma\mathrm{BL}}$[b)] [%]	M_n^{NMR}[c)]	M_n^{SEC}[d)]	Đ$^{\mathrm{SEC}}$[d)]	CAC[e)] [µg mL^{-1}]	DACCA[f)] [µg mg^{-1}]
B1	mPEO$_{45}$-*b*-PCL$_{81}$	4.6	92	0	11 200	8300	1.21	9	20
B2	mPEO$_{45}$-*b*-(PCL$_{39}$-*co*-P4HB$_{13}$)	2.8	62	20	7500	6700	1.45	15	9
B3	mPEO$_{45}$-*b*-(PCL$_{55}$-*co*-P4HB$_{19}$)	4.0	60	21	9900	10 500	1.58	11	10
B4	mPEO$_{114}$-*b*-(PCL$_{41}$-*co*-P4HB$_{12}$)	1.1	63	18	10 800	7600	1.25	14	7
B5	mPEO$_{114}$-*b*-(PCL$_{124}$-*co*-P4HB$_{45}$)	3.6	59	21	23 000	12 300	1.61	10	4

[a)] The hydrophobic ratio was defined as (M_n, hydrophobic block)/(M_n, hydrophilic block), where the M_n of the hydrophilic block was held at either 2000 or 5000 depending on which macroinitiator was used; [b)] The polymer composition ratios of hydrophobic blocks were calculated using ^{1}H NMR data by dividing the integrated peaks of the repeating unit of γBL (δ 1.95 ppm) by the sum of the integrated peaks of γBL and εCL (δ 1.37 ppm); [c)] The molecular weights were calculated using ^{1}H NMR by integrating the methoxy peak of mPEO at 3.37 ppm and the peak for the repeating units of εCL and γBL; [d)] Determined by SEC using tetrahydrofuran as the eluent; [e)] Critical aggregation concentrations were determined at room temperature in PBS; [f)] When DACCA-labeled copolymers were used, the content of DACCA was determined by UV–vis spectroscopy.

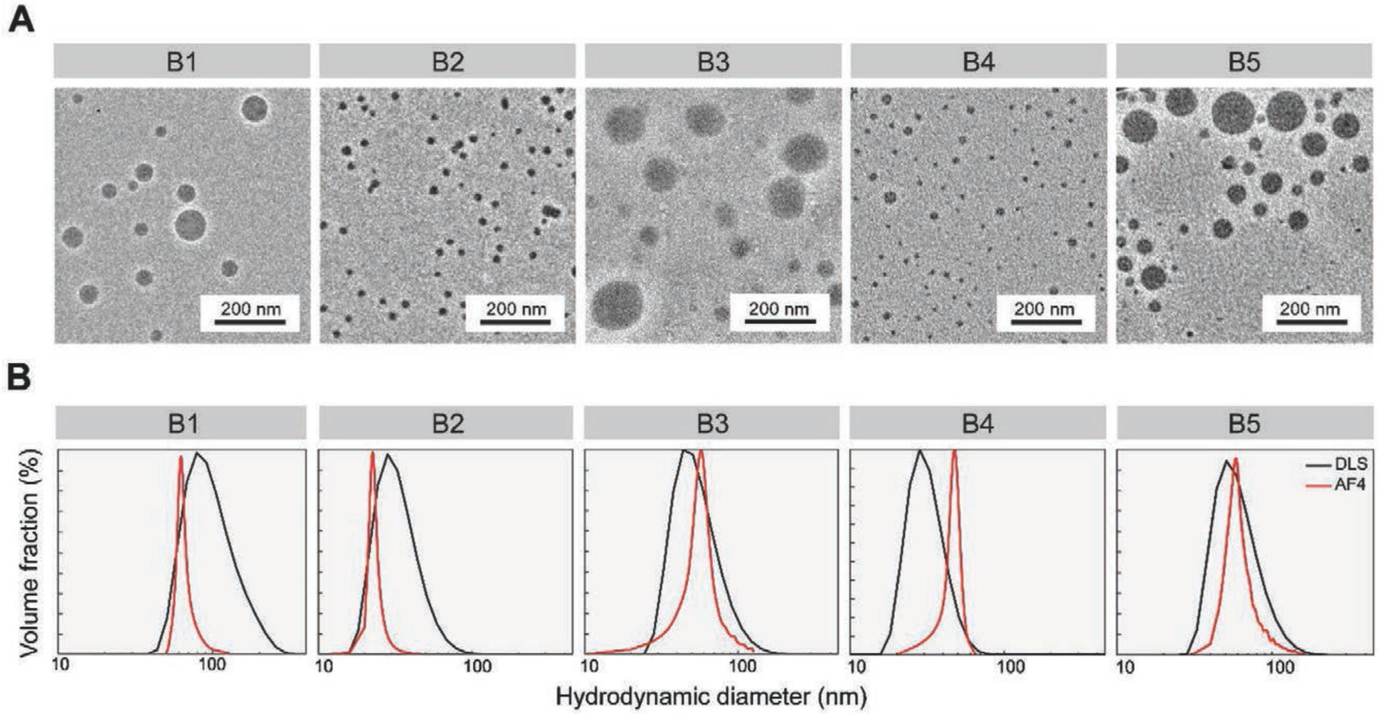

Figure 3. A) Cryo-TEM images and B) curves obtained from DLS and AF4.

in detail in the Experimental Section was used. The physicochemical characterization of the NPs was performed via cryo-TEM, DLS, SLS, and AF4 experiments.

It was hypothesized that the supramolecular structure of the mPEO-*b*-(PCL-*co*-P4HB)-based assemblies correlated to the structure of mPEO-*b*-PCL in some respects, as the only difference was the aliphatic chain length between the ester bonds in the repeating units. In the context of mPEO-*b*-PCL assemblies, several architectures were described in the literature, depending on the hydrophobic/hydrophilic ratio.[35,39] Note that if the solvent switch is fast during NP preparation, block copolymers tend to form spherical structures instead of cylindrical or planar ones because this is the fastest way to reduce the interfacial area.[28] This is in line with the cryo-TEM investigations that revealed that all of the samples inspected were found to largely be spherical polymeric nanoparticles (**Figure 3**A) with diameters in mutual agreement with those found by DLS, SLS, and AF4 (**Table 2**).

The DLS distribution functions (Figure 3B) are portrayed as relatively narrow peaks, with diameters ranging from ≈40–110 nm depending on the block lengths. To verify these findings, we performed additional AF4 experiments that provided the actual sizes and molecular weights. These values are in mutual agreement with those obtained by DLS or SLS. It should be noted, however, that light scattering techniques usually overestimate the size of particles.[36,40] In addition, the samples for the AF4 measurements were filtered through large-pore polyvinylidene fluoride filters (0.8 µm), as AF4 is not as sensitive to dust as conventional light scattering techniques. Thus, any influence of filtration on the size distribution of the nanoparticles can be excluded.

The DLS and AF4 results together with the cryo-TEM investigations allowed for us to obtain insight into the structure of the NPs. In the literature,[39,41,42] mPEO-*b*-PCL-based assemblies are often stated to be micelles. The AF4-estimated molecular weight values (Table 2), however, indicate that ≈400–9000 polymer chains comprise one nanoparticle. Micelles, in contrast, contain ≈10–100 polymer chains.[43]

The apparent structural density (ρ) of the particles was calculated as an equivalent average density from the average of the

Table 2. Characterization of nanoparticles.

Sample	$D_H^{DLS\,a)}$ [nm]	PDI$^{a)\,DLS}$	$D_G^{SLS\,b)}$ [nm]	$M_W^{SLS\,b)}$ [kDa]	$\rho^{SLS\,c)}$ [g mL^{-1}]	$D_G^{AF4\,b)}$ [nm]	$M_W^{AF4\,b)}$ [kDa]	$\rho^{AF4\,c)}$ [g mL^{-1}]	$N_{agg}^{AF4\,d)}$
B1	109	0.113	91	14 900	0.029	77	101 400	0.324	9050
B2	41	0.188	40	5800	0.134	26	8160	0.690	710
B3	71	0.166	120	13 800	0.012	85	24 700	0.060	1110
B4	36	0.109	48	1000	0.013	47	4180	0.060	420
B5	71	0.111	170	38 100	0.011	103	66 700	0.091	2510

a)The *Z*-average of the hydrodynamic diameter D_H and polydispersity index PDI; b)The molecular weight M_W and the *Z*-average of the diameter of gyration D_G; c)The apparent structural density was calculated from the equation $\rho = 6M_w/\pi N_A D^3$ considering a spherical shape ($D = 1.29 \cdot D_G$); d)The aggregation number is the quotient of the M_W of the particles (AF4) and the M_W of the polymer (SEC).

molecular weight M_w using the model of a sphere with a diameter of $D = 1.29\ D_G$; therefore, $\rho = 6M_w/\pi N_A D^3$. On average, the density of the mPEO-*b*-(PCL-*co*-P4HB) nanoparticles was three times lower than the density of the mPEO-*b*-PCL nanoparticles. Given this finding, we hypothesized that the 4HB-possessing NPs were less dense due to their irregular structure (two repeating units) within the hydrophobic core. This also means that the core of the mPEO-*b*-(PCL-*co*-P4HB) nanoparticles was less hydrophobic than that of the mPEO-*b*-PCL nanoparticles, which may influence cargo encapsulation. However, this issue was not addressed further.

One of the advantages of the AF4 method over conventional light scattering methods or cryo-TEM is the capability of AF4 to detect eventual nonassembled polymers in solution. The AF4 investigations revealed that no free nonassembled polymer was found in any of the samples investigated in this work. This is probably due to the favorably low estimated CAC values (i.e., 9–15 µg mL^{-1}) and supports the above-discussed fact that our assemblies are not micelles, which are known to be in thermodynamic equilibrium with unimers, but instead are probably nanogel-like polymeric NPs.

The described complex characterization of NPs allowed for us to fine-tune the nanoparticle parameters so that the particles could be designed more precisely in the future according to the particular application requirements.

3.4. ^{1}H NMR-Assessed Degradation

The enzyme-catalyzed degradation of the NPs was investigated using ^{1}H NMR. The degradation was observed as a decrease in the intensity of the proton signal of ε-caprolactone units in sample **B1** and ε-caprolactone and γ-butyrolactone units in sample **B3** during the experiment. Samples **B1** and **B3** were chosen for this more detailed study due to the comparable sizes of the blocks in these copolymers. For the quantitative characterization of the enzymatic degradation of the PCL and PCL-*co*-P4HB blocks, the time dependence of PCL and PCL-*co*-P4HB consumption was calculated for the measured samples. The integral intensity of the signal marked as "g" (Figure S9, Supporting Information) was defined as 2 (there are two equivalent protons) and used as an internal standard for monitoring degradation in the NMR spectra. Subsequently, the integral intensity of the signal "i + l" (Figure S9, Supporting Information) was used to calculate the percentage of PCL and PCL-*co*-P4HB blocks according to the relationship $[(I_t^{i+l}/I_0^{i+l}) \times 100]$, where the subscripts 0 and t represent the time points during degradation with $t = 0$ (i.e., before lipase addition) and $t = t$ (i.e., after lipase addition), respectively.

The results are shown in Figure S10 in the Supporting Information. It is evident that sample **B1** degraded faster than sample **B3.** Figure S9 in the Supporting Information shows the ^{1}H NMR spectra of **B3**-based NPs that were measured in deuterated PBS at 37 °C before (A) and after (B, C) lipase addition. The chemical structures and signal assignments are presented in the same figure. The comparison between the spectra was recorded in a solvent suitable for all of the blocks (deuterated chloroform, cf. Figure S6, Supporting Information) and PBS (Figure S9, Supporting Information), showing that the broader signals obtained from the PCL-*co*-P4HB hydrophobic block and the strong signals obtained from the hydrophilic mPEO demonstrate the presence of core–shell formation in the deuterated PBS system. These results demonstrate that the PCL-*co*-P4HB protons were restricted in mobility in the moderately hydrated solid-like core of the NPs, while the mPEO blocks created a liquid-like shell. After the addition of lipase, the intensity of the side methyl signals from the PCL-*co*-P4HB monomer unit ("i + l" and "j, e" protons, see Figure S9, Supporting Information) decreased, while the singlets related to the "f + h" and "k" protons split and the mPEO signals ("a", "b") remained unchanged. The second effect observed in this spectrum was the appearance of new signals related to the degradation products, which were identified as 6-hydroxyhexanoic acid and 4-hydroxybutanoic acid (Figure S9, Supporting Information).

Additionally, due to the appearance of the signals at 4.1, 2.2, and 2.0 ppm in Figure S9 in the Supporting Information, there was confirmation of an intermediate product during the degradation appeared before final the products (6-hydroxyhexanoic acid and 4-hydroxybutyric acid). From the chemical shifts of signals of this intermediate product, especially the peak at 4.1 ppm, which was shifted downfield to its respective signal from the polymer (i + l at 4.0 ppm), there was a high probability that this compound was a small cycle made from a small amount of CL and BL units. To support these considerations, one sample was chosen for ^{1}H 2D diffusion-ordered NMR spectroscopy experiments, which were measured before lipase addition (Figure S11, Supporting Information red spectrum) and 24 h after lipase addition (Figure S11, Supporting Information blue spectrum). From those spectra it followed that the intermediate product was still not fully degraded after this time and had a slightly lower self-diffusion coefficient (higher molecular weight) than that of the final products (6-hydroxyhexanoic acid).

The degradation process of the copolymer was confirmed by SEC analysis. The products of degradation were collected in different times. As evident in Figure S15 in the Supporting Information, the degradation of the copolymer was already significant in the first hour of the action of the lipase.

3.5. Cytotoxicity Evaluation

To assess the biorelevant properties of the manufactured NPs, their cytotoxicity and hemolytic activity were analyzed in terms of their interactions with red blood cells (RBCs) and their behavior in monocyte-macrophage cultures, as these cells are one of the first contact partners after systemic administration. In addition, the goal of this evaluation was to answer the questions of whether our synthetized NPs are safe and whether the biocompatibility of P4HB-based assemblies is affected when P4HB is introduced within the Food and Drug Administration-approved mPEO-*b*-PCL copolymer.[44] The mPEO-*b*-PCL copolymer was found to possess no or only minor toxic effects on the cell viability of different cells, such as the murine monocyte-macrophage cell line Raw 264.7,[27,28] zebrafish embryonic fibroblast cell line ZF4,[28] human hepatocellular carcinoma cell line HepG2,[42,45] and prostate cancer cell lines LNCaP and PC-3.[46]

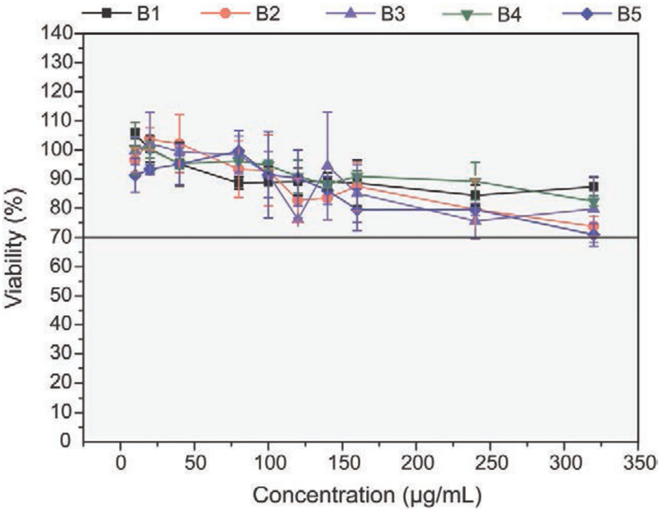

Figure 4. Viability of J774A.1 cells as detected by an MTT assay. Mϕs were incubated with different concentrations of the fabricated NPs for 24 h and their viability was analyzed via measurement of the concentration of metabolically produced formazan. The horizontal line in the panel indicates the level at which, in terms of cell viability, the distinction between cytotoxic (above) and noncytotoxic (below) was made.

First, we studied the effects of the prepared formulations **B1**–**B5** in terms of possible cytotoxicity by using the MTT method after a 24 h incubation of J774A.1 Mϕs with each prepared nanoformulation. As evident in **Figure 4**, the cell viability was influenced very little. The copolymer cytotoxicity was nearly negligible at clinically relevant concentrations. In the hemolytic study, none of the analyzed formulations (**B1**–**B5**) induced hemolysis within the tested concentration range (100–800 μg mL^{-1}) after an 8 h incubation at 37 °C.

Not surprisingly, the use of nanomedicines bears the risk of unwanted side effects.[44] Hence, an important step in the development of nanobead-based products is the assessment of any safety risks. Considering this, our results demonstrate that P4HB introduction within the copolymeric matrix did not affect its acute biocompatibility with both J774A.1 cells and RBCs.

3.6. Uptake and Intracellular Degradation Study

Our research group strives to rationally design nanobead-based interventions to benefit from the combination of the specific properties of NPs and those of biocompatible and biodegradable polymers in one self-assembled formulation allowing for drug delivery. Given this background, one of the crucial studied aspects was the question of whether the 4HB unit-possessing NPs could be taken up by J774A.1 Mϕs as a model cell type, which is an important subject of drug delivery research. Mϕs are the main hosts of intracellular pathogens and, thus, are pursued as a therapeutic target for the intracellular delivery of antibiotics. In addition, Mϕs have gained increasing interest as a therapeutic target for cancer immunotherapy due to its complex roles in the tumor microenvironment.[47]

The DACCA-labeled copolymers were visualized inside the J774A.1 cells using CLSM after an incubation time of 40 min. The microscopy study showed that all of the formulations tested, i.e., mPEO-*b*-PCL and mPEO-*b*-(PCL-*co*-P4HB), were successfully internalized in Mϕs (**Figure 5**), suggesting that such systems are usable as a logical strategy for effectively killing intracellular microbes.[48] Note that slight differences between the intracellular distribution patterns were evident. In other words, some of the samples revealed bright cytosolic localization (e.g., **B4**) compared to the vesicle-localized samples (e.g., **B1**). These findings seem to be in line with our previous mPEO-*b*-PCL-focused study,[28] which confirmed that control of the NP physicochemical properties also allows for control of their biorelevant behavior.

Given this, for a better view of the interactions between the NPs and J774A.1 cells, a marker for low pH compartments (i.e., presumably lysosomes) was applied to visualize the colocalization of the NPs. The cells were incubated for 40 min with DACCA-labeled NPs and LysoTracker Deep Red. These experiments indicated that all of the NP samples tested (**B1**–**B5**) were able to target acidic organelles (**Figure 6**), which was also proven by the analysis in terms of the PDM images and PCC value calculations. However, the DACCA-labeled nanoparticle colocalization with lysosomes was not found to be exclusive, as suggested by the PCC values found (0.43–0.59, Figure 6). As mentioned above, Pearson correlation analysis generates values ranging from −1 to 1, where a value of 1 suggests full colocalization. In other words, these results suggest that the nanocarriers are within low-pH compartments. It should be noted that this finding seems to be in line with our previous study.[27,28] Ultrastructural analysis by TEM revealed that mPEO-*b*-PCL nanoparticles can be found both within vesicular structures and freely in the cytoplasm within Raw 264.7 macrophage-like cells.

To study the cellular internalization kinetics of the NPs within J774A.1 Mϕs, DACCA-labeled NPs (2 nmol mL^{-1}) were added to Mϕ monolayers and incubated for different times. Subsequently, the cellular uptake was analyzed using flow cytometry (**Figure 7**A). All of the obtained cell-associated fluorescence data were normalized to the maximum fluorescence values to ensure the comparability of the results determined from samples with variable total cell fluorescence intensities.[28]

As shown in Figure 7A, the fabricated NPs were successfully taken up by J774A.1 cells, and the cell-associated fluorescence intensity increased as the incubation time increased for all of the samples tested. A maximum cell fluorescence intensity was reached after 60–100 min of incubation (Figure 7A); the data were normalized to the plateau-corresponding values of fluorescence, individually. Subsequently, internalization half-time values (Figure 7A) were calculated based on the internalization time course by curve-fitting of the data using the following equation[49]

$$F(t) = F_0 + \left(F_{\text{plateau}} - F_0\right)\left(1 - e^{-tk}\right) \tag{2}$$

where $F(t)$ is the cell fluorescence signal at time t, F_0 and F_{plateau} are the initial fluorescence signal and the maximum signal, respectively, and k is the internalization rate constant. The half-time of internalization ($\tau_{1/2}$) was calculated as the ratio of ln 2 and k.

The cellular uptake of nanobeads, in general, depends on several factors, such as the size, charge, shape, and

© 2020 WILEY-VCH Verlag GmbH & Co. KGaA, Weinheim

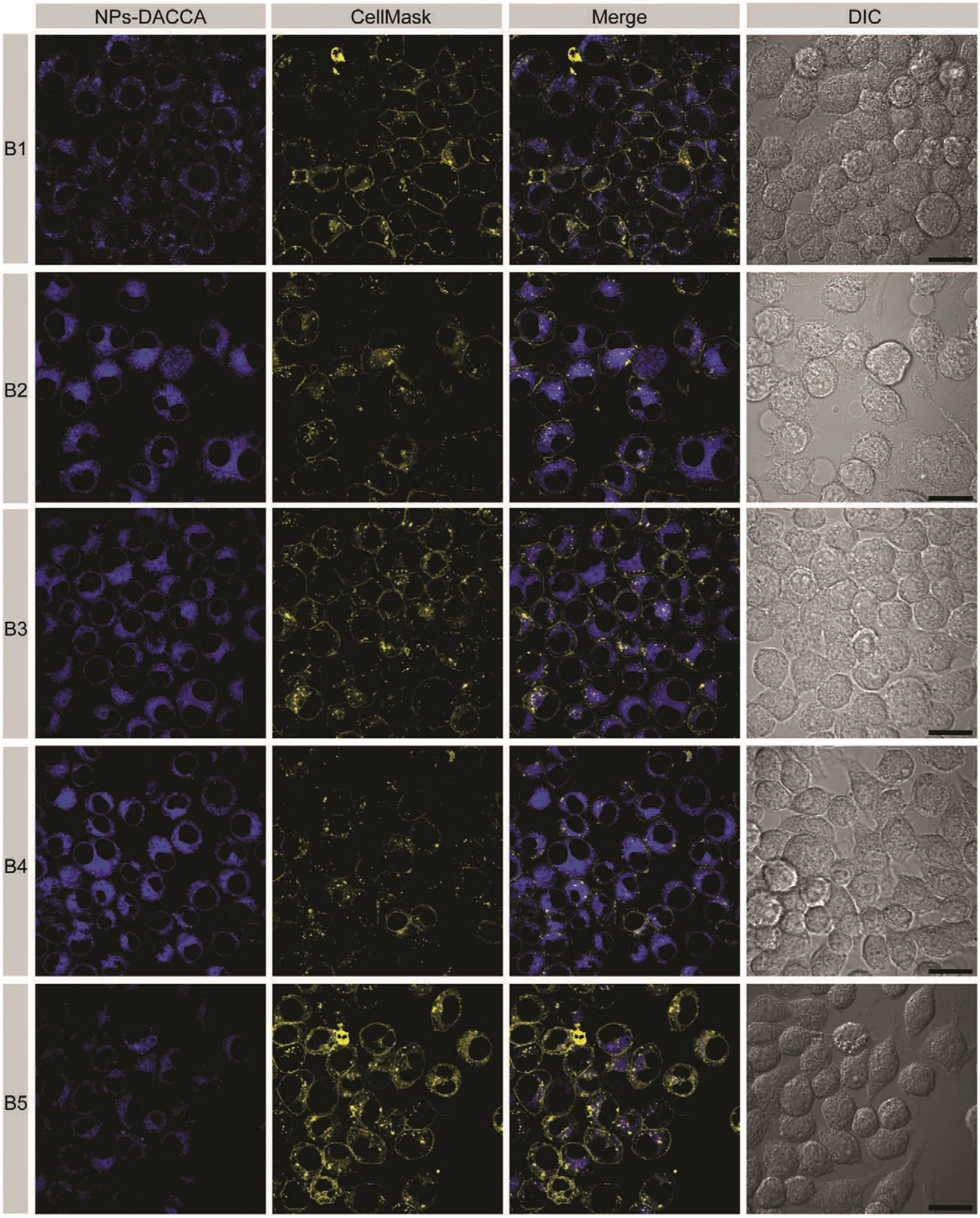

Figure 5. Study of DACCA-labeled NP uptake by J774A.1 cells. Fluorescence and differential interference contrast (DIC) images of J774A.1 cells are shown 40 min after the addition of DACCA-labeled NPs (2.8 nmol mL^{-1}, blue fluorescence). The plasma membrane-related CellMask Deep Red signal is pseudocolored in yellow. Scale bars: 20 µm.

© 2020 WILEY-VCH Verlag GmbH & Co. KGaA, Weinheim

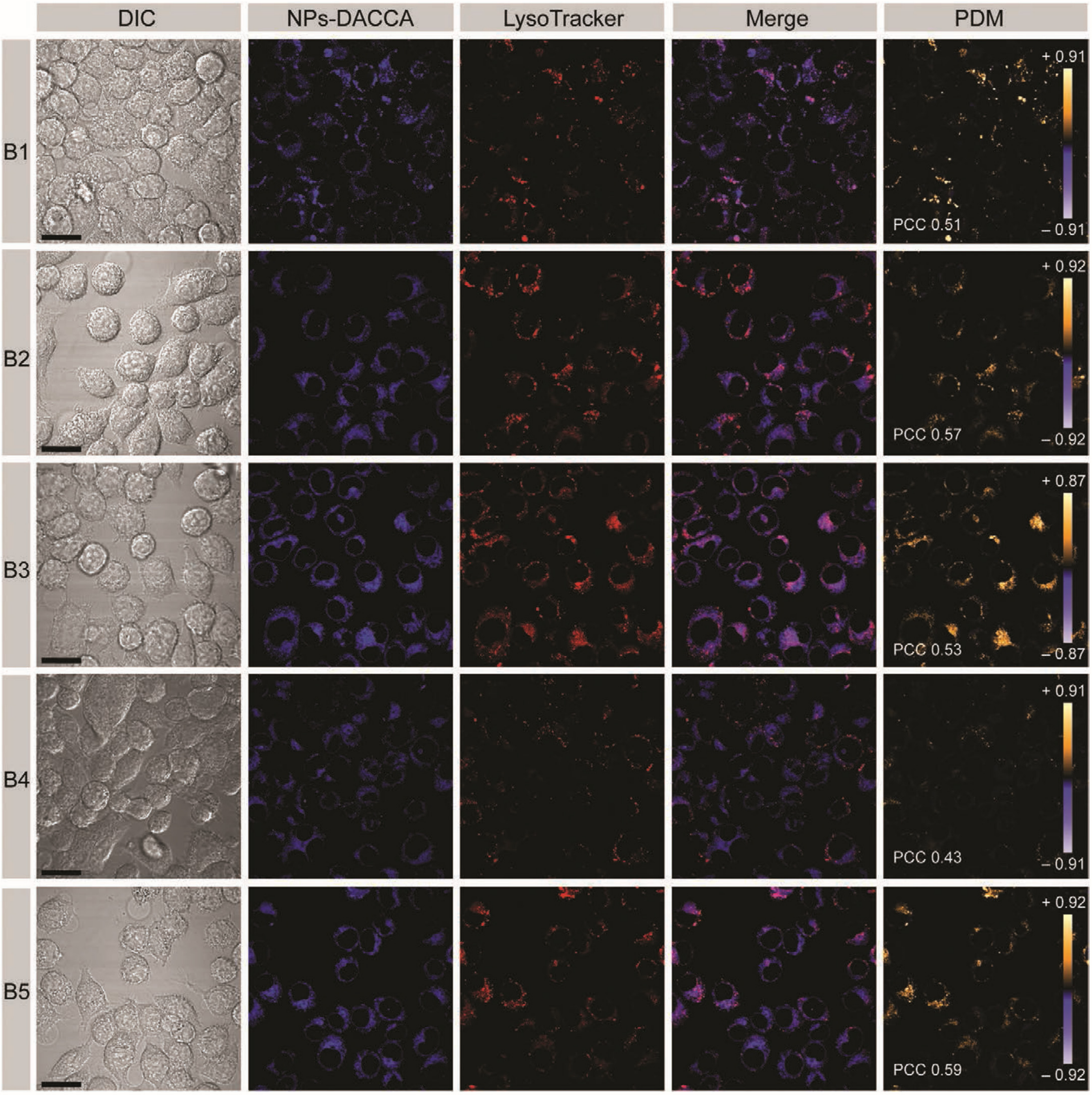

Figure 6. Study of DACCA-labeled NP localization within J774A.1 cells. CLSM images of J774A.1 Mϕs 40 min after the addition of DACCA-labeled NPs (2.8 nmol mL^{-1}) and LysoTracker. The analysis of colocalization was allowed by both the product of the differences from the mean (PDM) images and Pearson correlation coefficient (PCC) values. The PDM images are pseudocolored; each pixel is equal to the PDM value at that location and a PDM scale bar was inserted. The orange color indicates colocalized pixels and the blue color suggests segregation. Scale bars: 20 µm. DIC denotes differential interference contrast.

hydrophilic/hydrophobic ratio of the NPs.[42,50] Not surprisingly, the resulting uptake kinetics are then based on a combination of such parameters. Thus, a group of nanocarriers possessing several different variable properties makes interpretation of the kinetic results harder.[28] Despite this fact, the kinetics study carried out revealed a phenomenon worth mentioning; it was found that the P4HB-free mPEO$_{45}$-*b*-PCL$_{81}$-based sample **B1** exhibited a considerably high internalization $\tau_{1/2}$ value (≈54 min) compared to that of the rest of the samples analyzed.

Notably, the mPEO$_{45}$-*b*-(PCL$_{55}$-*co*-P4HB$_{19}$) copolymer (**B3**) exhibited an internalization $\tau_{1/2}$ of ≈9.5 min, even when having the same hydrophilic/hydrophobic ratio as that of **B1** as well as the same molecular weight. This may be due to the change in crystallinity and/or NP size, one of the main physicochemical aspects that influence cellular uptake. This finding suggests that the introduction of P4HB can strongly affect the biorelevant properties of such nanobead-based interventions. Such a hypothesis, however, must be investigated in

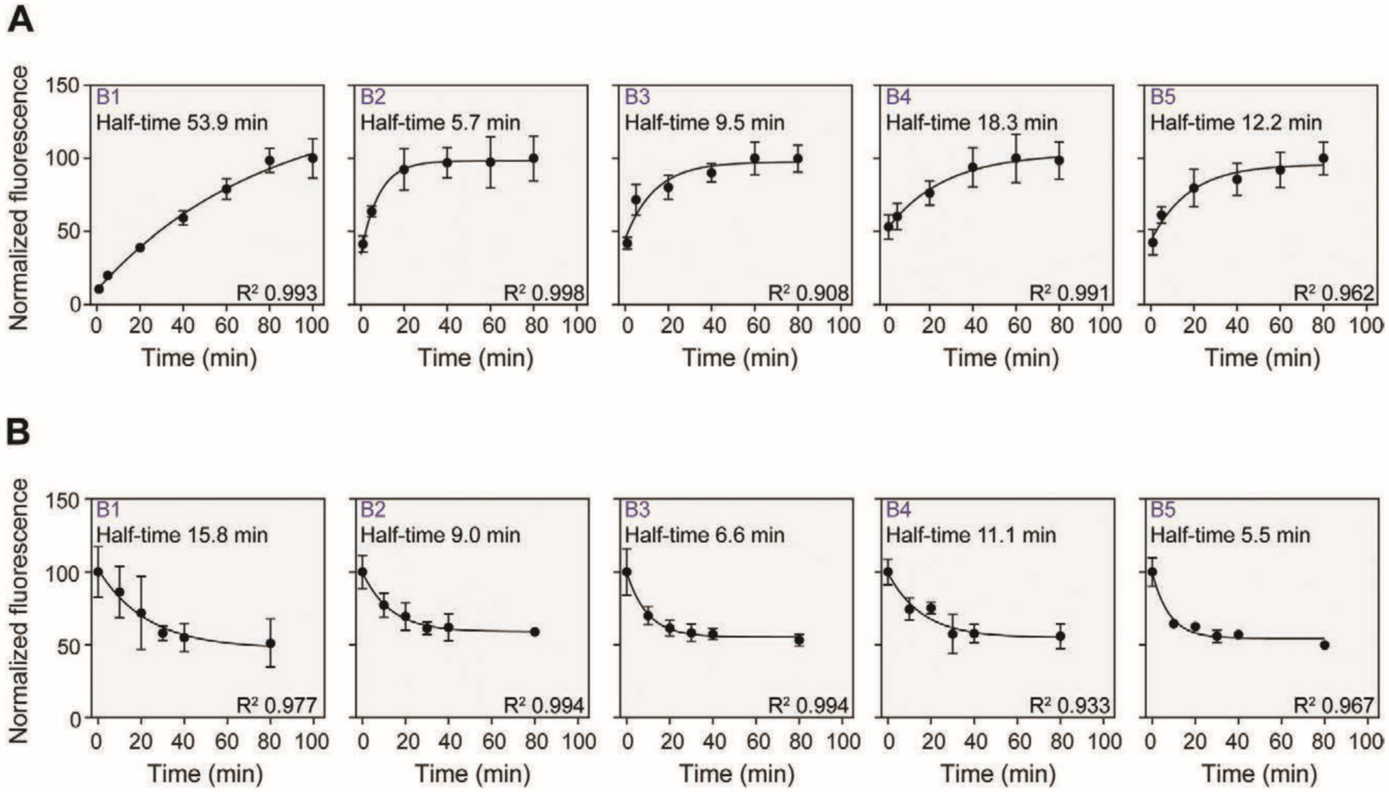

Figure 7. Study of DACCA-labeled NP fate. A) Time course of cell-associated fluorescence after the addition of 2 nmol mL^{-1} DACCA-labeled formulations. The data were normalized to the maximum fluorescence values (i.e., the plateau values reached). B) Time course of NP degradation observed after the monolayers were incubated with 2 nmol mL^{-1} DACCA-labeled formulations for 60 min. Both half-time and *R* squared values are shown. Note that **B1** exhibited different internalization as well as degradation kinetics compared to those of formulation **B3**, even when having the same hydrophilic/hydrophobic ratio as well as the same molecular weight.

more detail to come to any specific conclusions in terms of this phenomenon.

As mentioned above, a plateau in the cell-associated fluorescence was reached after 60–100 min of incubation with the DACCA-labeled formulations. Subsequently, a decrease in the cell-associated fluorescence values was observed (data not shown), as the enzymatic degradation of the DACCA-labeled matrix leads to quenching of its fluorescence.[27] Hence, to study the intracellular degradation kinetics, DACCA-labeled NPs (2 nmol mL^{-1}) were added to Mϕ monolayers and incubated for 60 min for each of the formulations tested. Subsequently, the cells were washed with PBS (i.e., time 0) and analyzed using flow cytometry at different time points (Figure 7B). The degradation rate constant values were determined by fitting the data to a single exponential decay model. The half-time of degradation was calculated as the ratio of ln 2 and the degradation rate constant.

In our recent study,[28] we suggested that there is a relationship between the lysosomal localization of a nanocarrier and its degradation kinetics in vitro. In other words, mPEO-*b*-PCL-based NPs with cytosolic localization within Raw 264.7 Mϕs exhibited slow intracellular degradation, and, vice versa, fast intracellular degradation was observed in the case of NPs colocalized with lysosomes, i.e., lipase-rich compartments.[51] It is evident from Figure 7B that all of the nanoformulations analyzed (i.e., **B1**, **B2**, **B3**, **B4**, and **B5**) revealed similar degradation patterns, probably because all of the samples exhibited similar colocalization within low-pH compartments. Similar to the uptake kinetics study, the P4HB-free sample **B1** was the most distinct, as it revealed the slowest degradation rate ($\tau_{1/2}$ of ≈16 min), which also suggests that the introduction of P4HB seems to be able to tune the biorelevant properties of the NPs. Similar to our recent study,[28] the flow cytometry results were not in line with the above-described ^{1}H NMR degradation study. This is probably because the ^{1}H NMR study was carried out in PBS only (i.e., without the presence of FBS or cell proteins), as protein-NP interactions play a crucial role in the biorelevant behavior. For the same reason, the flow cytometry results may be deemed to be more relevant, because they reflect interactions in biorelevant environments (i.e., in the presence of serum and intracellular proteins).

It is worth mentioning that enzymatic degradability suggests favorable behavior in vivo, as it can be assumed that the mPEO-*b*-(PCL-*co*-P4HB) copolymers undergo degradation to mPEO, 6-hydroxyhexanoic acid (the degradation product of PCL) and 4-hydroxybutyric acid. Both mPEO$_{44}$ (2000 Da) and mPEO$_{113}$ (5000 Da) do not exceed the threshold for the renal filtration of polymers 30–50 kDa.[52] The biocompatible 6-hydroxyhexanoic acid is converted to adipic acid by ω-oxidation in the endoplasmic reticulum of liver and kidney cells in vivo. Adipic acid is then metabolized by β-oxidation and the Krebs cycle to carbon dioxide and water.[53] Similarly, 4-hydroxybutyric acid is a ubiquitous molecule in vivo, derived both endogenously and exogenously and is catabolized by processes including β-oxidation to acetyl-CoA and glycolate, α-oxidation to 3-hydroxypropionate-CoA and formate, and cleavage of C-4 to yield 3-hydroxypropionate and carbon dioxide.[54]

© 2020 WILEY-VCH Verlag GmbH & Co. KGaA, Weinheim

4. Conclusions

The aim of this work was to describe, fundamentally characterize, and perform biorelevant analyses of biocompatible and biodegradable nanocarriers based on mPEO-*b*-(PCL-*co*-P4HB), where the γBL introduction would hopefully serve as a biorelevant behavior-controlling mechanism.

First, it has been shown that the copolymer composition of PCL-*co*-P4HB can be tuned not only by the feed ratio of the monomers but also by choosing a feasible catalyst. The difference in γBL incorporation was demonstrated when anionic or cationic catalysts were employed. A notable increase in incorporation was observed when anionic catalysis in a nonpolar environment were employed. The content of incorporated γBL was $\approx$30% when TBD was used as a catalyst of the copolymerization in toluene.

Additionally, we studied the biorelevant properties of P4HB-based nanocarriers. Their biocompatibility, cellular uptake, and degradation were evaluated. By combining flow cytometry and CLSM, we demonstrated that these nanocarriers can be internalized by macrophage-like cells in which the NPs underwent intracellular degradation. The influence of the presence of the γBL units on the biological behavior was observed. This method enabled control over the rate of degradation so that when the content of γ-butyrolactone increased, the rate of degradation increased.

Given our findings, this study provides a generalizable strategy for the future improvement of polyester nanobead-based interventions in application fields where fine-tuned properties are needed.

Supporting Information

Supporting Information is available from the Wiley Online Library or from the author.

Acknowledgements

Financial supports from the Czech Science Foundation (Grants Nos. 17-07164S and 17-09998S) the Ministry of Education, Youth and Sport of the Czech Republic (National sustainability program I, grant # POLYMAT LO1507) are gratefully acknowledged. T.U. and R.K. thank Dr. Sabina Nováková for her kind assistance with ^{1}H NMR analysis. J.T. acknowledges support from Charles University (Project No. SVV260440) and would like to thank Dr. Tomáš Mazel for his expert flow cytometry data fitting advice and Dr. Jakub Hraníček (Department of Analytical Chemistry, Faculty of Science, Charles University) for his kindness in assisting with the instrumentation necessary for fluorescence spectroscopy. D.R. and M.S. acknowledge support from the Scientific Grant Agency VEGA and the Slovak Research and Development Agency (Project Nos. 2/0177/17 and 16-0550). The authors would like to thank Ewa Pavlova, who performed the TEM measurements.

Conflict of Interest

The authors declare no conflict of interest.

Author Contributions

T.U. synthesized the polymers, carried out the physicochemical characterizations of both the polymers and nanoparticles, and wrote the paper. J.T. carried out the cytotoxicity and confocal microscopy experiments and wrote the paper. D.R. performed the AF4 experiments. K.G. performed the flow cytometry investigations. R.K. performed and evaluated the ^{1}H NMR analysis. M.Š. supervised the TEM investigations. M.S. supervised the AF4 experiments and evaluated the results. O.Š.J. supervised the flow cytometry investigations and cell-associated fluorescence data fitting. M.H. supervised the project and contributed to the final version of the paper.

Keywords

biodegradation, macrophages, nanomedicine, nanoparticles, γ-butyrolactone

Received: November 28, 2019
Revised: January 22, 2020
Published online:

[1] V. P. Torchilin, *Pharm. Res.* **2006**, *24*, 1.
[2] R. Palao-Suay, L. G. Gómez-Mascaraque, M. R. Aguilar, B. Vázquez-Lasa, J. S. Román, *Prog. Polym. Sci.* **2016**, *53*, 207.
[3] I. Schlachet, J. Trousil, D. Rak, K. D. Knudsen, E. Pavlova, B. Nyström, A. Sosnik. *Carbohydr. Polym.* **2019**, *212*, 412.
[4] A. C. Albertsson, I . K. Varma, *Biomacromolecules* **2003**, *4*, 1466.
[5] P. Markland, V. C. Yang, *Encyclopedia of Pharmaceutical Technology*, Vol. *1*, 3rd ed. (Ed: J. Swarbrick), Informa Helthcare USA, New York **2007**.
[6] L. S. Nair, C. T. Laurencin, *Prog. Polym. Sci.* **2007**, *32*, 762.
[7] T. Moore, R. Adhikari, P. Gunatillake, *Biomaterials* **2005**, *26*, 3771.
[8] A. Nakayama, N. Kawasaki, S. Aiba, Y. Maeda, I. Arvanitoyannis, N. Yamamoto, *Polymer* **1998**, *39*, 1213.
[9] D. P. Martin, S. F. Williams, *Biochem. Eng. J.* **2003**, *16*, 97.
[10] P. Olsén, K. Odelius, A. C. Albertsson, *Biomacromolecules* **2016**, *17*, 699.
[11] D. Myers, A. Cyriac, C. K. Williams, *Nat. Chem.* **2015**, *8*, 3.
[12] W. H. Carothers, *Chem. Rev.* **1931**, *8*, 353.
[13] F. Korte, W. Glet, *J. Polym. Sci, Part B: Polym. Lett.* **1966**, *4*, 685.
[14] K. Yamashita, K. Yamamoto, J.-i. Kadokawa, *Chem. Lett.* **2014**, *43*, 213.
[15] M. Hong, E. Y.-X. Chen, *Nat. Chem.* **2015**, *8*, 42.
[16] M. Hong, E. Y.-X. Chen, *Angew. Chem., Int. Ed.* **2016**, *55*, 4188.
[17] N. Zhao, C. Ren, H. Li, Y. Li, S. Liu, Z. Li, *Angew. Chem., Int. Ed.* **2017**, *56*, 12987.
[18] L. Lin, D. Han, J. Qin, S. Wang, M. Xiao, L. Sun, M. Yuezhong, *Macromolecules* **2018**, *51*, 9317.
[19] C.-J. Zhang, L.-F. Hu, H.-L. Wu, X.-H. Cao, X.-H. Zhang, *Macromolecules* **2018**, *51*, 8705.
[20] P. Walther, W. Frey, S. Naumann, *Polym. Chem.* **2018**, *9*, 3674.
[21] Y. Shen, Z. Zhao, Y. Li, S. Liu, F. Liu, Z. Li, *Polym. Chem.* **2019**, *10*, 1231.
[22] M. Hong, X. Tang, B. S. Newell, E. Y. X. Chen, *Macromolecules* **2017**, *50*, 8469.
[23] P. Walther, S. Naumann, *Macromolecules* **2017**, *50*, 8406.
[24] N. Dolan, D. P. Gavin, A. Eshwika, K. Kavanagh, J. McGinley, J. C. Stephens, *Bioorg. Med. Chem. Lett.* **2016**, *26*, 630.
[25] L. Luo, J. Tam, D. Maysinger, A. Eisenberg, *Bioconjugate Chem.* **2002**, *13*, 1259.
[26] S. Petrova, D. Klepac, R. Konefał, S. Kereïche, L. Kováčik, S. K. Filippov, *Macromolecules* **2016**, *49*, 5407.
[27] J. Trousil, S. K. Filippov, M. Hrubý, T. Mazel, Z. Syrová, D. Cmarko, S. Svidensk, J. Matějková, L. Kováčik, B. Porsch, R. Konefał, R. Lund, B. Nyström, I. Raškab, P. Štěpánek, *Nanomedicine* **2017**, *13*, 307.

© 2020 WILEY-VCH Verlag GmbH & Co. KGaA, Weinheim

[28] J. Trousil, Z. Syrová, N.-J. K. Dal, D. Rak, R. Konefał, E. Pavlova, J. Matějková, D. Cmarko, P. Kubíčková, O. Pavliš, T. Urbánek, M. Sedlák, F. Fenaroli, I. Raška, P. Štěpánek, M. Hrubý, *Biomacromolecules* **2019**, *20*, 1798.
[29] M. Bauer, C. Lautenschlaeger, K. Kempe, L. Tauhardt, U. S. Schubert, D. Fischer, *Macromol. Biosci.* **2012**, *12*, 986.
[30] P. Ralph, M. A. Moore, K. Nilsson, *J. Exp. Med.* **1976**, *143*, 1528.
[31] *Biological Evaluation of Medical Devices – Part 5: Tests for In Vitro Cytotoxicity*, International Organization for Standardization, Geneva, Switzerland **2009**.
[32] A. Duda, S. Penczek, P. Dubois, D. Mecerreyes, R. Jérôme, *Macromol. Chem. Phys.* **1996**, *197*, 1273.
[33] M. Danko, J. Mosnáček, *Polimery* **2017**, *62*, 272.
[34] A. Bhaw-Luximon, D. Jhurry, S. Motala-Timol, Y. Lochee, *Macromol. Symp.* **2005**, *231*, 60.
[35] M. Dionzou, A. Morère, C. Roux, B. Lonetti, J. D. Marty, C. Mingotaud, P. Joseph, D. Goudounèche, B. Payré, M. Léonettie, A.-F. Mingotaud, *Soft Matter.* **2016**, *12*, 2166.
[36] R. F. Domingos, M. A. Baalousha, Y. Ju-Nam, M. M. Reid, N. Tufenkji, J. R. Lead, G. G. Leppard, K. J. Wilkinson, *Environ. Sci. Technol.* **2009**, *43*, 7277.
[37] O. Sedlacek, B. D. Monnery, S. K. Filippov, R. Hoogenboom, M. Hruby, *Macromol. Rapid Commun.* **2012**, *33*, 1648.
[38] S. Agarwal, X. Xie, *Macromolecules* **2003**, *36*, 3545.
[39] A. Ianiro, J. Patterson, Á. González García, M. M. J. van Rijt, M. M. R. M. Hendrix, N. A. J. M. Sommerdijk, I. K. Voets, A. C. C. Esteves, R. Tuinier, *J. Polym. Sci., Part B: Polym. Phys.* **2018**, *56*, 330.
[40] S. Zolls, R. Tantipolphan, M. Wiggenhorn, G. Winter, W. Jiskoot, W. Friess, A. Hawe, *J. Pharm. Sci.* **2012**, *101*, 914.
[41] M. Ukawala, T. Rajyaguru, K. Chaudhari, A. S. Manjappa, S. Pimple, A. K. Babbar, R. Mathur, A. K. Mishra, R. S. Murthy, *Drug Delivery* **2012**, *19*, 155.
[42] Z. Zhang, Q. Qu, J. Li, S. Zhou, *Macromol. Biosci.* **2013**, *13*, 789.
[43] K. Kolouchova, O. Sedlacek, D. Jirak, D. Babuka, J. Blahut, J. Kotek, M. Vit, J. Trousil, R. Konefał, O. Janouskova, B. Podhorska, M. Slouf, M. Hruby, *Biomacromolecules* **2018**, *19*, 3515.
[44] P. Grossen, D. Witzigmann, S. Sieber, J. Huwyler, *J. Controlled Release* **2017**, *260*, 46.
[45] P. Grossen, G. Québatte, D. Witzigmann, C. Prescianotto-Baschong, L.-H. Dieu, J. Huwyler, *J. Nanomater.* **2016**, *2016*, 13.
[46] J. Jin, B. Sui, J. Gou, J. Liu, X. Tang, H. Xu, Y. Zhang, X. Jin, *PLoS One* **2014**, *9*, e112200.
[47] Y. Pei, Y. Yeo, *J. Controlled Release* **2016**, *240*, 202.
[48] S. M. Abaza, *Parasitol. United J.* **2016**, *9*, 1.
[49] I. Vainshtein, L. K. Roskos, J. Cheng, M. A. Sleeman, B. Wang, M. Liang, *Pharm. Res.* **2015**, *32*, 286.
[50] S. Behzadi, V. Serpooshan, W. Tao, M. A. Hamaly, M. Y. Alkawareek, E. C. Dreaden, D. Brown, A. M. Alkilany, O. C. Farokhzad, M. Mahmoudi, *Chem. Soc. Rev.* **2017**, *46*, 4218.
[51] M. J. Czaja, A. M. Cuervo, *Autophagy* **2009**, *5*, 866.
[52] M. E. Fox, F. C. Szoka, J. M. J. Fréchet, *Acc. Chem. Res.* **2009**, *42*, 1141.
[53] A. Orchel, K. Jelonek, J. Kasperczyk, Z. Dzierzewicz, *Acta Pol. Pharm.* **2010**, *67*, 710.
[54] S. Sadhukhan, G.-F. Zhang, G. P. Tochtrop, *ACS Chem. Biol.* **2014**, *9*, 1706.

© 2020 WILEY-VCH Verlag GmbH & Co. KGaA, Weinheim

PUBLICATION P4

Halamish M. H.[‡], **Trousil J.**[‡], Rak D., Knudsen D. K., Pavlova E., Nyström B., Štěpánek P., Sosnik A. Self-assembly and nanostructure of poly(vinyl alcohol)-graft-poly(methyl methacrylate) amphiphilic nanoparticles. *Journal of Colloid and Interface Science*. 2019, 553, 512–523. IF = 6.36

H.M.H. synthesized the copolymer, carried out its physicochemical characterization and wrote the paper. J.T. conceptualized the study of NPs' structure, carried out GPC, DLS, and SLS experiments and wrote the paper. D.R. carried out the AFFFF experiments and contributed to the final version of the paper. E.P. carried out the TEM investigations. K.D.K. and B.N. carried out the SANS investigations and contributed to the final version of the paper. P.Š. contributed to the final version of the paper. A.S. supervised the project, conceptualized the experiments, and wrote the paper.

[‡] Authors contributed equally to this work.

Journal of Colloid and Interface Science 553 (2019) 512–523

Contents lists available at ScienceDirect

Journal of Colloid and Interface Science

journal homepage: www.elsevier.com/locate/jcis

Regular Article

Self-assembly and nanostructure of poly(vinyl alcohol)-*graft*-poly-(methyl methacrylate) amphiphilic nanoparticles

Hen Moshe Halamish [a,1], Jiří Trousil [b,c,1], Dmytro Rak [d], Kenneth D. Knudsen [e], Ewa Pavlova [b], Bo Nyström [f], Petr Štěpánek [b], Alejandro Sosnik [a,*]

[a] *Laboratory of Pharmaceutical Nanomaterials Science, Department of Materials Science and Engineering, Technion-Israel Institute of Technology, Haifa, Israel*
[b] *Institute of Macromolecular Chemistry, Czech Academy of Sciences, Prague, Czechia*
[c] *Department of Analytical Chemistry, Charles University, Faculty of Science, Prague, Czechia*
[d] *Institute of Experimental Physics, Slovak Academy of Sciences, Košice, Slovakia*
[e] *Department of Physics, Institute for Energy Technology, Kjeller, Norway*
[f] *Department of Chemistry, University of Oslo, Oslo, Norway*

GRAPHICAL ABSTRACT

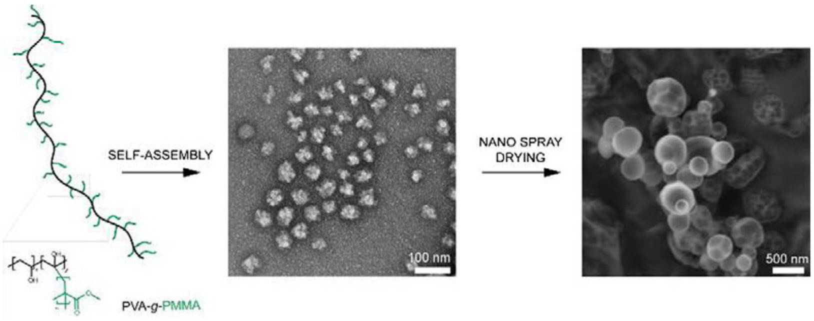

ARTICLE INFO

Article history:
Received 10 April 2019
Revised 14 June 2019
Accepted 15 June 2019
Available online 17 June 2019

Keywords:
Poly(vinyl alcohol)-poly(methyl methacrylate) amphiphilic nanoparticles
Polymer self-assembly
Asymmetric flow field-flow fractionation (A4F)
Small-angle neutron scattering (SANS)
Nano spray-drying

ABSTRACT

Hypothesis: Poly(vinyl alcohol)-g-poly(methyl methacrylate) (PVA-g-PMMA) amphiphilic copolymers self-assemble to form multi-micellar colloidal systems.
Experiments: A PVA-g-PMMA copolymer containing 16–17% w/w of PMMA was synthesized by the free radical graft polymerization of methyl methacrylate on a PVA backbone by utilizing cerium(IV) ammonium nitrate as initiator and tetramethylethylenediamine (TEMED) as initiation activator. The aggregation behavior of the copolymer in water was comprehensively characterized by dynamic light scattering (DLS) and static light scattering (SLS), small angle neutron scattering (SANS), asymmetrical flow field-flow fractionation (A4F) and transmission electron microscopy (TEM). The colloidal stability before and after non-covalent crosslinking of PVA domains with boric acid was assessed by DLS. Finally, nanoparticles were nano spray-dried.
Findings: This copolymer self-assembles in water to form a complex nanostructure of low aggregation number particles (ca. 12–15 nm in diameter) that aggregate into larger ones with size ca. 60–80 nm, as determined by SANS and TEM. In addition, boric acid-crosslinking preserves the nanoparticle size, while conferring full physical stability under extreme dilution conditions. Nano spray-drying consolidates the crosslnking and enables the production of a dry flowing powder that upon re-dispersion in water regenerates the nanoparticles without major size changes.

© 2019 Elsevier Inc. All rights reserved.

---

* Corresponding author.
E-mail address: sosnik@technion.ac.il (A. Sosnik).
[1] Authors equally contributed to this work.

https://doi.org/10.1016/j.jcis.2019.06.047
0021-9797/© 2019 Elsevier Inc. All rights reserved.

1. Introduction

Amphiphilic polymeric nanoparticles are colloidal systems formed by the self-aggregation of amphiphilic polymers above a critical concentration or temperature and based on their molecular structure and architecture, the array of hydrophilic and hydrophobic domains can vary [1,2]. For example, polymeric micelles display a well-defined core-corona structure [3,4], while polymersomes are vesicular nanoparticles with an aqueous core enclosed by a polymeric bilayer [5]. Owing to a great chemical versatility, polymeric micelles became one of the most valuable colloidal platforms for the encapsulation, delivery and targeting of lipophilic drugs [6]. Sosnik and coworkers pioneered the use of polymeric micelles in oral and other mucosal drug delivery strategies [7–9]. However, to enhance their interaction with mucus, features such as size, colloidal stability, and surface chemistry need to be properly tailored [10]. In addition, the encapsulation capacity is not only governed by the properties of the polymeric micelle and the same nanoparticle can display from excellent to very poor performance, depending on the structure, the lipophilicity and the functional groups of the cargo and the encapsulation method.

We recently engineered a type of amphiphilic colloidal drug delivery system that combines novel molecular architectures with improved physical stability by using mild selective chemical pathways [11,12]. The general synthetic rationale relies on the modification of the side-chain of a multifunctional hydrophilic polymeric backbone by graft polymerization of hydrophobic blocks to confer self-assembly properties. Then, non-covalent crosslinking of the hydrophilic domains is performed to prevent disassembly upon extreme dilution conditions in the biological medium and interaction with proteins. The feasibility of this strategy was for example demonstrated by the hydrophobization of the polysaccharide chitosan and the polyol poly(vinyl alcohol) (PVA) with thermo-responsive poly(*N*-isopropylacrylamide) (PNiPAAm) blocks and crosslinking with tripolyphosphate and boric acid, respectively [11,12]. The produced colloids show hydrodynamic diameter in the 150–400 nm range and good mucoadhesion *in vitro* [11,12]. After confirming their good cell compatibility, the ability of chitosan-made nanoparticles to cross mucosal barriers *in vitro* was also confirmed [13,14]. PVA is a very appealing biomaterial for the design of drug delivery systems because it is mucoadhesive, displays good cell and biocompatibility (e.g., in tissue engineering applications) and has been approved in different pharmaceutical products for administration by various routes [15–17].

On one hand, self-assembly of graft copolymers could be adjusted by controlling the weight ratio of the hydrophilic and hydrophobic components, their length and density and the intrinsic hydrophobicity of the tethered side-chains [18,19]. On the other, as opposed to linear block copolymers, their aggregation behavior is of more difficult prediction because of changes in the flexibility of the polymer backbone and steric constraints of hydrophobic segments of variable length and grafting density [20,21].

Herein, we report on the synthesis and the aggregation of an amphiphilic graft copolymer composed of PVA and poly(methyl methacrylate) (PMMA). Upon self-assembly in aqueous medium, the copolymer forms amphiphilic nanoparticles with a complex nanostructure characterized by the association of low aggregation number particles into larger ones, as determined by small-angle neutron scattering (SANS) and transmission electron microscopy (TEM). Crosslinking of PVA domains with boric acid preserves the nanoparticle size, while conferring physical stability under extreme dilution. Furthermore, nano spray-drying enables the production of dry flowing powders and consolidates the crosslinked PVA network without any detrimental effect on the nanoparticle size upon re-dispersion in water.

2. Experimental section

2.1. Materials

PVA (Mowiol® 4–88, weight-average molecular weight of 31,000 g/mol, 87–89% hydrolysis, Sigma-Aldrich, St. Louis, MO, USA), cerium(IV) ammonium nitrate (CAN, Strem Chemicals, Newburyport, MA, USA), tetramethylethylenediamine (99%, TEMED, Alfa Aesar, Heysham, England), hydroquinone (Merck, Hohenbrunn, Germany), nitric acid 70% (Bio-Lab, Jerusalem, Israel) and boric acid (Bio-Lab) were used as received. Methylmethacrylate (MMA) (99% purity, Alfa Aesar) was distilled under vacuum to remove inhibitors before use. MilliQ water (18.2 MΩ.cm at RT) was obtained from a Barnstead Smart2Pure 12L UV/UF water purification system (Thermo Electron LED GmbH, Niederelbert, Germany).

2.2. Synthesis of PVA-g-PMMA copolymer

PVA (0.4 g) was dissolved in distilled water (100 mL) at room temperature (RT) under gentle magnetic stirring. TEMED (0.18 mL) and nitric acid 70% (0.45 mL) were diluted in distilled water (50 mL) as well. The two solutions were degassed in two separate containers using an ultrasonic bath (Elmasonic S30, Elma Schmidbauer GmbH, Singen, Germany) at RT (30 min), mixed and purged with N_2 (30 min) at RT under magnetic stirring. At this stage, the original 70% w/w nitric acid (0.45 mL) undergoes a 1:333 dilution (0.45 mL of nitric acid in a total of 150 mL of aqueous medium) to a concentration of 0.21% w/w. Then, distilled MMA (0.133 g) was dispersed in degassed water (48 mL) and injected into the solution containing PVA, TEMED and nitric acid utilizing a syringe through a septum. The reaction mixture was heated to 35 °C and CAN (0.66 g) dissolved in degassed water (2 mL) was added to the reaction mixture. The final nitric acid concentration during the free radical graft polymerization was 0.16% w/w. The reaction was continued for 2 h at 35 °C and then, quenched with hydroquinone dissolved in water. The crude aqueous solution was dialyzed against water for three days with frequent water exchanges (regenerated cellulose dialysis membranes, MWCO of 12–14 kDa, Spectra/Por® 4 Dialysis Membrane; Spectrum Chemical MFG, New Brunswick, NJ, USA), frozen in liquid N_2 and freeze-dried (Labconco Free Zone 4.5 plus L Benchtop Freeze Dry System, Labconco, Kansas City, MO, USA). The copolymer prepared under these conditions contained 16–17% w/w of PMMA (average of at least five reactions), as quantified by proton-nuclear magnetic resonance (^{1}H NMR, see below). A blank reaction was carried out following the same procedure with the exception that MMA was not added to the reaction mixture. This product is referred as CAN-treated PVA.

2.3. Characterization of the copolymer

2.3.1. Proton- and Carbon-Nuclear magnetic resonance spectroscopy

^{1}H NMR and ^{13}C NMR spectra of pure PVA, CAN-treated PVA and the PVA-g-PMMA copolymer were acquired in a 400-MHz Bruker® Avance III high Resolution spectrometer (Bruker BioSpin GmbH, Rheinstetten, Germany) and Spinworks 4.0 software (University of Manitoba, MB, Canada) using 5% w/v solutions in DMSO d_6 as solvent (Cambridge Isotope Laboratories, Andover, MA, USA). The DMSO signal (at 2.5 and 39.5 ppm for ^{1}H- and ^{13}C NMR, respectively) was used as internal standard. The PMMA weight content in the graft copolymer (%PMMA) was determined using a calibration curve built by integrating the characteristics ^{1}H NMR peaks of each component in PVA:PMMA physical mixtures containing growing weight ratios (1:2, 1:1, 2:1, 3:1, 4:1, 5:1 and 6:1) (Fig. S1). The ratio between the integration of the peak of —OCH_3 groups of PMMA at 3.6 ppm and the signal of —CH— of PVA at 3.9 ppm for the copolymer was interpolated in the calibration curve and the percentage of grafting (%Grafting) was calculated from Eq. (1)

$$\%\text{Grafting} = \%\text{PMMA}/(100 - \%\text{PMMA}) \times 100 \tag{1}$$

2.3.2. Fourier Transform Infrared spectroscopy

Fourier Transform Infrared Spectroscopy (FTIR) spectra of pure PVA, CAN-treated PVA and the PVA-g-PMMA copolymer were recorded using an Equinox 55 spectrometer (Bruker Optics, Inc., Ettlingen, Germany) from 4000 to 500 cm^{-1} (32–64 scans with a resolution of 4 cm^{-1}) at RT using KBr (Merck KGaA, Darmstadt, Germany) disks produced under pressure. The KBr:sample weight ratio was 3:0.01. Spectra were obtained with Bruker OPUS 6.5 spectrum software (Bruker Optics, Inc.).

2.3.3. Gel permeation chromatography

The number-average molecular weight (M_n), weight-average molecular weight (M_w), and dispersity $Đ$ (M_w/M_n) of pure PVA, CAN-treated PVA and the PVA-g-PMMA copolymer was analyzed by gel permeation chromatography (GPC) using a Deltachrom pump (Watrex Ltd., Prague, Czechia), Midas Spark autosampler (DataApex Ltd., Prague, Czechia) and Reprosil *SEC* 4000 (30 × 0.8 cm, pore size 45 nm, Dr. Maisch GmbH, Ammerbuch-Entringen, Germany). Two detectors were used, namely multiangle light scattering (MALS) DAWN EOS and refractive index (RI) both of Wyatt Technology Corp. (Santa Barbara, CA, USA). DMSO (supplemented with 0.1% LiBr, Sigma-Aldrich) was used as the mobile phase and the injection volume was 0.1 mL. GPC separations were performed at a mobile phase flow rate of 0.12 mL/min. Refractive index increment d*n*/d*c* values were measured using a BI-DNDCW differential refractometer (Brookhaven Instrument Corp., Holtsville, NY, USA). The d*n*/d*c* value was obtained using calibration solutions of KCl (0.5–5 mg/mL).

2.3.4. Critical aggregation concentration

The critical aggregation concentration (CAC) of the PVA-g-PMMA copolymer was determined at 25 and 37 °C utilizing dynamic light scattering (DLS, Zetasizer Nano-ZS, Malvern Instruments, Malvern, UK) with 4Mw He-Ne laser ($\lambda = 633$ nm), digital correlator ZEN3600 and Non-Invasive Back Scatter (NIBS®) technology at scattering angle of 173° to the incident beam and data analyzed using CONTIN algorithms (Malvern Instruments). For this, a stock solution (10 mg/mL) of the copolymer was diluted in water under magnetic stirring at room temperature to obtain a series of solutions ranging from 0.001 to 5 mg/mL. Then, samples were incubated at the corresponding temperature for 12 h and analyzed by DLS. Data of each dilution was the result of six runs and in each run eleven repetitions. The intensity of the scattered light (expressed in kilo counts per second, kcps) was plotted as a function of the concentration and the CAC established as the intersection between the two straight lines and expressed in mg/mL.

2.4. Production and crosslinking of PVA-g-PMMA nanoparticles

The PVA-g-PMMA copolymer was solubilized in distilled water (0.8 mg/mL) and left at room temperature for 12 h to allow the self-assembly. For physical stabilization, PVA domains in the amphiphilic nanoparticle were crosslinked with boric acid. For this, boric acid solution (4 µL, 50 mg/mL) was added to the nanoparticle dispersion (1 mL) and the solution incubated at room temperature for 12 h. To conduct SANS (see below) analysis, samples were prepared as mentioned above at a concentration of 5 mg/mL in deuterium oxide (D_2O, Sigma-Aldrich Ltd., Prague, Czechia). The nanoparticle preparation was carried out with or without filtration through a Chromafil® PVDF syringe filter (0.22 µm, Macherey-Nagel GmbH & Co. KG, Düren, Germany), as referred in the Section 3.

2.5. Nanoparticle characterization

2.5.1. Light scattering

The size (hydrodynamic diameter, D_h) and size distribution (polydispersity index, PDI) of the nanoparticles before and after crosslinking was characterized by DLS, static light scattering (SLS) and electrophoretic light scattering (ELS), at 25 °C. Initially, samples were characterized by means of DLS and SLS in an ALV-6010 instrument (ALV-GmbH, Langen, Germany) with a 22 mW He–Ne laser in the angular range 30–150°. The relaxation time (τ) values-providing algorithm REPES [22] were used for the correlation functions obtained analysis. The hydrodynamic diameter (D_h) values were obtained from the Stokes-Einstein Eq. (2)

$$D = \frac{\mathrm{k_B}T}{3\pi\eta D_\mathrm{h}}, \tag{2}$$

where T is absolute temperature, η is the viscosity of the solvent and $\mathrm{k_B}$ is the Boltzmann constant [23]. SLS data were analyzed using the Zimm Eq. (3)

$$\frac{Kc}{R(q)} = \frac{1}{M_\mathrm{w}} + \frac{D_\mathrm{g}^2 q^2}{12M_\mathrm{w}^\mathrm{NPs}}, \tag{3}$$

where K is an optical constant, c is the concentration of the copolymer, $R(q)$ is the Rayleigh ratio of the scattering intensity, q is the scattering vector defined as $q = (4\pi n/\lambda)\sin(\theta/2)$, n is the refractive index of the solvent, θ is the scattering angle, λ is the wavelength in vacuum, $M_w{}^{\mathrm{NPs}}$ is the weight-average molar mass of the particles, and D_g is the diameter of gyration. The refractive index increment d*n*/d*c* was measured as mentioned below. The aggregation number (N_agg) of the nanoparticles was calculated according to Eq. (4)

$$N_\mathrm{agg} = \frac{M_\mathrm{w}^\mathrm{NPs}}{M_\mathrm{w}}, \tag{4}$$

where M_w is the GPC-measured molecular weight of the copolymer and $M_w{}^{\mathrm{NPs}}$ is the molecular weight of the nanoparticles, as determined by SLS.

The colloidal stability of the nanoparticles was assessed also by DLS (see above) at a sample concentration of 0.8 mg/mL and 25 °C. Data were analyzed using the Zetasizer Software (7.10, Malvern Instruments). For data representation, the mean positions of the peaks within the intensity-D_h distributions were used. In addition, PVA-g-PMMA nanoparticles (0.8 mg/mL) were crosslinked with boric acid as described above, incubated overnight at RT, diluted to final concentration of 0.08 mg/mL, which is below the measured CAC, and incubated at the same temperature for one more week. After one week, samples were reanalyzed by DLS. Then, a new dilution to a final concentration of 0.008 mg/mL was carried out and the size was monitored by DLS over five more weeks and compared to the size measured immediately after preparation. A non-crosslinked sample was used as control. Zeta-potential (ζ, mV) measurements were carried out using the same instrument. Each measurement was carried out in triplicate and each value obtained is expressed as mean ± S.D.

2.5.2. Asymmetric flow field-flow fractionation

AF4 experiments were carried out on an Eclipse 3+ Separation System (Wyatt Technology Europe, Dernbach, Germany) coupled with a 1260 Infinity isocratic pump and 1260 Infinity degasser (Agilent Technologies), MALS detector DAWN HELEOS II equipped with a 120 mW gallium-arsenide laser at a wavelength of 661 nm (Wyatt Technology), and RI detector RI-101 (Shodex, Munich, Germany). Samples were fractionated in a 275 mm long channel assembled with 490 μm spacer and 5 kDa cut-off regenerated cellulose membrane. Deionized water filtered through 0.2 μm membrane filter was used as a carrier liquid. Collection and processing of data were carried out by using Astra 6 software (version 6.1.7.17, Wyatt Technology).

Non-crosslinked PVA-g-PMMA and boric acid-crosslinked PVA-g-PMMA nanoparticles were analyzed using the procedure described below. One hundred microliters of the sample diluted to 0.1 mg/mL was manually injected at a flow rate of 0.2 mL/min through a Rheodyne 7725(i) injection valve (Rheodyne, Rohnert Park, CA, USA). The sample was focused for 5 min at the crossflow of 3.0 mL/min. After focusation, the system was switched to elution mode and the sample was fractionated under a constant crossflow of 3.0 mL/min (5 min) followed by linear decrease to 0.1 mL/min during 5 min and constant crossflow of 0.1 mL/min for 20 min. Then, the crossflow was turned off and the channel flushed (10 min). A constant detector flow rate of 0.5 mL/min was maintained during the separation. The molar mass (M_w) and the R_g were calculated from the acquired data using the Zimm Equation (see above). The refractive index increment dn/dc used in the calculations was 0.166 mL/g for both samples.

2.5.3. Small-angle neutron scattering

For SANS analysis, the wavelength resolution ($\Delta\lambda/\lambda$) was 10%. A pin-hole geometry with an input collimator of 8.0 or 18.4 mm diameter and a circular 7 mm sample aperture was used to define the beam divergence. Three independent measurements were conducted for each complete scattering curve, using wavelength-distance combinations of 5.1 Å/1.0 m, 5.1 Å/3.4 m, and 10.2 Å/3.4 m. This resulted in a q-range for the experiment of 0.006–0.35 Å^{-1}, where $q = (4\pi/\lambda)\sin(\theta/2)$. Specimens were poured into quartz cuvettes with 2 mm path length (Starna Scientific Ltd., Essex, UK). These were mounted in a copper-base for good thermal contact with the temperature-controlled sample stage. The temperature was maintained to within ±0.1 °C at each target temperature. D_2O was used as solvent to have good contrast and low background. Prior to analysis, raw data were properly reduced by incorporating results collected from the empty cell and the blocked-beam background, and taking into account also transmission corrections. Measurements were subsequently normalized to the beam monitor of the incoming beam, hence accounting for possible variations in the incoming flux. As a last step, data were transformed to absolute scale (coherent differential cross section ($d\Sigma/d\Omega$) in units of cm^{-1}), via open beam measurements, and radially averaged to produce the final scattering profile.

For the case of a spherical particle model, the SANS model curve can generally be represented by Eq. (5)

$$I(q) = \frac{N}{V}(\Delta\rho)^2 V_p^2 P(q) S(q), \tag{5}$$

where P(q) is the particle form factor and S(q) is the particle structure factor, V_p is the particle volume, N/V is the number of particles per volume unit V and $\Delta\rho$ is the difference in scattering length density (SLD) between the particle and the surrounding solvent (scattering contrast). Due to the low concentration used in these measurements, one can assume non-interacting particles, for which case $S(q) = 1$. Eq. (6) gives the form factor $P(q)$ for homogenous spherical objects with a radius R

$$P(q) = \left[\frac{3}{(qR)^3}\{\sin(qR) - qR\cos(qR)\}\right]^2 \tag{6}$$

The SLD values of PMMA, PVA and D_2O are 1.07×10^{-6} [24], 0.72×10^{-6} [25] and 6.36×10^{-6} Å^{-2}, respectively.

Given the TEM results (see below), we also utilized the Beaucage model that describes entities with different characteristic sizes that coexist in the same sample. This model was found to give a good representation of several systems that are based on individual particles with a certain polydispersity that cluster together into larger structures with varying overall characteristic radii [26,27]. As evident from Eq. (7), the basic version of this function (1-level) is the combination of a Guinier term describing a characteristic size R_g plus a power-law term describing the scattering of the tail of the pattern (G and B give the overall scaling of the intensity for each of these two terms).

$$I(q) = G\exp\left(\frac{-q^2R_g^2}{3}\right) + B\left\{\left[\mathrm{erf}\left(\frac{qR_g}{\sqrt{6}}\right)\right]^3/q\right\}^\alpha \tag{7}$$

where α is a power law exponent and "erf" is the standard error function.

2.5.4. Transmission electron microscopy

The shape and nanostructure of the colloidal system were visualized using a TEM microscope Tecnai G2 Spirit Twin 12 (FEI, Brno, Czechia) under bright-field imaging mode at an accelerating voltage value of 120 kV. Samples for TEM imaging were prepared as follows. Each sample to be tested was dropped (4 μL, 0.8 mg/mL) onto a microscopic Cu TEM grid (300 mesh) coated with a thin and electron-transparent carbon film. The sample excess was removed using a filter paper (fast drying method) after 15 min. This was performed to minimize oversaturation during the drying process [28]. After this, samples were negatively stained with a solution of uranyl acetate (2% w/v, Electron Microscopy Sciences, Hatfield, PA, USA). For this, the solution was dropped onto the dried grid and removed as mentioned before and the sample was finally allowed to dry at RT. In order to confirm the TEM-observed morphology and rule out possible artifacts during sample preparation, one chosen sample was additionally inspected by utilizing cryogenic-TEM (cryo-TEM). For this, 3 μL of the sample was dropped onto a grid covered with a holey carbon supporting film (Electron Microscopy Sciences). The grid used was hydrophilized immediately before the experiment by glow discharge (Expanded Plasma Cleaner, Harrick Plasma, Ithaca, NY, USA). The solution excess was removed using a piece of filter paper (blotting for 1 s). Subsequently, the grid was plunged into liquid ethane (−181 °C) and the vitrified sample was then transferred to a TEM equipped with a cryo-holder using a cryo-transfer holder (Gatan Inc., Pleasanton, CA, USA) and visualized at −173 °C (accelerating voltage of 120 kV).

2.6. Spray-drying

A suspension of PVA-g-PMMA nanoparticles (1 mg/mL) was spray-dried in a Nano Spray Dryer Büchi B-90 HP (Büchi Labortechnik AG, Flawil, Switzerland) using an open loop configuration that is feasible for aqueous systems. After optimization of the process conditions, we utilized 110 °C inlet temperature, 80% spraying, 30 mbar pressure, 112 kHz frequency, 90% feeding rate and 125 L/min airflow rate. Collected samples were characterized utilizing high-resolution scanning electron microscopy (HR-SEM, Zeiss Ultra-Plus FEG-SEM, Carl Zeiss NTS GmbH, Oberkochen, Germany) equipped with energy dispersive spectroscopy (EDS, active area of 80 mm^2) and In-lens secondary electrons detectors with an energy resolution of 127 eV Oxford Instruments, High Wycome, UK). Samples were prepared on carbon tape. Then, dry powders were re-dispersed in the original volume of water and re-characterized by DLS.

3. Results and discussion

Colloids have become valuable platforms to improve the biological performance of drugs by different administration routes. Among them, polymeric micelles are the most popular and clinically relevant of the polymer-based ones [6]. However, a better understanding of the self-assembly behavior of the polymeric amphiphile and the nanostructure of the formed particle are crucial to anticipate the drug encapsulation and release performance and the interaction of the colloidal system with the biological milieu (e.g., mucosal tissues, cells). Regardless of the broad use of comb-type amphiphilic copolymers in the production of particles, the inner array of hydrophilic and hydrophobic blocks has not been thoroughly investigated. A priori, the formation of more complex nanostructures than in the case of linear or branched block copolymers that upon aggregation usually result in well-defined core-corona micelles could be anticipated. In this work, we investigated the self-aggregation of an amphiphilic PVA-g-PMMA copolymer by utilizing a set of powerful and complementary analytical techniques.

3.1. Synthesis of the copolymer

Aiming to confer amphiphilic nature and self-assembly features to a hydrophilic PVA backbone, we grafted PMMA blocks by the free radical graft polymerization in aqueous medium using CAN as initiator and TEMED as activator, at 35 °C for 2 h (Fig. 1).

The product purification was carried by dialysis in water and freeze-dried and the synthesis yield was ~75%. PVA was selected as hydrophilic template because it has been described as mucoadhesive through the formation of H bonds with mucin and it is an approved pharmaceutical excipient with excellent biocompatibility. For instance, PVA has been categorized as “Generally Recognized as Safe” (GRAS) by the US-Food and Drug Administration (FDA) and thus, there are no major restrictions for oral administration [17,29]. Moreover, PVA forms very stable non-covalently crosslinked gels with boric acid [30]. As opposed to the previously reported PVA-g-PNiPAAm copolymers that become amphiphilic and undergo aggregation only above the lower critical solution concentration of PNiPAAm (30–35 °C) [12], in this work, we grafted PMMA hydrophobic blocks because this polymer is not thermo-responsive and we anticipated the formation of self-assembled nanoparticles also at room temperature. Furthermore, PMMA has been approved as pharmaceutical for oral drug delivery systems [31,32] and in chronic biomedical implants and combination products such as intraocular lenses, bone cements fixation devices and fillers and vertebrae stabilization in osteoporotic patients and their medicated versions [33–35]. Since previous studies demonstrated the scission of the PVA backbone in the presence of CAN due to the oxidation of diol units present along the polyol chain [36–38], we also conducted a blank reaction that contained all the reagents with the exception of MMA, and the product was purified by dialysis and characterized by the same techniques utilized for the characterization of the PVA-g-PMMA copolymer.

3.2. Copolymer characterization

Fig. 1A presents ^{1}H NMR spectra of pure PVA, CAN-treated PVA and the corresponding graft copolymer. PVA presents characteristic peaks at 4.5, 3.9 and 3.2 ppm due to —OH pendant moieties, and —CH— and —CH_2— of the polymer backbone, respectively. PVA exposed to a blank reaction without the addition of MMA showed identical spectrum (Fig. 1A). As expected, PVA-g-PMMA presented signals of both PVA and PMMA (—CH_3 at 0.73 and 0.93 ppm and of —OCH_3 at 3.6 ppm) [14,39]. To confirm the grafting of PMMA blocks to the PVA backbone, PVA, CAN-treated PVA and the copolymer were also analyzed by ^{13}C NMR. All the samples showed two triplets of PVA at 45.3 and 65.9 ppm and peaks of poly (vinyl acetate) at 21.0, 169.7 and 170.1 ppm. In addition, the copolymer exhibited the appearance of new peaks of PMMA at 43.9 and 51.6 ppm that were absent in PVA (Fig. 1B). These findings were in good agreement with previous reports [40]. In addition, the PMMA content was 16–17% w/w (%Grafting of 120%), as calculated by interpolating the integration ratio between the ^{1}H NMR signals at 3.9 and 3.6 ppm of PVA and PMMA, respectively, in a calibration curve built using different PVA:MMA physical mixtures (Table S1, Fig. S1).

The grafting of PMMA was confirmed by FTIR. The spectrum of pure PVA and the counterpart exposed to a blank reaction presented characteristic peaks of O—H stretching at 3430 cm^{-1} and C—H stretching and bending of the methylene group at 2900 and 1450 cm^{-1}, respectively, and of C=O stretching of carbonyl bond of acetyl moieties 1725–1727 cm^{-1} (Fig. 2C). It is noteworthy that exposure PVA to the reaction conditions did not substantially affect the relative intensity of the bands, suggesting that a major change in the degree deacetylation did not take place. In PVA-g-PMMA, the band of PMMA carbonyl shifted to 1734 cm^{-1} and its relative intensity increased owing to its overlapping with the one belonging to C=O of PVA acetyl groups. In addition, the copolymer showed a new band at 1200 cm^{-1} of C—O—C stretching of —O—CH_3 and the total disappearance of the peak of pure MMA at 1638 cm^{-1} (stretching of C=C), confirming that there was no residual monomer in the final product (Fig. 2C) [14,39]. Finally, pure PVA, CAN-treated PVA and the PVA-g-PMMA copolymer were also analyzed by GPC using LiBr-supplemented DMSO as the mobile phase. Pure PVA revealed M_w and M_n of 23,000 and 20,000 g/mol ($Đ$ of 1.15), respectively, which is lower than the molecular weight reported by the supplier (Table S1, Fig. 2D).

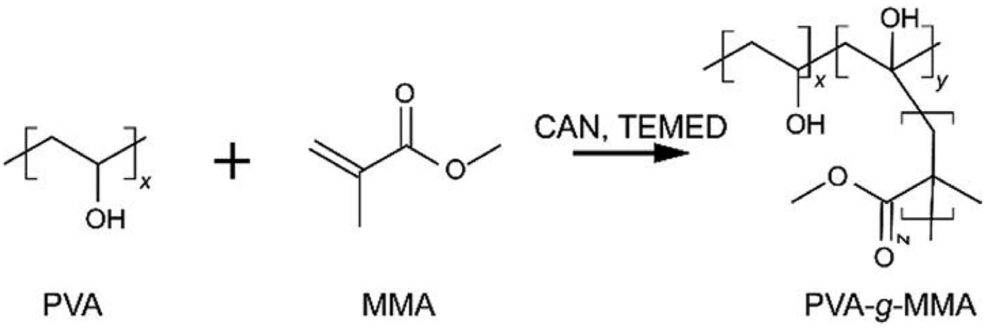

Fig. 1. Synthetic pathway of the PVA-g-PMMA copolymer.

P4

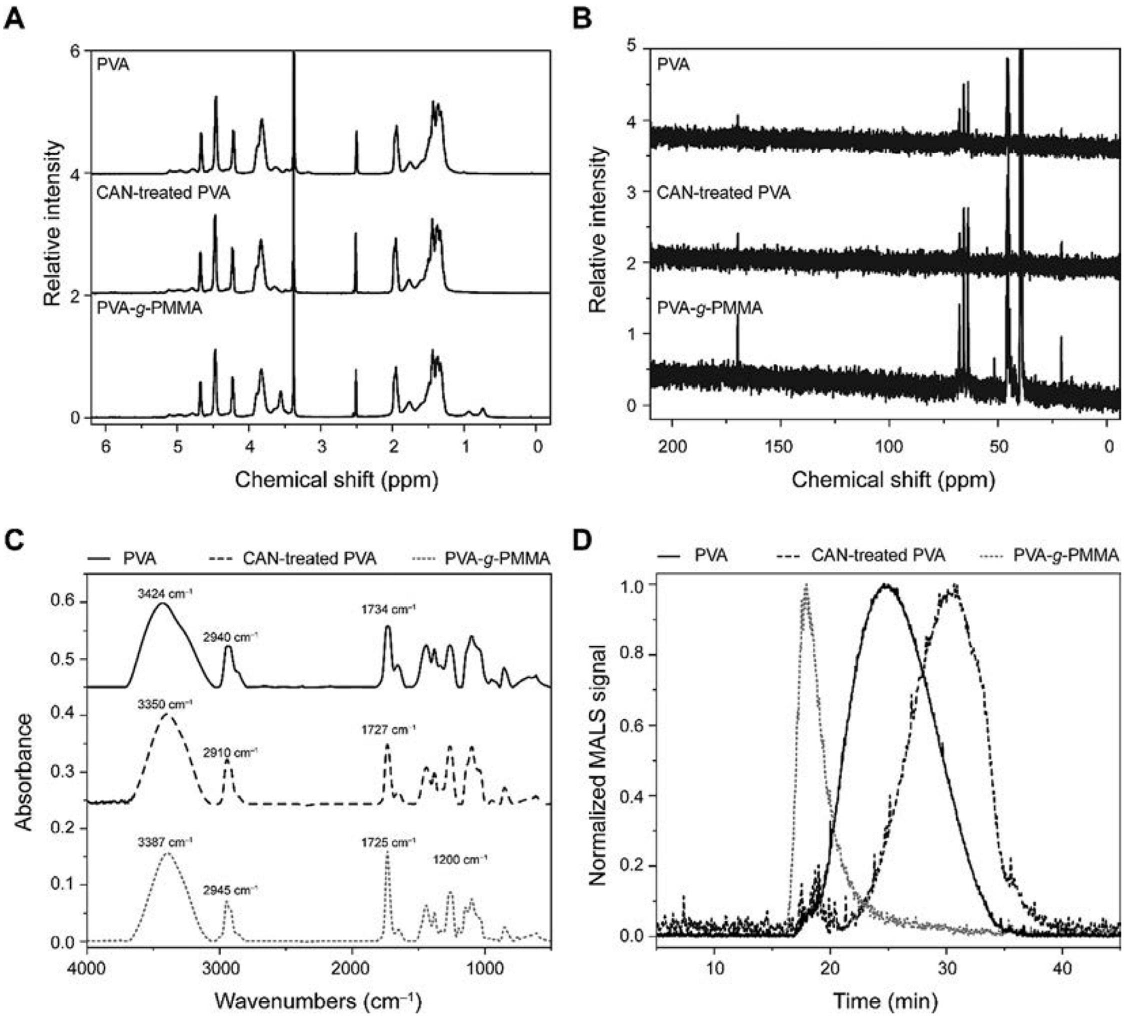

Fig. 2. Characterization of pure PVA, CAN-treated PVA and the PVA-g-PMMA copolymer. (A) ^{1}H NMR spectra, (B) ^{13}C NMR spectra, (C) FTIR spectra and (D) normalized GPC chromatograms; MALS detector signals are shown. Note the sharp decrease of the PVA-g-PMMA retention times, indicating an increase of the M_w.

As mentioned above, PVA undergoes degradation in the presence of nitric acid and CAN owing to the presence of glycol moieties along the polymer backbone [36–38]. In this context, we carried out a blank reaction to assess the impact of the reactants on PVA. In this case, a sharp increase in the retention time that was associated to a decrease in the molecular weight was observed; M_w and M_n values being 6500 and 5900 g/mol ($Đ$ of 1.10), respectively (Table S1, Fig. 2D). PMMA grafting led to molecular weight recovery to M_w and M_n of 75,000 and 43,000 g/mol ($Đ$ of 1.74), respectively. These findings further supported the successful synthesis of the PVA-g-PMMA copolymer. It is worth mentioning that according to ^{1}H NMR analysis, the copolymer contained 16–17% w/w of PMMA which would not explain the increase in molecular weight found between CAN-treated PVA and the copolymer in GPC analysis. These findings strongly suggest that the addition of MMA to the reaction mixture may reduce the extent of PVA degradation due to CAN or different measurement deviations for polymers with substantial gap in molecular weight when the molecular weight is obtained by light-scattering calculations in MALS. Remarkably, all the analyzed polymers displayed a monomodal molecular weight distribution due to the efficient purification by dialysis.

3.3. Self-assembly of PVA-g-PMMA copolymer

3.3.1. Critical aggregation concentration

The CAC estimated by DLS was 0.4 mg/mL at both 25 and 37 °C, confirming that the temperature does not affect the aggregation trend of this copolymer owing to the negligible thermo-responsiveness of PMMA.

3.3.2. Nanoparticle preparation and crosslinking

One of the well-known "Achilles' heels" of self-assembled colloids is their thermodynamic tendency to disassemble upon uncontrolled and extreme dilution conditions to final concentrations below the CAC [41,42]. Different synthetic pathways (e.g., covalent crosslinking) were attempted to physically stabilize them, though many of them are not biodegradable and compromise the drug encapsulation capacity or/and the chemical structure of the cargo [41]. The use of mild and selective crosslinking methods that can be conducted in the presence of the drug without altering its structure appears as an appealing strategy to overcome this drawback [11,12,14,43].

It was previously shown that PVA undergoes crosslinking with boric acid by a stoichiometric non-covalent mechanism and generates three possible complex structures [44,45]. The use of this crosslinker to stabilize self-assembled PVA nanoparticles is a new approach recently proposed by Moshe et al. [12]. Ideally, the crosslinking should ensure maximum physical stability by intra-nanoparticle complexation, while minimizing inter-nanoparticle bridging. To note is that boric acid is a pharmaceutical excipient that causes low acute oral toxicity, the lethal dose 50 in mouse and rat being between 2200 and 4000 mg/kg of body weight [46,47], which suggests the good biocompatibility of such a system. In addition, boric acid eye drops (e.g., 1.9% w/v) are used as mild antibiotic and antifungal and as absorption enhancer [48,49].

P4

Our nanoparticles were prepared by direct dissolution of the PVA-*g*-PMMA copolymer in water above the experimental CAC, 0.4 mg/mL, and then we fine-tuned the conditions for boric acid crosslinking and stabilization of the formed colloid. For this, different volumes (3, 4 or 5 μL) of a boric acid solution in the 10–50 mg/mL range were added to one mL of the nanoparticle suspension (0.8 mg/mL). Subsequently, the samples were investigated in terms of colloidal stability under different dilution extents by DLS.

When the nanoparticles were diluted 10 times (final concentration of 0.08 mg/mL, five times lower than the CAC), they remained assembled and preserved the size, regardless of the crosslinking or not, for at least one week (Table S2). Thus, we conducted a new dilution to a final concentration of 0.008 mg/mL (50 times below the CAC). Non-crosslinked nanoparticles began to disassemble only after six weeks, which stresses the relatively high physical stability of the nanoparticles even under these extreme conditions. These findings also indicated that the disassembly kinetics of these nanoparticles is very slow, most probably due to the formation of very stable amorphous PMMA domains by means of hydrophobic interactions that are in glassy state at RT [50]. According to these results, these nanoparticles undergo disassembly only once they are diluted far below the CAC and enough time is given. As anticipated, crosslinked nanoparticles remained assembled beyond the time limit of the experiment and they could probably undergo disassembly under even more extreme dilution conditions and at longer time owing to the biodegradation of the non-covalently crosslinked network [51]. Given these results, in advance, we crosslinked the nanoparticles with 4–5 μL of boric acid (50 mg/mL) per mL of colloidal dispersion.

A complementary analysis was performed by means of A4F, a separation technique based on fractionation and independent characterization of entities contained in the analyzed sample. Since fractionation is done in the flow field that crosses the detector flow and inevitably results in significant dilution of the sample, results of A4F also reflect to a certain extent the physical stability of a self-assembled colloid below the CAC. Another advantage of A4F is its ability to monitor the content of unassembled (free) polymer in the presence of assembled polymeric nanoparticles [52]. A4F experiments revealed that more than 90% of the copolymer self-assembled and formed nanoparticles, regardless of whether the crosslinker was used or not. These findings evidenced that PVA-*g*-PMMA colloids are stable even when subjected to A4F separation-related dilution.

Volume weighted distributions of gyration diameter D_g and molar mass M_w of non-crosslinked and boric acid-crosslinked PVA-*g*-PMMA samples are shown in Fig. S2. In both cases, distributions are bimodal with particle sizes covering the range from approximately 60 up to 300 nm. The values of average molecular weight M_w and z-average diameter of gyration D_g calculated separately for each mode are given in Table S3. In the case of the non-crosslinked sample, the first population possesses D_g of 114 nm and molecular weight M_w of 1.2×10^6 g/mol, whereas in the case of the second population, the D_g is 166 nm and the molecular weight M_w is 40.6×10^6 g/mol. The boric acid-crosslinked sample is characterized by D_g of 120 nm and M_w of 40.6×10^6 g/mol for the first population that was juxtaposed with a population possessing D_g of 180 nm and M_w of 53.7×10^6 g/mol. In addition, A4F results showed that the crosslinking resulted in greater aggregation numbers, most probably owing to the physical stabilization of the nanoparticle.

In A4F measurements, potential dust particles and large aggregates are removed by the separation process itself. Thus, thorough filtration of the sample that is typical for conventional light scattering methods such as DLS was not required; A4F results presented above are therefore for unfiltered samples. However, we decided to characterize samples filtered through 0.22 μm filters (see below) because this type of filtration is usually carried out prior to nanoparticle analysis by light scattering techniques [52,53]. Intriguingly, filtered samples revealed only one population (see the results below), suggesting that the filtration step limited the second population observed in A4F, even though that the size of the second population does not exceed the pore size of the filter membrane.

3.3.3. Light scattering

Using the optimized crosslinking protocol, PVA-*g*-PMMA copolymer was assembled and crosslinked with boric acid. A detailed physicochemical characterization was then carried by DLS, SLS, ELS, TEM and SANS. For these measurements, we used 0.8 mg/mL samples, a concentration that is far above the CAC value estimated by DLS.

Similarly as in the preliminary experiments, light scattering analysis found that direct solubilization of the PVA-*g*-PMMA copolymer in water leads to spontaneous self-association and the formation of nanoparticles with an overall negative surface charge, in line with results reported elsewhere [54,55]. For both non-crosslinked and crosslinked colloidal systems, the DLS distribution function is portrayed as a relatively narrow peak with a hydrodynamic diameter ca. 70 nm (Fig. 3, Table 1) which, as described below, was in good agreement with TEM analysis.

A slight increase in D_h value (from 70 to 74 nm) was observed when the sample was crosslinked, indicating a good control of the process and that the crosslinking was mainly intra- and not inter-micellar.

PDI values before and after crosslinking were <0.15, consistent with a monomodal size distribution.

At the same line, SLS revealed D_g of ca. 80 nm and showed that crosslinking with boric acid leads to a slight increase in both M_w and N_{agg}. The apparent structural density d of the particles was calculated as an equivalent average density from the weight-average of molecular weight M_w using the model of a sphere with the diameter D, with no correction for polydispersity, as expressed by Eq. (8)

$$d = \frac{6M_w^{NPs}}{\pi N_A D_{geom}^3}, \tag{8}$$

where D_{geom} is the geometrical dimension (diameter) $D_{geom} = 1.29 \cdot D_g$ and N_A is Avogadro's constant.

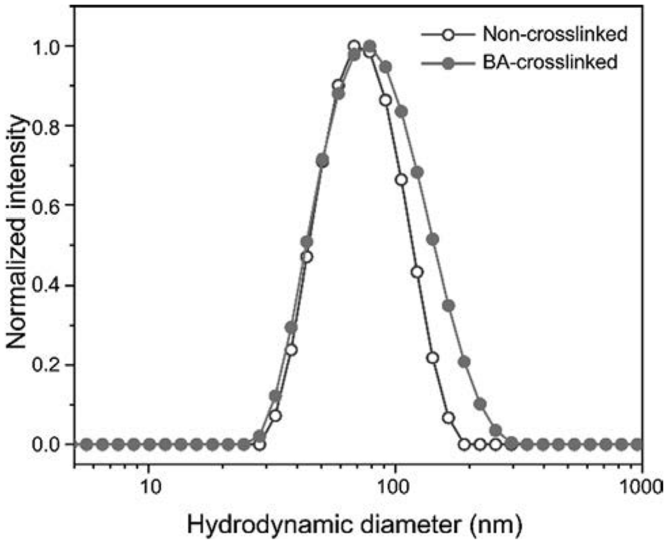

Fig. 3. Normalized intensity-weighted distribution functions of non-crosslinked and boric acid (BA)-crosslinked PVA-*g*-PMMA nanoparticles, as measured by DLS. The sample concentration is 0.8 mg/mL. Measurements were conducted at 25 °C.

Table 1
Characterization of PVA-g-PMMA nanoparticles.

Nanoparticle	D_h (nm)[a]	D_g (nm)[b]	M_w (g/mol)[b]	N_{agg}[b]	d (g/cm^3)[b]	ζ (mV)[c]
Non-crosslinked PVA-g-PMMA	70	77	4.3×10^6	57	0.014	−14.6
Boric acid-crosslinked PVA-g-PMMA	74	78	4.4×10^6	63	0.014	−15.5

[a] Determined by DLS.
[b] Determined by SLS.
[c] Determined by ELS.

The density of the assemblies was found to be reasonably low (0.014 g/cm^3 for both samples), suggesting that PVA-g-PMMA nanoparticles are most probably porous and water-swollen. The D_g/D_h ratio can be used as a measure of the distribution of the material through the particle. When PVA-g-PMMA nanoparticles were crosslinked, the D_g/D_h ratio decreased from 1.10 to 1.05, suggesting that they are more compact and with less dangling chains than the non-crosslinked counterparts. For instance, homogenous spheres are known to possess D_g/D_h of 0.775. The values found in this work hence suggest that the assemblies represent swollen structures.

3.3.4. Small-angle neutron scattering

Preliminary DLS and SLS results suggested that boric acid-crosslinking stabilizes the particles and does not introduce any significant density change within the polymeric assemblies. At the same time, it is generally accepted that size and size distribution values measured by DLS are not accurate because the analysis usually overestimates the actual size. This is due to the fact that the scattering intensity strongly depends on the nanoparticle radius (to the power of six in the Rayleigh approximation). Thus, the resulting intensity-weighted size distributions are often biased towards higher values of size [56]. Given this, we combined SANS and TEM to gain a better understanding of the aggregate size before and after the boric acid-crosslinking.

SANS data for non-crosslinked and crosslinked PVA-g-PMMA samples are presented in Fig. 4. It is worth stressing that results were normalized to an absolute scale, as described in the Section 2. In addition, to assess the thermal colloidal stability, SANS measurements were conducted at different temperatures.

SANS data showed an exceptional stability for both non-crosslinked and crosslinked colloidal systems at the three measured temperatures, namely 25, 35 and 40 °C (Fig. 5). Usually, temperature at least slightly affects the self-assembly of polymeric amphiphiles and the scattering pattern of the formed nanoparticles, though this was not the case for these ones. This behavior is due to the use of thermo-unresponsive PMMA as the hydrophobic component of the copolymer. In other words, the crosslinking process used here performs as intended and it does not introduce any major modifications of the ordering or structuring of the polymer chains within the particle, even in the small-scale (local) range probed by SANS, apart from the creation of the crosslinking points themselves that physically stabilize the colloidal system upon extreme dilution and for a long time of at least six weeks. This very high colloidal stability is of major relevance considering the harsh biological conditions to which colloidal drug delivery systems are exposed upon administration. Since SANS probes structures < 100 nm, this shows that at least the local structure is fully maintained. In addition, the full overlap of the scattering data obtained at 35 and 40 °C is a strong indication that the results would be the same at 37 °C, the physiologically relevant temperature. Based on these SANS findings, we can claim that the sizes at 37 °C are the same as those found at 25 °C, i.e. a small size population of D_g = 12 nm, and a larger size of D_g = 84 nm. However, SANS probes only the size-range below 100 nm, and the formation of some large-scale complexes (not detectable with SANS) at 37 °C (and the other temperatures) cannot be ruled out. In any event, this phenomenon is highly unlikely due to the excellent temperature stability of these colloids, as demonstrated by SANS. By visual inspection, the scattering patterns resemble that of micelles. This is therefore an indication that self-assembly of the PVA-g-PMMA chains has taken place, driven by the hydrophobicity of the PMMA-grafting, and stabilized against the surrounding water by PVA. For a given concentration (5 mg/mL), the patterns for the non-crosslinked and crosslinked nanoparticles are found to overlap, showing that there are no major structural differences between them (in the nano-scale range). This is reasonable, since the crosslinking of PVA domains with boric acid is not expected to produce significant local density changes that could give independent contribution to the scattering.

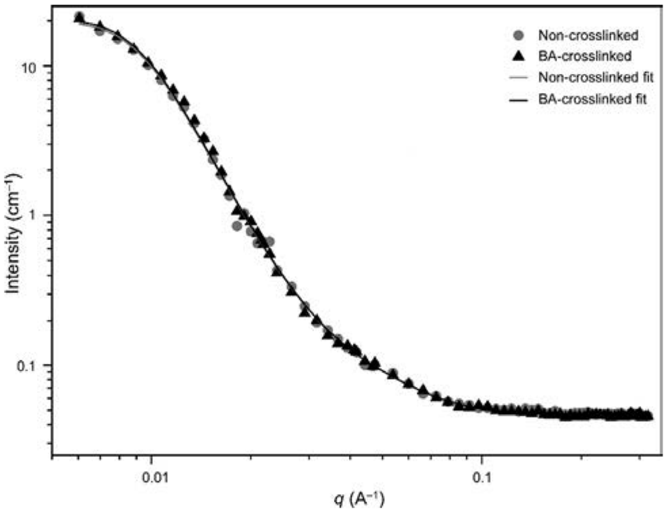

Fig. 4. SANS analysis of non-crosslinked and boric acid (BA)-crosslinked PVA-g-PMMA nanoparticles (5 mg/mL), at 25 °C. Both lines show fit with a 2-level Beaucage model.

Despite the fact that a simple Guinier analysis gave a quite favorable fit, given the TEM-related results that showed the formation of small clustered particles (see below), the Beaucage model (2-level) was utilized to fit the curves (Fig. 4). This gives as output a small size population of D_g = 12 nm and a larger size of D_g = 84 nm, though it was not possible to conclude whether the small size-related population corresponds to free PVA-g-PMMA coils having a diameter ca. 10–15 nm, as visualized by electron microscopy (see below). In any case, our SANS findings would be in line with a situation where the nanoparticles are based on small particles clustered together into larger structures, which is in line with TEM results presented in the next section.

3.3.5. Transmission electron microscopy

Representative TEM microphotographs of both non-crosslinked and boric acid-crosslinked samples are presented in Fig. 6. In standard TEM analysis, negative sample staining with uranyl acetate revealed the presence of white polymeric nanoparticles on a dark (stained) background. It is evident that both kinds of assemblies

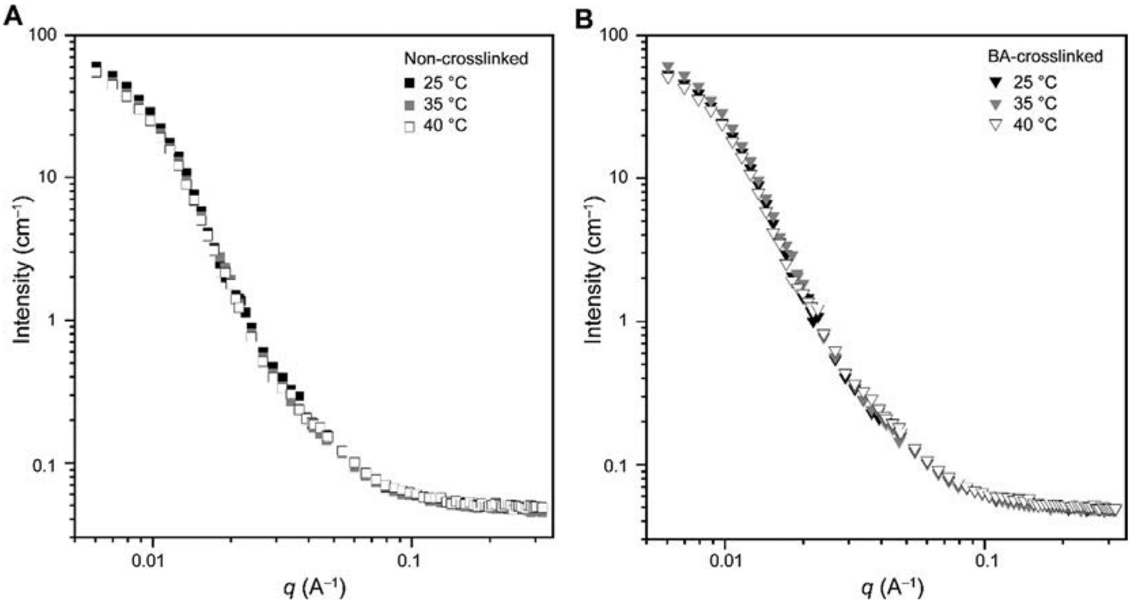

Fig. 5. Small angle neutron scattering (SANS) data at different temperatures for PVA-g-PMMA particles (5 mg/mL). (A) Non-crosslinked and (B) boric acid (BA)-crosslinked.

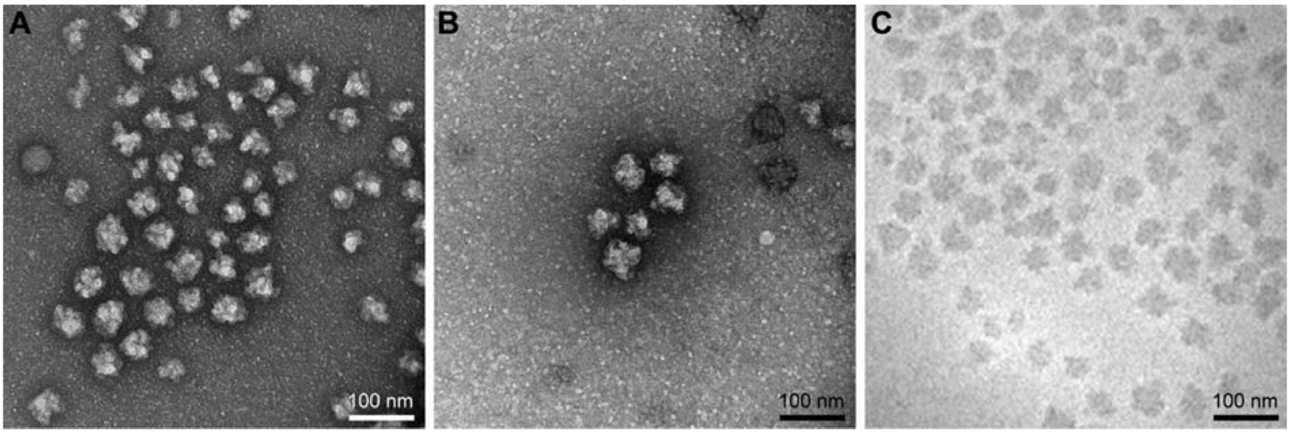

Fig. 6. Micrographs of (A) non-crosslinked and (B) boric acid-crosslinked nanoparticles obtained by conventional TEM with negative 2% w/w uranyl acetate staining. (C) Non-crosslinked nanoparticles were also imaged by cryo-TEM. Both methods showed the same morphology and nanostructure.

(before and after crosslinking) possess isometric, though non-spherical shape.

The nanoparticles appeared to be formed from small spherical units, probably unimolecular or low aggregation number-possessing micelles, having size ca. 12–15 nm, which formed clusters (Fig. 6A, B; Fig. 7). The diameters of both investigated samples in TEM micrographs were in the range between 50 and 60 nm, which was in very good agreement with DLS results.

In order to verify the somewhat unusual morphology, non-crosslinked PVA-g-PMMA nanoparticles were also visualized by using cryo-TEM. In contrast to simple TEM, cryo-TEM enables the analysis in hydrated state, which should be free from possible artifacts due to the drying process. The cryo-TEM image confirmed that the isometric non-spherical clusters were present also in the original colloid and that they were not formed during the drying (Fig. 6C). In other words, the aggregates were present also in the hydrated state. The boric acid-crosslinked nanoparticles were slightly more compact and homogeneous, as the individual primary units were harder to differentiate (Fig. 6A).

3.4. Spray-drying

The physicochemical stabilization of nanoparticles can be usually achieved by drying. Freeze-drying is a well-established drying industrial technique though in the case of nanoparticles, it may result in significant agglomeration and difficult re-dispersion, also when feed liquid samples are diluted [57]. In this context, the addition of cryo/lyoprotectants in high weight percentage is often required. In addition, the process may take several days or weeks and the operating cost is high [58].

Spray-drying is a relatively new industrial technique based on the conversion of a liquid into a dry powder by atomization in a stream of hot gas (air or nitrogen depending on the solvent) and the separation and the collection of the dry matter [59,60]. Owing to the relatively short time exposure to heat (seconds) and fast drying, this method could be also feasible for thermo-sensitive pharmaceuticals, biomaterials and drugs. In addition, spray-drying preserves better the properties of nanoparticles and it enables higher throughput and more continuous rather than batch processes. In this scenario, spray-drying has emerged as a very attractive technology to stabilize colloidal systems in dry form for long periods and it may play a key role to pave the way for the industrial production of colloidal drug delivery systems. In this context, non-crosslinked and boric acid-crosslinked PVA-g-PMMA nanoparticles were spray-dried by utilizing the Nano Spray Dryer B-90 HP that, as opposed to other spray-dryers based on cyclone collectors, enables the efficient collection of all the nanoparticle size populations. In the past, Moshe et al. demonstrated the usefulness of this

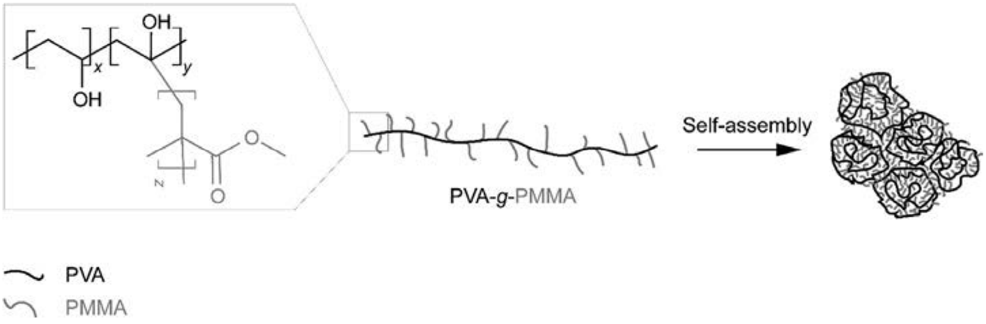

Fig. 7. Proposed self-association pattern of PVA-*g*-PMMA in aqueous media.

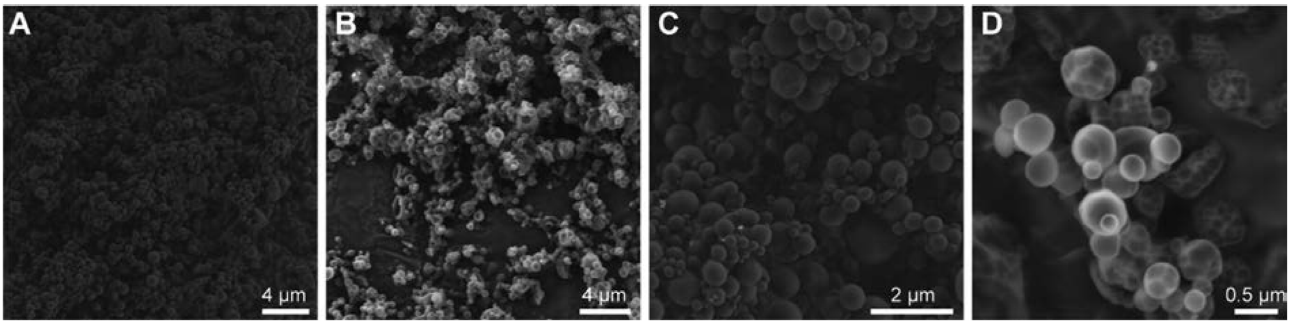

Fig. 8. HR-SEM micrographs of PVA-*g*-PMMA (1 mg/mL) nanoparticles after NSD. (A, B) Non-crosslinked and (C, D) boric acid-crosslinked nanoparticles.

technology to consolidate boric acid-crosslinked PVA nanoparticles [12]. Then, dry powders of non-crosslinked and boric acid-crosslinked nanoparticles were visualized by HR-SEM. In general, all the powders presented a similar morphology (Fig. 8). The relatively large size of the particles (in the micron-scale) stems from the unique spraying mechanism of the B-90 HP instrument that relies on the peristaltic pumping of the liquid feed through a micron-sized mesh [59]. It is important to highlight that each spray-dried particle observed under the HR-SEM is formed by several amphiphilic nanoparticles. Upon re-dispersion, nanoparticles with the original size are expected to form.

To assess the re-dispersion properties of both non-crosslinked and crosslinked nanoparticles, powders were re-dispersed in the same volume of water from which theiy were obtained and the size of regenerated particles measured by DLS. Remarkably, the D_h value of non-crosslinked nanoparticles increases from 70 nm to 205 ± 23 nm, indicating that a change in the aggregation pattern takes places, probably owing to the physical crosslinking of PVA domains upon drying [61]. Conversely, boric acid-crosslinked counterparts remained almost unchanged with a relatively small size growth from 74 to 91 nm. These results highlight the key role of the boric acid crosslinking to preserve the nanoparticle size. Further optimization of the spray-drying conditions such as sample concentration could be used to minimize the size growth even more.

4. Conclusions

In the current study, we investigated for the first time the self-assembly and complex nanostructure of an amphiphilic PVA-*g*-PMMA colloidal system. By combining DLS, SLS, SANS and TEM, we demonstrated the formation of a multi-micellar colloids of isometric non-spherical shape comprised of low aggregation number particles (ca. 12–15 nm in diameter) assembled into larger assemblies with sizes of several hundreds of nanometers. These findings represent a major contribution to the understanding of the aggregation behavior of comb-like polymeric amphiphiles and suggests that colloidal drug delivery systems based on this kind of copolymer could lead to more complex release patterns where the drug molecules hosted in more superficial "building blocks" is released faster than those inner ones. Indeed, this hypothesis will need experimental confirmation.

One of the greatest limitations of polymeric amphiphiles is that a major polymer fraction remains disassembled, as previously reported for poly(ethylene oxide)-*b*-poly(propylene oxide) copolymers [62–64]. These polymer molecules are basically "wasted" as they do not participate of the encapsulation of drug molecules. The low aggregation efficiency could stem from the low relative hydrophobicity of the hydrophobic component, steric hindrance in the copolymer backbone, electrostatic repulsion, among others. Moreover, the aggregation extent cannot be easily estimated. In this work, we utilized A4F and revealed that more than 90% of the PVA-*g*-PMMA copolymer is in the nanoparticles. These results have two main implications: (i) the need for a more thorough investigation of the aggregation extent of polymeric amphiphiles used in pharmaceutical development and (ii) the potential utilization of A4F to investigate the relationship between polymer structure and its aggregation pattern and drug encapsulation and release performance.

Another important drawback of self-assembly colloids is the low physical stability upon profuse dilution that in the biological medium may represent the release of the encapsulated cargo in an off-target body site [41,65,66]. This phenomenon jeopardizes the bench-to-bedside translation of colloidal drug delivery systems [67]. In the current work, we confirmed that the formation of PVA-boric acid complexes, a selective and mild chemical reaction, can be capitalized to crosslink and hence, stabilize PVA-based colloids under very extreme dilution conditions without any substantial detrimental effect on the size and the nanoparticle nanostructure. This stabilization pathway is compatible with different drugs and, as shown here, can be coupled with spray-drying which is a technology that enables the production of dry colloidal systems with eventually very long shelf life and good re-dispersion capacity. This stage will facilitate production scale-up under an industrial setting and needless to say, translation into products. Overall, this study opens new horizons towards the application of self-assembled colloids in general and PVA-*g*-PMMA-made in particular as drug delivery platforms.

Acknowledgments

A.S. and H.M.H. acknowledge the funding of the European Union's - Seventh Framework Programme under grant agreement #612765-MC-NANOTAR, the Israel Science Foundation (ISF Grant #269/15) and the Russell Berrie Nanotechnology Institute (Technion). Financial support from the Czech Academy of Sciences (project no. ISR-17-21) that contributed to the Czech-Israeli collaboration is gratefully acknowledged. J.T. acknowledges the support received from the Charles University (project no. SVV260440) and the Czech Science Foundation (grant no. 17-07164S and no. 17-09998S) and thanks the kind help of Dr. Miloš Netopilík in the instrumentation necessary for GPC analysis. D.R. acknowledges support from the Scientific Grant Agency VEGA (grant no. 2/0177/17) and the Slovak Research and Development Agency (project NANOSEG No. 16-0550). Electron microscopy at the Institute of Macromolecular Chemistry AS CR was supported by project TE01020118 (Technology Agency of Czech Republic).

Appendix A. Supplementary material

Supplementary data to this article can be found online at https://doi.org/10.1016/j.jcis.2019.06.047.

References

[1] R. Palao-Suay, L.G. Gómez-Mascaraque, M.R. Aguilar, B. Vázquez-Lasa, J.S. Román, Self-assembling polymer systems for advanced treatment of cancer and inflammation, Prog. Polym. Sci. 53 (2016) 207–248.
[2] V.P. Torchilin, Micellar nanocarriers: pharmaceutical perspectives, Pharm. Res. 24 (2007) 1–16.
[3] H.M. Aliabadi, A. Lavasanifar, Polymeric micelles for drug delivery, Expert Opin. Drug Deliv. 3 (2006) 139–162.
[4] A.S. Deshmukh, P.N. Chauhan, M.N. Noolvi, K. Chaturvedi, K. Ganguly, S.S. Shukla, M.N. Nadagouda, T.M. Aminabhavi, Polymeric micelles: basic research to clinical practice, Int. J. Pharm. 532 (2017) 249–268.
[5] R.P. Brinkhuis, Floris P.J.T. Rutjes, Jan C.M.van Hest, Polymeric vesicles in biomedical applications, Polym. Chem. 2 (2011) 1449–1462.
[6] ETP Nanomedicine, ERA-Net EuroNanoMed Nanomedicine Strategic Research, Innovation Agenda 2016–2030.
[7] D.A. Chiappetta, C. Hocht, C. Taira, A. Sosnik, Efavirenz-loaded polymeric micelles for pediatric anti-HIV pharmacotherapy with significantly higher oral bioavailability [corrected], Nanomedicine (Lond.) 5 (2010) 11–23.
[8] D.A. Chiappetta, C. Hocht, C. Taira, A. Sosnik, Oral pharmacokinetics of the anti-HIV efavirenz encapsulated within polymeric micelles, Biomaterials 32 (2011) 2379–2387.
[9] A. Sosnik, A.M. Carcaboso, Nanomedicines in the future of pediatric therapy, Adv. Drug Deliv. Rev. 73 (2014) 140–161.
[10] A. Sosnik, M. Menaker Raskin, Polymeric micelles in mucosal drug delivery: Challenges towards clinical translation, Biotechnol. Adv. 33 (2015) 1380–1392.
[11] M.M. Raskin, I. Schlachet, A. Sosnik, Mucoadhesive nanogels by ionotropic crosslinking of chitosan-g-oligo(NiPAam) polymeric micelles as novel drug nanocarriers, Nanomedicine (Lond.) 11 (2016) 217–233.
[12] H. Moshe, Y. Davizon, M. Menaker Raskin, A. Sosnik, Novel poly(vinyl alcohol)-based amphiphilic nanogels by non-covalent boric acid crosslinking of polymeric micelles, Biomater. Sci. 5 (2017) 2295–2309.
[13] I. Schlachet, A. Sosnik, Protoporphyrin IX-modified chitosan-g-oligo(NiPAAm) polymeric micelles: from physical stabilization to permeability characterization in vitro, Biomater. Sci. 5 (2016) 128–140.
[14] I. Noi, I. Schlachet, M. Kumarasamy, A. Sosnik, Permeability of novel chitosan-g-poly(methyl methacrylate) amphiphilic nanoparticles in a model of small intestine in vitro, Polymers 10 (2018) 478.
[15] N.A. Peppas, N.K. Mongia, Ultrapure poly(vinyl alcohol) hydrogels with mucoadhesive drug delivery characteristics, Eur. J. Pharm. Biopharm. 43 (1997) 51.
[16] A. Kumar, S.S. Han, PVA-based hydrogels for tissue engineering: a review, Int. J. Polym. Mater. PO. 66 (2016) 159.
[17] FDA, Agency Response Letter GRAS Notice No. GRN 000141 [Polyvinyl Alcohol], U.S. Food and Drug Administration (FDA), 2004. https://www.accessdata.fda.gov/scripts/fdcc/?set=GRASNotices&id=141.
[18] C. Cai, J. Lin, T. Chen, X. Tian, Aggregation behavior of graft copolymer with rigid backbone, Langmuir 26 (2010) 2791–2797.
[19] Y. Wang, L. Wang, B. Li, Y. Cheng, D. Zhou, X. Chen, X. Jing, Y. Huang, Compact vesicles self-assembled from binary graft copolymers with high hydrophilic fraction for potential drug/protein delivery, ACS Macro Lett. 6 (2017) 1186–1190.
[20] Leonard Ionut Atanase, Gerard Riess self-assembly of block and graft copolymers in organic solvents: an overview of recent advances, Polymers 2018, 10, 62.
[21] L. Zhang, J. Lin, S. Lin, Aggregate morphologies of amphiphilic graft copolymers in dilute solution studied by self-consistent field theory, J. Phys. Chem. B 111 (2007) 9209–9217.
[22] J. Jakeš, Regularized positive exponential sum (REPES) program – a way of inverting Laplace transform data obtained by Dyn 1997, amic light scattering, Collect. Czech. Chem. Commun. 60 (1995) 1781–1797.
[23] P. Štěpánek, Koňák, Č Quasielastic light scattering from polymers, colloids and gels, Adv. Colloid Interface Sci. 21 (1984) 195–274.
[24] P.W. Akers, A.R.J. Nelson, D.E. Williams, D.J. McGillivray, Formation of hydrated layers in PMMA thin films in aqueous solution, Appl. Surf. Sci. 353 (2015) 829–834.
[25] I. Berts, Y. Gerelli, J. Hilborn, A.R. Rennie, Structure of polymer and particle aggregates in hydrogel composites, J. Polym. Sci. Part B: Polym. Phys. 51 (2012) 421–429.
[26] G. Beaucage, Approximations leading to a unified exponential/power-law approach to small-angle scattering, J. Appl. Cryst. 28 (1995) 717–728.
[27] G. Beaucage, H.K. Kammler, S.E. Pratsinis, Particle size distributions from small-angle scattering using global scattering functions, J. Appl. Cryst. 37 (2004) 523–535.
[28] S. Petrova, E. Jäger, R. Konefał, A. Jäger, C. G. Venturini, J. Spěváček, E. Pavlova, P. Štěpánek, Novel poly(ethylene oxide monomethyl ether)- b -poly(ε-caprolactone) diblock copolymers containing a pH-acid labile ketal group as a block linkage, Polym. Chem. 5 (2014) 3884–3893.
[29] N.B. Halima, Poly(vinyl alcohol): review of its promising applications and insights into biodegradation, RSC Adv. 6 (2016) 39823–39832.
[30] M. Shibayama, M. Sato, Y. Kimura, H. Fujiwara, S. Nomura, 11B n.m.r. study on the reaction of poly(vinyl alcohol) with boric acid, Polymer 29 (1988) 336–340.
[31] A. Bettencourt, A.J. Almeida, Poly(methyl methacrylate) particulate carriers in drug delivery, J. Microencapsul. 29 (2012) 353–367.
[32] E. Shaked, Y. Shani, M. Zilberman, M. Scheinowitz, Poly(methyl methacrylate) particles for local drug delivery using shock wave lithotripsy: in vitro proof of concept experiment, J. Biomed. Mater. Res. Part B Appl. Biomater. 103 (2015) 1228–1237.
[33] N. Gozum, E.S. Unal, R. Altan-Yaycioglu, A. Gucukoglu, C. Ozgun, Visual performance of acrylic and PMMA intraocular lenses, Eye 17 (2003) 238–242.
[34] R.Q. Frazer, R.T. Byron, P.B. Osborne, K.P. West, PMMA: an essential material in medicine and dentistry, J. Long Term. Eff. Med. Implants 15 (2005) 629–639.
[35] R. Vaishya, M. Chauhan, A. Vaish, Bone cement, J. Clin. Orthop Trauma 4 (2013) 157–163.
[36] G. Mino, S. Kaizerman, E. Rasmussen, The oxidation of polyvinyl alcohol by ceric ion, J. Poly. Sci. 39 (1959) 523.
[37] Y. Ikada, Y. Nishizaki, H. Iwata, I. Sakurada, Reaction of poly(vinyl alcohol) with tetravalent ceric ion, J. Poly. Sci. Poly. Chem. Ed. 15 (1977) 451.
[38] R.F. Storey, L.J. Goff, Investigation of the ceriumIV oxidation of poly(vinyl alcohol), J. Poly. Sci. A Polym. Chem. 27 (1989) 3837.
[39] D.H. Kim, M.S. Park, H.H. Cho, J.T. Park, J.H. Kim, Synthesis of organized mesoporous metal oxide films templated by amphiphilic PVA–PMMA comb copolymer, RSC Adv. 6 (2016) 67849–67857.
[40] M.A.M. Oliveira, P.A. Melo Jr., M. Nele, J.C. Pinto, In-situ incorporation of amoxicillin in PVA/PVAc-coPMMA particles during suspension polymerizations, Macromol. Symp. 299 (300) (2011) 34–40.
[41] S.C. Owen, D.P.Y. Chan, M.S. Shoichet, Polymeric micelle stability, Nano Today 7 (2012) 53–65.
[42] Y. Shi, T. Lammers, G. Storm, W.E. Hennink, Physico-chemical strategies to enhance stability and drug retention of polymeric micelles for tumor-targeted drug delivery, Macromol. Biosci. 17 (2017) 1600160.
[43] J. Talal, I. Abutbul-Ionita, I. Schlachet, D. Danino, A. Sosnik, Amphiphilic nanoparticle-in-nanoparticle drug delivery systems exhibiting cross-linked inorganic rate-controlling domains, Chem. Mater. 29 (2017) 873–885.
[44] T. Itou, H. Kitai, A. Shimazu, T. Miyazaki, K. Tashiro, Clarification of cross-linkage structure in boric acid doped poly(vinyl alcohol) and its model compound as studied by an organized combination of X-ray single-crystal structure analysis, Raman spectroscopy, and density functional theoretical calculation, J. Phys. Chem. B 118 (2014) 6032–6037.
[45] I.Y. Prosanov, S.T. Abdulrahman, S. Thomas, N.V. Bulina, K.B. Gerasimov, Complex of polyvinyl alcohol with boric acid: structure and use, Mater. Today Comm. 14 (2018) 77–81.
[46] J.J. Heindel, C.J. Price, E.A. Field, M.C. Marr, C.B. Myers, R.E. Morrissey, B.A. Schwetz, Developmental toxicity of boric acid in mice and rats, Fund. Appl. Toxicol. 18 (1992) 266–277.
[47] European Medicines Agency, Background review for the excipient boric acid https://www.ema.europa.eu/documents/report/background-review-excipient-boric-acid-context-revision-guideline-excipients-label-package-leaflet_en.pdf (accessed in April 2019).
[48] A.C. José, B. Castelo Branco, L.E. Ohkawara, M.C. Yu, A.L. Lima, Use conditions of boric acid solution in the eye: handling and occurrence of contamination, Arq. Bras. Oftalmol. 70 (2007) 201.

[49] P.W.J. Morrison, V.V. Khutoryanskiy, Advances in ophthalmic drug delivery, Ther. Deliv. 5 (2014) 1297.

[50] H. Teng, K. Koike, D. Zhou, Z. Satoh, Y. Koike, Y. Okamoto, High glass transition temperatures of poly(methyl methacrylate) prepared by free radical initiators, J. Polym. Sci.: Part A Polym. Chem. 47 (2009) 315–317.

[51] J. Tavakoli, Y. Tang, Honey/PVA hybrid wound dressings with controlled release of antibiotics: Structural, physico-mechanical and in-vitro biomedical studies, Mater. Sci. Eng. C 77 (2017) 318.

[52] J. Trousil, Z. Syrová, N.K. Dal, D. Rak, R. Konefal, E. Pavlova, J. Matějková, D. Cmarko, P. Kubíčková, O. Pavliš, T. Urbánek, M. Sedlak, F. Fenaroli, I. Raška, P. Stepanek, M. Hruby, Rifampicin nanoformulation enhances treatment of tuberculosis in Zebrafish, Biomacromolecules 20 (2019) 1798.

[53] I. Schlachet, J. Trousil, D. Rak, K.D. Knudsen, E. Pavlova, B. Nyström, A. Sosnik, Chitosan-graft-poly(methyl methacrylate) amphiphilic nanoparticles: Self-association and physicochemical characterization, Carbohydr. Polym. 212 (2019) 412–420.

[54] N.D. Thorat, K.P. Shinde, S.H. Pawar, K.C. Barick, C.A. Betty, R.S. Ningthoujam, Polyvinyl alcohol: an efficient fuel for synthesis of superparamagnetic LSMO nanoparticles for biomedical application, Dalton Trans. 41 (2012) 3060–3071.

[55] S.K. Sahoo, J. Panyam, S. Prabha, V. Labhasetwar, Residual polyvinyl alcohol associated with poly (d, l-lactide-co-glycolide) nanoparticles affects their physical properties and cellular uptake, J. Control. Release 82 (2002) 105–114.

[56] R.F. Domingos, M.A. Baalousha, Y. Ju-Nam, M.M. Reid, N. Tufenkji, J.R. Lead, G. G. Leppard, K.J. Wilkinson, Characterizing manufactured nanoparticles in the environment: multimethod determination of particle sizes, Environ. Sci. Technol. 43 (2009) 7277–7284.

[57] W. Abdelwahed, G. Degobert, S. Stainmesse, H. Fessi, Freeze-drying of nanoparticles: formulation, process and storage considerations, Adv. Drug Deliv. Rev. 58 (2006) 1688.

[58] P. Vass, B. Démuth, E. Hirsch, B. Nagy, S.K. Andersen, T. Vigh, G. Verreck, I. Csontos, Z.K. Nagy, G. Marosi, Drying technology strategies for colon-targeted oral delivery of biopharmaceuticals, J. Control. Release 296 (2019) 162.

[59] A. Sosnik, K.P. Seremeta, Advantages and challenges of the spray-drying technology for the production of pure drug particles and drug-loaded polymeric carriers, Adv. Colloid Interface. Sci. 223 (2015) 40–54.

[60] L. Peltonen, H. Valo, R. Kolakovic, T. Laaksonen, J. Hirvonen, Electrospraying, spray drying and related techniques for production and formulation of drug nanoparticles, Expert Opin. Drug Deliv. 7 (2010) 705–719.

[61] S. Sasaki, T. Murakami, A. Suzuki, Frictional properties of physically cross-linked PVA hydrogels as artificial cartilage, Biosurf. Biotribol. 2 (2016) 11–17.

[62] P. Alexandridis, J.F. Holzwarth, T.A. Hatton, Micellization of poly(ethylene oxide)-poly(propylene oxide)-poly(ethylene oxide) triblock copolymers in aqueous solutions: thermodynamics of copolymer association, Macromolecules 27 (1994) 2414–2425.

[63] D.A. Chiappetta, A. Sosnik, Poly(ethylene oxide)-Poly(propylene oxide) block copolymer micelles as drug delivery agents: improved hydrosolubility, stability and bioavailability of drugs, Eur. J. Pharm. Biopharm. 66 (2007) 303–317.

[64] J. Gonzalez-Lopez, C. Alvarez-Lorenzo, P. Taboada, A. Sosnik, I. Sandez-Macho, A. Concheiro, Self-associative behavior and drug solubilizing ability of poloxamine (Tetronic) block copolymers, Langmuir 24 (2008) 10688–10697.

[65] A. Patist, J.R. Kanicky, P.K. Shukla, D.O. Shah, Importance of micellar kinetics in relation to technological processes, J. Colloid Interface Sci. 245 (2002) 1–15.

[66] J. Lu, S.C. Owen, M.S. Shoichet, Stability of self-assembled polymeric micelles in serum, Macromolecules 44 (2011) 6002–6008.

[67] J. Shi, Z. Xiao, N. Kamaly, O. Farokhzad, Self-assembled targeted nanoparticles: evolution of technologies and bench to bedside translation, Acc. Chem. Res. 44 (2011) 1123–1134.

PUBLICATION P5

Schlachet I.[‡], **Trousil J.**[‡], Rak D., Knudsen D. K., Pavlova E., Nyström B., Sosnik A. Chitosan-graft-poly(methyl methacrylate) amphiphilic nanoparticles: Self-association and physicochemical characterization. *Carbohydrate Polymers*. 2019, 212, 412–420. IF = 6.04

I.S. synthesized the copolymer, carried out its physicochemical characterization and wrote the paper. J.T. conceptualized the study of NPs' structure, carried out GPC, DLS, and SLS experiments and wrote the paper. D.R. contributed to the final version of the paper. E.P. carried out the TEM investigations. K.D.K. and B.N. carried out the SANS investigations and contributed to the final version of the paper. A.S. supervised the project, conceptualized the experiments, and wrote the paper.

[‡] Authors contributed equally to this work.

Carbohydrate Polymers 212 (2019) 412–420

Contents lists available at ScienceDirect

Carbohydrate Polymers

journal homepage: www.elsevier.com/locate/carbpol

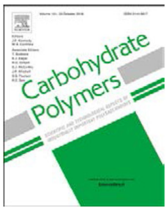

Chitosan-*graft*-poly(methyl methacrylate) amphiphilic nanoparticles: Self-association and physicochemical characterization

Inbar Schlachet[a,1], Jiří Trousil[b,c,1], Dmytro Rak[d], Kenneth D. Knudsen[e], Ewa Pavlova[b], Bo Nyström[f], Alejandro Sosnik[a,*]

[a] *Laboratory of Pharmaceutical Nanomaterials Science, Department of Materials Science and Engineering, Technion-Israel Institute of Technology, 320003 Haifa, Israel*
[b] *Institute of Macromolecular Chemistry, Czech Academy of Sciences, Heyrovského náměstí 2, 162 06 Prague 6, Czechia*
[c] *Department of Analytical Chemistry, Charles University, Faculty of Science, Hlavova 8, 128 43 Prague 2, Czechia*
[d] *Institute of Experimental Physics, Slovak Academy of Sciences, Watsonova 47, 040 01 Košice, Slovakia*
[e] *Department of Physics, Institute for Energy Technology, P. O. Box 40, N-2027 Kjeller, Norway*
[f] *Department of Chemistry, University of Oslo, P.O. Box 1033, Blindern, N-0315 Oslo, Norway*

ARTICLE INFO

Keywords:
Chitosan-*graft*-poly(methyl methacrylate) copolymers
Self-assembly
Amphiphilic polymeric nanoparticles
Small-angle neutron scattering (SANS)
Static light scattering (SLS) and dynamic light scattering (DLS)

ABSTRACT

In this work, we synthesized and characterized the self-assembly behavior of a chitosan-poly(methyl methacrylate) graft copolymer and the properties of the formed nanoparticles by static and dynamic light scattering, small-angle neutron scattering, and transmission electron microscopy. Overall, our results indicate that the hydrophobization of the chitosan side-chain with PMMA leads to a complex array of small unimolecular and/or small-aggregation number "building blocks" that further self-assemble into larger amphiphilic nanoparticles.

1. Introduction

Mucosal drug delivery capitalizes on the presence of mucus to prolong the residence time of drugs and to increase their local and systemic bioavailability. Depending on the surface properties, particles as large as 500 nm in diameter can diffuse across the highly porous structure of mucus (mesh size in the 20–200 nm range) (Barua & Mitragotri, 2014; Lai, Wang, & Hanes, 2009; Olmsted et al., 2001).

Amphiphilic polymeric nanoparticles are produced by the self-assembly of block or graft copolymer amphiphiles in aqueous media above a critical concentration and/or critical temperature and they are one of the most versatile platforms for parenteral drug delivery and targeting (Chiappetta & Sosnik, 2007; Croy & Kwon, 2006; Lukyanov & Torchilin, 2004; Torchilin, 2001). The fundamental molecular features to extend their application to mucosal drug delivery were comprehensively discussed (Sosnik & Menaker Raskin, 2015). The aggregation pattern, the shape and the structure of the nanoparticle depend on the molecular weight, the hydrophilic-hydrophobic balance and the architecture of the copolymer. For example, amphiphilic diblock and triblock block copolymers with relatively high hydrophilic-lipophilic balance (HLB) tend to form core-corona nanostructures known as polymeric micelles (Zhang & Eisenberg, 1995) where the outer hydrophilic corona stabilizes the species in the aqueous dispersion medium and the inner hydrophobic core is capable of hosting hydrophobic cargos (Chiappetta & Sosnik, 2007). More hydrophobic block copolymers assemble into polymeric vesicles, the so-called polymersomes, that combine a hydrophobic membrane enclosing an aqueous core (Lee & Feijen, 2012). Multifunctional amphiphilic graft copolymers broaden our ability to design and tailor the properties of the nanoparticles, though the aggregation pattern of these molecules is more difficult to anticipate (Zhang, Lin, & Lin, 2007).

Polycationic polymers such as the polysaccharide chitosan (CS) emerged as one of the most extensively investigated building blocks for the synthesis of mucoadhesive nanocarriers (Sogias, Williams, & Khutoryanskiy, 2008; Sosnik, Neves, & Sarmento, 2014). Recently, we reported on the synthesis of mucoadhesive amphphilic nanogels (hydrodynamic diameter of approximately 200–400 nm) produced by the ionotropic crosslinking of self-assembled CS amphiphiles synthesized by the hydrophobization of the polymer backbone with poly(*N*-isopropylacrylamide) (PNiPAAm) and demonstrated their ability to bind mucin in solution (Menaker Raskin, Schlachet, & Sosnik, 2016). Preliminary nanostructural studies conducted by high-resolution scanning

---

[*] Corresponding author.
E-mail address: sosnik@technion.ac.il (A. Sosnik).
[1] Authors equally contributed to this work.

https://doi.org/10.1016/j.carbpol.2019.02.022
Received 17 December 2018; Received in revised form 3 February 2019; Accepted 8 February 2019
Available online 16 February 2019
0144-8617/ © 2019 Elsevier Ltd. All rights reserved.

electron microscopy and cryogenic transmission electron microscopy (cryo-TEM) suggested that CS-*g*-PNiPAAm copolymers self-assemble into spherical multi-micellar aggregates, though these results were not conclusive (Menaker Raskin et al., 2016). The use of temperature-independent and more hydrophobic blocks such as poly(methyl methacrylate) (PMMA) to produce amphiphilic CS nanoparticles has been also reported (Liu, Zhao, & Yu, 2011; Zheng, Lian, Yang, & Wang, 2016). We demonstrated the ability of non-crosslinked and ionotropically crosslinked CS-*g*-PMMA nanoparticles to cross a co-culture model of intestinal epithelium *in vitro* (Noi, Schlachet, Kumarasamy, & Sosnik, 2018). In addition, we investigated the influence of different nanoparticle features on their interaction with mucin secreted by goblets cells (Noi et al., 2018). The shape and the structure of the aggregates affect not only the size, the physical stability (Jakeš, 1995), and the drug loading capacity but also the cell-nanoparticle interaction, the permeability across biological barriers and the biodistribution (Blanco, Shen, & Ferrari, 2015; Cabral et al., 2011). However, the self-assembly pattern of CS-based amphiphilic nanoparticles in general and CS-*g*-PMMA counterparts in particular has not been fully elucidated yet. In addition, the effect of sodium tripolyphosphate (TPP) ionotropic crosslinking on the nanostructure and the density of preformed nanoparticles is even less known. In this scenario, a more comprehensive characterization is critical to anticipate their drug encapsulation and release performance and their interaction with the biological milieu.

Aiming to gain further understanding on the nanostructure of CS-*g*-PMMA nanoparticles, in this work, we characterized the self-assembly of a CS-*g*-PMMA block copolymer utilizing static (SLS) and dynamic light scattering (DLS), small-angle neutron scattering (SANS) and TEM and cryo-TEM. Overall, our results are in line with the reassembly of low aggregation number-nanoparticles into larger aggregates.

2. Experimental section

2.1. Materials

Low molecular weight CS (GC9009, batch 769FGD, molecular weight of ~50,000 g/mol, degree of deacetylation of 94%, and viscosity of ≤100 mPa.s) was supplied by Glentham Life Sciences, Corsham, UK). The degree of deacetylation of CS, as determined by proton nuclear magnetic resonance (^{1}H-NMR, see below) in our laboratory, was 94.5% (Hirai, Odani, & Nakajima, 1991). TPP (Sigma-Aldrich, MO, USA), cerium(IV) ammonium nitrate (CAN, Strem Chemicals, Inc., Newburyport, MA, USA), nitric acid 70% (Bio-Lab, Jerusalem, Israel), hydroquinone (HQ, Merck, Hohenbrunn, Germany) and tetramethylethylenediamine (TEMED, Alfa Aesar, Heysham, UK) were used as received. Methyl methacrylate (MMA) (99% purity, Alfa Aesar) was distilled under vacuum immediately before use.

2.2. Synthesis of CS-g-PMMA copolymer

A CS-*g*-PMMA copolymer containing 30% w/w PMMA was synthesized by the graft free radical polymerization of MMA in water (Noi et al., 2018). In brief, CS (0.4 g) was dissolved in nitric acid aqueous solution (0.05 M, 100 mL) previously degassed by sonication (30 min). TEMED solution (0.18 mL in 50 mL of degassed water) was added to the CS solution and purged with N_2 (30 min) at room temperature. The CS solution was heated to 35 °C and MMA dispersed in degassed water (48 mL) and added. Finally, a CAN solution (0.66 g in 2 mL of degassed water) was added and the reaction was allowed to proceed under N_2 atmosphere (3 h, 35 °C). The polymerization was terminated by the addition of HQ (0.13 g). Reaction crudes were dialyzed against distilled water (regenerated cellulose dialysis membrane, MWCO of 12–14 kDa, Spectra/Por® 4 nominal flat width of 75 mm, diameter of 48 mm and volume/length ratio of 18 mL/cm; Spectrum Laboratories, Inc., Rancho Dominguez, CA, USA) for at least 48 h with frequent water exchanges, frozen and freeze-dried (Labconco Free Zone 4.5 plus L Benchtop Freeze Dry System, Kansas City, MO, USA). The product was stored at 4 °C until use. The reaction yield was ~70%.

2.3. Characterization of the copolymer

2.3.1. Proton nuclear magnetic resonance spectroscopy (^{1}H-NMR)

^{1}H-NMR spectra were recorded in a 400-MHz Bruker® Avance III High Resolution spectrometer (Bruker BioSpin GmbH, Rheinstetten, Germany) and SpinWorks 4.0 software (University of Manitoba, Winnipeg, MB, Canada). To analyze the degree of deacetylation of pure CS, a 5% w/v solution was prepared in deuterium oxide (D_2O, Sigma-Aldrich) and trifluoroacetic acid (5% v/v, Sigma-Aldrich). The relative integration of the peak of CH_3- of the acetyl group at 1.8 ppm (*Intensity CH3*) and the sum of the relative integration of peaks at 2.8 and 3.3–4.0 ppm (*Intensity H2-H6*) were used to calculate the degree of deacetylation according to Eq. (1) (Hirai et al., 1991)

$$Degree\ of\ deacetylation\ (\%) = [1 - (\frac{1}{3} Intensity\ CH3 / \frac{1}{6}\ Intensity\ H2 - H6)] \tag{1}$$

The CS-*g*-PMMA copolymer was analyzed in 5% w/v DMSO-*d6* solution, since analysis in D_2O was inaccurate due to self-assembly that reduced the relative intensity of PMMA signals with respect to those of CS (Noi et al., 2018). Chemical shifts are expressed in ppm using the signal of DMSO (2.50 ppm) as internal standard. To quantify the relative PMMA weight content in the copolymer, a calibration curve of CS and MMA in D_2O was constructed using different CS/MMA weight ratios. The amount of PMMA in the CS-*g*-PMMA copolymer was determined by the integration of characteristic signals of each component in physical mixtures of CS:MMA of different weight ratios (0.67–10) and calculating the ratio between the integration of the characteristic signals of CS and PMMA and 2.8 and 0.8–1.0 ppm, respectively ($R^2 = 0.9851$). The ratio between the relevant peaks in the copolymer was calculated and interpolated in the calibration curve to determine the weight percentage (% w/w) of the hydrophobic component in the copolymer. For the physical mixture, pure CS and MMA were analyzed in D_2O with the addition of trifluoroacetic acid (5% v/v).

2.3.2. Fourier transform-infrared spectroscopy (FTIR)

Fourier Transform Infrared Spectroscopy (FTIR) samples were prepared at 25 °C on KBr (Merck Chemicals GmbH, Darmstadt, Germany) disks and pressed to transparency (Noi et al., 2018). FTIR spectra were recorded in an Equinox 55 spectrometer (Bruker Optics Inc., Ettlingen, Germany) from 4 000 to 400 cm^{-1} (32–64 scans with a resolution of 4 cm^{-1}).

2.3.3. Gel permeation chromatography (GPC)

GPC was used to determine the M_w, M_n and M_w/M_n (dispersity, $Đ$) and for molar mass distribution control. GPC separations were performed using a Deltachrom pump (Watrex Ltd., Prague, Czechia), Midas Spark autosampler (DataApex Ltd., Prague, Czechia), a PLaquagel-OH MIXED-H column (particle size 8 µm), and a DAWN Heleos II multi-angle light-scattering detector (MALS, Wyatt Technology Corp., Santa Barbara, CA, USA). Acetate buffer (0.2 M) was used as the mobile phase. The injection volume of the GPC system was 0.1 mL. Separations were performed at a mobile phase flow rate of 1 mL/min. The refractive index increment d*n*/d*c* of the copolymer was measured on a BI-DNDCW differential refractometer (Brookhaven Instruments Corp., Holtsville, NY, USA). The d*n*/d*c* value was obtained using potassium chloride calibration solutions (0.5–5 mg/mL).

2.3.4. Critical aggregation concentration (CAC)

The CAC was determined by DLS using a Zetasizer Nano-ZS (Malvern Instruments, Malvern, UK) operating at a scattering angle of 173°. Briefly, a stock aqueous solution (10 mg/mL) was prepared, serially diluted in the same medium to a final concentration range between 0.001 and 1 mg/mL with subsequent overnight stabilization at both 25 and 37 °C. Then, the intensity of the scattered light (derived count rate, DCR) expressed in kilo counts per second (kcps) was measured and plotted as a function of CS-*g*-PMMA concentration (% w/v). Data of these measurements were analyzed using CONTIN algorithms (Malvern Instruments). Data for each single specimen was the result of at least six runs. The aggregation was evidenced by a sharp increase in the scattering intensity and the intersection between the two straight lines was established as the CAC expressed in % w/v.

2.4. Preparation of CS-g-PMMA nanoparticles in water

Self-assembled nanoparticles were prepared by the solution casting method utilized for drug encapsulation that comprises the cosolubilization of the hydrophobic drug and the copolymer in the same solvent namely DMSO, drying under vacuum and redispersion in water (Gaucher et al., 2005). For this, CS-*g*-PMMA was dissolved in DMSO (5 mg/mL) with continuous stirring (24 h), at 37 °C. Subsequently, the solution was dried under deep vacuum, the product redispersed in water supplemented with acetic acid (pH = 5–5.5) and filtered through a 0.45 µm polyvinyl difluoride (PVDF) syringe filter (Merck Millipore Ltd., Tullagreen, Ireland). The final concentration of the copolymers was 1 mg/mL.

For physical stabilization, self-assembled nanoparticles were ionotropically crosslinked right after preparation by the addition of TPP water solution (1% w/v, 10 µL per 1 mL of nanoparticle dispersion) under continuous stirring (200 rpm, 25 °C) (Noi et al., 2018). Finally, the nanoparticles were filtered (0.45 µm PVDF syringe filter) into dust-free glass vials and incubated overnight at room temperature. To conduct SANS analysis, samples were prepared as mentioned above at a concentration of 5 mg/mL in D_2O supplemented with acetic acid-*d4* (Sigma-Aldrich).

2.5. Characterization of the nanoparticles

2.5.1. Light scattering

Nanoparticles were characterized by SLS and DLS by using an ALV-6010 instrument (ALV-GmbH, Langen, Germany) equipped with a 22 mW He–Ne laser in the angular range 30–150°. The obtained correlation functions were analyzed at each angle using the REPES algorithm (Jakeš, 1995), providing relaxation times τ. From the Stokes-Einstein Equation (Eq. (2)), the values of the hydrodynamic radii (R_h) were obtained.

$$D = \frac{k_B T}{6\pi\eta R_h} \tag{2}$$

where T is the absolute temperature, η is the viscosity of the solvent and k_B is the Boltzmann constant (Štepánek & Koňák, 1984). SLS data were analyzed using Zimm plots (Eq. (3))

$$\frac{Kc}{R(q)} = \frac{1}{M_w} + \frac{R_g^2 q^2}{3M_w^{NPs}} \tag{3}$$

where $R(q)$ is the Rayleigh ratio of the scattering intensity, q is the scattering vector defined as $q = (4\pi n/\lambda)\sin(\theta/2)$, n is the refractive index of the solvent, θ is the scattering angle, λ is the wavelength in vacuum, K is an optical constant and c is the concentration of the copolymer. $M_w{}^{NPs}$ is the weight-average molar mass of the particles and R_g is the radius of gyration.

The refractive index increment dn/dc of the solutions was measured as described above.

For some of the studies, a Zetasizer Nano-ZS operating at a scattering angle of 173° was used (see above). Measurements of zeta-potential were performed in the same instrument by converting measurements of electrophoretic mobility to zeta-potential (ζ, mV) using the Smoluchowski approximation.

Aggregation number N_{agg} of the nanoparticles was calculated according to Eq. (4)

$$N_{agg} = \frac{M_w^{NPs}}{M_w} \tag{4}$$

where M_w is the copolymer molecular weight measured by GPC and $M_w{}^{NPs}$ is the molecular weight of the nanoparticles, as determined by SLS.

2.5.2. Small-angle neutron scattering

SANS experiments were carried out at the SANS facility of the JEEP-II reactor (Kjeller, Norway). The wavelength was set with a velocity selector (Dornier), using a resolution ($\Delta\lambda/\lambda$) of 10%. The beam divergence was set by an input collimator (18.4 or 8.0 mm diameter), together with a circular 7 mm sample aperture. Each complete scattering curve was composed of three independent measurements, using different wavelength-distance combinations (5.1 Å/1.0 m, 5.1 Å/3.4 m, and 10.2 Å/3.4 m). The resulting q-range for the experiment was 0.006–0.35 Å^{-1}, where $q = (4\pi/\lambda)\sin(\theta/2)$.

Solutions were filled in 2 mm quartz cuvettes (Starna Scientific Ltd., Essex, UK). The cells were placed onto a copper-base for good thermal contact before being mounted onto the sample stage. The temperature was controlled by a water circulator, maintaining the set value to within ± 0.1 °C. In all of the SANS measurements, D_2O was used as a solvent instead of H_2O to obtain good contrast and low background.

Standard reductions of the scattering data, including transmission corrections, were conducted by incorporating data collected from the empty cell and the blocked-beam background. All the measurements were normalized to the beam monitor counts to compensate for any possible variations in the incoming beam flux. Finally, all data were transformed into an absolute scale (coherent differential cross section ($d\Sigma/d\Omega$)), making use of the intensity value registered in open beam measurements, before averaging radially to produce a $d\Sigma/d\Omega$ vs. q scattering profile.

We initially explored a spherical model to fit the data of the SANS patterns. The model curve is generally given by Eq. (5)

$$I(q) = \frac{N}{V}(\Delta\rho)^2 V_p^2 P(q) S(q) \tag{5}$$

where N is the number of particles within a volume V, $\Delta\rho$ is the difference in scattering length density (SLD) between particle and solvent (scattering contrast), V_p is the particle volume, P(q) is the particle form factor, and S(q) is the particle structure factor. Since the suspensions of particles in the present case are quite diluted, we assumed non-interacting particles and for this case S(q) = 1. The form factor for homogenous spherical objects with a radius R is expressed by Eq. (6)

$$P(q) = \left[\frac{3}{(qR)^3}\{\sin(qR) - qR\cos(qR)\}\right]^2 \tag{6}$$

The SLD values of PMMA, CS and D_2O are 1.07×10^{-6} (Akers, Nelson, Williams, & McGillivray, 2015), 1.4×10^{-6} and 6.36×10^{-6} Å^{-2}, respectively.

Due the lack of good fitting with the spherical model (even when including significant polydispersity), we also utilized a model that can describe entities with different characteristic sizes that coexist in the same sample, namely the unified power-R_g model (Beaucage model), to analyze the SANS data obtained with these self-assembled nanoparticles. This model has been shown to give a good representation of many systems that consist of individual particles with a certain polydispersity that can cluster together into larger structures with varying overall characteristic sizes (Beaucage, 1995; G. Beaucage, Kammler, & Pratsinis, 2004). As can be inferred from Eq. (7), the basic version of this function (1-level) is the combination of a Guinier term describing a characteristic size R_g plus a power-law term describing the scattering of the tail of the pattern (G and B give the overall scaling of the intensity for each of these two terms).

$$I(q) = G\exp\left(\frac{-q^2R_g^2}{3}\right) + B\left\{\left[\mathrm{erf}\left(\frac{qR_g}{\sqrt{6}}\right)\right]^3/q\right\}^\alpha \tag{7}$$

Where α is a power law exponent and "erf" is the standard error function.

2.5.3. Transmission electron microscopy

Micrographs of the amphiphilic species were obtained with a TEM microscope Tecnai G2 Spirit Twin 12 (FEI, Brno, Czechia) using the bright field imaging mode at the accelerating voltage 120 kV. The specimens for TEM were prepared by dropping 4 µL of sample onto a microscopic copper TEM grid (300 mesh) coated with a thin and electron-transparent carbon film. After 15 min of sedimentation, the sample excess was removed by touching the bottom of the grid with a filtering paper (fast drying method). This fast removal of the solution was performed to minimize oversaturation during the drying process (Petrova, Jager, & Venturini, 2014). Subsequently, the particles were negatively stained with uranyl acetate (Electron Microscopy Sciences, Hatfield, PA, USA). For this purpose, 2% w/w solution was dropped onto the dried nanoparticles and removed after 15 s in the same way as the previous solution. The sample was finally left to dry completely at ambient temperature in air and then observed in the TEM microscope.

In order to confirm the morphology observed by TEM, one chosen sample was additionally observed using cryo-TEM for which 3 µL of the sample solution was dropped to an electron microscopy grid covered with a holey carbon supporting film (Electron Microscopy Sciences), which was hydrophilized just before the experiment by means of glow discharge (Expanded Plasma Cleaner, Harrick Plasma, Ithaca, NY, USA). The excess of the solution was removed by blotting with a piece of filter paper for 1 s, and the grid was plunged into liquid ethane held at −181 °C. The frozen sample was then immediately transferred into the microscope equipped with a cryo-holder (cryo-specimen holder, Gatan Inc., Pleasanton, CA, USA) and visualized at −173 °C at an accelerating voltage of 120 kV.

3. Results and discussion

3.1. Synthesis and characterization of the CS-g-PMMA copolymer

The amphiphilic CS-g-PMMA copolymer was synthesized by the free radical polymerization of MMA using CAN as initiator (Noi et al., 2018; Pourjavadi, Mahdavinia, Zohuriaan-Mehr, & Omidian, 2003; Menaker Raskin et al., 2016), as presented in Fig. 1.

^{1}H-NMR and FTIR spectra confirmed the graft polymerization (Noi et al., 2018). The content of PMMA was determined using ^{1}H-NMR and was found to be 30% w/w. GPC analysis of the copolymer revealed a monomodal distribution with a decrease in the molar mass (M_n = 8700 g/mol, M_w = 11,000 g/mol, Đ = 1.26) when compared to pristine CS (M_n = 53,000 g/mol, M_w = 79,000 g/mol, Đ = 1.49) (Fig. 2). These results indicated that under the reaction conditions, CS undergoes free radical-induced depolymerization (Menaker Raskin et al., 2016; Thimma, Reddy, & Tammishetti, 2003). However, unimers or unimolecular micelles of size < 10 nm could not be detected utilizing scattering techniques (Menaker Raskin et al., 2016).

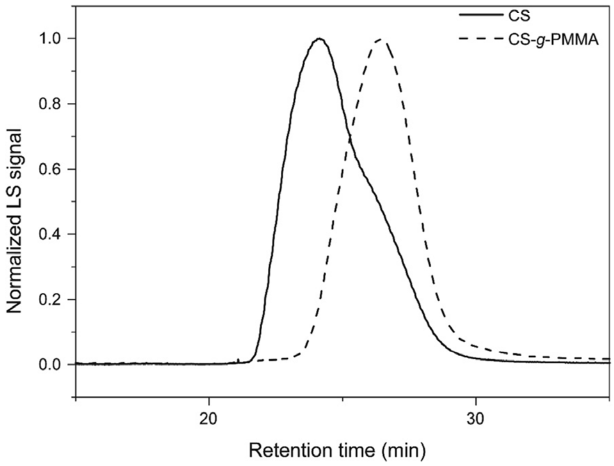

Fig. 2. Normalized GPC curves of pure CS and CS-g-PMMA. Normalized light scattering (LS) detector signals are shown.

3.2. Preparation and characterization of the CS-g-PMMA nanoparticles

The self-assembly of amphiphilic copolymers governs the structure, size, size distribution and ultimately the encapsulation capacity of the self-assembled structures. The self-assembly mechanism of non-ionic block copolymers such as poly(ethylene oxide)-poly(propylene oxide) derivatives is often entropy-driven and associated with the release of water hydration molecules from the hydrophobic block (Alexandridis, Holzwarth, & Hatton, 1994). In addition, the structure of the aggregates can often be easily anticipated by means of the weight ratio between hydrophilic and hydrophobic blocks (Discher & Ahmed, 2006). Conversely, the introduction of electrostatic interactions in the polymer backbone or the side-chain affects both the single polymer behavior and the micellar structure (Behrens, Kjøniksen, Zhu, Nystrom, & Pedersen, 2012). In the case of graft amphiphiles, additional parameters such as molecular architecture, chemical nature and flexibility/rigidity of the

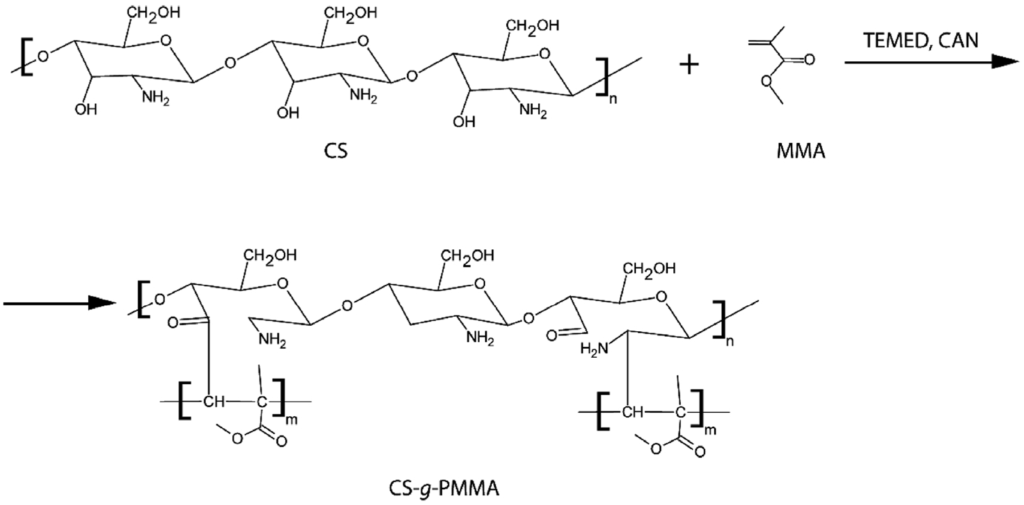

Fig. 1. Synthetic pathway of CS-g-PMMA copolymers by the free radical graft polymerization of MMA.

hydrophilic backbone, length and density of tethered side-chain blocks and the presence of functional groups that contribute to the physical stabilization of the assembled structure by inter- and intramolecular bonds also play a key role in the aggregation pattern (Cai, Lin, Chen, & Tian, 2010; Zhang et al., 2007). Graft amphiphiles can also form unimolecular micelles that are fully physically stable (Fan, Li, & Loh, 2016; Newkome, Baker, & Saunders, 1991). Under the nanoparticle preparation conditions (pH = 5.5), CS is partly positively-charged because its pK_a is approximately 6.5. On one hand, this pH favors CS self-assembly (Dey, Kamat, Nayak, Danino, & Kesselman, 2018), while on the other it might alter the aggregation pattern (Behrens et al., 2012).

In a previous work, we characterized the nanostructure of CS-*g*-PNiPAAm amphiphilic nanoparticles after ionotropic crosslinking with an optimized amount of TPP using cryo-TEM (Menaker Raskin et al., 2016). Results suggested the formation of multi-micellar particles. A similar analysis using non-crosslinked counterparts failed probably due to the fast disintegration of the thermo-responsive nanoparticles upon sample preparation or insufficient contrast between the nanoparticles and water. PMMA is more hydrophobic than PNiPAAm and its chain flexibility is different. Hence, in this work, we conducted for the first time a comprehensive characterization of the self-assembly behavior of a CS-*g*-PMMA copolymer containing 30% w/w and an estimated hydrophilic-lipophilic balance (HLB) of 14 according to the Griffin's method (Griffin, 1954).

As we previously reported, this CS-*g*-PMMA displays a CAC of 0.05% w/v (0.5 mg/mL) at 25 and 37 °C (Supplementary Fig. S1). This CAC value is approximately two orders of magnitude higher than that of CS-*g*-oligo(ε-caprolactone) (CS-*g*-PCL) copolymers (Glisoni et al., 2015) or CS hydrophobized with *N*-palmitoyl (Jiang, Quan, Liao, & Wang, 2006). The reason for this behavior is the lower intrinsic hydrophobicity of PMMA with respect to PCL or fatty acids (Son, Linh, Yang, & Lee, 2013). In this work, nanoparticles were produced by the solvent casting and water redispersion method (Fig. 3A). For physical stabilization, self-assembled nanoparticles were ionotropically crosslinked by the addition of a small volume of TPP water solution immediately after preparation.

3.2.1. Light scattering

Prepared dispersions were primarily subjected to light scattering analysis. For this purpose, samples prepared at a concentration of 1 mg/mL were used for both DLS and SLS. Not surprisingly, light scattering analysis indicated that direct solubilization of CS-*g*-PMMA in water leads to spontaneous self-association and the formation of nanoparticles with an overall positive surface charge owing to the presence of positively-charged amine moieties in the side-chain of CS (Table 1). It is worth pointing out that TPP ionotropic crosslinking led to a decrease of the zeta-potential from + 42 to + 22 mV owing to the partial neutralization of the amine groups (Jonassen, Kjøniksen, & Hiorth, 2012).

The DLS distribution function of the non-crosslinked CS-*g*-PMMA nanoparticle dispersion is portrayed as a broad peak, suggesting a relatively broad size distribution of nanoparticles (Fig. 4). The z-averaged hydrodynamic radius, R_h, was found to be 94 nm (Table 1). The average density of the nanoparticles (d) can be estimated according to Eq. (8) (Koňák et al., 2008)

$$d = \frac{3M_w^{NPs}}{4\pi N_A R_h^3}, \tag{8}$$

where N_A is Avogadro's constant. The average density d of the non-crosslinked nanoparticles was found to be 0.002 g/mL. This indicates that a major part of the nanoparticle volume is filled with water and that the particles are very highly swollen in the aqueous medium. TPP-crosslinked nanoparticles also revealed a relatively broad distribution (Fig. 4); with R_h being 67 nm A decrease of the R_h and an increase in the density d from 0.002 to 0.11 mg/mL suggest that a denser matrix is formed upon crosslinking. This matrix shrinkage also explains the decrease in size (Fig. 4).

As described below, the DLS distribution functions and corresponding R_h values were in line with TEM analysis (see below). In addition, TPP increased the aggregation number from approximately 455 (in the non-crosslinked) to 6455 in the crosslinked counterparts due to inter- and intra-micellar crosslinking (Jonassen & Kjøniksen, 2011; Jonassen, Kjøniksen, & Hiorth, 2012). To prevent the formation of these multi-micellar structures, the crosslinking stage should be conducted under more diluted conditions (still above the CAC) that

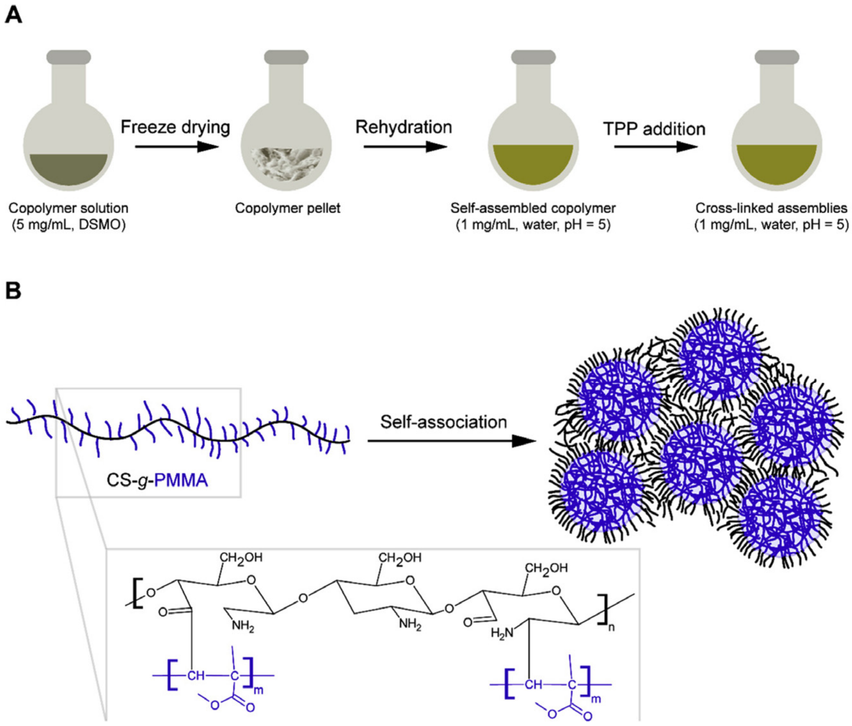

Fig. 3. (A) Preparation of CS-*g*-PMMA nanoparticles by the solvent casting and water redispersion method and (B) proposed self-association pattern of CS-*g*-PMMA in water to form nanoparticles. Physical stabilization was achieved by ionotropic crosslinking with a small volume of TPP (A).

Table 1
Characterization of CS-*g*-PMMA nanoparticles by DLS and SLS.

Sample	R_h (nm)[a]	R_g (nm)[b]	M_w^{NP} (g/mol)[b]	*d* (g/mL)[c]	N_{agg}[c]	*Zeta-potential* (mV)
Non-crosslinked nanoparticles	94	106	5.0×10^6	0.002	455	+42
TPP-crosslinked nanoparticles	67	84	7.1×10^7	0.11	6455	+22

[a] Measured by DLS.
[b] Measured by SLS.
[c] Values obtained from GPC and SLS were used for the calculation.

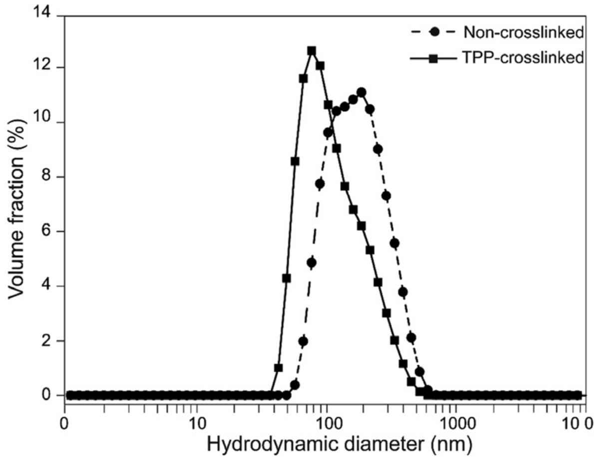

Fig. 4. Volume-weighted distribution functions of non-crosslinked and TPP-crosslinked CS-*g*-PMMA nanoparticles, as measured by DLS. The concentration is 1 mg/mL.

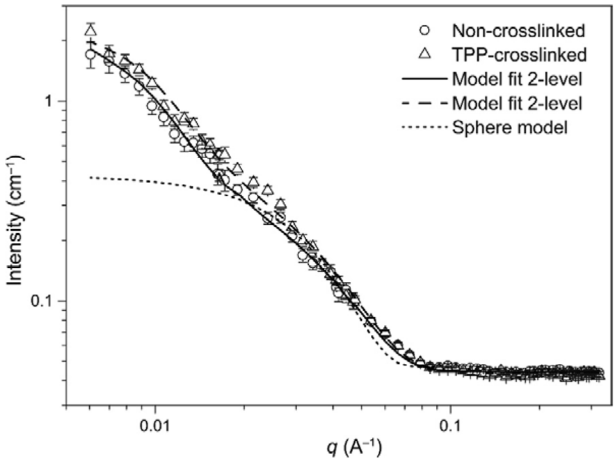

Fig. 5. SANS analysis of non-crosslinked and TPP-crosslinked CS-*g*-PMMA nanoparticles (5 mg/mL), at 25 °C. Both continuous and dashed lines show fit with a 2-level Beaucage model. The dotted line shows a fit with a spherical model with a radius corresponding to the smallest size in the Beaucage model.

increase the distance between nanoparticles.

The ratio between R_g and R_h can be used as a measure of the distribution of material through the particle. For monodisperse hard spheres of constant density, this ratio is equal to 0.77 (Varga, Gilanyi, Meszaros, Filipcsei, & Zrinyi, 2001). We found a R_g/R_h ratio of 1.12 for the non-crosslinked particles and 1.31 for the crosslinked ones, suggesting that both cases represent swollen structures. Furthermore, the higher ratio for the crosslinked particles indicates a smaller contribution of loose chains in the surface layer after crosslinking, which may be expected. This behavior is reflected also in the lower R_h observed for the crosslinked particles. Of note is that the crosslinking does not seem to introduce strong density changes inside the particles. This was corroborated by the SANS data (discussed later) that indicated that the particles are relatively open structures internally, both before and after crosslinking.

As explained above, the zeta-potential became less positive owing to the involvement of primary amine groups of CS in the formation of a polyelectrolyte complex with TPP (Table 1). These results were in good agreement with the study by Jonassen et al. who investigated the effect of TPP-crosslinking on the stability and colloidal properties of CS (Jonassen et al., 2012a).

3.2.2. *Small-angle neutron scattering*

In many cases, DLS analysis does not accurately measure the size and size distribution of nanoparticles and the averages that are obtained usually overestimate the actual size, as the scattering intensity depends very strongly on the radius (to the power of six in the Rayleigh approximation). Hence, the resulting size distributions by intensity are therefore biased towards larger sizes (Domingos et al., 2009; Zölls, Tantipolphan, Wiggenhorn, Winter, Jiskoot, Friess & Hawe, 2012). Due to this fact, smaller species present in the CS-*g*-PMMA samples (i.e., probably unimolecular particles; see above) could not be probed and on this basis, we used a combination of SANS and TEM to gain a better understanding of the aggregate sizes before and after the crosslinking. Normalized SANS data for both non-crosslinked and TPP-crosslinked CS-*g*-PMMA nanoparticles are shown in Fig. 5.

The scattering patterns do not resemble typical polymeric micelles (He & Garamus, 2002), and a low absolute value of the scattering (approximately 1 cm^{-1} in the low-*q* range) indicates that the scattering entities are relatively open structures, giving limited contrast to the surroundings, also after crosslinking. This fact also supports the low *d* values of both non-crosslinked and crosslinked nanoparticles (Table 1), and it is likely that the nanostructures are highly hydrated in water which is in good agreement with the high hydrophilicity of CS, especially at slightly acid pH.

A simple Guinier analysis did not give concluding results with respect to sizes due to the particular shape of the pattern, and a spherical model could not be properly fitted to the data either (*cf.* dotted curve in Fig. 5). However, the shape of the SANS plots (*cf.* a small plateau in the medium *q*-range and start of a plateau in the lowest *q*-range) can be explained by the presence of at least two characteristic sizes consistent with a population of small particles together with larger particles, or conversely, small particles clustered into larger multi-micellar nanostructures. The fitting of the curves in Fig. 5 was carried out using the Beaucage model (2-level). This gives as output a small size population of R_g = 50 Å, and a larger size of R_g = 380 Å. If one assumes that these sizes represent spherical structures, one can calculate the corresponding radii from the expression $R_g^2 = (3/5)R^2$, which gives values of approximately 65 and 490 Å, respectively, or diameters of 130 (13 nm) and 980 Å (98 nm). It is not, however, possible to conclude whether the small size population corresponds to free copolymer or, as visualized by TEM, to building blocks having a size ca 6–10 nm (see below).

The results were the same for the two samples – within the uncertainty of the analysis – since the small difference observed in the patterns could be removed by a simple vertical scaling. The fact that a plateau is not fully developed in the low-*q* range means that the size of the large particle cannot be clearly determined from SANS, and that there could be even larger entities present (too large to be fully probed by SANS, *cf.* results from DLS and TEM). In any case, our SANS findings

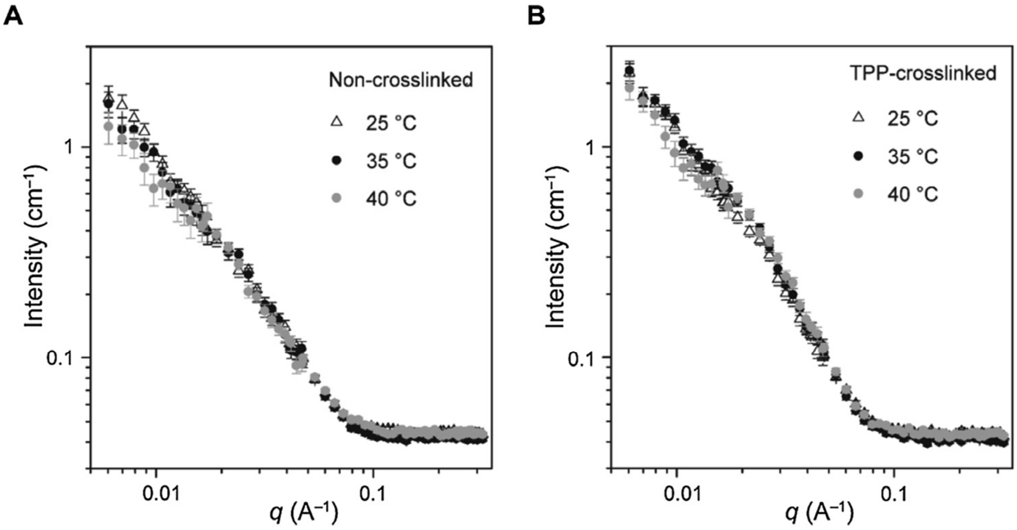

Fig. 6. SANS of CS-*g*-PMMA nanoparticles (5 mg/mL) at different temperatures. (A) Non-crosslinked and (B) TPP-crosslinked nanoparticles.

would be in accordance with a situation where CS-*g*-PMMA nanoparticles are formed by small particles clustered together into larger units, which is in good agreement with data reported elsewhere for CS-*g*-PNiPAAm nanoparticles (Menaker Raskin et al., 2016).

The self-assembly of CS-g-PMMA copolymers as estimated by CAC is similar at 25 and 37 °C (Noi et al., 2018). However, the drug encapsulation process could undergo changes under different temperature conditions owing to the alteration of the nanoparticle physical stability. In this context, SANS measurements were also conducted at different temperatures and, in general, the nanoparticles showed good temperature stability due to the low thermo-responsiveness of the components (Fig. 6).

For non-crosslinked nanoparticles there was a slight though systematic drop in the low-*q* intensity upon the temperature increase from 25 to 40 °C. This could be a sign of a small physical instability or some re-arrangement within the nanoparticle after 2 h incubation at higher temperatures. On the other hand, results showed full overlap in the medium and high-*q* range, demonstrating that the interior of the particles was not affected by the change in temperature. For the crosslinked nanoparticles, data overlapped (within the uncertainty) over the whole range, and no significant changes with temperature could be observed, confirming the higher physical stability after the crosslinking.

3.2.3. *Transmission electron microscopy*

Representative TEM microphotographs of both non-crosslinked and TPP-crosslinked samples are presented in Fig. 7. Non-crosslinked CS-*g*-PMMA nanoparticles showed a major population of isometric and spherical-like aggregates with a size of approximately 40–50 nm together with a small amount of particles with a size between 6 and 10 nm that would fit well the presence of unimolecular micelles (Fig. 7A). The cryo-TEM results (Fig. 7B) proved that the aggregates were present also in the hydrated state and were not formed during the drying process (i.e., possible sample preparation artifacts). At the same time, it evidenced that some aggregates deviated from the almost spherical shape.

In any case, these results were in good agreement with the above discussed SANS analysis and suggested that this CS-*g*-PMMA copolymer presents a complex self-association pattern where small aggregates re-assemble into larger ones (Fig. 3B).

The negative staining with uranyl acetate (Fig. 7**A** and **7 C**) revealed the presence of small building blocks (probably unimolecular micelles having size ca 6–10 nm). These smaller nanoparticles were present in both non-crosslinked (Fig. 7A) and TPP-crosslinked sample (Fig. 7C). Larger aggregates in the TPP-crosslinked sample (Fig. 7C) exhibited similar size like those within the non-crosslinked system (c.f., Fig. 7A), though their structure was more compact and homogeneous. Moreover, certain fraction of the agglomerates in the TPP-crosslinked system formed even larger entities (ca 100–200 nm). For more TEM micrographs showing the morphology of the studied particles, see the Supplementary Information File (Supplementary Figs. S2 and S3). Of note, that sizes measured by TEM are usually smaller than by DLS, due to the above-mentioned overestimation effects of DLS. At the same time, the statistical relevance of scattering experiments is higher than microscopy. Despite this fact, these findings were in agreement with DLS results. In other words, broad size distributions were revealed for both non-crosslinked and TPP-crosslinked samples.

Overall, our results indicate that the hydrophobization of the CS side-chain leads to a complex array of small unimolecular and/or small-aggregation number "building blocks" that further self-assemble into larger amphiphilic nanoparticles (Dashtimoghadam, Mirzadeh, Taromi,

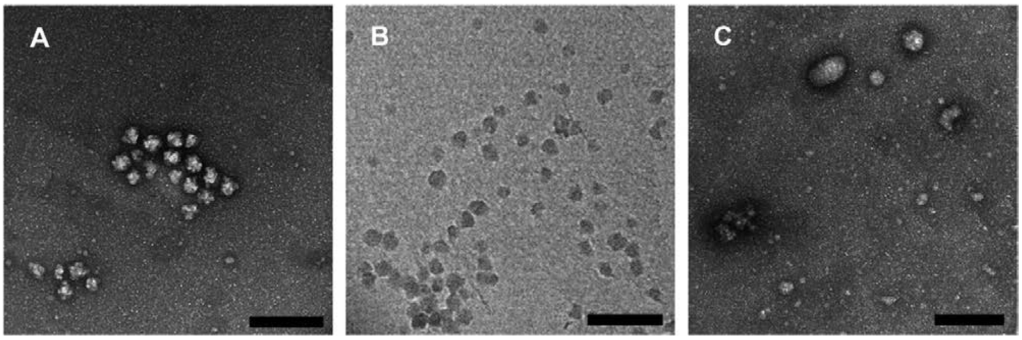

Fig. 7. Micrographs of (A, B) non-crosslinked and (C) TPP-crosslinked nanoparticles. Micrographs as results from (A, C) conventional TEM performed with negative staining with 2% w/w uranyl acetate and (B) cryo-TEM. Scale bars: 200 nm.

& Nyström, 2013). It is unknown if this phenomenon is unique for CS, as such comprehensive physicochemical investigation of CS-based nanoparticles, to the best of our knowledge, was not previously described in the literature. Overall, these results support our preliminary studies dealing with CS-*g*-PNiPAAm (Menaker Raskin et al., 2016) and CS-*g*-PMMA (Noi et al., 2018) and highlight that owing to the polycationic nature, the self-association of CS-based graft amphiphiles remains a very complex phenomenon that may be influenced not only by the medium conditions (e.g., pH and ionic strength) but also by molecular features such as molecular weight of the CS backbone and the grafted blocks, architecture, and the density of the tethered side chains.

4. Conclusions

In this study, we investigated a novel mucoadhesive CS-*g*-PMMA amphiphilic copolymer and its spontaneous behavior after solubilization in water. By means of a comprehensive analysis by different complementary techniques, we found that the CS-*g*-PMMA self-assembled dispersions exhibit a complex self-assembled hierarchical structure based on low aggregation number particles (ca 6–10 nm in diameter) associating into larger species revealing a broad size-distribution. Furthermore, our study highlights the need for more in-depth investigations to characterize the self-association of CS amphiphiles and the difficulty to extrapolate this behavior to a broad spectrum of derivatives.

Acknowledgments

A.S. and I.S. acknowledge the funding of the European Union's - Seventh Framework Programme under grant agreement #612765-MC-NANOTAR, the Israel Science Foundation (ISF Grant #269/15) and the Russell Berrie Nanotechnology Institute (Technion). Financial support from the Czech Academy of Sciences (project no. ISR-17-21) that contributed to the Czech-Israel collaboration is gratefully acknowledged. J.T. acknowledges support from the Charles University (project no. SVV260440) and the Czech Science Foundation (grant nos. 17-07164S and 17-09998S), and thanks Dr. Petr Štěpánek for his critical reading of the manuscript. D.R. acknowledges support from the Scientific Grant Agency VEGA (grant no. 2/0177/17) and the Slovak Research and Development Agency (project NANOSEG No. 16-0550). Electron microscopy at the Institute of Macromolecular Chemistry AS CR was supported by project TE01020118 (Technology Agency of Czechia).

Appendix A. Supplementary data

Supplementary material related to this article can be found, in the online version, at doi:https://doi.org/10.1016/j.carbpol.2019.02.022.

References

Akers, P. W., Nelson, A. R. J., Williams, D. E., & McGillivray, D. J. (2015). Formation of hydrated layers in PMMA thin films in aqueous solution. *Applied Surface Science, 353*, 829–834.

Alexandridis, P., Holzwarth, J. F., & Hatton, T. A. (1994). Micellization of polyethylene oxide)-poly(propylene oxide)-poly(ethylene oxide) triblock copolymers in aqueous solutions: Thermodynamics of copolymer association. *Macromolecules, 27*(9), 2414–2425.

Barua, S., & Mitragotri, S. (2014). Challenges associated with penetration of nanoparticles across cell and tissue barriers: A review of current status and future prospects. *Nano Today, 9*(2), 223–243.

Beaucage, B. Y. G. (1995). Approximations leading to a unified exponential/power-Law approach to small-angle scattering. *Journal of Applied Crystallography, 28*, 717–728.

Beaucage, G., Kammler, H. K., & Pratsinis, S. E. (2004). Particle size distributions from small-angle scattering using global scattering functions. *Journal of Applied Crystallography, 37*, 523–535.

Behrens, M. A., Kjøniksen, A., Zhu, K., Nystrom, B., & Pedersen, J. S. (2012). Small-angle X-ray scattering study of charged triblock copolymers as a function of polymer concentration, temperature, and charge screening. *Macromolecules, 45*(1), 246–255.

Blanco, E., Shen, H., & Ferrari, M. (2015). Principles of nanoparticle design for overcoming biological barriers to drug delivery. *Nature Biotechnology, 33*(9), 941–951.

Cabral, H., Matsumoto, Y., Mizuno, K., Chen, Q., Murakami, M., Kimura, M., et al. (2011). Accumulation of sub-100 nm polymeric micelles in poorly permeable tumours depends on size. *Nature Nanotechnology, 6*(12), 815–823.

Cai, C., Lin, J., Chen, T., & Tian, X. (2010). Aggregation behavior of graft copolymer with rigid backbone. *Langmuir, 26*(4), 2791–2797.

Chiappetta, D. A., & Sosnik, A. (2007). Poly(ethylene oxide)-poly(propylene oxide) block copolymer micelles as drug delivery agents: Improved hydrosolubility, stability and bioavailability of drugs. *European Journal of Pharmaceutics and Biopharmaceutics, 66*(3), 303–317.

Croy, S. R., & Kwon, G. S. (2006). Polymeric micelles for drug delivery. *Current Pharmaceutical Design, 12*(36), 4669–4684.

Dashtimoghadam, E., Mirzadeh, H., Taromi, F. A., & Nyström, B. (2013). Microfluidic self-assembly of polymeric nanoparticles with tunable compactness for controlled drug delivery. *Polymer, 54*(18), 4972–4979.

Dey, A., Kamat, A., Nayak, S., Danino, D., & Kesselman, E. (2018). Colloids and Surfaces B: Biointerfaces Role of proton balance in formation of self-assembled chitosan nanoparticles. *Colloids and Surfaces B: Biointerfaces, 166*, 127–134.

Discher, D. E., & Ahmed, F. (2006). Polymersomes. *Annual Reviews in Biomedical Engineering, 8*, 323–341.

Domingos, R. F., Ju-nam, Y. O. N., Reid, M. M., Tufenkji, N., Lead, J. R., & Leppard, G. G. (2009). Characterizing manufactured nanoparticles in the environment: Multimethod determination of particle sizes. *Environmental Science & Technology, 43*(19), 7277–7284.

Fan, X., Li, Z., & Loh, X. J. (2016). Recent development of unimolecular micelles as functional materials and applications. *Polymer Chemistry, 7*, 5898–5919.

Friess, W., & Hawe, A. (2012). Particles in therapeutic protein formulations: Part 1. *Journal of Pharmaceutical Sciences, 101*(3), 914–935.

Gaucher, G., Dufresne, M. H., Sant, V. P., Kang, N., Maysinger, D., & Leroux, J. C. (2005). Block copolymer micelles: Preparation, characterization and application in drug delivery. *Journal of Controlled Release, 109*(1-3), 169–188.

Glisoni, R. J., Quintana, L., Molina, M, S. S., Calderón, M., Moglioni, A. G., & Sosnik, A. (2015). Chitosan-g-oligo(epsilon-caprolactone) polymeric micelles: Microwave-assisted synthesis and physicochemical and cytocompatibility characterization. *Journal of Materials Chemistry B, 3*, 4853–4864.

Griffin, W. C. (1954). Calculation of HLB values of non-ionic surfactants. *Journal of the Society of Cosmetic Chemists, 5*(4), 249–256.

He, L., & Garamus, V. M. (2002). Comparison of small-angle scattering methods for the structural analysis of octyl-maltopyranoside micelles. *The Journal of Physical Chemistry B, 106*(31), 7596–7604.

Hirai, A., Odani, H., & Nakajima, A. (1991). Determination of degree of deacetylation of chitosan by ^{1}H NMR spectroscopy. *Polymer Bulleting, 26*(1), 87–94.

Jakeš, J. (1995). Regularized positive exponential sum (REPES) program - a way of inverting laplace transform data obtained by dynamic light scattering. *Collections of Czechoslovak Chemical Communications, 60*(11), 1781–1797.

Jiang, G., Quan, D., Liao, K., & Wang, H. (2006). Novel polymer micelles prepared from chitosan grafted hydrophobic palmitoyl groups for drug delivery. *Molecular Pharmaceutics, 3*(2), 152–160.

Jonassen, H., & Kjøniksen, A. (2011). Optical-scattering method for the determination of the local polymer concentration inside nanoparticles. *Physical Review E, 84*(2), 1–4.

Jonassen, H., Kjøniksen, A., & Hiorth, M. (2012a). Effects of ionic strength on the size and compactness of chitosan nanoparticles. *Colloid and Polymer Science, 290*(10), 919–929.

Jonassen, H., Kjøniksen, A., & Hiorth, M. (2012b). Stability of chitosan nanoparticles cross-linked with tripolyphosphate. *Biomacromolecules, 13*(11), 3747–3756.

Koňák, C., Šubr, V., Kostka, L., Štepánek, P., Ulbrich, K., & Schlaad, H. (2008). Coating of vesicles with hydrophilic reactive polymers. *Langmuir, 24*(14), 7092–7098.

Lai, S. K., Wang, Y. Y., & Hanes, J. (2009). Mucus-penetrating nanoparticles for drug and gene delivery to mucosal tissues. *Advanced Drug Delivery Reviews, 61*(2), 158–171.

Lee, J. S., & Feijen, J. (2012). Polymersomes for drug delivery : Design, formation and characterization. *Journal of Controlled Release, 161*(2), 473–483.

Liu, Z., Zhao, G., & Yu, J. (2011). Preparation and properties of chitosan-graft-poly(methyl methacrylate) nanoparticles using potassium diperiodatocuprate (III) as an initiator. *Journal of Applied Polymer Science, 120*(5), 2707–2715.

Lukyanov, A. N., & Torchilin, V. P. (2004). Micelles from lipid derivatives of water-soluble polymers as delivery systems for poorly soluble drugs. *Advanced Drug Delivery Reviews, 56*(9), 1273–1289.

Newkome, G. R., Baker, G. R., & Saunders, M. J. (1991). Unimolecular micelles. *Angewandte Chemie International Edition, 30*(9), 1178–1180.

Noi, I., Schlachet, I., Kumarasamy, M., & Sosnik, A. (2018). Permeability of novel chitosan- g -poly (methyl methacrylate) amphiphilic nanoparticles in a model of small intestine in vitro. *Polymers, 2018*(10), 478.

Olmsted, S. S., Padgett, J. L., Yudin, A. I., Whaley, K. J., Moench, T. R., & Cone, R. A. (2001). Diffusion of macromolecules and virus-like particles in human cervical mucus. *Biophysical Journal, 81*(4), 1930–1937.

Petrova, S. P., Jager, A., & Venturini, C. (2014). Novel poly(ethylene oxide monomethyl ether)-b- poly(3-caprolactone) diblock copolymers containing a pH-acid labile ketal group as a block linkage. *Polymer Chemistry, 5*, 3884–3893.

Pourjavadi, A., Mahdavinia, G. R., Zohuriaan-Mehr, M. J., & Omidian, H. (2003). Modified chitosan. I. Optimized cerium ammonium nitrate-induced synthesis of chitosan-graft-polyacrylonitrile. *Journal of Applied Polymer Science, 88*(8), 2048–2054.

Menaker Raskin, M., Schlachet, I., & Sosnik, A. (2016). Mucoadhesive nanogels by ionotropic crosslinking of chitosan-g-oligo(NiPAam) polymeric micelles as novel drug nanocarriers. *Nanomedicine (London), 11*(3), 217–233.

Sogias, I. A., Williams, A. C., & Khutoryanskiy, V. V. (2008). Why is chitosan mucoadhesive? *Biomacromolecules, 9*(7), 1837–1842.

Son, S.-R., Linh, N.-T. B., Yang, H.-M., & Lee, B. T. (2013). In vitro and in vivo evaluation of electrospun PCL/PMMA fibrous scaffolds for bone regeneration. *Science and Technology of Advanced Materials, 14*(1), 015009.

Sosnik, A., & Menaker Raskin, M. (2015). Polymeric micelles in mucosal drug delivery: Challenges towards clinical translation. *Biotechnology Advances, 33*(6), 1380–1392.

Sosnik, A., Neves, J. das, & Sarmento, B. (2014). Mucoadhesive polymers in the design of nano-drug delivery systems for administration by non-parenteral routes: A review. *Progress in Polymer Science, 39*(12), 2030–2075.

Štepánek, P., & Koňák, Č. (1984). Quasielastic light scattering from polymers, colloids and gels. *Advances in Colloid and Interface Science, 21*(3–4), 195–274.

Thimma, R. T., Reddy, N. S., & Tammishetti, S. (2003). Synthesis and characterization of guar gum-grafted-polyacrylonitrile. *Polymers for Advanced Technologies, 14*(10), 663–668.

Torchilin, V. P. (2001). Structure and design of polymeric surfactant-based drug delivery systems. *Journal of Controlled Release, 73*(2–3), 137–172.

Varga, I., Gilanyi, T., Meszaros, R., Filipcsei, G., & Zrinyi, M. (2001). Effect of cross-link density on the internal structure of poly(N-isopropylacrylamide) microgels. *The Journal of Physical Chemistry B, 105*(38), 9071–9076.

Zhang, L., & Eisenberg, A. (1995). Multiple morphologies of “crew-cut” aggregates of polystyrene-b-poly (acrylic acid) block copolymers. *Science, 263*, 1728–1730.

Zhang, L., Lin, J., & Lin, S. (2007). Aggregate morphologies of amphiphilic graft copolymers in dilute solution studied by self-consistent field theory. *The Journal of Physical Chemistry B, 111*(31), 9209–9217.

Zheng, X. F., Lian, Q., Yang, H., & Wang, X. (2016). Surface molecularly imprinted polymer of chitosan grafted Poly(methyl methacrylate) for 5-fluorouracil and controlled release. *Scientific Reports, 6*, 21409.

PUBLICATION P6

Trousil J., Hrubý M. Novel nanoparticle delivery systems for rifampicin: an effective strategy against tuberculosis? *Nanomedicine (Lond.).* 2017, 12 (12), 1359–1361. IF = 5.00

J.T. wrote the paper. M.H. conceptualized the manuscript structure.

Editorial

For reprint orders, please contact: reprints@futuremedicine.com

Nanomedicine

Novel nanoparticle delivery systems for rifampicin: an effective strategy against tuberculosis?

First draft submitted: 3 April 2017; Accepted for publication: 11 April 2017; Published online: 19 May 2017

Keywords: nanoparticles • rifampicin • tuberculosis

Tuberculosis (TB) is a highly infectious disease caused by *Mycobacterium tuberculosis*. Approximately, a third of the world's population is infected with *M. tuberculosis*, resulting in a global health problem. Although potentially curative treatments have been available for approximately 50 years, TB remains the leading cause of preventable death in the world [1,2].

The major cause of failure in the treatment and eradication of TB is the ability of mycobacteria to survive and persist in alveolar macrophages, which become reservoirs for this intracellular pathogen. This strategy allows mycobacterial cells to not only become hidden from immune defense but also insusceptible to the effects of conventional drugs. The waxy coating on the surface of the mycobacterial cell wall, which is mainly composed of long-chain 2-alkyl-branched 3-hydroxyl fatty acids called mycolic acids, contributes to this ability to survive. Because of this hydrophobic surface, *M. tuberculosis* is resistant to dehydration, has low permeability to antituberculotics and has a high ability to persist [3].

Two final and important complications of TB are the evolution of *M. tuberculosis* strains that possess multidrug resistant (defined as resistance to both rifampicin and isoniazid) and extensively drug resistant (defined as resistance to at least one second-line injectable drug and any fluoroquinolone drug) characteristics and the increase in the number of patients with TB who are coinfected with HIV [1].

Despite these complications, the existing anti-TB drugs and treatment schedule are still largely effective. Drug-susceptible TB can be effectively treated with a cocktail of first-line drugs administered daily for 6–9 months or longer by the oral route [4].

Fifty years of rifampicin

Also known as rifampin, rifampicin is a semisynthetic drug that was discovered by Dow-Lepetit Research Laboratories (Milan, Italy) in 1965 as part of a program involving the chemical modification of rifamycins, the natural metabolites of *Nocardia mediterranei,* which were named after the French film *Rififi chez les hommes* (1955). Rifampicin and other approved rifamycins such as rifabutin, rifaximin and rifapentine act by inhibiting bacterial DNA-dependent RNA polymerase. Additionally, they have bactericidal activity, whereas most other anti-TB drugs have only bacteriostatic activity [5,6].

Although rifampicin has impressive qualities, it still has a number of shortcomings. Especially problematic is the rapid evolution of resistant mutants, particularly when used in monotherapy. For this reason, it has often been combined with other first-line drugs, such as isoniazid, pyrazinamide and ethambutol, as a 'front-line' anti-TB drug combination for almost 50 years, in alignment with the WHO-recommended treatment regimen [4]. Even with this cocktail-based 6–9 months therapy, however, the evolution of drug-resistant mutants is enhanced due to

Jiří Trousil
Institute of Macromolecular Chemistry of the Academy of Sciences of the Czech Republic, Heyrovsky sq. 2, Prague 6, 162 06, Czech Republic

Martin Hrubý
Author for correspondence:
Institute of Macromolecular Chemistry of the Academy of Sciences of the Czech Republic, Heyrovsky sq. 2, Prague 6, 162 06, Czech Republic
mhruby@centrum.cz

10.2217/nnm-2017-0117 © 2017 Future Medicine Ltd **Nanomedicine (Lond.)** (Epub ahead of print) ISSN 1743-5889

poor patient compliance with treatment, which is common [6].

Thus, experts concur that a shorter treatment regimen, ideally 3 or fewer months, and more efficient therapy against multidrug resistant and latent TB are needed.

Nanoparticle drug delivery systems for TB therapy

Nanomedicine has emerged as one of the most promising approaches for overcoming the above-listed shortcomings associated with TB therapy. Utilizing nanocarriers for drug delivery into the lungs, the primary target organ for TB treatment due to the presence of *M. tuberculosis*-infected alveolar macrophages, offers an elegant way to circumvent numerous difficulties associated with conventional therapy. For example, this method reduces systemic toxicity and achieves a higher drug concentration at the main site of infection. At inflamed sites, the endothelium becomes permeable due to pathologic processes. Nanoparticles follow the route of particulate patterns including intracellular pathogens, and they are preferentially taken up by macrophages, which further enhance their targeting [2].

In this context, polymeric nanocarriers have clear advantages over inorganic nanoparticles due to the fact that nanotoxicology and biodegradability issues arise in cases involving nonbiodegradable formulations. Thus, many studies focusing on rifampicin delivery have shown potential, especially regarding lipase-degradable polyesters such as poly(lactic-co-glycolic acid) (PLGA) [7,8], PCL and PLA or its copolymers [3,9,10] as well as nature-based matrixes such as lysozyme-degradable chitosan and alginate or solid-lipid nanoparticles [11].

Recently, we studied a system for rifampicin delivery based on methoxy poly(ethylene oxide)-*block*-poly(e-caprolactone) (MPEO-*b*-PCL) copolymers [3] that showed efficient delivery into macrophages, where mycobacteria typically persist as well as efficient eradication of mycobacteria infection *in vitro*. However, despite the widespread use of poly(ethylene oxide) (PEO) as a hydrophilic block as well as its US FDA approval for medicinal use, it must be noted that a certain portion of the population possesses pre-existing anti-PEO antibodies. This phenomenon is thought to be related to the fact that PEO and PEO derivatives are common ingredients in personal care and household cleaning products as well as processed foods [12]. These findings must be taken into account when designing drug delivery systems to avoid immunogenic reactions, which can significantly affect the effectiveness and safety of therapy. Consequently, PEO replacements such as 2-alkyl-2-oxazolines are a current topic of interest [13].

Combined therapy-based delivery systems

It follows from the previous discussion that combination therapy-based nanoparticle drug delivery systems offer the most advantageous option to avoid the selection of drug-resistant mutants, which is enhanced by anti-TB monotherapy. Therefore, an important task in the field of anti-TB delivery involves the creation of nanoparticle assemblies based on standard cocktail therapy. For example, Sato and colleagues [14] synthesized micelle-forming tuberculostatic prodrugs based on poly(ethylene oxide)-*block*-poly(aspartic acid) covalently modified by rifampicin, isoniazid and pyrazinamide. Additionally, a formulation of noncovalently encapsulated rifampicin and isoniazid that could be administered via spray-dried PLGA nanoparticles was described by du Plessis and colleagues [15]. Unfortunately, studies focusing on mono-anti-TB delivery still dominate, probably because anti-TB-drugs have varying acido-basic properties as well as lipophilicity. The development of user-friendly preparations of physicochemically stable formulations should overcome such difficulties.

In addition to combining various currently available anti-TB drugs, another elegant strategy related to combined therapy involves the combination of anti-TB drugs with immunotherapy or vaccine delivery, which increases the therapeutic response of the host. Morse and colleagues [8] described a system for intracellular rifampicin delivery based on PLGA nanoparticles with a chitosan shell that took advantage of the immunomodulatory effect of 1,3-β-glucan. Internalization into human alveolar-like macrophages led to the stimulation of reactive oxygen/nitrogen species production as well as proinflammatory cytokine secretion.

Both Rodrigues and Silva [16,17] studied the synergic effect of immunotherapy and chemotherapy *in vivo*. They found that intramuscular injection of plasmid DNA encoding the *M. leprae* 65 kDa heat-shock protein (hsp65) increased the efficiency of the immune system and shortened the duration needed for rifampicin and isoniazid treatment. The encapsulation of hsp65 into PLGA nanoparticles was also described [18]. The emerging field of delivery systems combining not only anti-TB chemotherapeutics but also immunomodulators or TB vaccines based on proteins, peptides or particle matrix-protected DNA offers substantial advantages over conventional therapy.

Challenges & future perspective

The successful development of novel nanoparticle delivery systems for rifampicin and other anti-TB drugs must take into consideration many aspects of TB infection. Hence, only with a detailed understanding of host–pathogen interactions, mycobacteria-infection biology and also of microbe-associated molecular patterns, the design of molecularly targeted and tailored anti-TB delivery systems will be possible.

The various complications still associated with TB mean that the above-described anti-TB delivery systems still face major challenges that must be overcome, one of which is the increasing prevalence of TB and HIV coinfection. HIV infection is the most powerful risk factor for predisposition to *M. tuberculosis* infection and progression to active disease and increases the risk of latent TB reactivation by 20-fold [19]. Unfortunately, the mechanisms underlying the breakdown of immune defenses in coinfected individuals are not well known.

In the next few years, researchers will likely continue to struggle with striking a balance between identifying adequate physico-chemical formulations for novel molecularly targeted and stimuli-responsive anti-TB delivery systems and overcoming gaps in detailed biological understanding of TB pathology.

Financial & competing interests disclosure

This work was supported by the Ministry of Education, Youth and Sports of CR within the National Sustainability Program I (NPU I), Project POLYMAT LO1507. The authors have no other relevant affiliations or financial involvement with any organization or entity with a financial interest in or financial conflict with the subject matter or materials discussed in the manuscript apart from those that have been disclosed.

No writing assistance was utilized in the production of this manuscript.

References

1 Sosnik A, Carcaboso AM, Glisoni RJ, Moretton MA, Chiappetta DA. New old challenges in tuberculosis: potentially effective nanotechnologies in drug delivery. *Adv. Drug. Deliv. Rev.* 62(4–5), 547–559 (2010).

2 Gelperina S, Kisich K, Iseman MD, Heifets L. The potential advantages of nanoparticle drug delivery systems in chemotherapy of tuberculosis. *Am. J. Respir. Crit. Care Med.* 172(12), 1487–1490 (2005).

3 Trousil J, Filippov SK, Hruby M *et al.* System with embedded drug release and nanoparticle degradation sensor showing efficient rifampicin delivery into macrophages. *Nanomed. Nanotech. Biol. Med.* 13(1), 307–315 (2017).

4 Griffiths G, Nystrom B, Sable SB, Khuller GK. Nanobead-based interventions for the treatment and prevention of tuberculosis. *Nat. Rev. Microbiol.* 8(11), 827–834 (2010).

5 Sensi P. History of the development of rifampin. *Rev. Infect. Dis.* 5(Suppl. 3), S402–S406 (1983).

6 Aristoff PA, Garcia GA, Kirchhoff PD, Showalter HD. Rifamycins – obstacles and opportunities. *Tuberculosis (Edinb.)* 90(2), 94–118 (2010).

7 Onoshita T, Shimizu Y, Yamaya N *et al.* The behavior of PLGA microspheres containing rifampicin in alveolar macrophages. *Colloids Surf. B* 76(1), 151–157 (2010).

8 Dube A, Reynolds JL, Law WC, Maponga CC, Prasad PN, Morse GD. Multimodal nanoparticles that provide immunomodulation and intracellular drug delivery for infectious diseases. *Nanomed. Nanotech. Biol. Med.* 10(4), 831–838 (2014).

9 Rajan M, Raj V. Formation and characterization of chitosan-polylacticacid-polyethylene glycol-gelatin nanoparticles: a novel biosystem for controlled drug delivery. *Carbohydr. Polym.* 98(1), 951–958 (2013).

10 Moretton MA, Glisoni RJ, Chiappetta DA, Sosnik A. Molecular implications in the nanoencapsulation of the anti-tuberculosis drug rifampicin within flower-like polymeric micelles. *Colloids Surf. B* 79(2), 467–479 (2010).

11 Singh H, Bhandari R, Kaur IP. Encapsulation of rifampicin in a solid lipid nanoparticulate system to limit its degradation and interaction with isoniazid at acidic pH. *Int. J. Pharm.* 446(1–2), 106–111 (2013).

12 Yang Q, Jacobs TM, Mccallen JD *et al.* Analysis of pre-existing IgG and IgM antibodies against polyethylene glycol (PEG) in the general population. *Anal. Chem.* 88(23), 11804–11812 (2016).

13 Sedlacek O, Monnery BD, Filippov SK, Hoogenboom R, Hruby M. Poly(2-oxazoline)s – are they more advantageous for biomedical applications than other polymers? *Macromol. Rapid Commun.* 33(19), 1648–1662 (2012).

14 Silva M, Ferreira EI, Leite CQF, Sato DN. Preparation of polymeric micelles for use as carriers of tuberculostatic drugs. *Trop. J. Pharm. Res.* 6(4), 815–824 (2007).

15 Booysen LLIJ, Kalombo L, Brooks E *et al. In vivo/in vitro* pharmacokinetic and pharmacodynamic study of spray-dried poly-(dl-lactic-co-glycolic) acid nanoparticles encapsulating rifampicin and isoniazid. *Int. J. Pharm.* 444(1–2), 10–17 (2013).

16 Silva CL, Bonato VL, Coelho-Castelo AA *et al.* Immunotherapy with plasmid DNA encoding mycobacterial hsp65 in association with chemotherapy is a more rapid and efficient form of treatment for tuberculosis in mice. *Gene Ther.* 12(3), 281–287 (2004).

17 Rodrigues RF, Zarate-Blades CR, Rios WM *et al.* Synergy of chemotherapy and immunotherapy revealed by a genome-scale analysis of murine tuberculosis. *J. Antimicrob. Chemother.* 70(6), 1774–1783 (2015).

18 Trombone APF, Silva CL, Almeida LP *et al.* Tissue distribution of DNA-Hsp65/TDM-loaded PLGA microspheres and uptake by phagocytic cells. *Genet. Vaccines Ther.* 5(9), 1–8 (2007).

19 Pawlowski A, Jansson M, Sköld M, Rottenberg ME, Källenius G. Tuberculosis and HIV co-infection. *PLoS Pathog.* 8(2), 1–7 (2012).

PUBLICATION P7

Trousil J., Ulmann V., Hrubý M. Fluorescence and bioluminescence in the quest for imaging, probing and analysis of mycobacterial infections. *Future Microbiology*. 2018, 13 (8), 933–951. IF = 3.19

J.T. and V.U. wrote the paper. M.H. contributed to the final version of the paper.

Future P7
MICROBIOLOGY

Review

For reprint orders, please contact: reprints@futuremedicine.com

Fluorescence & bioluminescence in the quest for imaging, probing & analysis of mycobacterial infections

Jiří Trousil[1,2], Vít Ulmann[3] & Martin Hrubý*,[1]
[1]Department of Supramolecular Polymer Systems, Institute of Macromolecular Chemistry of the Academy of Sciences of the Czech Republic, Heyrovského náměstí 2, 162 06 Prague 6, Czech Republic
[2]Department of Analytical Chemistry, Charles University, Faculty of Science, Hlavova 8, 128 43 Praha 2, Czech Republic
[3]Laboratory for Mycobacterial Diagnostics and Tuberculosis, Regional Institute of Public Health in Ostrava, Partyzánské náměstí 7, 702 00 Ostrava, Czech Republic
*Author for correspondence: mhruby@centrum.cz

Mycobacterioses represent a global health problem and rapid diagnostic improvements are urgently required. Mycobacteria-specific fluorescence and bioluminescence phenomena have been found to be useful for a wide range of mycobacteria-focused research. Here, we present a critical survey of the most promising techniques in this field and the potential of new methods under investigation. These approaches include acid-fast staining, intrinsic fluorescence of the coenzyme F_{420}, fluorogenic substrates (e.g., β-lactamase-sensitive coumpounds) and recombination of mycobacteria or mycobacteriophages. Probably the most interesting and emerging host-inspecting approach is *in vivo* imaging. Detection of fluorescence *in vivo*, however, is complicated by light scattering, light absorption, and autofluorescence, caused by the tissues. Despite this, many of these systems show promise as the foundations for improved rapid analysis and imaging of mycobacterial infections, both *in vitro* and *in vivo*.

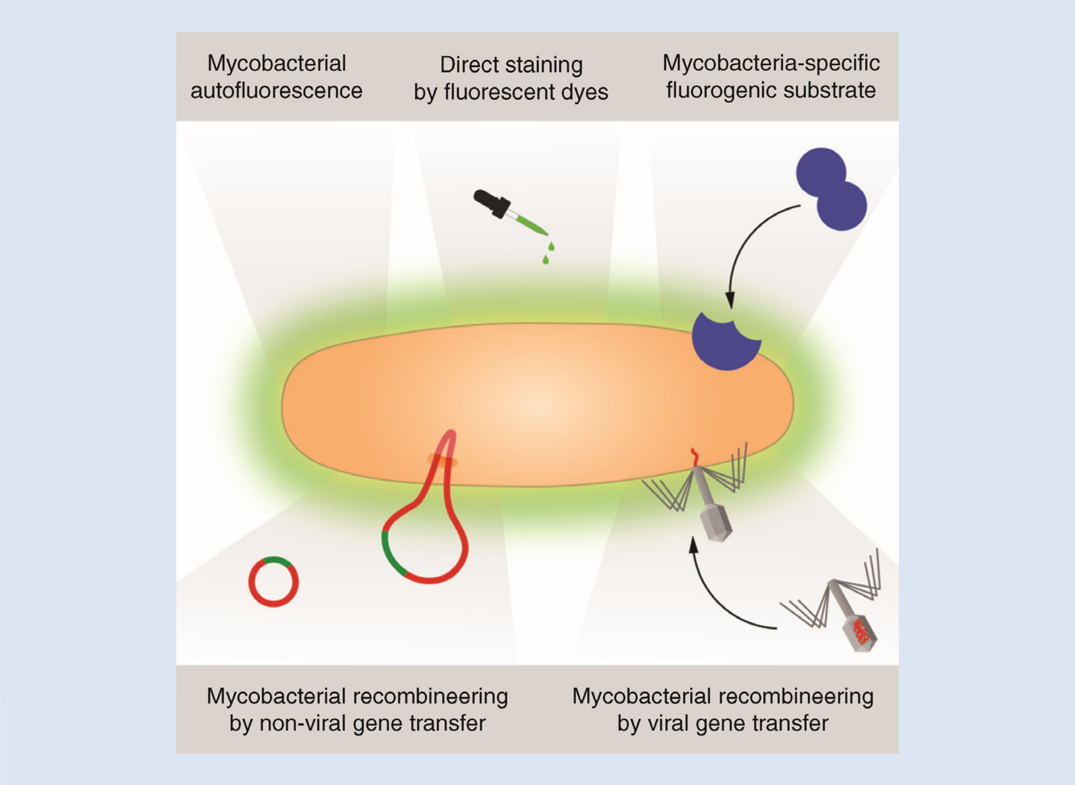

First draft submitted: 13 December 2017; Accepted for publication: 9 March 2018; Published online: 12 June 2018

Future Medicine

Keywords: fluorescence and bioluminescence • mycobacteria • tuberculosis

Tuberculosis (TB) and other diseases caused by mycobacterial infections represent a global health problem, although a potentially curative therapy has been available for approximately 50 years. The host–pathogen relationship is highly adapted. Emerging resistance, and an inability to detect all stages of the disease as well as inadequate medical care in most of the world, has resulted in the widespread, unresolved pandemic spread of diseases caused by mycobacteria.

In addition, infectious diseases, including TB, remain the leading cause of preventable death in the world [1,2]. TB kills 1.5 million people per year. The WHO estimate for overall new disease cases is 10.4 million per year [3]. Even in developed countries, the possibility of this disease exists as regional epidemics. Moreover, it is estimated that a third of the affected world population is latently infected, which is a serious concern.

The causative bacterial agent of TB, *Mycobacterium tuberculosis*, grows very slowly in culture. Obtaining visible *M. tuberculosis* colonies on egg- or agar-based media plates requires weeks after inoculation to determine colony forming units (CFU). Thus, in addition to the focus on novel and well-thought-out therapeutic systems, it is necessary to develop rapid, sufficiently sensitive and specific diagnostic methods, especially those that are useful for both basic TB research and clinical diagnostics. This is because only early diagnosis and treatment significantly reduces the risk of the further spread of this disease [4]. Finally, it is also needed to develop research methods allowing deeper insight into the disease and host–pathogen interactions. For this purpose, optical methods using fluorescence and bioluminescence are especially valuable.

Over the last two decades, mycobacteria-specific luminescence-based methods have been found to be elegant and powerful tools for probing mycobacterial infections and for analysis and optical imaging. These methods have been useful not only for research on host–pathogen interactions but also in the field of anti-TB efficiency and in the development of new nanoformulation-based therapeutic systems. The four main fluorescence- and bioluminescence-based diagnostic options described in this review came about during this time period. As is shown in Figure 1, these approaches are based on recombinant biology, microbiology and chemistry methods. These tools use advanced instrumental and physicochemical methods, and phenomena such as fluorescence spectroscopy and its applied techniques, including Förster resonance energy transfer, fluorescence-activated cell sorting and *in vivo* optical imaging as detection tools.

To the best of our knowledge, this review is the first critical evaluation of approaches for the study of mycobacterial infections that use fluorescence- and bioluminescence-based detection methods to take advantage of a mycobacteria-specific properties.

Mycobacterial infections

The class *Mycobacteriaceae* is comprised of obligate pathogens, from the *M. tuberculosis* complex and *Mycobacterium leprae* to more than 180 opportunistic, potentially pathogenic and saprophytic species [5]. Cell wall complexity and slow metabolism are common characteristics of all mycobacterial species. The modified peptidoglycan layer is linked to arabinogalactan with mycolic acids, long-chained (C_{60}–C_{90}), cyclopropanated fatty acids that are important for bacterial outer membrane structure, virulence and persistence within the host [6]. These complex structures together form an almost impermeable, hydrophobic envelope.

In addition to the *M. tuberculosis* complex, naturally occurring saprophytes and animal pathogens, potentially pathogenic mycobacteria or nontuberculous mycobacteria (NTM) represent clinically important groups of microbes [7]. Most NTM diseases involve species of the *M. avium* complex, rapidly growing mycobacteria such as *M. fortuitum*, *M. abscessus*, *M. marinum* and *M. kansasii*.

Infections caused by NTM are believed to be incidental and are acquired from environmental exposures. Most mycobacterial species are primarily equipped for survival in the environment, rather than to invade human hosts. However, factors such as the increasing prevalence of predisposing conditions, an aging population and a loss of overall fitness have led to the current emergence of diseases caused by opportunistic microorganisms, including mycobacteria.

Tuberculosis

Thousands of years of coevolution between *M. tuberculosis* and its human host has resulted in an almost reciprocal adaptation. The effectiveness of the ecological strategy of *M. tuberculosis* lies in its persistence within the human population and the adeptness of TB bacilli at using the natural defenses of the human body to its own advantage. In

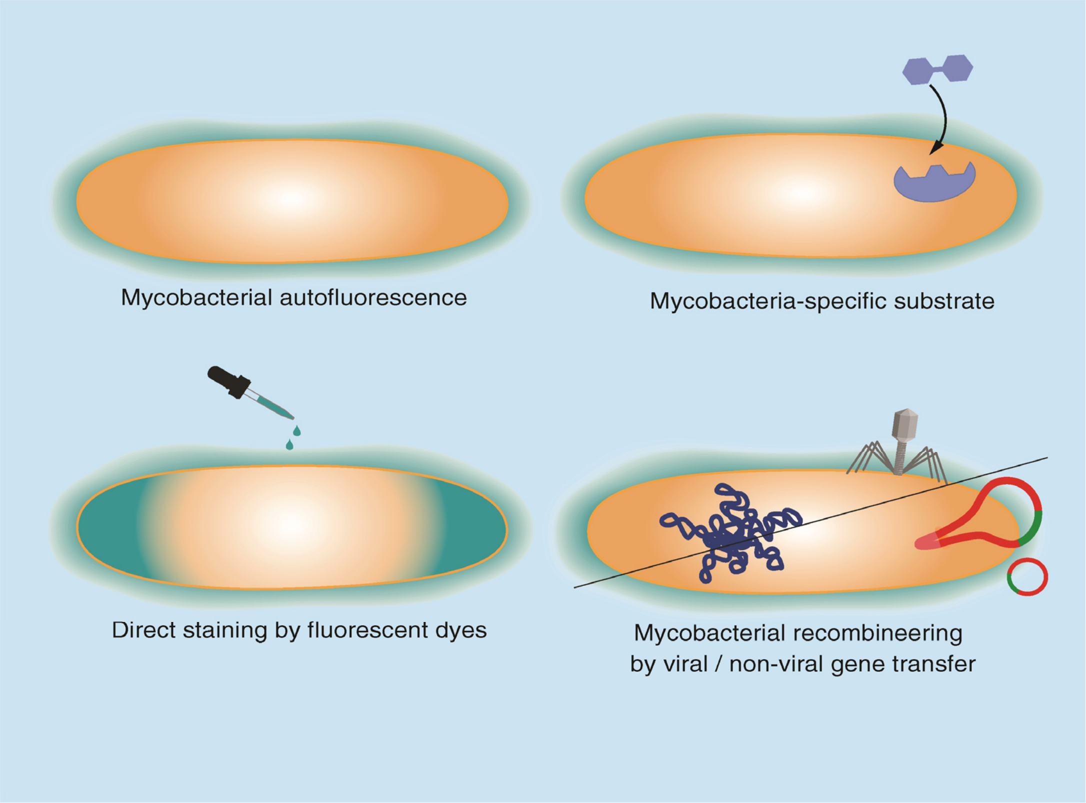

Figure 1. Primary approaches available for study of mycobacteria-specific fluorescence or bioluminescence.

terms of TB pathogenesis (Figure 2), it is primarily transmitted via inhalation of aerosol droplets expelled by infected hosts, with the main site of infection being the lungs. Innate cell-mediated immunity and alveolar macrophages that interact with the invading pathogen represent the first line of cellular defense. Macrophages are unable to eliminate deposed mycobacterial cells, which continue to divide until overgrowing and disseminating from ruptured host cells, after which an adaptive immune response occurs. Dendritic cells can also play an important role in host defense by presenting antigens and activating T and B cells [8].

It is known that infected macrophages in the lungs, through the production of chemokines, attract inactivated monocytes, lymphocytes and neutrophils, none of which kill the bacteria very efficiently [9]. Afterward, granulomatous focal lesions that are composed of macrophage-derived giant cells and lymphocytes begin to form. This process typically lasts from 2 to 12 weeks. As cellular immunity develops, macrophages loaded with bacilli are killed, resulting in the formation of the caseous center of the granuloma, which is surrounded by a cellular zone of fibroblasts, lymphocytes and blood-derived monocytes. In individuals with efficient cell-mediated immunity, the infection may be suspended their entire lives [10].

Progressive disease only occurs in 5–15% of previously infected individuals, while the remaining individuals are able to terminate the infection in a stable, asymptomatic stage under immune control called latent TB (LTB). Individuals with LTB make up a third of the world population, representing a massive reservoir of potential disease.

The continuation of the disease can then be allowed by any insufficiency comprising regulatory mechanism, interleukin pathway and white cell abnormalities. Typical predisposing factors are age (elderly and infant patients), the loss of overall fitness in elderly individuals and self-inflicted risk factors, including malnutrition, alcohol abuse, HIV infection and therapies (e.g., anti-TNF, corticotherapy and oncotherapy) [11]. As Figure 2 illustrates, secondary TB continually develops after the primary infection or reactivation of LTB. Accumulation of mycobacterial antigens and their release initiates a fulminant immune response. Activated T-cells, cytokines secreted by natural killer cells and TNF production initiate the apoptosis of white and parenchymal cells, culminating in heavy tissue damage and cavity formation [12].

Treatment of TB is difficult and must be complex. Usually, the preferred regimen consists of an intensive phase of first-line anti-TB drugs (including isoniazid, rifampicin, pyrazinamide and ethambutol) followed by a 4-month

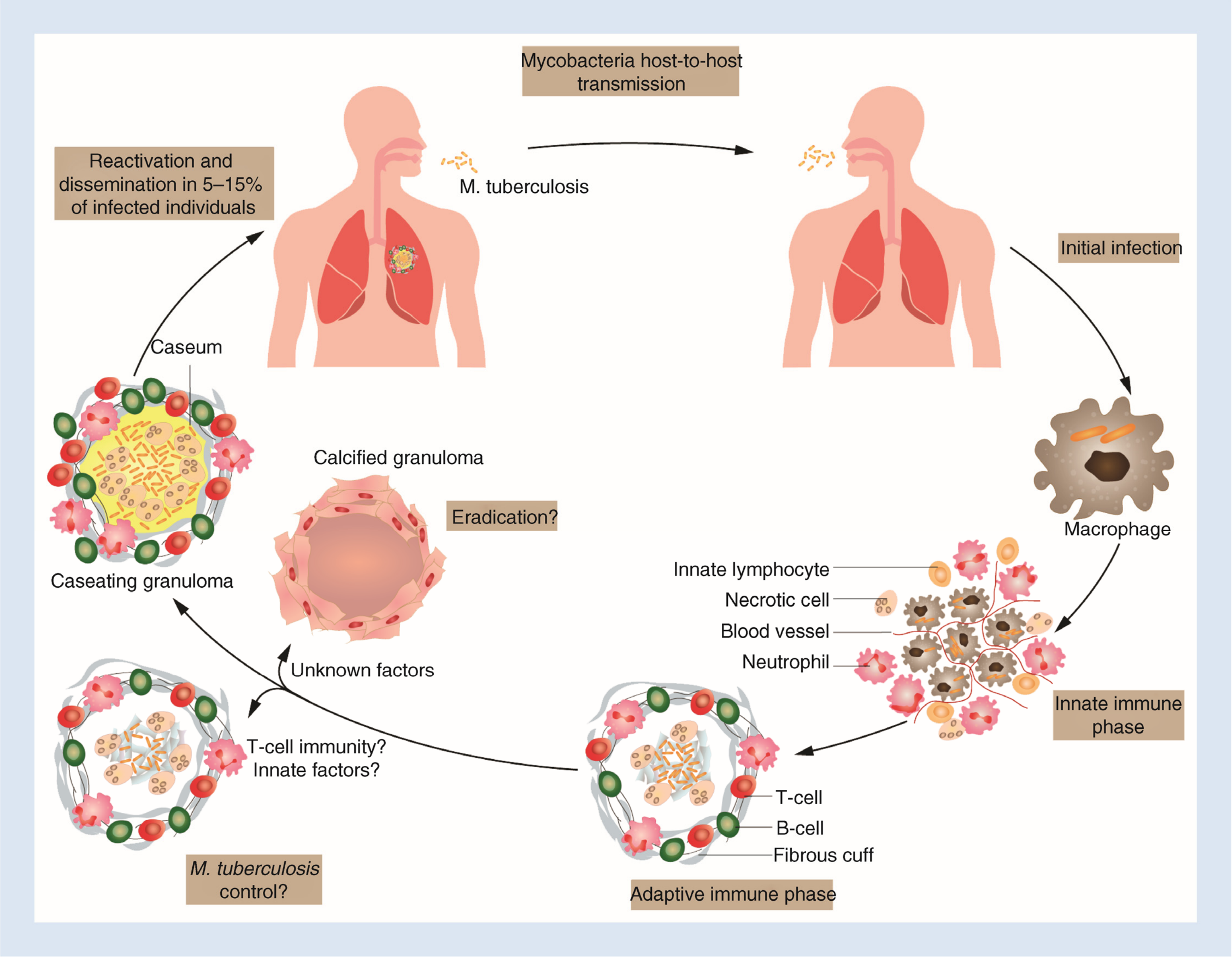

Figure 2. Tuberculosis pathogenesis. Infection is transmitted via inhalation of bacteria expelled by an infected host. Primary defense mechanisms involve an innate immune response of inflammation-related cells to the lung. An adaptive immune response, based on the recruitment of T cells, B cells and other leukocytes, occurs after dividing bacilli overgrow and rupture host cells and then disseminate. This leads to formation of granulomas, also called tuberculous lesions. In most cases, this promotes the nonsterile control of the mycobacteria. At this stage, the majority of infected individuals will remain in a stable asymptomatic stage called latent TB, while in hosts with efficient cell-mediated immunity, the infection may be eradicated permanently. Subsequently, healed granulomas leave small calcified lesions. Progressive (active) TB will eventually occur in a small percentage of previously infected individuals, where the hallmark of the reactivation is the failure of the host immune response. The exacerbation of necrotic cell death then leads to extensive caseous lesions. Consequently, the rupture of the granulomas into the airways occurs. Individuals affected by an active TB infection can then generate infectious aerosol via coughing.
Adapted with permission from [11].

continuation phase of isoniazid and rifampicin. The treatment, however, is complicated by selection of resistant mutants.

Finally, it is worth mentioning that nanomedicine has emerged as one of the most promising and efficient TB treatment approaches to overcome unsuccessful eradication. Because *M. tuberculosis*-infected macrophages are able to take up nanobead-based structures, nanosized drug-delivery systems administered into the lungs offer an elegant way to circumvent numerous difficulties associated with conventional therapies. Recently, our lab studied a system for rifampicin delivery based on methoxy poly(ethylene oxide)-*block*-poly(ϵ-caprolactone) copolymers, which exhibited efficient delivery into macrophages, where mycobacteria typically persist and efficiently eradicated mycobacterial infections *in vitro* [13]. One of the emphasized aspects of this study was the use of a fluorescence-based approach to assess a therapeutic system.

Diagnosis of mycobacterial infections

Unsurprisingly, in clinical practice, rapid diagnosis of mycobacterial infections can be difficult, and prompt diagnosis is a priority for its control, both for treating the individual and for public health intervention to reduce further spread [14]. One of the fastest methods to evaluate the specific nature of mycobacterial diseases is direct microscopy of clinical samples after acid-fast staining [15,16], which is based on the high retention of dye by the mycolic acid present in the cell wall of mycobacteria [17]. Two procedures are commonly used for acid-fast staining. Firstly, the carbol fuchsin method, which is known as Ziehl–Neelsen staining. Secondly, a fluorochrome-based procedure using auramine O or its mixture with rhodamine B, which leads to specific coloration of mycobacterial cells. This coloration results in a reddish-yellow fluorescence after UV light illumination. The most modern approach utilizes an light-emitting diode (LED) source to excite fluorescence. This method provides a higher procedural sensitivity and is easier to perform compared with classical light microscopy and Ziehl–Neelsen staining [15,17].

Cultivation of pretreated clinical material on egg- or agar-based media has the highest clinical sensitivity [14]. The major limitation of this procedure is the time required (weeks) to obtain a positive result, although there is a significant benefit in the recovery of viable mycobacterial cells for the ultimate confirmation of the causative agent. An accelerated procedure utilizes an automated metabolic system based on a mycobacterial growth redox indicator. For this method, metabolic activity is detected by an increase in fluorescence due to oxygen consumption by the growing culture, an approach that has been shown to detect mycobacteria weeks sooner than methods relying on the formation of visible colonies [18].

Remarkable progress continues to be made in the field of molecular methods, such as nucleic acid amplification, line probe assay and Xpert MTB/RIF (Cepheid, CA, USA). Modern multiplex systems, such as line probe assay and Xpert MTB/RIF [19], allow for simultaneous detection of agents in clinical samples and genetic changes in pathogens that correspond with drug resistance (e.g., the genes *InhA*, *katG* and *rpo*) [14]. The use of molecular methods to clinically identify isolates can reach approximately 100% positive predictive values, similar to what is obtained by cultivation methods.

Not surprisingly, the sensitivity of these methods is limited by the number of mycobacterial cells in a sample and the quality of the sample. The presence of inhibitors in a sample influences the analytical process and can lead to a false-negative result. Moreover, these systems are useless for treatment monitoring due to the long-term persistence of residual mycobacterial nucleic acid, even in treated or cured individuals [20]. The molecular methods' importance for rapid diagnosis of TB and mycobacterioses, however, is undisputed.

Finally, conventional diagnosis is carried out by several methods that, with respect to the main topic of this review, cannot be described in depth. Such additional diagnosis is based on conventional radiography, computed tomography, MRI and positron emission tomography [21,22]. These methods, usually indicated together with cellular immunity testing (e.g., Mantoux tuberculin test), provide a unique opportunity to noninvasively image the whole body for diagnosing, staging and assessing therapy response in TB.

Acid-fast staining by fluorescent dyes

As indicated above, acid-fast staining represents the gold standard for the clinical diagnosis of mycobacterial infections. Smear microscopy is simple, inexpensive and the most accessible tool in resource-limited settings for TB diagnosis [17]. The auramine O-based method has been used for tracking mycobacteria within macrophages [23,24], but is rarely used for imaging and research of mycobacterial infections, since this method cannot distinguish between viable and dead bacilli [17].

To overcome this limitation, fluorescent-staining techniques for viable mycobacterial cells were developed. The fluorescein diacetate (FDA)/ethidium bromide method, typically used in tissue culture assays, can be used for imaging and viability evaluations of mycobacterial cultures, similarly to how it is used for mammalian cells [17]. Viable bacilli hydrolyze FDA to free fluorescein and exhibit a yellow-green fluorescence, whereas nonviable mycobacteria are unable to hydrolyze FDA and absorb the ethidium bromide counterstain and therefore appear orange [25]. Another approach described by Nasu and colleagues [26] is based on modified Auramine O staining for the detection of respiratory bacteria, a method that was described in 1996 [27]. In this study, non-TB mycobacteria were easily dual-stained with Auramine O and 5-cyano-2,3-ditoryl tetrazolium chloride (CTC), a redox fluorescent dye. Respiratory-active mycobacteria appeared both yellow (Auramine O-based) and red (CTC-based), whereas

Table 1. Selected endogenous fluorescently active biomolecules and their spectral properties.

Molecule type	Biomolecule	Excitation maxima (nm)	Emission maxima (nm)
Amino acids	Tryptophan	280	350
	Tyrosine	275	300
	Phenylalanine	260	280
Coenzymes	FAD	450	535
	F_{420}[†]	420	470
	NADH	290, 351	440, 460
	NADPH	336	464
Pigments	Legioliulin[‡]	340	450
	Pyoverdines[§]	398	470

[†] Two-electron transfer coenzyme found in some prokaryotes (e.g., *Mycobacterium* sp.) [31].
[‡] Isocoumarin-based compound produced by *Legionella* sp. [88].
[§] Yellow–green fluorescent pigments produced by *Pseudomonas* sp. [89,90].
FAD: Flavin adenine dinucleotide; NADH: Nicotinamide adenine dinucleotide.

nonactive mycobacteria only appeared yellow. Interestingly, the CTC-based approach may be useful in the field of probing progressive hypoxia and other models involving microaerobic conditions within host necrotic granulomas and *M. tuberculosis* latent infections.

Natural autofluorescence of mycobacteria

It is well-known that some bacteria, such as *Legionella* sp. and *Pseudomonas* sp., exhibit fluorescence after their colonies are illuminated by UV light. One of the first observations of this phenomenon described by Schoeter, who first isolated and described a bacterium that produced a green-fluorescent pigment in 1872 [28]. This natural intrinsic fluorescence (autofluorescence) of bacteria is due to viable bacteria possessing numerous intracellular biomolecules that have specific spectral properties. The fluorophore-like biomolecules (Table 1) include aromatic amino acid-containing proteins, nucleic acids, coenzymes and other bacterial pigments that have excitation maxima ranging from 250 to 450 nm, whereas the emission maxima range from 280 to 540 nm. Mycobacterial autofluorescence is often discussed in connection with the fluorescent coenzyme F_{420}, which is present in some archaea, aerobic actinomycetes (to which mycobacteria belong) and cyanobacteria [29–31]. F_{420} is a two-electron transfer coenzyme composed of 7,8-didemethyl-8-hydroxy-5-deazariboflavin (FO), a phospholactyl moiety, and various numbers of glutamate residues (Figure 3).

Although the presence of F_{420} or its metabolic intermediate 7,8-didemethyl-8-hydroxy-5-deazariboflavin has previously been reported in *M. avium* [31,32], *M. smegmatis* [30,33], *M. fortuitum* [31], *M. bovis* BCG [31], *M. phlei* [34] and *M. tuberculosis* [31,35], the role of F_{420} within *Mycobacterium* sp. has not been fully elucidated [29].

Unsurprisingly, the fluorescent characteristics of both mycobacterial cells and F_{420} at specific excitation and emission wavelengths make them very attractive detection and characterization probes. As a detection tool, mycobacterial intrinsic fluorescence was studied by Salazar and colleagues [29], who explored the cyan fluorescence range of several *Mycobacterium* sp. Mycobacterial cells that exhibited an emission maximum at 475 nm after their excitation with a laser at a wavelength of 405 nm (Figure 3C) were visualized by fluorescence microscopy as brilliant bacilli and were easily tracked during macrophage infection (Figure 3D). Although probably the result of the photoreduction of F_{420}, the quick decay of mycobacterial autofluorescence can be marked as topic requiring further investigation. In spite of this, the limit of detection of *M. tuberculosis* cells was found to be 7.8×10^5 bacilli per ml of sputum under the assay conditions used.

Tkaczyk and colleagues [30] studied mycobacterial autofluorescence as a tool for differentiating between live and dead cells, which is, as was noted above, a limiting factor of the conventional acid-fast staining method [26]. Using a *M. smegmatis* model, they showed that viable and dead mycobacteria undergo different photobleaching rates. It was shown that the fluorescence intensity of the viable mycobacterial cells increased within the first 30 s of the experiment, while dead mycobacteria appeared to show a trend of continuously decreasing fluorescence intensity over time. This approach may have limited use for both LTB infections and nonreplicating persistent *M. tuberculosis* cells, as the authors reported.

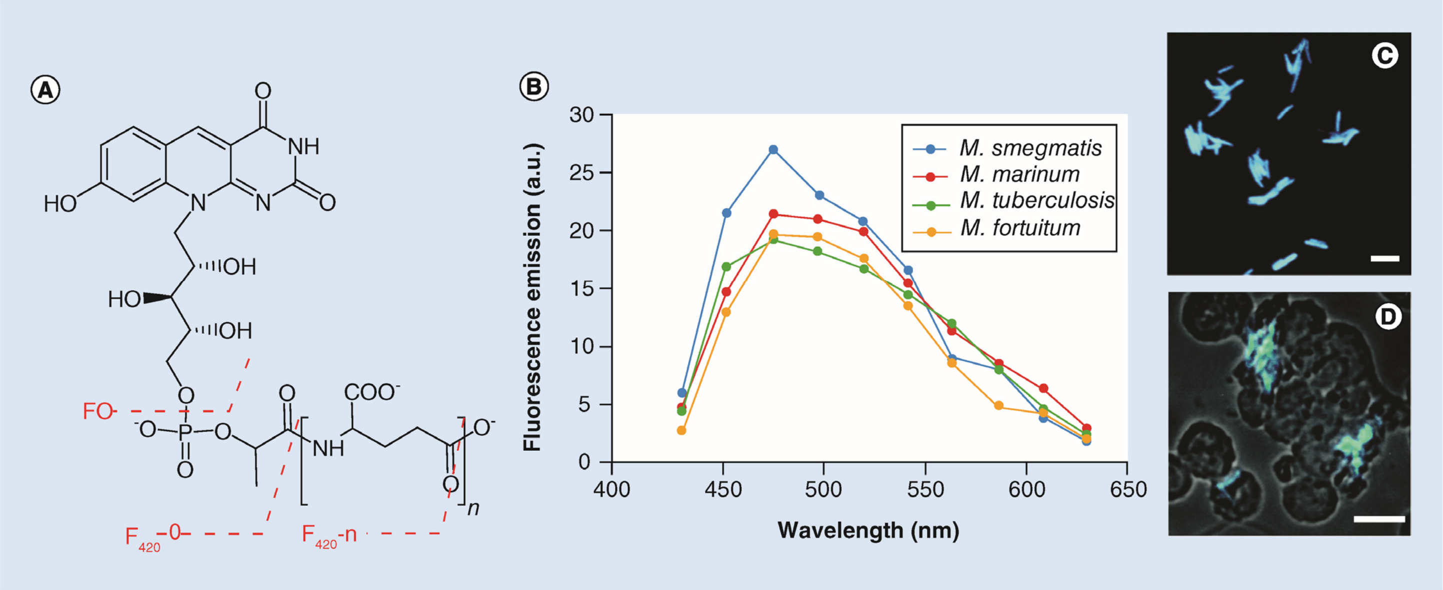

Figure 3. Coenzyme F_{420}-based mycobacterial autofluorescence as a tool for detection and tracking. (A) Schematic representation of F_{420} and parts of its molecule. F_{420} is a coenzyme composed of 7,8-didemethyl-8-hydroxy-5-deazariboflavin, a phospholactyl moiety, and various numbers of glutamate residues, on which the number *n* in the coenzyme F_{420}-*n* denotation depends [91]. **(B)** Emission spectra of *Mycobacterium* sp. recorded at an excitation wavelength of 405 nm. Tubercule bacilli (*M. tuberculosis*) are traceable by their cyan autofluorescence as free cells in culture **(C)** and after having been taken up by macrophages **(D)**. Scale bars: 3 and 10 μm, respectively. **(B–D)** Adapted and reprinted with permission from [29].

Fluorescent protein-expressing mycobacteria

Most likely, the biggest disadvantage of the intrinsic fluorescence-based probing could be considered its cyan spectral range. This range has high light scattering and poor tissue permeability. Thus, the spectral parameters of any experiment are limited by the F_{420}-based cyan fluorescence, precluding its use *in vivo* (Figure 4). For deep-tissue *in vivo* imaging, which is based on the illumination of a target tissue with a light source of a specific wavelength range that is able to excite fluorophores, far-red and near-infrared (NIR) fluorescent probes are required because in this spectral region the combined absorption of hemoglobin, melanin and water is minimal [36]. An option for solving this problem is fluorescence based on recombinant mycobacteria expressing a fluorescent protein (FP) with appropriate spectral properties.

The history of the use of FPs dates back to the early 1960s, when *Aequorea victoria* jellyfish green FP (GFP) was first described by Osamu Shimomura. While FPs were an obscure and poorly understood biochemical oddity two decades ago, today they are used daily in thousands of labs around the world as powerful tools for elucidating molecular mechanisms in cells and bacteria [37]. A Nobel Prize was awarded to Osamu Shimomura, Martin Chalfie and Roger Tsien for the discovery and development of the GFP in 2008 [38].

Structure of FPs

All FPs share the same β-barrel that is based on a β-sheet fold that, in addition to being vital for fluorescence, works as a protecting shell in which their unique chromophore is located in the central α-helix. The chromophore is self-generated from an internal tripeptide, X65Tyr66Gly67, through a multistep reaction that includes cyclization, dehydration, oxidation and, in some cases, hydrolysis [37–39]. The ability of FPs to fluorescence in the visible spectral region is imparted by the chromophore hidden in this β-barrel scaffold. The position of the FP on the spectral scale is primarily determined by the chemical structure of the chromophore, where the more extended the system of π-conjugated electrons, the more redshifted the emission [40,41].

Moreover, together with structural similarity, virtually all FPs have the same drawbacks, primarily a propensity for oligomerization and aggregation. However, this quaternary structure can affect the experimental outcome [38]. Thus, modification of the FP amino acid sequence can overcome the oligomerization and suppress intermolecular binding.

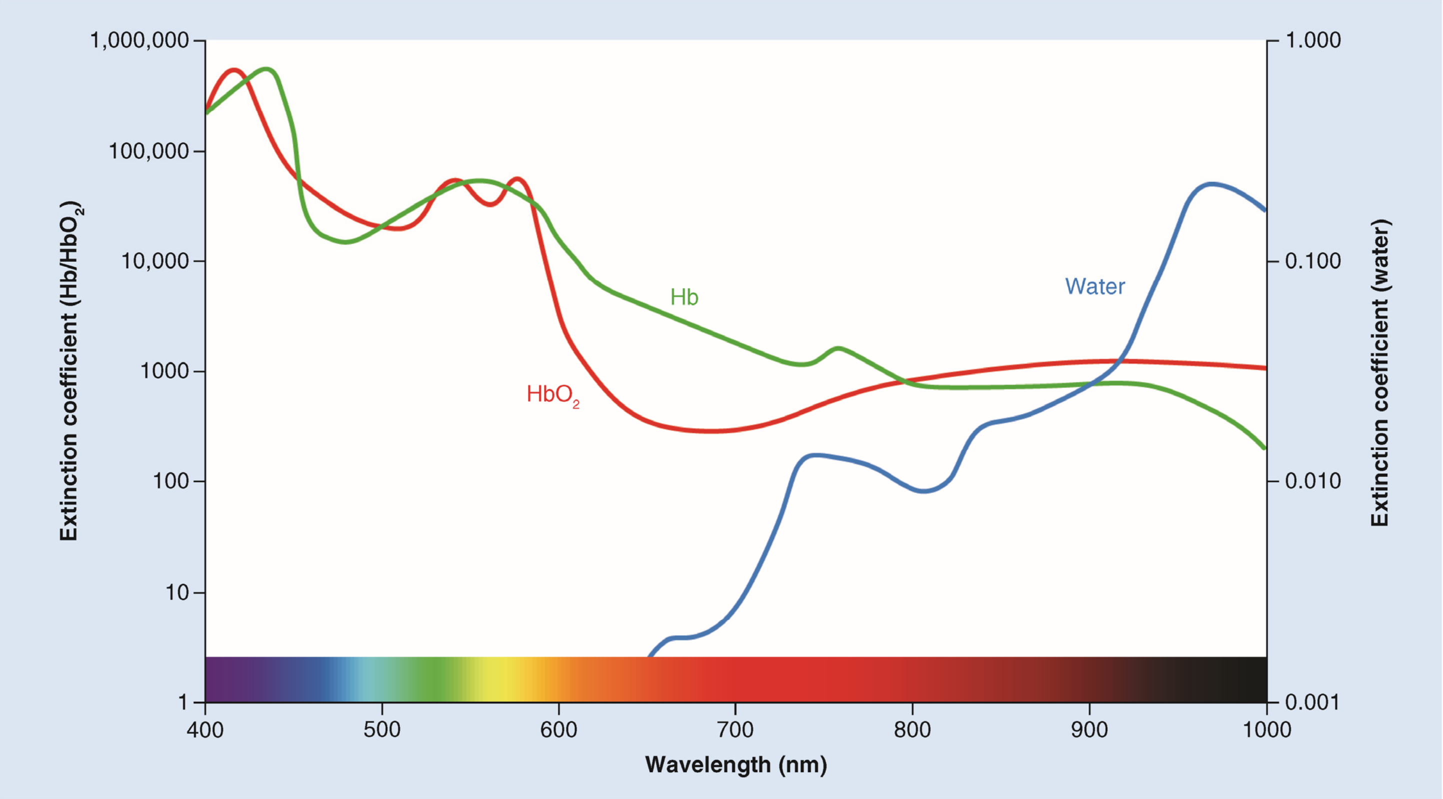

Figure 4. Wavelength-dependent absorption in tissue restricts the optical imaging spectrum.
Adapted with permission from [92] © American Chemical Society (2017).

Mycobacterial recombineering

An essential prerequisite of mycobacterial recombineering (i.e., recombination-mediated genetic engineering) is FP-coding DNA transfer. In general, this process occurs in three primary ways. The first two are transformation and transduction, mechanisms of horizontal gene transfer that do not involve cell-to-cell contact. The remaining way is bacterial conjugation, a mechanism based on the transfer of genetic material by direct cell-to-cell contact. From the perspective of this work, however, only transformation (i.e., nonviral gene transfer) of plasmid DNA (pDNA) and transduction by phages (see below) have greater significance (Figure 5).

Plasmids naturally exist in bacterial cells and are small, circular, double-stranded DNA molecules that are distinct from the chromosomal DNA of a cell. In their simplest form (Figure 5A), the backbone of a plasmid requires at least one unique restriction enzyme recognition site to allow for cloning of an insert to be studied, a bacterial origin of replication and an antibiotic-resistance gene or another selectable marker. The antibiotic resistance provided by pDNA provides a survival advantage to the bacterial host. However, the intrinsic resistance of mycobacteria to many agents reduces the number of selection markers that can be used [42]. The most common markers for mycobacteria are kanamycin (10–50 μg/ml), streptomycin (30 μg/ml), hygromycin (100 μg/ml), gentamycin (5–20 μg/ml) and apramycin (30–50 μg/ml).

Finally, a promoter region drives transcription of the insert. This is a region of DNA that recruits transcriptional machinery from a particular organism or group of organisms (e.g., mycobacteria). Thus, promoter selection, with respect to recombineering, is crucial to the level of transgene expression that is obtained, and to control FP expression various promoters have been studied. Both the mycobacterial heat-shock protein promoter (*hsp60*) [4,43–45] and the mycobacterial strong promoter (*msp12*) [43,46,47] showed strong expression across the spectrum of mycobacterial species (Table 2) both *in vitro* and *in vivo*.

The widespread use of the *hsp60* promoter [48] makes sense because heat-shock proteins are essential under all mycobacterial growth conditions but are expressed at higher levels in response to stress. In addition, the *M. marinum* and *M. smegmatis* promoters, *G13* [44] and *smyc* [44,45], respectively, have also been used in the context of recombinant mycobacteria. However, a number of studies [4,49] have suggested that mycobacteriophage promoters are efficient and interesting choices for the expression of foreign genes in mycobacteria. For example, Cirillo and colleagues [4]

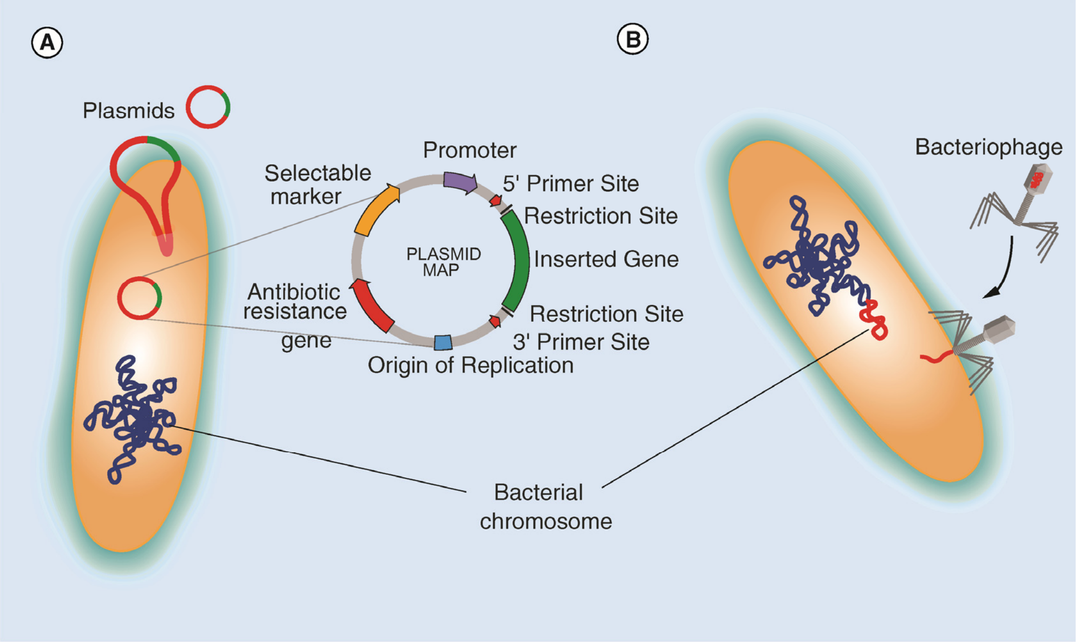

Figure 5. Schematic illustration of gene transfer. (A) Nonviral gene transfer via plasmid DNA and a diagram of modular plasmid design for mycobacteria recombineering. **(B)** Lysogenic process after the infection of a bacillus by a mycobacteriophage.

Table 2. Overview of chosen studies using recombinant mycobacteria expressing fluorescent proteins.

Class	Protein	Ex/Em	Strain	Promoter	Selection	Usage	Ref.
Cyan	CFP	435/485	*M. avium*	*msp12*	Kan	*In vivo* infection (mice), host–pathogen interaction study	[43]
			M. avium	*msp12*	Kan	*In vitro* infection, bacterial tracking	[46]
Green	GFPmut3	501/511	*M. marinum*	*msp12*	Kan	*In vivo* imaging (zebrafish), NPs colocalization	[47]
			M. avium	*hsp60*	Kan	*In vivo* infection (mice), host–pathogen interaction study	[43]
Red	tdTomato	554/581	*M. bovis* BCG	*hsp60, L5*	Kan	*In vitro* and *in vivo* treatment efficacy study	[4]
			M. tuberculosis	*smyc*	Hyg	*In vivo* imaging (mice), efficacy of treatment, study of expression	[44,45]
			M. smegmatis	*hsp60, smyc*	Kan	Study of expression	[45]
	DsRed2	563/582	*M. marinum*	*msp12*	Kan	*In vivo* imaging (zebrafish), NPs colocalization	[47]
			M. bovis BCG	NR	NR	*In vitro* infection, NPs colocalization	[55]
	mCherry	587/610	*M. bovis* BCG	*hsp60, L5*	Kan	*In vitro* and *in vivo* treatment efficacy study	[4]
			M. tuberculosis	*hsp60, smyc, G13*	Hyg	*In vivo* imaging (mice), efficacy of treatment, study of expression	[44,45]
			M. smegmatis, M. marinum	*hsp60, smyc*	Kan, hyg	Study of expression	[45]
Far-red	Keima	440/616	*M. bovis* BCG	*hsp60*	Kan	*In vitro* and *in vivo* treatment efficacy study	[4]
	mKate	588/635	*M. bovis* BCG *M. smegmatis*	*hsp60* *hsp60, smyc*	Kan kan	*In vitro* and *in vivo* treatment efficacy study of expression	[4] [45]
	Katushka	588/635	*M. bovis*BCG	*hsp60*	Kan	*In vitro* and *in vivo* treatment efficacy study	[4]
			M. tuberculosis	*smyc*	Hyg	*In vivo* imaging (mice), efficacy of treatment, study of expression	[44,45]
			M. smegmatis, M. marinum	*hsp60, smyc*	Kan, hyg	Study of expression	[45]
	mPlum	590/649	*M. bovis* BCG	*hsp60*	Kan	*In vitro* and *in vivo* treatment efficacy study	[4]
			M. smegmatis	*hsp60, smyc*	Kan	Study of expression	[45]

Hyg: Hygromycin; Kan: Kanamycin; NP: Nanoparticle; NR: Not reported.

compared the impact of mycobacterial phage promoter *L5* and *hsp60* on tdTomato protein fluorescence. It was found that the *L5*-based strain had higher fluorescence, which was due to more plasmid copies in *M. bovis* BCG. Despite this, few mycobacteriophage promoters have been described [49].

After construction of the FP-coding pDNA, the pDNA has to be transferred into the mycobacterial cells. The most widely used and highly efficient method for introducing pDNA into mycobacterial cells is electroporation, a process in which bacterial cells are subjected to high-voltage electrical pulse, allowing the entry of pDNA into the cell and enabling the genetic manipulation of both fast- and slow-growing mycobacterial species.

Application of recombinant mycobacteria

In general, FP-expressing mycobacteria allow for the study of gene expression and host–pathogen interactions [45,48,50,51]. For example, Carroll *et al.* [45] used optimized expression systems with several FPs from the far-red region of the spectrum (mCherry, mKate, mPlum, tdKatushka, tdTomato, Turbo-635) to sensitively detect gene expression in mycobacteria (*M. tuberculosis*, *M. smegmatis* and *M. marinum*) under replicating and nonreplicating conditions *in vitro*. In the context of optimizing *M. bovis* BCG as a vehicle for live recombinant vaccines, the effect of different combinations of promoters and post-translational signals on gene expression and plasmid vector stability was investigated in three *M. bovis* BCG substrains by Al-Zarouni and Dale [48].

Recombinant mycobacteria are not applicable for diagnostic purposes or other clinical applications. Despite this, a great advantage of recombinant mycobacteria-based assays is that the mycobacteria-specific fluorescence correlates with CFU, both *in vitro* and *in vivo*, as was previously described [4,44,45]. This, together with the need for studies of high-throughput screening of new antituberculous agents and TB biology, resulted in the development of an *in vivo* model based on zebrafish [52–54] by Ramakrishnan and colleagues. For the first time, this system used the close relatives *M. tuberculosis* and *M. marinum*, which expressed red or GFPs, for a fluorescent mycobacteria-based study *in vivo*. On the other hand, with respect to a mammalian *in vivo* model, the situation is more complicated because hemoglobin present in tissues highly absorbs light from approximately the blue to the orange region of the visible spectrum. Thus, the development of red and far-red FP-based reporters was necessary.

Schaible and colleagues [44] and subsequently Cirillo and colleagues [4] described the development of a number of fluorescent mycobacteria expressing various FPs (mCherry, mPlum, mKate, Katushka, Keima and tdTomato; see Table 2) with a focus on *in vivo* imaging with a detection limit ranging from 6.5×10^4 to 8×10^7 CFU/lung in living mice.

The use of fluorescent mycobacteria is an elegant way of studying the fate and efficiency of drug-delivery systems. In several studies [47,55–57] dealing with antituberculous drug-delivery system development, nanocarrier-mycobacteria colocalization in macrophages was studied using FP-expressing mycobacteria *in vitro*. Moreover, by combining fluorescent *M. marinum* and poly(lactide-*co*-glycolide) (PLGA) nanoparticles, Griffiths and colleagues showed [47,58] that the zebrafish model of TB (Figure 6) offers a powerful system for monitoring antituberculotic nanoparticles *in vivo*.

It is worth mentioning that the biosynthesis of FPs within recombinant organisms does not require any other enzymes except for the ribosomal apparatus, which is necessary for protein synthesis. In other words, the only intervention needed to introduce the fluorescence into bacteria is genetic engineering. In contrast, despite the fact that these assays can be considered as a noninvasive, suitable and rapid way to quantify bacterial load in animals and to estimate the treatment efficiency to avoid CFU determination in organs as is typically necessary in TB research [4,44], it is necessary to take into account the tissues-caused light scattering, light absorption and some possible autofluorescence (e.g., from fur) that make the fluorescence detection harder.

Finally, recombineering of mycobacteria can allow slightly different approach based on luciferases. Luciferases are a large family of enzymes that catalyze the oxidation of a D-luciferin (4,5-dihydro-2-(6-hydroxy-2-benzothiazolyl)-4-thiazolecarboxylic acid) substrate. In this well-known bioluminescence reaction, D-luciferin is converted into luciferyl adenylate, which reacts with oxygen in the presence of luciferase to form oxyluciferin, with the concomitant production of light.

However, it is obvious that in this case the substrate D-luciferin has to be converted by a mycobacterial-produced enzyme. Thus, preparation of mycobacteria-expressing eukaryotic [59–67] or prokaryotic [62,68–72] luciferase, which is not naturally produced by mycobacterial species, was a necessary step in all the mentioned studies.

Some of the first works describing the preparation of luciferase-expressing *M. tuberculosis* and *M. smegmatis* for antimicrobial agent-screening purposes *in vitro* were the studies done by Shinnick and colleagues [60] and Roberts and colleagues [68], respectively. In two decades after these studies, additional studies of this phenomenon were

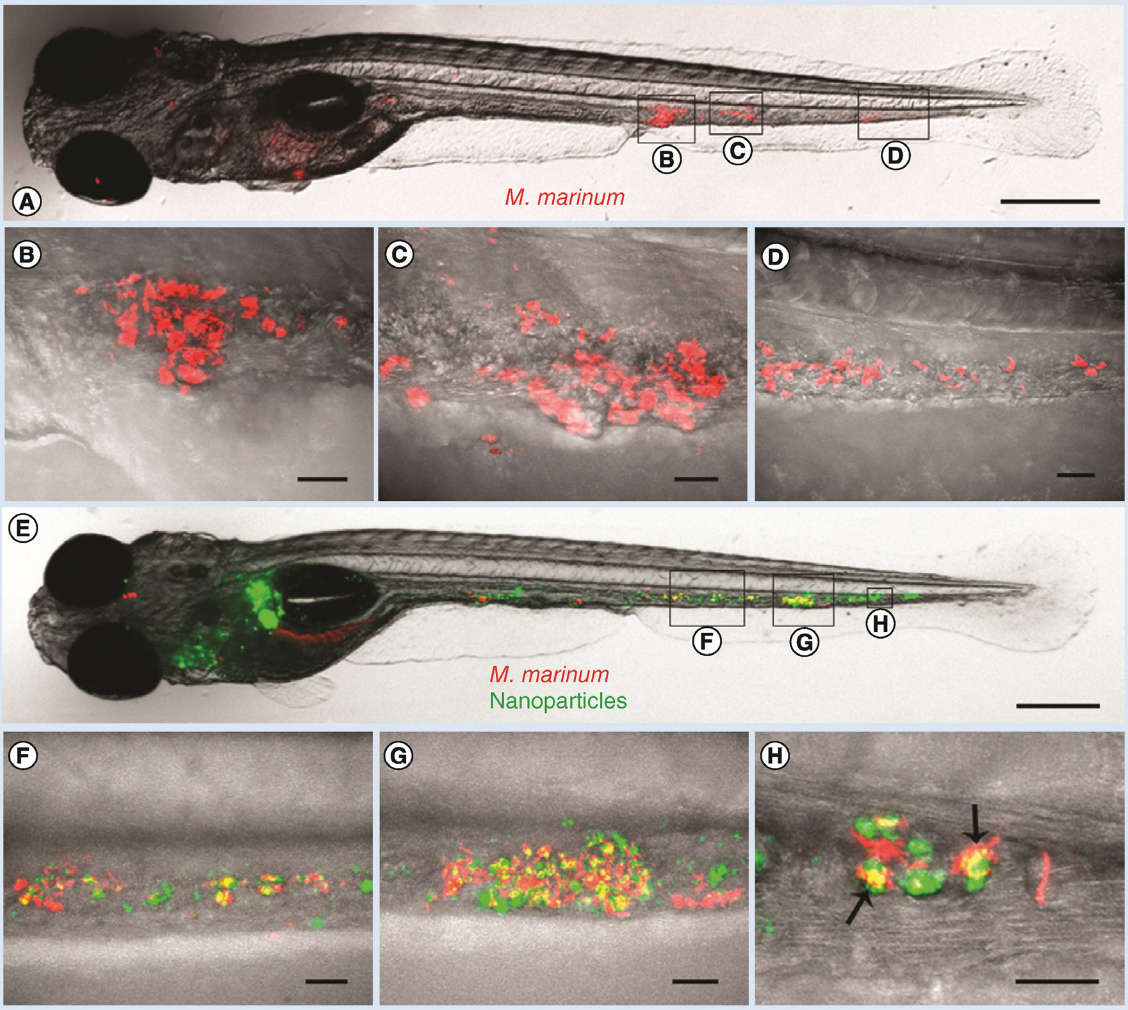

Figure 6. Use of a nanosized-based therapeutic system for the eradication of a *Mycobacterium marinum* infection and a zebrafish embryo-based *in vivo* study described by Griffiths and colleagues. Localization of fluorescently labeled NPs in the vicinity of bacterial cells. **(A & E)** Lateral views of the whole zebrafish embryos. **(B, D, F & H)** Lateral views of selected areas from **(A)** and **(E)**, respectively. **(A)** *M. marinum* cells injected into the posterior caudal vein are able to survive and grow, leading to the formation of granulomas **(B & C)**, as well as individually infected cells **(D)** 3-day postinfection. **(E)** NPs injected in the posterior caudal vein at 3-day postinfection are able to target granulomas **(G)** as well as individually infected cells **(F)**. NPs and mycobacteria are likely to be found in the same cells, as shown by arrows **(H)**. Scale bars: 300 μm **(A & E)**; 20 μm **(B, D, F & H)**, respectively.
Reprinted with permission from [47] © American Chemical Society (2014).

published for recombinant *M. aurum* [64], *M. avium* [63,65], *M. bovis* BCG [59,63,66,67,71], *M. intracellulare* [63,67], *M. smegmatis* [62,68], *M. tuberculosis* [60–63,69,70], *M. ulcerans* [72] and *M. marinum* [73].

One of the recent studies, for example, dealt with the aforementioned zebrafish larvae model in terms of screening of antimycobacterial compounds *in vivo*. Wiles and colleagues [73] studied whether zebrafish larvae could be naturally infected with bioluminescent *M. marinum*, and whether infected larvae could be used for screening using bioluminescence. They showed that the treatment caused retardation of a bioluminescent *M. marinum* infection that correlated with the retardation of *M. tuberculosis* growth *in vitro*, suggesting its usefulness as an assay for the rapid screening of antimycobacterial compounds.

It was shown that bioluminescence of luciferase-expressing mycobacteria correlates with the CFU values determined both *in vitro* and *in vivo*. Furthermore, the time required for the determination of MIC values can be greatly reduced using this approach.

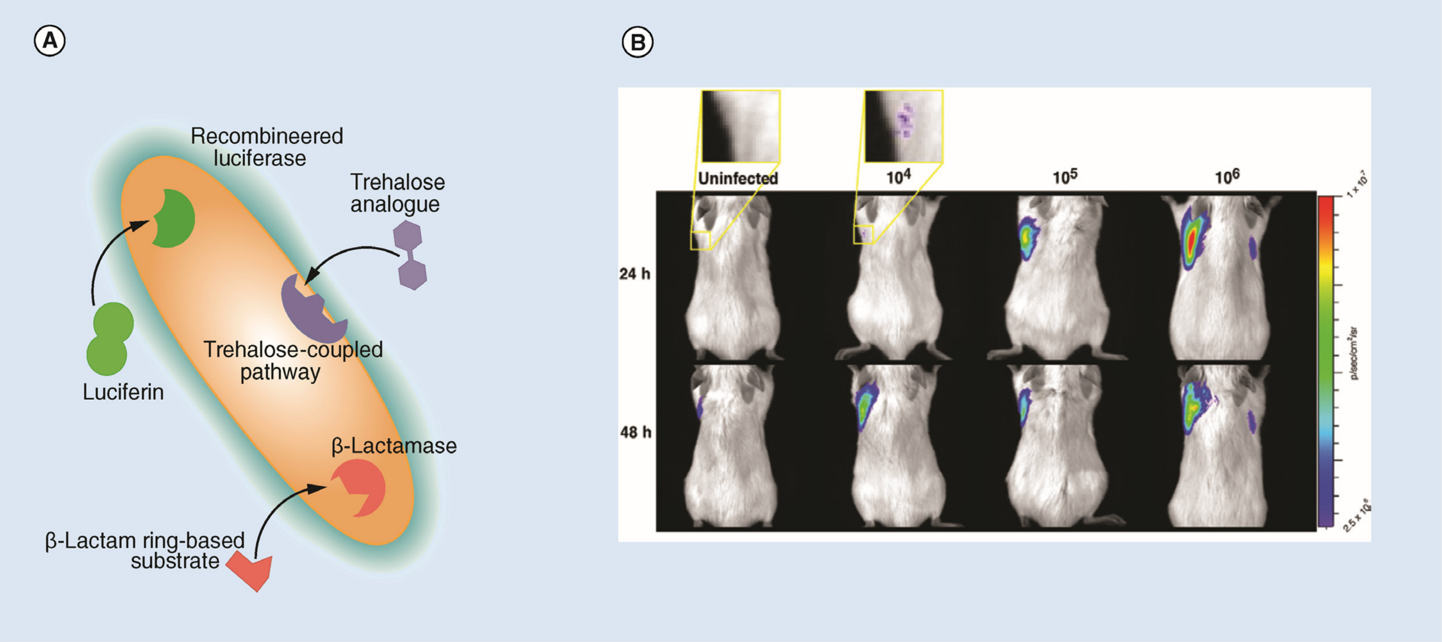

Figure 7. Reporter enzyme approaches. (A) Illustration of three reporter enzyme approaches for probing of mycobacteria. **(B)** *In vivo* application of a β-lactamase reporter described by Cirillo and colleagues [79]. Signal levels from mice infected with *M. bovis* BCG by the pulmonary route 1- and 2-day postinfection with different inoculum levels. The NIR β-lactamase substrate was administered immediately after infection. The yellow boxes within the first two mouse image panels indicate the regions that were magnified fourfold.
NIR: Near-infrared.
Reprinted with permission from [79].

A potential drawback is that except for several of the aforementioned approaches, all require the external addition of a luciferase substrate to the studied culture or animals. This limitation was overcome by the development of autoluminescent mycobacteria expressing both luciferase and the substrate [62,68–70].

Reporter mycobacteriophages

A specific but related option for the reporting of mycobacteria is their infection by mycobacteriophages recombineered to carry an FP gene. Various bacteriophage-based reporters have been investigated for the detection of specific mycobacteria [74–78], offering the advantages of rapid, sensitive and specific host detection and drug resistance for study.

For example, Piuri *et al.* [76] prepared recombinant mycobacteriophage Tm4 (phAE87) to detect *M. tuberculosis* by introducing genes encoding enhanced GFP and ZsYellow FP under the control of the *M. bovis* BCG *hsp60* promoter. The diagnostic assay was based on fluorescence microscopy after the infection, fixation and washing steps. In a report described by Mayer *et al.* [78], both fluorescent *M. tuberculosis* and NTM were generated using mVenus FP-carrying DS6A phages.

It is worth mentioning that despite all of the mentioned advantages, this tool may not be able to be used as a probe in the case of macrophage infection experiments as well as *in vivo* testing, due to a considerable doubt as to whether they would effectively reach their bacterial hosts, which may be intracellular and within granulomas.

Mycobacteria-specific reporters

Although the previously described recombinant approaches are suggested to be promising as tools for many research studies and assays in the field of infection biology, they require specific facilities for the recombinant strain preparation. Mycobacteria-specific luminescence (fluorescence or bioluminescence), however, can occur when mycobacteria-specific enzyme-substrate interactions result in bioluminescence or the formation of fluorescently active molecules *in situ* (Figure 7). As suspected, this principle, known as reporter enzyme fluorescence, is very similar to the above-described luciferase-based approach except no recombineering is required.

β-Lactamase-based reporters

Cirillo and colleagues [79,80] and Rao and colleagues [81,82], for example, developed substrates sensitive to the mycobacterial β-lactamase, an enzyme providing resistance to β lactam antibiotic for noninvasive imaging *in vivo*.

Substrates described in these studies were designed as fluorophore-quencher pairs connected by a cephalosporin-based β-lactamase-sensitive linkage (Figure 8A). During the initial state, no fluorescence is observable, because the energy donor (fluorophore) and energy acceptor (quencher) are sufficiently close to each other. Fluorescence occurs only when the β-lactamase-sensitive linkage is degraded, which is a widely used phenomenon called Förster resonance energy transfer [13].

The development of β-lactam ring-based substrates (Figure 8B) allowed for mycobacteria-analysis and imaging in the fluorescein- and umbelliferone-related visible spectral range [81,82], while the NIR substrates [79,80] were based on cyanine dyes, such as Cy5 or Cy5.5. Within the *in vivo* experiments, intravenous [79] and intraperitoneal [80] administration routes were used.

Trehalose-based reporters

A nonmammalian glucose disaccharide, trehalose, is a crucial player in the assembly and architecture of the remarkable cell envelope of mycobacteria. It is found in the mycobacterial cell wall, along with the glycolipids trehalose dimycolate and trehalose monomycolate, which participate in the cell wall associated pathogenicity of *M. tuberculosis* [83,84]. Biogenesis of the trehalose-containing cell envelope is based on a complex trehalose-coupled enzymatic apparatus that includes the extracellular proteins Ag85 mycolyltransferases and a high-affinity trehalose transporter system [85] that transports exogenous trehalose into the mycobacterial cytoplasm to be utilized in this complex trehalose-coupled metabolism.

In work by Backus *et al.* [86], it was demonstrated that a fluorescein isothiocyanate-conjugated trehalose analog is incorporated into trehalose dimycolate via the Ag85 complex. This finding underscores another possible route by which unnatural substrates might access trehalose glycolipids, resulting in a fluorescent probe that can label *M. tuberculosis* in both culture and in infected macrophages.

Subsequently, Swarts *et al.* [87] described a slightly different strategy for exploiting trehalose metabolic pathways to label mycobacterial glycolipids with azide-modified trehalose analogs. In this study, visualization of cell surface glycolipids was accomplished by subsequent biorthogonal ligation with an alkyne-functionalized fluorophore, enabling the interrogation of the trehalome in live mycobacteria. In general, these strategies can be used in terms of imaging and analysis of glycolipid distribution, trafficking and dynamics as well as metabolite profiling. In addition, Swarts *et al.* concluded that many of compounds may be employed to assess the effects of various perturbations, such as antibiotic treatment, genetic manipulations, etc.

Conclusion & future perspective

As the global number of infections caused by tubercle pathogens continues to rise, there is an urgency to determine whether novel treatment strategies are effective, how the pathogen interacts with its hosts both *in vitro* and *in vivo*, and how efficient mycobacterial probing and reporting is in terms of infection biology research. Hence, the aim of this work was to obtain a critical evaluation of approaches for the study of mycobacterial infections that use fluorescence- and bioluminescence-based detection methods.

Within this review, we described numerous mycobacteria-specific probes and reporters. These approaches include acid-fast staining, intrinsic fluorescence of the coenzyme F_{420}, fluorogenic substrates and recombination of mycobacteria or mycobacteriophages. Importantly, in recent years, fluorescence imaging *in vivo* has become an integral part of new and advanced anti-TB research approaches due in part to the adaptability of these methods in obtaining highly relevant data with regard to therapy efficacy, infection localization and pharmacokinetics. The expanding field of fluorescence-based probe design presents an alternative means to detect infections *in situ*. While fluorescence imaging approaches have several potential limitations, such as low sensitivity, poor depth penetration and unavoidable tissue autofluorescence in the case of *in vivo* experiments, advances in detection technology and the availability of advanced fluorescence spectroscopy-based systems could minimize these limitations and offer advantages for the elegant study of mycobacterial infections.

Despite the fact that recombinant bacteria are so widely used for high-throughput testing of new treatment procedures and drug-delivery systems with a small collection of known and described mycobacterial strains, we assume that the likeliest options for analysis, imaging and probing of mycobacterial infections, will be based on newly described mycobacteria-specific enzymatic pathways due to their possible in yielding mycobacterial strains

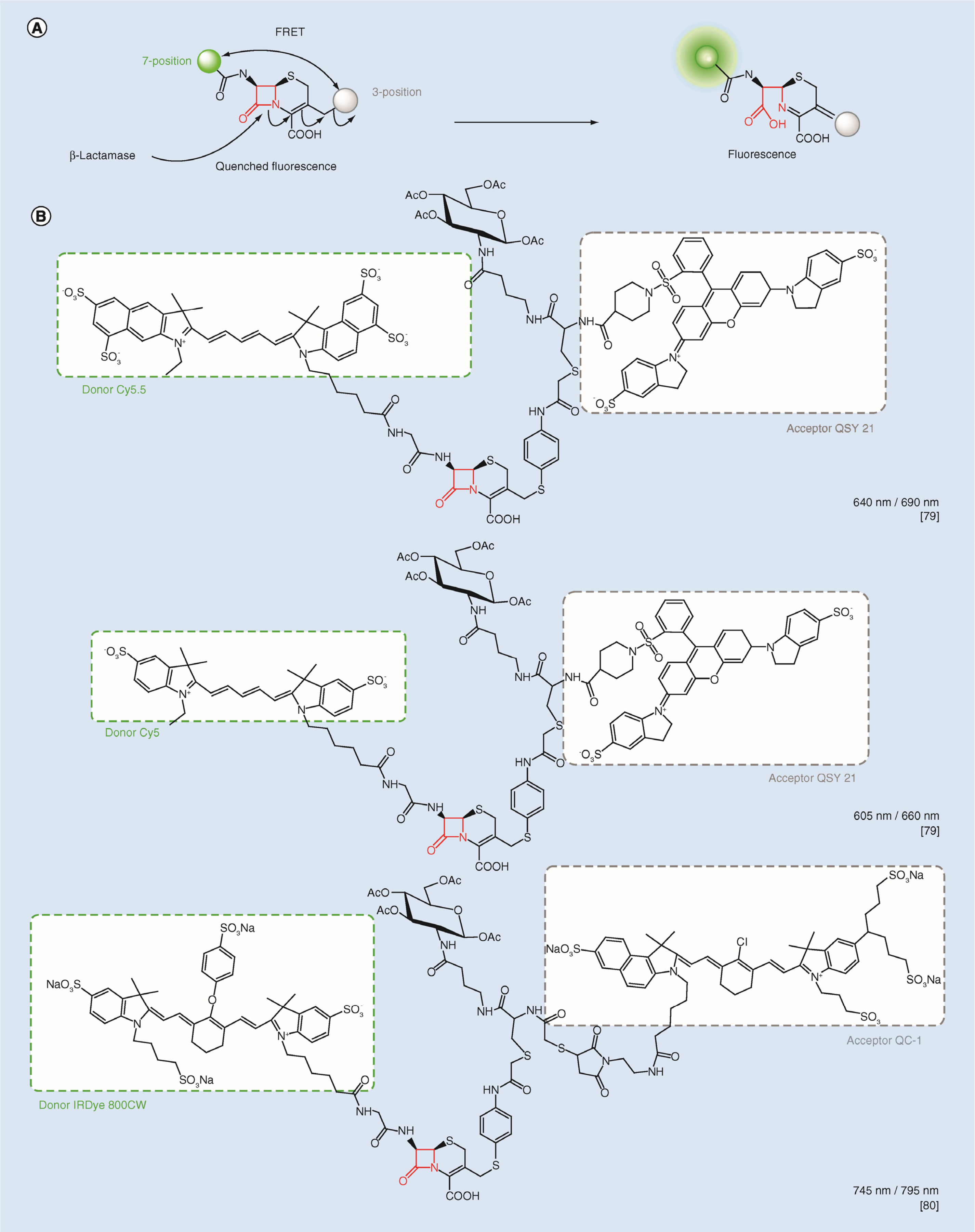

Figure 8. Mycobacteria-specific substrates. (A) Cephalosporin-based substrate reaction. β-Lactamase induces hydrolytic cleavage of the β-lactam ring, which causes a secondary reaction leading to the release of the energy acceptor molecule (quencher) in the 3-position. **(B)** Chosen β-lactamase-sensitive far-red/NIR substrates and their spectral maxima (Ex/Em). Fluorophores and quenchers are framed with green and shadow lines, respectively.

Em: Emission maxima; Ex: Excitation maxima; NIR: Near-infrared.

without the need to recombineering of the pathogens, an aspect allowing study of mycobacterial infections in terms of clinical diagnostics that is relevant, especially in developing countries struggling with TB. Specificity of such approaches, however, can be affected because some species can possess the same biochemical pathways or enzymes (e.g., β-lactam antibiotics-resistant bacteria). In contrast, the use of recombinant phages is very attractive due to the host specificity. However, we believe that the biggest challenge in this field of research is the doubt over whether the phages effectively reach intracellularly persisting mycobacteria both *in vitro* and *in vivo*.

Executive summary

- Mycobacteria-caused infections represent a global health problem.
- These diseases urgently require rapid diagnostic improvements and new methods to detect, analyze, image and probe the infect for both clinical diagnostics and mycobacterial research.
- Multiple fluorescence- and bioluminiscence-based approaches have been developed that allow us to analyze, probe and image mycobacterial infections both *in vitro* and *in vivo*. Each has its strengths and weaknesses.
- Since mycobacteria-specific fluorescence and bioluminescence correlates with CFU, recombineering of mycobacteria is relevant in terms of high-throughput screening of new antituberculous formulations and TB biology.
- Both mycobacteria-specific substrates and reporter mycobacteriophages have potential in terms of clinical diagnostics and analyzing of wild-type-caused infections.
- Tissues caused light scattering, light absorption and autofluorescence, however, they make the fluorescence detection harder.

Acknowledgements

The authors thank G Griffiths and A Sosnik for critical reading of the manuscript and M Havelková for help with graphics.

Financial & competing interests disclosure

Financial support from the Czech Science Foundation (grants 17-07164S and 17-09998S) and Charles University (project SVV260440) is gratefully acknowledged. The authors have no other relevant affiliations or financial involvement with any organization or entity with a financial interest in or financial conflict with the subject matter or materials discussed in the manuscript apart from those disclosed.

Writing assistance from American Journal Experts was utilized in the production of this manuscript.

References

Papers of special note have been highlighted as: • of interest; •• of considerable interest

1. Gelperina S, Kisich K, Iseman MD, Heifets L. The potential advantages of nanoparticle drug delivery systems in chemotherapy of tuberculosis. *Am. J. Respir. Crit. Care. Med.* 172(12), 1487–1490 (2005).
2. Sosnik A, Carcaboso ÁM, Glisoni RJ, Moretton MA, Chiappetta DA. New old challenges in tuberculosis: potentially effective nanotechnologies in drug delivery. *Adv. Drug Deliv. Rev.* 62(4), 547–559 (2010).
3. WHO. *Global Tuberculosis Report 2017.* World Health Organization (2017). www.who.int/tb/publications/global_report/en/
4. Kong Y, Yang D, Cirillo SLG *et al.* Application of fluorescent protein expressing strains to evaluation of anti-tuberculosis therapeutic efficacy *in vitro* and *in vivo*. *PLoS ONE* 11(3), e0149972 (2016).

•• **Recombineering of mycobacteria for the study of antituberculotic efficacy *in vitro* and *in vivo*.**

5. Magee JG, Ward AC. Mycobacterium. In: *Bergey's Manual of Systematics of Archaea and Bacteria.* Whitman WB (Ed.), John Wiley & Sons Ltd., NJ, USA, 1–84 (2015).
6. Barry CE, Mdluli K. Drug sensitivity and environmental adaptation of myocobacterial cell wall components. *Trends Microbiol.* 4(7), 275–281 (1996).
7. Griffith DE, Aksamit T, Brown-Elliott BA *et al.* An official ATS/IDSA statement: diagnosis, treatment, and prevention of nontuberculous mycobacterial diseases. *Am. J. Respir. Crit. Care Med.* 175(4), 367–416 (2007).
8. Mihret A. The role of dendritic cells in *Mycobacterium tuberculosis* infection. *Virulence* 3(7), 654–659 (2012).
9. Fenton MJ, Vermeulen MW. Immunopathology of tuberculosis: roles of macrophages and monocytes. *Infect. Immun.* 64(3), 683–690 (1996).
10. Hunter RL. Tuberculosis as a three-act play: a new paradigm for the pathogenesis of pulmonary tuberculosis. *Tuberculosis* 97, 8–17 (2016).

11. Nunes-Alves C, Booty MG, Carpenter SM, Jayaraman P, Rothchild AC, Behar SM. In search of a new paradigm for protective immunity to TB. *Nat. Rev. Micro.* 12(4), 289–299 (2014).

12. Amaral EP, Lasunskaia EB, D'império-Lima MR. Innate immunity in tuberculosis: how the sensing of mycobacteria and tissue damage modulates macrophage death. *Microbes Infect.* 18(1), 11–20 (2016).

13. Trousil J, Filippov SK, Hruby M *et al.* System with embedded drug release and nanoparticle degradation sensor showing efficient rifampicin delivery into macrophages. *Nanomedicine* 13(1), 307–315 (2017).

14. Ryu YJ. Diagnosis of pulmonary tuberculosis: recent advances and diagnostic algorithms. *Tuberc. Respir. Dis.* 78(2), 64–71 (2015).

15. Hendry C, Dionne K, Hedgepeth A, Carroll K, Parrish N. Evaluation of a rapid fluorescent staining method for detection of mycobacteria in clinical specimens. *J. Clin. Microbiol.* 47(4), 1206–1208 (2009).

16. Nema V. Tuberculosis diagnostics: challenges and opportunities. *Lung India* 29(3), 259–266 (2012).

17. Dezemon Z, Muvunyi CM, Jacob O. Staining techniques for detection of acid fast bacilli: what hope does fluorescein-diacetate (FDA) vitality staining technique represent for the monitoring of tuberculosis treatment in resource limited settings. *Trends Bacteriol.* doi:10.7243/2055-0901-1-1 (2014) (Online).

18. Pfyffer GE, Wittwer F. Incubation time of mycobacterial cultures: how long is long enough to issue a final negative report to the clinician? *J. Clin. Microbiol.* 50(12), 4188–4189 (2012).

19. Rufai SB, Kumar P, Singh A, Prajapati S, Balooni V, Singh S. Comparison of Xpert MTB/RIF with line probe assay for detection of rifampin-monoresistant *Mycobacterium tuberculosis*. *J. Clin. Microbiol.* 52(6), 1846–1852 (2014).

20. Friedrich SO, Rachow A, Saathoff E *et al.* Assessment of the sensitivity and specificity of Xpert MTB/RIF assay as an early sputum biomarker of response to tuberculosis treatment. *Lancet Respir. Med.* 1(6), 462–470 (2013).

21. Skoura E, Zumla A, Bomanji J. Imaging in tuberculosis. *Int. J. Infect. Dis.* 32, 87–93 (2015).

22. Ankrah AO, Van Der Werf TS, De Vries EF, Dierckx RA, Sathekge MM, Glaudemans AW. PET/CT imaging of *Mycobacterium tuberculosis* infection. *Clin. Transl. Imaging* 4, 131–144 (2016).

23. Daniel J, Maamar H, Deb C, Sirakova TD, Kolattukudy PE. *Mycobacterium tuberculosis* uses host triacylglycerol to accumulate lipid droplets and acquires a dormancy-like phenotype in lipid-loaded macrophages. *PLOS Pathog.* 7(6), e1002093 (2011).

24. Zhang M, Gong J, Lin Y, Barnes PF. Growth of virulent and avirulent *Mycobacterium tuberculosis* strains in human macrophages. *Infect. Immun.* 66(2), 794–799 (1998).

25. Kanade S, Nataraj G, Ubale M, Mehta P. Fluorescein diacetate vital staining for detecting viability of acid-fast bacilli in patients on antituberculosis treatment. *Int. J. Mycobacteriol.* 5(3), 294–298 (2016).

26. Ichijo T, Izumi Y, Yamaguchi N, Nasu M. Rapid enumeration of respiratory active mycobacteria with fluorescent double staining. *J. Microbiol. Methods* 82(3), 327–329 (2010).

27. Yamaguchi N, Nasu M. Flow cytometric analysis of bacterial respiratory and enzymatic activity in the natural aquatic environment. *J. Appl. Microbiol.* 83(1), 43–52 (1997).

28. Seleen WA, Stark CN. Some characteristics of green-fluorescent pigment-producing bacteria. *J. Bacteriol.* 46(6), 491–500 (1943).

29. Patiño S, Alamo L, Cimino M *et al.* Autofluorescence of mycobacteria as a tool for detection of *Mycobacterium tuberculosis*. *J. Clin. Microbiol.* 46(10), 3296–3302 (2008).

30. Wong C, Ha NP, Pawlowski ME, Graviss EA, Tkaczyk TS. Differentiating between live and dead *Mycobacterium smegmatis* using autofluorescence. *Tuberculosis (Edinb.)* 101(Suppl.), S119–S123 (2016).

31. Bair TB, Isabelle DW, Daniels L. Structures of coenzyme F(420) in *Mycobacterium* species. *Arch. Microbiol.* 176(1–2), 37–43 (2001).

32. Naraoka T, Momoi K, Fukasawa K, Goto M. Isolation and identification of a naturally occurring 7,8-didemethyl-8-hydroxy-5-deazariboflavin derivative from *Mycobacterium avium*. *Biochim. Biophys. Acta* 797(3), 377–380 (1984).

33. Isabelle D, Simpson DR, Daniels L. Large-scale production of coenzyme F(420)-5,6 by using *Mycobacterium smegmatis*. *Appl. Environ. Microbiol.* 68(11), 5750–5755 (2002).

34. Sutton WB. Properties of a new TPN-like electron transport component from mycobacteriumphlei. *Biochem. Biophys. Res. Commun.* 15(5), 414–419 (1964).

35. Daniels L, Bakhiet N, Harmon K. Widespread distribution of a 5-deazaflavin cofactor in actinomyces and related bacteria. *Syst. Appl. Microbiol.* 6(1), 12–17 (1985).

36. Shcherbakova DM, Verkhusha VV. Near-infrared fluorescent proteins for multicolor *in vivo* imaging. *Nat. Methods* 10(8), 751–754 (2013).

37. Frommer WB, Davidson MW, Campbell RE. Genetically encoded biosensors based on engineered fluorescent proteins. *Chem. Soc. Rev.* 38(10), 2833–2841 (2009).

38. Day RN, Davidson MW. The fluorescent protein palette: tools for cellular imaging. *Chem. Soc. Rev.* 38(10), 2887–2921 (2009).

39. Stepanenko OV, Verkhusha VV, Kuznetsova IM, Uversky VN, Turoverov KK. Fluorescent proteins as biomarkers and biosensors: throwing color lights on molecular and cellular processes. *Curr. Protein. Pept. Sci.* 9(4), 338–369 (2008).

40. Stepanenko OV, Stepanenko OV, Kuznetsova IM, Verkhusha VV, Turoverov KK. Beta-barrel scaffold of fluorescent proteins: folding, stability and role in chromophore formation. *Int. Rev. Cell. Mol. Biol.* 302, 221–278 (2013).
41. Craggs TD. Green fluorescent protein: structure, folding and chromophore maturation. *Chem. Soc. Rev.* 38(10), 2865–2875 (2009).
42. Goude R, Roberts DM, Parish T. Electroporation of mycobacteria. In: *Methods in Molecular Biology Mycobacteria Protocols*. Parish T, Brown AC (Eds). Springer NYUSA. 203–215 (2015).
43. Halaas Ø, Steigedal M, Haug M *et al.* Intracellular *Mycobacterium avium* intersect transferrin in the Rab11(+) recycling endocytic pathway and avoid lipocalin 2 trafficking the lysosomal pathway. *J. Infect. Dis.* 201(5), 783–792 (2010).
44. Zelmer A, Carroll P, Andreu N *et al.* A new *in vivo* model to test anti-tuberculosis drugs using fluorescence imaging. *J. Antimicrob. Chemother.* 67(8), 1948–1960 (2012).

•• **Recombineering of mycobacteria for the imaging of tuberculous infects *in vivo*.**

45. Carroll P, Schreuder LJ, Muwanguzi-Karugaba J *et al.* Sensitive detection of gene expression in mycobacteria under replicating and non-replicating conditions using optimized far-red reporters. *PLoS ONE* 5(3), e9823 (2010).
46. Beckwith MS, Beckwith KS, Sikorski P, Skogaker NT, Flo TH, Halaas Ø. Seeing a mycobacterium-infected cell in nanoscale 3D: correlative imaging by light microscopy and FIB/SEM tomography. *PLoS ONE* 10(9), e0134644 (2015).
47. Fenaroli F, Westmoreland D, Benjaminsen J *et al.* Nanoparticles as drug delivery system against tuberculosis in zebrafish embryos: direct visualization and treatment. *ACS Nano* 8(7), 7014–7026 (2014).

•• **A very important example for using of the zebrafish model in terms of novel nanobead-based interventions against TB.**

48. Al-Zarouni M, Dale JW. Expression of foreign genes in *Mycobacterium bovis* BCG strains using different promoters reveals instability of the hsp60 promoter for expression of foreign genes in *Mycobacterium bovis* BCG strains. *Tuberculosis* 82(6), 283–291 (2002).
49. Oldfield LM, Hatfull GF. Mutational analysis of the mycobacteriophage BPs promoter PR reveals context-dependent sequences for mycobacterial gene expression. *J. Bacteriol.* 196(20), 3589–3597 (2014).
50. Yang D, Ding F, Mitachi K, Kurosu M, Lee RE, Kong Y. A fluorescent probe for detecting *Mycobacterium tuberculosis* and identifying genes critical for cell entry. *Front. Microbiol.* 7, 2021 (2016).
51. Eitson JL, Medeiros JJ, Hoover AR *et al.* Mycobacterial shuttle vectors designed for high-level protein expression in infected macrophages. *Appl. Environ. Microbiol.* 78(19), 6829–6837 (2012).
52 . Ramakrishnan L. Looking within the zebrafish to understand the tuberculous granuloma. In: *The New Paradigm of Immunity to Tuberculosis*. Divangahi M (Ed.). Springer, NY, USA, 251–266 (2013).
53. Davis JM, Clay H, Lewis JL, Ghori N, Herbomel P, Ramakrishnan L. Real-time visualization of mycobacterium-macrophage interactions leading to initiation of granuloma formation in zebrafish embryos. *Immunity* 17(6), 693–702 (2002).

•• **First evidence of using of zebrafish larvae as an *in vivo* model of mycobacteria-caused infection.**

54. Takaki K, Cosma Christine L, Troll Mark A, Ramakrishnan L. An *in vivo* platform for rapid high-throughput antitubercular drug discovery. *Cell Rep.* 2(1), 175–184 (2012).
55. Kalluru R, Fenaroli F, Westmoreland D *et al.* Poly(lactide-co-glycolide)-rifampicin nanoparticles efficiently clear *Mycobacterium bovis* BCG infection in macrophages and remain membrane-bound in phago-lysosomes. *J. Cell. Sci.* 126(14), 3043–3054 (2013).
56. Clemens DL, Lee B-Y, Xue M *et al.* Targeted intracellular delivery of antituberculosis drugs to *Mycobacterium tuberculosis*-infected macrophages via functionalized mesoporous silica nanoparticles. *Antimicrob. Agents Chemother.* 56(5), 2535–2545 (2012).
57. Choi S-R, Britigan BE, Moran DM, Narayanasamy P. Gallium nanoparticles facilitate phagosome maturation and inhibit growth of virulent *Mycobacterium tuberculosis* in macrophages. *PLoS ONE* 12(5), e0177987 (2017).
58. Vibe CB, Fenaroli F, Pires D *et al.* Thioridazine in PLGA nanoparticles reduces toxicity and improves rifampicin therapy against mycobacterial infection in zebrafish. *Nanotoxicology* 10(6), 680–688 (2016).
59. Hickey MJ, Arain TM, Shawar RM *et al.* Luciferase *in vivo* expression technology: use of recombinant mycobacterial reporter strains to evaluate antimycobacterial activity in mice. *Antimicrob. Agents Chemother.* 40(2), 400–407 (1996).
60. Cooksey RC, Crawford JT, Jacobs WR, Shinnick TM. A rapid method for screening antimicrobial agents for activities against a strain of *Mycobacterium tuberculosis* expressing firefly luciferase. *Antimicrob. Agents Chemother.* 37(6), 1348–1352 (1993).
61. Andreu N, Zelmer A, Sampson SL *et al.* Rapid *in vivo* assessment of drug efficacy against *Mycobacterium tuberculosis* using an improved firefly luciferase. *J. Antimicrob. Chemother.* 68(9), 2118–2127 (2013).
62. Andreu N, Zelmer A, Fletcher T *et al.* Optimisation of bioluminescent reporters for use with mycobacteria. *PLoS ONE* 5(5), e10777 (2010).
63. Arain TM, Resconi AE, Hickey MJ, Stover CK. Bioluminescence screening *in vitro* (Bio-Siv) assays for high-volume antimycobacterial drug discovery. *Antimicrob. Agents Chemother.* 40(6), 1536–1541 (1996).
64. Deb DK, Srivastava KK, Srivastava R, Srivastava BS. Bioluminescent *Mycobacterium aurum* expressing firefly luciferase for rapid and high throughput screening of antimycobacterial drugs *in vitro* and in infected macrophages. *Biochem. Biophys. Res. Commun.* 279(2), 457–461 (2000).

65. Cooksey RC, Morlock GP, Beggs M, Crawford JT. Bioluminescence method to evaluate antimicrobial agents against *Mycobacterium avium*. *Antimicrob. Agents Chemother.* 39(3), 754–756 (1995).

66. Chang M, Anttonen KP, Cirillo SLG, Francis KP, Cirillo JD. Real-time bioluminescence imaging of mixed mycobacterial infections. *PLoS ONE* 9(9), e108341 (2014).

67. Shawar RM, Humble DJ, Van Dalfsen JM *et al.* Rapid screening of natural products for antimycobacterial activity by using luciferase-expressing strains of *Mycobacterium bovis* BCG and *Mycobacterium intracellulare*. *Antimicrob. Agents Chemother.* 41(3), 570–574 (1997).

68. Andrew PW, Roberts IS. Construction of a bioluminescent mycobacterium and its use for assay of antimycobacterial agents. *J. Clin. Microbiol.* 31(9), 2251–2254 (1993).

69. Andreu N, Fletcher T, Krishnan N, Wiles S, Robertson BD. Rapid measurement of antituberculosis drug activity *in vitro* and in macrophages using bioluminescence. *J. Antimicrob. Chemother.* 67(2), 404–414 (2012).

70. Zhang T, Li S-Y, Nuermberger EL. Autoluminescent *Mycobacterium tuberculosis* for rapid, real-time, non-invasive assessment of drug and vaccine efficacy. *PLoS ONE* 7(1), e29774 (2012).

71. Heuts F, Carow B, Wigzell H, Rottenberg ME. Use of non-invasive bioluminescent imaging to assess mycobacterial dissemination in mice, treatment with bactericidal drugs and protective immunity. *Microbes Infect.* 11(14–15), 1114–1121 (2009).

72. Zhang T, Li S-Y, Converse PJ, Almeida DV, Grosset JH, Nuermberger EL. Using bioluminescence to monitor treatment response in real time in mice with *Mycobacterium ulcerans* infection. *Antimicrob. Agents Chemother.* 55(1), 56–61 (2011).

73. Dalton JP, Uy B, Okuda KS *et al.* Screening of anti-mycobacterial compounds in a naturally infected zebrafish larvae model. *J. Antimicrob. Chemother.* 72(2), 421–427 (2017).

74. Da Silva JL, Piuri M, Broussard G *et al.* Application of BRED technology to construct recombinant D29 reporter phage expressing EGFP. *FEMS Microbiol. Lett.* 344(2), 166–172 (2013).

75. Rondón L, Piuri M, Jacobs WR, De Waard J, Hatfull GF, Takiff HE. Evaluation of fluoromycobacteriophages for detecting drug resistance in *Mycobacterium tuberculosis*. *J. Clin. Microbiol.* 49(5), 1838–1842 (2011).

76. Piuri M, Jacobs WR Jr., Hatfull GF. Fluoromycobacteriophages for rapid, specific, and sensitive antibiotic susceptibility testing of *Mycobacterium tuberculosis*. *PLoS ONE* 4(3), e4870 (2009).

77. Jain P, Thaler DS, Maiga M *et al.* Reporter phage and breath tests: emerging phenotypic assays for diagnosing active tuberculosis, antibiotic resistance, and treatment efficacy. *J. Infect. Dis.* 204(Suppl. 4), S1142–S1150 (2011).

78. Mayer O, Jain P, Weisbrod TR *et al.* Fluorescent reporter DS6A mycobacteriophages reveal unique variations in infectibility and phage production in mycobacteria. *J. Bacteriol.* 198(23), 3220–3232 (2016).

79 . Kong Y, Yao H, Ren H *et al.* Imaging tuberculosis with endogenous β-lactamase reporter enzyme fluorescence in live mice. *Proc. Natl Acad. Sci. USA* 107(27), 12239–12244 (2010).

•• **A very important example for reporting enzyme fluorescence in live mice.**

80. Yang HJ, Kong Y, Cheng Y *et al.* Real-time imaging of *Mycobacterium tuberculosis*, using a novel near-infrared fluorescent substrate. *J. Infect. Dis.* 215(3), 405–414 (2017).

• **Shows the application of near-infrared fluorescent substrate in live mice.**

81. Cheng Y, Xie H, Sule P *et al.* Fluorogenic probes with substitutions at the 2 and 7 positions of cephalosporin are highly BlaC-specific for rapid *Mycobacterium tuberculosis* detection. *Angew. Chem. Int. Ed. Engl.* 53(35), 9360–9364 (2014).

82. Xie H, Mire J, Kong Y *et al.* Rapid point-of-care detection of the tuberculosis pathogen using a BlaC-specific fluorogenic probe. *Nat. Chem.* 4(10), 802–809 (2012).

83. Yamagami H, Matsumoto T, Fujiwara N *et al.* Trehalose 6,6′-dimycolate (cord factor) ofmycobacterium tuberculosis induces foreign-body- and hypersensitivity-type granulomas in mice. *Infect. Immun.* 69(2), 810–815 (2001).

84. Nobre A, Alarico S, Maranha A, Mendes V, Empadinhas N. The molecular biology of mycobacterial trehalose in the quest for advanced tuberculosis therapies. *Microbiology* 160(8), 1547–1570 (2014).

85. Kalscheuer R, Weinrick B, Veeraraghavan U, Besra GS, Jacobs WR. Trehalose-recycling ABC transporter LpqY-SugA-SugB-SugC is essential for virulence of *Mycobacterium tuberculosis*. *Proc. Natl Acad. Sci. USA* 107(50), 21761–21766 (2010).

86. Backus KM, Boshoff HI, Barry CS *et al.* Uptake of unnatural trehalose analogs as a reporter for *Mycobacterium tuberculosis*. *Nat. Chem. Biol.* 7(4), 228–235 (2011).

87. Swarts BM, Holsclaw CM, Jewett JC *et al.* Probing the mycobacterial trehalome with bioorthogonal chemistry. *J. Am. Chem. Soc.* 134(39), 16123–16126 (2012).

88. Amemura-Maekawa J, Hayakawa Y, Sugie H *et al.* Legioliulin, a new isocoumarin compound responsible for blue-white autofluorescence in Legionella (Fluoribacter) dumoffii under long-wavelength UV light. *Biochem. Biophys. Res. Commun.* 323(3), 954–959 (2004).

89. Silva GAD, Almeida EAD. Production of yellow-green fluorescent pigment by *Pseudomonas fluorescens*. *Braz. Arch. Biol. Technol.* 49, 411–419 (2006).

90. Meyer JM, Abdallah MA. The fluorescent pigment of pseudomonas fluorescens: biosynthesis, purification and physicochemical properties. *Microbiology* 107(2), 319–328 (1978).

91. Bashiri G, Rehan AM, Greenwood DR, Dickson JMJ, Baker EN. Metabolic engineering of cofactor F420 production in *Mycobacterium smegmatis*. *PLoS ONE* 5(12), e15803 (2011).

92. Kobayashi H, Ogawa M, Alford R, Choyke PL, Urano Y. New strategies for fluorescent probe design in medical diagnostic imaging. *Chem. Rev.* 110(5), 2620–2640 (2010).